Turbulent patterns in wall-bounded shear flows: invariant solutions and their bifurcations

Thèse N° 7263

Présentée le 15 novembre 2019

à la Faculté des sciences et techniques de l'ingénieur
Complexité émergente dans les systèmes physiques
Programme doctoral en mécanique

pour l'obtention du grade de Docteur ès Sciences

par

Florian REETZ

Acceptée sur proposition du jury

Prof. W. Curtin, président du jury
Prof. T. Schneider, directeur de thèse
Prof. L. Tuckerman, rapporteuse
Prof. E. Knobloch, rapporteur
Prof. F. Gallaire, rapporteur

2019

ÉCOLE POLYTECHNIQUE
FÉDÉRALE DE LAUSANNE

"The next great era of awakening of human intellect may well produce a method of understanding the qualitative content of equations. Today we cannot. Today we cannot see that the water flow equations contain such things as the barber pole structure of turbulence that one sees between rotating cylinders. Today we cannot see whether Schrödinger's equation contains frogs, musical composers, or morality - or whether it does not."

— The Feynman lectures on physics, Vol. 2 (1964)

To Romy and Björn ...

Abstract

When laminar shear flows in large wall-bounded domains transition to turbulence, the flow exhibits spatio-temporally chaotic dynamics. Despite its chaotic dynamics, the flow may self-organize into characteristic spatially periodic patterns of unknown origin. To understand how regular patterns emerge in a turbulent flow, a nonlinear theory is needed. In this thesis we apply dynamical systems theory to explain the spatial structure, origin and dynamics of turbulent patterns. To this end, we construct and analyze exact invariant solutions of the 3D nonlinear fluid flow equations that capture the non-trivial spatial structure of the patterns. This approach requires high-performance computational tools, that have been developed as part of this thesis and are now publicly available within the widely used state-of-the-art open source software *Channelflow 2.0*. Using the developed tools, we explain turbulent patterns in two different wall-bounded shear flows:

In plane Couette flow, the flow between two parallel walls moving in opposite direction, turbulent flow emerges subcritically and may coexist with regions of laminar flow. For specific wall velocities, the turbulent-laminar flow self-organizes into an intricate pattern of periodically alternating laminar and turbulent bands oriented obliquely against the direction of the wall movement. Experiments and simulations have reproduced the oblique stripe pattern for more than 50 years but the pattern characteristics, in particular the wavelength and the oblique orientation, remain to be explained. We present the first unstable equilibrium solution of the fully nonlinear Navier-Stokes equations that captures the flow structure of oblique turbulent-laminar stripes. Using numerical continuation, we show how the stripe equilibrium bifurcates from the well-known Nagata equilibrium via two successive symmetry-breaking bifurcations. Within the subspace of the symmetry that is broken by the second bifurcation, we identify three obliquely patterned periodic orbits embedded in the edge of chaos. The spatial structure of these invariant solutions suggests a nonlinear mechanism by which weakly turbulent Couette flow selects the wavelength and the oblique orientation of turbulent-laminar stripes.

The second studied system is inclined layer convection, a thermally driven shear flow in an inclined channel. Like Rayleigh-Bénard convection, the case of zero inclination, inclined layer convection shows a large variety of different convection patterns when the control parameters are varied. While linear stability analysis has explained the onset of some of these patterns,

their spatio-temporally complex dynamics is not well understood. We identify a multitude of invariant solutions underlying previously observed pattern motifs at a Prandtl number of 1.07 and show how the nonlinear time evolution in inclined layer convection follows dynamical connections between invariant solutions. Numerical continuation of stable and unstable invariant solutions under changing thermal driving and inclination angle reveals an extensive network of bifurcating solution branches. The bifurcation structures indicate existence, stability and dynamical connectivity of invariant solutions. We thereby reveal how spatio-temporally complex convection patterns depend on the control parameters in inclined layer convection.

Keywords: Transition to turbulence, pattern formation, shear flows, thermal convection, nonlinear dynamical systems, bifurcation theory, high-performance computing, computational fluid dynamics

Résumé

Dans cette thèse, nous nous intéressons aux écoulements de cisaillement dans un large domaine délimité par des parois. Lorsque ce type d'écoulements effectue une transition d'un état laminaire vers un état turbulent, le flux manifeste une dynamique spatio-temporelle chaotique. Malgré cette évolution chaotique, l'écoulement peut s'organiser de lui-même en structures caractéristiques, spatialement périodiques et d'origine inconnue. Il est nécessaire de mobiliser une théorie non-linéaire afin de comprendre comment ces structures régulières émergent dans un écoulement turbulent. Dans cette thèse, nous mobilisons la théorie des systèmes dynamiques pour expliquer l'organisation spatiale, l'origine et l'évolution de structures turbulentes. Pour cela, nous construisons et analysons des solutions exactes et invariantes aux équations tridimensionnelles et non-linéaires de la mécanique des fluides. Ces solutions capturent l'organisation spatiale non-triviale de ces structures. Cette approche requiert des outils de calcul à hautes-performances, qui ont été développés dans le cadre de cette thèse et sont désormais disponible publiquement dans un logiciel de recherche de pointe, open-source et largement utilisé, *Channelflow 2.0*. A l'aide de ces outils, nous expliquons les structures turbulentes dans deux types différents d'écoulements limités par des parois :

Dans un écoulement de Couette (c'est-à-dire où le flux évolue entre deux parois parallèles se déplaçant dans des directions opposées), un écoulement turbulent émerge de manière sous-critique et peut coexister avec des régions d'écoulement laminaire. Pour des vitesses de parois spécifiques, l'écoulement turbulent-laminaire s'organise de lui-même en une formation complexe de bandes obliques, alternant périodiquement entre écoulement laminaire et turbulent et orientées par rapport à la direction du mouvement des parois. Depuis plus de 50 ans, des expérimentations et simulations ont reproduit la structure en bandes obliques, mais ses caractéristiques, et en particulier sa longueur d'onde et son orientation oblique, reste à expliquer. Nous présentons ici la première solution d'équilibre instable des équations de Navier-Stokes, entièrement non-linéaires, qui capture la structure oblique de bandes turbulentes-laminaires. A l'aide de continuation numérique, nous montrons comment cet équilibre bifurque du célèbre équilibre de Nagata via deux bifurcations successives, rompant chacune une symétrie. A l'intérieur du sous-espace de la symétrie rompue par la seconde bifurcation, nous identifions trois orbites périodiques à motif oblique, incrustées dans le bord du chaos. La structure spatiale de ces solutions invariantes suggère un mécanisme non-linéaire

par lequel l'écoulement de Couette faiblement turbulent sélectionne la longueur d'onde et l'orientation oblique des bandes turbulentes-laminaires.

Le second système étudié est la convection de couche inclinée, soit un flux de cisaillement thermiquement entraîné dans un canal incliné. La convection de couche inclinée témoigne d'une grande variété de structures convectives quand les paramètres de commande sont modifiés, comme pour la convection de Rayleigh-Bénard où l'inclinaison est nulle. Alors que l'analyse de stabilité linéaire a expliqué l'apparition de certaines de ces structures, leurs dynamiques spatio-temporelles complexes n'est pas entièrement comprise. Nous identifions ici une multitude de solutions invariantes, à l'origine de motifs déjà observés au nombre de Prandtl de 1.07, et montrons comment l'évolution temporelle non-linéaire de la convection de couche inclinée découle de connexions dynamiques entre solutions invariantes. La continuation numérique de solutions invariantes stables et instables, soumises à des variations de contraintes thermiques et d'angle d'inclinaison, révèle un vaste réseau de solutions. Celles-ci sont interconnectées entre-elles grâce des bifurcations, dont l'organisation indique l'existence, la stabilité et la connectivité dynamique de solutions invariantes. Nous révélons ici comment ces motifs de convection, a l'évolution spatio-temporelle complexe, dépendent des paramètres de commande dans la convection de couche inclinée.

Mots-clefs : Transition vers la turbulence, formation de motifs, écoulement de cisaillement, convection thermique, systèmes dynamiques non-linéaires, théorie de la bifurcation, informatique haute-performance, mécanique des fluides numériques.

Zusammenfassung

Wenn laminare Scherströmungen in einem schmalen Spalt zwischen zwei räumlich ausgedehnten Wänden turbulent werden, zeigt die Strömung raum-zeitlich chaotische Dynamik. Trotz der chaotischen Dynamik kann sich die Strömung in charakteristischen, räumlich periodischen Mustern unbekannten Ursprungs selbst organisieren. Um die Entstehung dieser regelmäßigen Muster in einer turbulenten Strömung zu verstehen, bedarf es einer nichtlinearen Theorie. In dieser Doktorarbeit wenden wir die Theorie dynamischer Systeme an, um die räumliche Struktur, den Ursprung und die Dynamik von turbulenten Mustern zu erklären. Hierzu konstruieren und analysieren wir exakt invariante Lösungen der 3D nichtlinearen Strömungsgleichungen, welche die nichttriviale räumliche Struktur der Muster erfassen. Diese Herangehensweise benötigt Tools für Hochleistungsrechnungen, die im Rahmen dieser Doktorarbeit entwickelt wurden und nun öffentlich zugänglich sind als Teil der hochmodernen Open-Source-Software *Channelflow 2.0*. Dank der entwickelten Tools können wir turbulente Muster in zwei verschiedenen, durch Wände begrenzten Scherströmungen erklären:

In ebener Couette Strömung, einer Strömung zwischen zwei parallelen Wänden die sich in entgegengesetzte Richtungen bewegen, entstehen turbulente Strömungen subkritisch und können mit Regionen laminarer Strömung im Raum koexistieren. Für spezifische Wandgeschwindigkeiten organisiert sich die turbulent-laminare Strömung selbst zu einem komplizierten Muster, in dem laminare und turbulente Bänder periodisch wechseln und geneigt gegen die Bewegungsrichtung der Wände orientiert sind. Experimente und Simulationen haben dieses geneigte Streifenmuster über 50 Jahre hinweg immer wieder reproduziert. Dennoch bleiben die Mustereigenschaften, insbesondere die Wellenlänge und die geneigte Orientierung, nach wie vor unerklärt. Wir beschreiben die erste instabile Gleichgewichtslösung der vollen nichtlinearen Navier-Stokes-Gleichungen, welche die Strömungsstruktur der geneigten turbulent-laminaren Streifen erfasst. Unter Verwendung numerischer Fortführungsmethoden zeigen wir wie die Streifenlösung von der bekannten Nagata-Lösung in zwei aufeinanderfolgenden symmetriebrechenden Bifurkationen entsteht. Innerhalb des Symmetrieunterraums der Symmetrie, die durch die zweite Bifurkation gebrochen wird, identifizieren wir drei periodische Orbits mit geneigtem Muster, welche in der Schwelle zum Chaos (“edge of chaos”) eingebettet sind. Die räumliche Struktur dieser invarianten Lösungen legt einen nichtlinearen Mechanismus nahe mittels dessen schwach turbulente Couette Strömung die Wellenlänge

und die geneigte Orientierung der turbulent-laminaren Streifen auswählt.

Das zweite untersuchte System ist Schrägschichtkonvektion, eine thermisch getriebene Scherströmung in einem schrägen Kanal. Wie im nicht-schrägen Fall der Rayleigh-Benard-Konvektion, zeigt Schrägschichtkonvektion eine große Vielfalt von unterschiedlichen Konvektionsmustern, wenn Kontrollparameter verändert werden. Während die beginnende Entstehung einiger dieser Muster schon durch lineare Stabilitätsanalyse erklärt werden konnte, ist deren raumzeitlich komplexe Dynamik nicht gut verstanden. Wir identifizieren eine Vielzahl von invarianten Lösungen, die Mustermotiven zugrunde liegen, welche in vorhergehenden Studien bei einer Prandtl-Zahl von 1.07 beobachtet wurden, und zeigen wie die nichtlineare Zeitentwicklung in Schrägschichtkonvektion dynamischen Verbindungen zwischen invarianten Lösungen folgt. Numerische Fortführung von stabilen und instabilen invarianten Lösungen unter veränderlicher Schräge und thermischem Antrieb offenbart ein umfangreiches Netzwerk von Lösungsästen. Die Bifurkationsstruktur weist auf Existenz, Stabilität und dynamische Verbindung von invarianten Lösungen hin. Dadurch können wir zeigen wie raum-zeitlich komplexe Dynamik von Konvektionsmustern von den Kontrollparametern in Schrägschichtkonvektion abhängen.

Stichwörter: Turbulenzübergang, Musterbildung, Scherströmung, Thermische Konvektion, Nichtlineare Dynamische Systeme, Bifurkationstheorie, Numerische Strömungsmechanik, Hochleistungsrechnung

Contents

1 Introduction

A fluid resides in a narrow gap between two extended walls. Moving or heating the two walls differently creates forces in the fluid that drive a flow. One example for such a wall-bounded flow, driven by moving the walls, is Taylor-Couette flow (TCF). Here, two concentric cylinders rotate at different angular velocities and drive a flow in the gap between the cylinders. At particular angular velocities, the flow may adopt stable flow structures that periodically repeat in the two directions along the walls and thereby form a regular pattern in space. Figure 1.1a shows a snapshot of an experimentally observed regular pattern in TCF called wavy vortex flow. Bright and dark regions represent different orientations of the flow and indicate a wavy pattern with clear pattern wavelengths along the walls. The preferred pattern wavelengths and the critical driving forces at which stable regular patterns, like wavy vorticies in TCF, emerge can often be explained by applying methods from pattern formation theory for non-equilibrium systems (Cross and Hohenberg, 1993; Cross and Greenside, 2009). These methods include linear stability analysis and the construction of weakly nonlinear amplitude equations. When the relative velocity of the two cylinders is increased, the regular wavy vortex pattern becomes unstable and the flow may eventually become turbulent, giving rise to turbulent patterns (e.g. Andereck et al., 1986). In this context, *turbulence* does not imply a fully developed turbulent flow with an energy cascade across multiple spatial scales but a flow that shows spatio-temporally chaotic dynamics. Nevertheless, the strongly nonlinear dynamics of even such weakly turbulent flow makes turbulent patterns to large extent inaccessible to linear or weakly nonlinear analyses.

The situation is very similar in Rayleigh-Bénard convection (RBC), an example for a wall-bounded flow which is driven by heating two parallel horizontal walls differently. Like TCF, RBC exhibits a large variety of different patterns (Cross and Hohenberg, 1993; Cross and Greenside, 2009) which, when increasing the temperature difference between the walls, become more and more complicated and eventually turbulent. Figure 1.1c shows an example for a regular steady stripe pattern in RBC that becomes unstable to a spatially localized modulation. While the

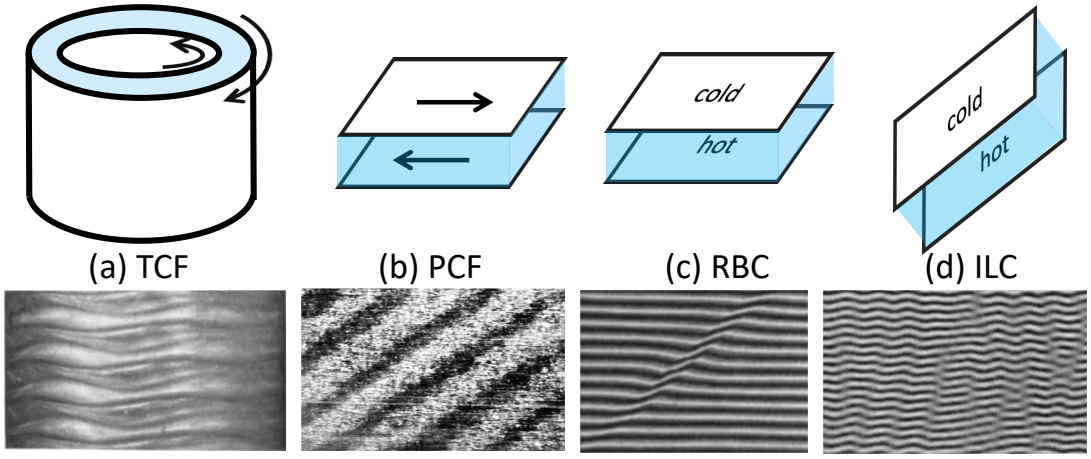

Figure 1.1 – Different nonlinear flow patterns observed experimentally in four different wall-bounded flows (sketched). The fluid (blue) resides in a narrow gap between two parallel walls with two extended space dimensions. The patterns are shown over the two extended space dimensions along the walls. (a) Taylor-Couette flow (TCF) may exhibit a regular pattern called wavy vortex flow (Fenstermacher et al., 1979). (b) Plane Couette flow (PCF) may exhibit a regular oblique stripe pattern of periodically alternating turbulent and laminar bands (Prigent et al., 2002). (c) Rayleigh-Bénard convection may exhibit spatially localized skewed varicose modulations within regular straight convection rolls (Bodenschatz et al., 2000). (d) Inclined layer convection may exhibit regular wavy convection rolls coexisting at various orientations (Daniels et al., 2000). Note that the aspect ratio relative to the gap size and the visualization method is not equal between the images. The pattern in (a) is well understood. Explaining the regularity in pattern (b) and the complex features related to spatial coexistence of different patterns in (c) and (d) is subject of the present thesis.

onset of this so-called skewed varicose instability can be characterized using linear stability analysis (Busse and Clever, 1979), it may generate defects in the pattern with a non-trivial time evolution (Figure 7 in Bodenschatz et al., 2000) and eventually may lead to a highly irregular and turbulent pattern called spiral defect chaos (Morris et al., 1993).

The discovery of non-periodic solutions (Lorenz, 1963) and “strange attractors” supporting chaos in deterministic nonlinear equations (Ruelle and Takens, 1971) changed the view on turbulent flow, governed by the deterministic nonlinear Navier-Stokes equations. Instead of describing the onset of turbulence as an increasing number of superimposed periodic flows (Landau and Lifschitz, 1987; Hopf, 1948), many different routes to turbulence have been described within nonlinear dynamical systems theory (see Eckmann, 1981; Argyris et al., 1993, for reviews). These routes to turbulence have been identified in both TCF (Gollub and Swinney, 1975, e.g.) and RBC (Swinney and Gollub, 1978, e.g.). Thus, dynamical systems theory seems to apply to turbulent flows providing useful descriptions of the strongly nonlinear dynamics.

Nonlinear dynamical systems theory is often used to explain the complex temporal dynamics of turbulence. However, when wall-bounded flows like TCF or RBC transition to turbulence, regular spatial patterns may exist in the flow, thereby forming a turbulent pattern. In order to explain a turbulent pattern, the regular features in the pattern, like pattern wavelength or orientation, must be explained together with the complex features that exhibit turbulent dynamics. Here, turbulent dynamics refers to spatio-temporally complex or weakly chaotic dynamics, in contrast to fully developed turbulence with certain statistical properties (Frisch, 1995). For the present thesis, two different wall-bounded flows are studied that each gives rise to turbulent patterns in a different way:

(a) The flow has self-organized into a regular spatial pattern. When the driving forces are changed, the regular pattern develops increasingly complex features, like evolving defects or intermittent bursts, leading to a turbulent pattern.

(b) The flow is turbulent and unpatterned. When the driving forces are changed, the turbulent flow self-organizes into a turbulent pattern with regular features like a pattern wavelength and orientation.

First, turbulent patterns of type (a) are studied in inclined layer convection (ILC). Like RBC, ILC is a thermally driven flow between two differently heated parallel walls. Unlike in RBC, the walls may be inclined against gravity in ILC. Buoyancy forces along the walls drive hot and cold fluid up and down the incline creating a thermally driven shear flow. At moderate inclinations and moderate temperature differences, ILC gives for example rise to a steady regular pattern of wavy convection rolls. When the temperature difference between the walls is increased, the regular wavy rolls become more complex by incorporating defects that dynamically evolve and create spatial coexistence of wavy rolls with different orientations. Figure 1.1d shows an experimental snapshot of weakly turbulent wavy rolls. Besides wavy rolls, many other spatio-temporal patterns with weakly turbulent dynamics have been observed in experiments of ILC. The turbulent dynamics of these spatio-temporal convection patterns in ILC is not well understood. Section 1.2 introduces the problem of spatio-temporal patterns in ILC in more detail.

Second, turbulent patterns of type (b) are studied in plane Couette flow (PCF). Here, a wall-bounded shear flow is driven by moving two parallel planar walls against each other. In contrast to TCF, PCF is not subject to centrifugal forces that may destabilize the laminar flow and create patterns. In PCF observed patterns are always turbulent. For particular relative wall velocities, turbulent PCF may self-organize into a regular pattern of oblique turbulent-laminar stripes (Figure 1.1b). How turbulent PCF selects a pattern wavelength and the oblique orientation is not well understood. Section 1.3 introduces the problem of oblique turbulent-laminar stripes in PCF in more detail.

Turbulent patterns in ILC and PCF are studied using a numerical nonlinear dynamical systems analysis of fully resolved three-dimensional flows. This approach is introduced in the following subsection.

1.1 Numerical dynamical systems approach to turbulent shear flows

Dynamical systems theory is often applied to study complex dynamics in simple nonlinear model equations, like the Lorenz model mentioned above. In the Lorenz model, three coupled nonlinear ordinary differential equations describe the dynamics in a three-dimensional state space which is sufficient to accommodate a chaotic 'strange' attractor. For a "strange attractor theory of turbulence" (Lanford, 1982), one needs to consider the nonlinear partial differential equations that govern fluid flow and have in principle, an infinite dimensional state space. However, these equations may be solved accurately in direct numerical simulations where time and the three-dimensional space is discretized at sufficiently high resolution. The discretized description of a flow yields a finite set of coupled ordinary differential equations and thus, a state space of finite dimension. The number of equations and dimensions depends on the specific flow that is solved. The wall-bounded shear flows discussed in the present thesis can be described in a state space with $\mathcal{O}(10^4)$-$\mathcal{O}(10^6)$ dimensions. This state space comprises all possible flows for specific boundary conditions. A vector $\boldsymbol{x}(t)$ in this state space represents one particular three-dimensional flow field. The time evolution of this flow field, as simulated in the direct numerical simulation, corresponds to a unique state space trajectory of the corresponding state space vector $\boldsymbol{x}(t)$.

Several methods for obtaining information about the state space structure that supports turbulence in a high-dimensional state space are described in Cvitanović et al. (2016). One of the most basic methods are low-dimensional projections. Here, state space trajectories $\boldsymbol{x}(t)$ are projected onto typically two or three dimensions representing certain quantities of the flow. Examples for projections of turbulent state space trajectories in PCF can be found in Gibson et al. (2008b). The present thesis refers to two-dimensional projections as 'phase portraits'.

Not all trajectories in a turbulent state space represent chaotic dynamics. The identification of steady or periodic states is an essential step towards a dynamical systems description of a turbulent shear flow, just like fixed points or limit cycles in low-dimensional chaotic dynamical systems (e.g. Strogatz, 2018). These states are called invariant solutions or invariant states and are defined as exactly steady or recurrent flow fields whose state space vectors $\boldsymbol{x}(t)$ satisfy

$$\mathcal{G}(\boldsymbol{x}(t)) = \sigma \mathcal{F}^T(\boldsymbol{x}(t)) - \boldsymbol{x}(t) = 0\,, \tag{1.1}$$

where $\mathcal{F}^T()$ is a time evolution operator that evolves state vector $\boldsymbol{x}(t)$ over period T according to the governing fluid flow equations. Operator σ represents a coordinate transformation of the flow field which allows for propagating solutions but may also be an identity operation. Invariant solutions in shear flows are either steady equilibrium solutions, traveling waves or periodic orbits.

Invariant solutions may be dynamically stable or unstable. In shear flows with a linearly stable laminar flow, like pipe flow or PCF, almost all invariant solutions are dynamically unstable. Hence, it is necessary to numerically identify these dynamically unstable solutions in order to make progress in describing the nonlinear turbulent dynamics in these flows (Kerswell, 2005; Eckhardt et al., 2007; Kawahara et al., 2012, and references therein). The relevance of unstable invariant solutions is based on their ability to transiently attract the dynamics along their stable manifolds. When embedded in a 'strange' turbulent attractor or saddle, unstable invariant solutions with their entangled stable and unstable manifolds support turbulent dynamics which may transiently visit the state space neighborhood of these invariant solutions. In the case of transiently visited equilibrium solutions, their spatial flow structure emerges transiently in the flow (Gibson et al., 2008b; Suri et al., 2017). Transiently visited periodic orbits additionally influence the temporal dynamics and may be used to describe the associated statistical properties of the flow (Chandler and Kerswell, 2013; Budanur and Cvitanović, 2017). Thus, coexisting unstable invariant solutions with their stable and unstable manifolds provide a 'dynamical scaffold' for a turbulent state space.

When changing the driving forces of shear flows, invariant solutions may be created or destroyed in bifurcations. Bifurcations are structural changes in the state space across which the dynamics changes qualitatively (e.g. Guckenheimer and Holmes, 1983). To compute bifurcations, a bifurcating invariant solution must be numerically continued under changing control parameters towards its bifurcation point. Bifurcations that occur along a continued solution branch of an invariant solution change the stability properties of this invariant solution and thereby modify its dynamical relevance. Thus, the bifurcation structure associated to relevant invariant solutions describes how complex state space structures might change under changing control parameters.

In summary, a numerical dynamical systems approach to turbulent patterns in shear flows requires tools and methods for
a) direct numerical simulations to compute state space trajectories,
b) solving (1.1) to identify stable and unstable invariant solutions,
c) analyzing the dynamical stability of invariant solutions,
d) continuing invariant solutions under changing control parameters.
The open source software *Channelflow 2.0* developed in-house (channelflow.ch) provides such tools and methods for studying PCF. To study turbulent patterns in ILC, *Channelflow*

2.0 had to be extended for this thesis. A review of tools and methods in *Channelflow 2.0* and the implementation details for the code extension module *Channelflow-ILC* are given in Section 2.2. The following two sections describe how the dynamical systems analysis is applied to the specific problems of spatio-temporal patterns in ILC (Section 1.2) and oblique turbulent-laminar stripes in PCF (Section 1.2).

1.2 Spatio-temporal patterns in inclined layer convection

Inclined layer convection (ILC) is a thermally driven flow between two parallel walls at two different fixed temperatures and inclined against gravity (Figure 1.1d). Experiments of ILC in spatially extended domains report on many different convection patterns, most of which exhibit some form of spatio-temporal chaos (Daniels et al., 2000). Direct numerical simulations in spatially extended domains reproduce the different patterns and their complex dynamics (Subramanian et al., 2016). This implies that the large variety of experimentally observed turbulent patterns and their complex dynamics are fully contained in the nondimensional incompressible Oberbeck-Boussinesq equations

$$\frac{\partial \boldsymbol{U}}{\partial t} + (\boldsymbol{U}\cdot\nabla)\,\boldsymbol{U} = -\nabla p + \sqrt{\frac{\mathrm{Pr}}{\mathrm{Ra}}}\nabla^2\boldsymbol{U} - \hat{\boldsymbol{g}}\mathcal{T}\,, \tag{1.2}$$

$$\frac{\partial \mathcal{T}}{\partial t} + (\boldsymbol{U}\cdot\nabla)\,\mathcal{T} = \sqrt{\frac{1}{\mathrm{Pr}\,\mathrm{Ra}}}\nabla^2\mathcal{T}\,, \tag{1.3}$$

$$\nabla\cdot\boldsymbol{U} = 0\,, \tag{1.4}$$

for the fields of total velocity $\boldsymbol{U}(x,y,z,t)$, total temperature $\mathcal{T}(x,y,z,t)$, and pressure $p(x,y,z,t)$ relative to the hydrostatic pressure. Bold quantities denote vectors, and $\hat{\boldsymbol{g}} = -\sin(\gamma)\boldsymbol{e}_x - \cos(\gamma)\boldsymbol{e}_y$ denotes the unit vector of gravitational acceleration that may be inclined in the frame of reference. The equations are complemented by no-slip and fixed temperature boundary conditions at the walls and periodic boundary conditions in lateral directions. The equations have three control parameters. The Rayleigh number Ra parametrizes the strength of thermal driving. The Prandtl number Pr parametrizes the ratio between kinematic viscosity and thermal diffusivity. The angle of inclination of the fluid layer against gravity parametrizes the direction of buoyancy force in the flow and is measured between the wall-normal and the vector of gravitational acceleration. A zero inclination corresponds to the horizontal Rayleigh-Bénard case (Figure 1.1d).

The experimental and numerical observations raise the question of how the various convection patterns arise and how their spatio-temporally complex dynamics depends on the control parameters of ILC. Linear stability analysis has identified two primary and five different secondary instabilities at Pr = 1.07. This analysis suggests that regular pattern motifs at critical

stability thresholds are related to the observed patterns (Subramanian et al., 2016). Explaining however the observed weakly turbulent dynamics in the patterns, including intermittent bursting, chaos, temporally evolving defects, and spatial coexistence of different patterns, requires a nonlinear dynamical systems description. Following a dynamical systems approach (Section 1.1), the present thesis discusses three main steps towards explaining the arising complex dynamics in ILC

1) Development of the tools and methods for a numerical dynamical systems analysis of ILC. The open source software *Channelflow 2.0* is extended by equations (1.2-1.4). To solve (1.1), an interface for the nonlinear solver library is implemented (Section 2.2.4-2.2.7). In the context of this code development, the modular code structure became more flexible (Section 2.2.1-2.2.3) and the input/output performance was improved (Section 2.2.8). These general code contributions are part of the published version *Channelflow 2.0*, reviewed in Section 2.1.

2) Construction of exact invariant solutions of (1.2-1.4) underlying the relevant spatially periodic convection patterns in ILC. The temporal dynamics of ILC is analyzed via direct numerical simulations in small periodic domains at specific control parameters where the convection patterns are observed. Domain sizes are chosen according to the pattern wavelengths suggested by linear stability analysis. This yields a collection of stable and unstable invariant solutions that capture the spatial feature of relevant spatially periodic patterns. The nonlinear temporal dynamics is found to either asymptotically approach or transiently visit these invariant solutions (Section 4).

3) Computation of the bifurcations and branches of the invariant solutions under changing control parameters. We numerically continued the constructed invariant solutions in Ra and inclination angle at fixed Pr = 1.07 (as studied by Daniels et al., 2000; Subramanian et al., 2016). The resulting bifurcation diagrams illustrate coexistence, stability and parametric connections between invariant solutions, including a range of different types of bifurcations (Section 5).

1.3 Oblique turbulent-laminar stripes in plane Couette flow

Plane Couette flow (PCF) is the flow between two parallel walls moving in opposite directions (Figure 1.1b). Experiments of PCF in spatially extended domains show that weakly turbulent PCF may self-organize into a regular stripe pattern of alternating turbulent and laminar bands that coexist in space. These stripes have a pattern wavelength much larger than the gap size and are oriented at oblique orientation against the direction of wall movement (Prigent et al., 2002, and Figure 1.1b). Since the first observation of a single oblique turbulent band in Taylor-Couette flow (Coles and Van Atta, 1966), regular oblique turbulent-laminar patterns

have been found in various wall-bounded shear flows (see Tuckerman et al., 2020, for a recent review). Direct numerical simulations reproduce the oblique stripe pattern in a periodic domain of minimal spatial extent and tilted against the direction of wall movement (Barkley and Tuckerman, 2005). Since oblique turbulent-laminar stripes can be reproduced in direct numerical simulations, the regular pattern, including the selection mechanism for the pattern wavelength and the oblique orientation, must be fully contained in the incompressible Navier-Stokes equations

$$\frac{\partial \boldsymbol{U}}{\partial t} + (\boldsymbol{U}\cdot\nabla)\,\boldsymbol{U} = -\nabla p + \frac{1}{\mathrm{Re}}\nabla^2\boldsymbol{U}\,, \tag{1.5}$$

$$\nabla\cdot\boldsymbol{U} = 0\,, \tag{1.6}$$

for the fields of total velocity $\boldsymbol{U}(x,y,z,t)$ and pressure $p(x,y,z,t)$. The equations are complemented by no-slip boundary conditions at the walls and periodic boundary conditions in lateral directions. The single control parameter of the equations is the Reynolds number Re parametrizing the driving shear force due to the relative velocity of the counter-moving walls.

The experimental and numerical observations raise the question of how the regular pattern of large-scale oblique stripe emerges. In particular, the mechanism that selects the pattern wavelength and the oblique orientation in the flow is unknown. Due to the turbulent dynamics of transitional PCF, a nonlinear theory is required to explain the pattern characteristics of oblique turbulent-laminar stripes. Following a dynamical systems approach (Section 1.1), the present thesis discusses three main steps towards explaining the arising regular pattern in weakly turbulent PCF

1) Construction of an invariant solution that captures the spatial features of oblique turbulent-laminar stripes in a minimal periodic domain with tilted orientation relative to the direction of the wall movement. Using a windowing approach, a spatially modulated variant of Nagata's equilibrium solution (Nagata, 1990) is identified. This new equilibrium captures the pattern of oblique stripes (Section 7).

2) Numerical continuation of the stripe equilibrium traces the solution branch to a symmetry-breaking bifurcation from the unpatterned Nagata equilibrium. The emergence of the oblique large-scale pattern along a sequence of two symmetry-breaking bifurcations and the corresponding solution branches illustrate how the pattern forms and in what parameter ranges an underlying invariant solutions exists (Section 8).

3) The temporal dynamics of oblique turbulent stripe patterns are studied in different symmetry subspaces. By confining the dynamics further to the edge of chaos, three periodic orbits are found that represent slow standing wave oscillations. Using a projection that captures the essential oscillatory mechanism of the periodic orbits, turbulent state space trajectories inside and outside the edge of chaos are analysed (Section 9).

2 Methods and tools for a numerical dynamical systems analysis

The open source software *Channelflow* provides a numerical framework for direct numerical simulations (DNS) and dynamical systems analysis of shear flows in periodic domains with channel geometry. During the period of research leading towards the present thesis, a MPI-parallel in-house version of Channelflow 1.5 (see Gibson et al., 2008b, and channelflow.org) has been developed further in collaboration between members of the *Emergent complexity in physical systems laboratory* (ECPS), including the author of the present thesis, EPFL's *Scientific IT and applications support* (SCITAS), and John Gibson (University of New Hampshire). This development project lead to the publication of *Channelflow 2.0* in September 2018 (see Gibson et al., 2019, and channelflow.ch). Section 2.1 reviews the code design and the numerical algorithms of *Channelflow 2.0*.

The present thesis includes an analysis of turbulent plane Couette flow (PCF). PCF is one type of shear flow for which *Channelflow* has initially been developed and which can be studied using *Channelflow* without modifying the set of equations being solved. In order to also study turbulent patterns in inclined layer convection (ILC), the author has extended *Channelflow* specifically for the present thesis. The code development, detailed in Section 2.2, may be summarized in three main contributions to *Channelflow*:

- The time-stepping algorithms have been encapsulated from applications to the Navier-Stokes equations only. The new implementation invokes terms of a general nonlinear equation (Section 2.2.1) and allows users to easily extend *Channelflow* to systems with other governing equations. The practical steps necessary for implementing a new system are outlined in Section 2.2.3.

- The implementation of the Oberbeck-Boussinesq equations for ILC as an extension module to *Channelflow* is discussed in Section 2.2.4 and validated in Section 2.2.7.

- Some turbulent patterns in wall-bounded shear flows require spatially extended flow domains, increasing the computational cost of input/output of data files (I/O). Parallel I/O using *NetCDF-4* has been implemented to improve the I/O performance (Section 2.2.8).

The generalized time-stepping algorithms and the better performing I/O with *NetCDF-4* have already been publicly released with *Channelflow 2.0*. The ILC extension module will be published with the next release version as *Channelflow-ILC*.

2.1 Channelflow 2.0 - a review

The purpose of this review is to provide both an overview and relevant references on the design and the content of *Channelflow 2.0*. As a technical description, this section is especially targeted at future developers of the code. More detailed explanations of the main algorithms are found elsewhere (Gibson et al., 2019). First, Section 2.1.1 discusses code design, development guidelines and tools used for code development. Second, Section 2.1.2 reviews the numerical algorithms in *Channelflow 2.0* with references to literature. Algorithms implemented by the author of this thesis are described in the following subsection (Section 2.2).

2.1.1 Code design and development

Channelflow 2.0 is written in C++, object-oriented, and uses C++11 standards. A class diagram indicating the main classes with their inheritance structure and their dependencies on external libraries is given in Figure 2.1. The code utilizes standard language features like abstract classes and smart pointers. The time integration of the fluid flow equations is parallelized with the message passing interface (MPI) (Kreilos, 2014). Certain parts of *Channelflow 2.0*, such as the ILC extension module, are only conditionally compiled depending on user settings and available external libraries. The build process is managed using *CMake* (https://cmake.org).

Code development towards *Channelflow 2.0* followed essentially three design guidelines:

- **Encapsulation**: The two main purposes of *Channelflow* are DNS of shear flows in three-dimensional rectangular domains and a nonlinear dynamical systems analysis of such flows. Code for these two main purposes is independent from each other and separated in two libraries: `chflow` for DNS, and `nsolver`, short for "nonlinear solver", for dynamical systems analysis. This separation allows to link any dynamical system against `nsolver`, not only shear flows. In order to link a time integrator for a dynamical system to `nsolver`, a dynamical systems interface (DSI) must be implemented which translates between states and equations of a physical system, like that implemented in `chflow`,

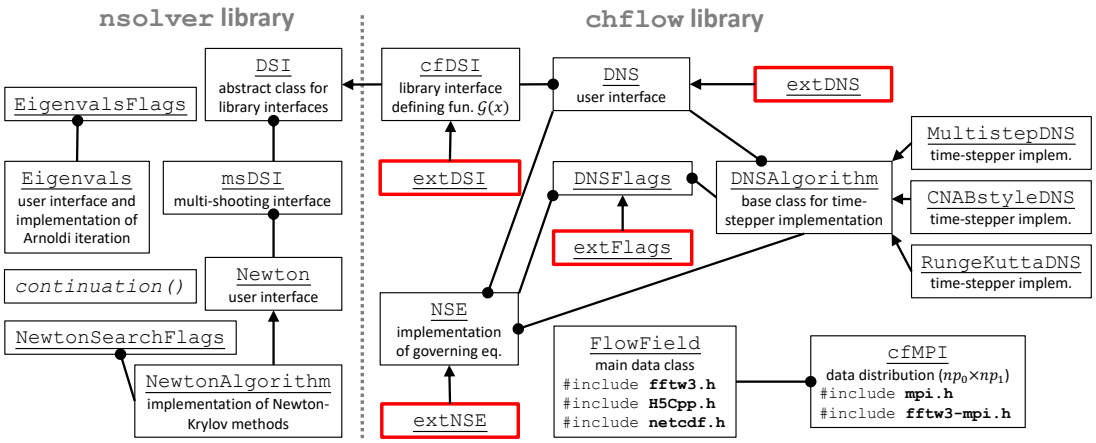

Figure 2.1 – Class diagram of the main classes in the `nsolver` and `chflow` library of *Channelflow 2.0*. Numerical continuation is not implemented as a class but as a separate function *continuation()*. The relations between the classes are indicated by arrows for inheritance (derived class → base class) and by bullet points for dependence ($A-\bullet B$ means class A has a member of type B). Classes with prefix "ext" (framed in red) need to be implemented for extending the Navier-Stokes equations to other/additional governing equations (Section 2.2.3).

and abstract state space vectors and maps, like Equation (1.1). Besides this major design decision, classes within each library should encapsulate their functionality to a level that does not require to re-code their implementation when extending the software.

- **Usability**: *Channelflow* may be used via command line tools or by writing scripts in C++ or python that call types and functions from the `chflow` or `nsolver` libraries. If the problem size is small, users might want to run *Channelflow* on a laptop device. If the problem size is large, users might want to run *Channelflow* on high-performance computing (HPC) clusters. *Channelflow* is most widely used for research in computational fluid dynamics where the problem size can be very large. Thus, much development towards *Channelflow 2.0* was driven by enhancing performance. However, optimizing the performance must not conflict with attempts to increase the readability of the code, the flexibility in usage, or the interchangeability between computing platforms.

- **Backward compatibility**: *Channelflow* has a large user community which produced many scientific results over the past 10 years (see Gibson et al., 2019, for a review of results). To ensure that existing data can be reproduced and studied further, any development must be compatible with previous code versions. Integration tests and an increasing number of unit tests help developers to write compatible code.

Several tools and applications have been employed to aid the development of *Channelflow 2.0*. Version controlled collaborative programming has been coordinated on the platform *GitHub* (https://github.com). A specific style format of the code is enforced using *ClangFormat* (https://clang.llvm.org). Integration tests are incorporated into *Make*. Unit tests can be implemented using *Google Test* (https://github.com/google/googletest). Continuous integration with *Travis-CI* (https://travis-ci.com) checks style format and the success of compilation and tests, prior to pull requests. Code coverage is measured using *Codecov* (https://codecov.io).

2.1.2 Numerical algorithms

The `chflow` library contains algorithms for DNS of the incompressible Navier-Stokes equations (1.5) and (1.6) in double-periodic wall-bounded domains. A Galerkin approximation with Fourier-Chebychev-Fourier expansions of the three-dimensional flow field is inserted into the Navier-Stokes equations and solved using the pseudo-spectral method (Canuto et al., 2006, p.133ff). Fourier transforms of the nonlinear terms in (1.5) are obtained via transform routines of the FFTW library (Frigo and Johnson, 2005) and are specified in `FlowField`. Different expressions of the nonlinear terms are implemented in `NSE`, including convection, divergence, skew-symmetric and rotation form (Zang, 1991) which can be dealiased using the 2/3 rule (Canuto et al., 2006, p.133f). Pressure is obtained by the influence matrix method for a Chebyshev Tau approximation (Kleiser and Schumann, 1980; Canuto and Landriani, 1986) in `TauSolver`. The time-stepping algorithms in `DNSAlgorithm` are implicit-explicit methods (Ascher et al., 1995). These include second-order Crank-Nicolson/Adams-Bashforth (Canuto et al., 2006, Sec.D.2.2), three-stage Runge-Kutta (Spalart et al., 1991), both in `CNABstyleDNS`, three-stage Crank-Nicolson/Runge-Kutta (Zang and Hussaini, 1985; Peyret, 2002, p.146), in `RungeKuttaDNS`, and multistep Adams-Bashforth/Backward-Differentiation of first- to fourth-order (Peyret, 2002, p.130ff), in `MultistepDNS`.

The `nsolver` library contains algorithms to analyze a dynamical system. Based on a given time-integrating function $\mathcal{G}^T(\boldsymbol{x};\mu)$, defined in (1.1), iterative matrix-free Krylov subspace methods (Edwards et al., 1994; Knoll and Keyes, 2004) allow the construction, continuation and stability analysis of invariant solutions with many degrees of freedom. The construction of invariant solutions employs Newton-Krylov iterations (Kelley, 2003; Sanchez et al., 2004) implemented in `NewtonAlgorithm` with different solver methods including GMRES, short for generalized minimum residual method, (Trefethen and Bau, 1997; Saad, 2003), BiCGStab, short for bi-conjugate gradient method - stabilized, (Saad, 2003, p.244ff), and flexible GMRES (Saad, 2003, p.287ff). The convergence radius of the Newton-Krylov iteration is increased by an Hookstep trust-region optimization (Dennis and Schnabel, 1996; Viswanath, 2007). Numerical continuation of invariant solutions follows a predictor-corrector scheme with quadratic extrapolation in the predictor step and a Newton-Krylov iteration in the corrector

step. Two types of numerical continuation are available: control parameter continuation and pseudo-arclength continuation (Sanchez et al., 2004; Dijkstra et al., 2014). Convergence of very long unstable periodic orbits may require a multi-shooting formulation (van Veen et al., 2011; Sánchez and Net, 2010), implemented in `MultishootingDSI`. A linear stability analysis is performed by Arnoldi iteration (e.g. Antoulas, 2005) using a finite difference approximation of the linearized time evolution (Gibson et al., 2008a, A.3), implemented in `Arnoldi`.

2.2 Extending Channelflow to thermal convection

This section describes the individual development steps towards a validated and well-performing code for studying turbulent patterns in ILC. First, the implementations of the DNS algorithms have been restructured. The time-stepping algorithms have been encapsulated such that they became independent from the Navier-Stokes equations (Section 2.2.1). The new modular class structure simplifies extensions to other governing equations, as explained in Section 2.2.3. The Oberbeck-Boussinesq equations have been non-dimensionalized (Section 2.2.4), solved for the laminar base flow (Section 2.2.5), and implemented into the framework of *Channelflow* as ILC extension module *Channelflow-ILC* (Section 2.2.6). Validations of *Channelflow-ILC* are discussed in Section 2.2.7. The data input/output using *NetCDF-4* is described and analyzed in Section 2.2.8.

2.2.1 Generalizing the time-stepping algorithms

In previous versions of *Channelflow*, each of the three different time-stepping classes (Section 2.1.2) was closely tied to applications governed by the Navier-Stokes equations. Every loop over time-steps in each time-stepper class contained the loops over the spectral modes to add the individual 'hard-coded' terms of the Navier-Stokes equations. Already this implementation produced code duplications in each time-stepper class. Without generalizing the time-stepping classes, extending *Channelflow* to other systems with different governing equations would have implied further code duplications. In line with the encapsulation guideline (Section 2.1.1), the time-stepping classes have been encapsulated from the governing equations. This development step happened before implementing the Oberbeck-Boussinesq equations for inclined layers. The encapsulation does not change the code performance substantially but simplifies the implementation of new code extensions as discussed in the subsequent section. The generalized time-stepping algorithms described here are part of the published release version *Channelflow 2.0*.

The time-stepping algorithms advance a set of coupled nonlinear partial differential equations in time. These equations have the form

$$\frac{\partial}{\partial t}\hat{\boldsymbol{x}} = \mathcal{L}_{\xi_i}\hat{\boldsymbol{x}} - \mathcal{N}_{\xi_i}(\hat{\boldsymbol{x}}) \tag{2.1}$$

where $\hat{\boldsymbol{x}} = [\hat{\xi}_1, \hat{\xi}_2, ...]$ is a vector of arrays $\hat{\xi}_i$ in spectral representation, as denoted by $\hat{}$, and $\mathcal{L}_{\xi_i}\hat{\boldsymbol{x}}$ and $\mathcal{N}_{\xi_i}(\hat{\boldsymbol{x}})$ are the linear and nonlinear terms, respectively, defining the evolution of field quantity ξ_i. In the case of the Navier-Stokes equations (1.5) and (1.6) for velocity fluctuations $\boldsymbol{u} = \boldsymbol{U} - \boldsymbol{U}_0(y)$ around a laminar base solution $\boldsymbol{U}_0(y)$, the vector of spectral arrays is $\hat{\boldsymbol{x}} = [\hat{\xi}_1, \hat{\xi}_2] = [\hat{\boldsymbol{u}}, \hat{p}]$ and

$$\mathcal{L}_{\boldsymbol{u}}\hat{\boldsymbol{x}} = \frac{1}{\mathrm{Re}}\left(\hat{\nabla}\cdot\hat{\nabla}\right)\hat{\boldsymbol{u}} - \hat{\nabla}\hat{p}\,, \tag{2.2}$$

$$\mathcal{N}_{\boldsymbol{u}}(\hat{\boldsymbol{x}}) = \mathbb{F}\left(\mathbb{F}^{-1}(\hat{\boldsymbol{U}})\cdot\mathbb{F}^{-1}(\hat{\nabla}\hat{\boldsymbol{U}})\right) + C_{\boldsymbol{u}}\,, \tag{2.3}$$

with linear spectral operator

$$\hat{\nabla} = \left(2\pi i\left(\frac{k_x}{L_x}\hat{\boldsymbol{e}}_x + \frac{k_z}{L_z}\hat{\boldsymbol{e}}_z\right) + \frac{\partial}{\partial y}\hat{\boldsymbol{e}}_y\right)\,, \tag{2.4}$$

and Fourier-Chebyshev transform operator $\mathbb{F}$. The pressure field p does not have a separate evolution equation since p is directly implied by the instantaneous velocity field in an incompressible flow. The constants $C_{\boldsymbol{u}}$ may contain additional fixed body forces.

During time-stepping, $\mathcal{N}_{\xi_i}(\hat{\boldsymbol{x}})$ in (2.1) is always treated fully explicitly and $\mathcal{L}_{\xi_i}\hat{\boldsymbol{x}}$ is treated either fully implicitly or semi-implicitly.
Multistep Adams-Bashforth/Backward-Differentiation in `MultistepDNS` with k stages/steps at time-step n of size Δt is given by

$$\frac{a_0}{\Delta t}\hat{\boldsymbol{x}}^{n+1} - \mathcal{L}\hat{\boldsymbol{x}}^{n+1} = \sum_{j=1}^{k}\frac{-a_j}{\Delta t}\hat{\boldsymbol{x}}^{n+1-j} - b_{j-1}\mathcal{N}\left(\hat{\boldsymbol{x}}^{n+1-j}\right)\,. \tag{2.5}$$

The coefficients a_j and b_j are found in Peyret (2002, Tab.4.4,p.131).
The Crank-Nicolson/Adams-Bashforth (CNAB) and Runge-Kutta algorithms in `CNABstyleDNS` have been generalized to the form

$$\left(\frac{1}{\beta_j\Delta t} - \mathcal{L}\right)\hat{\boldsymbol{x}}^{n,j+1} = \left(\frac{1}{\beta_j\Delta t} - \frac{\alpha_j}{\beta_j}\mathcal{L}\right)\hat{\boldsymbol{x}}^{n,j} + \frac{\gamma_j}{\beta_j}\mathcal{N}\left(\hat{\boldsymbol{x}}^{n,j}\right) + \frac{\zeta_j}{\beta_j}\mathcal{N}\left(\hat{\boldsymbol{x}}^{n,j-1}\right)\,, \tag{2.6}$$

for Runge-Kutta substep $j \in \{0, 1, ..., k\}$ at time-step n, such that $\hat{\boldsymbol{x}}^{n+1,0} = \hat{\boldsymbol{x}}^{n,k+1}$. Here, $k = 2$ for Runge-Kutta and $k = 0$ for CNAB. The coefficients $\alpha_j, \beta_j, \gamma_j, \zeta_j$ are found in Table 4 of the *Channelflow* user manual (channelflow.org).

The three-stage Crank-Nicolson/Runge-Kutta in `RungeKuttaDNS`,

$$\left(\frac{1}{C_j\Delta t}-\mathcal{L}\right)\hat{\boldsymbol{x}}^{n,j}=\left(\frac{1}{C_j\Delta t}+\mathcal{L}\right)\hat{\boldsymbol{x}}^{n,j-1}+\frac{B_j}{C_j\Delta t}Q^{n,j}\,, \tag{2.7}$$

$$Q^{n,j}=A_jQ^{n,j-1}+\Delta t\mathcal{N}\left(\hat{\boldsymbol{x}}^{n,j-1}\right)\,, \tag{2.8}$$

for Runge-Kutta substep $j\in\{1,2,...,k\}$ at time-step n, such that $\hat{\boldsymbol{x}}^{n+1,1}=\hat{\boldsymbol{x}}^{n,k+1}$. Here, $k=3$ with coefficients $[C_1,C_2,C_3]=[1/6,5/24,1/8]$ and others specified in (Peyret, 2002, Eq.4.110,p.146).

Vector $\hat{\boldsymbol{x}}$ is of type `std::vector<FlowField>` and may be of larger dimension than $\mathcal{L}\hat{\boldsymbol{x}}$ and $\mathcal{N}_{\boldsymbol{x}}(\hat{\boldsymbol{x}})$. In the case of the incompressible Navier-Stokes equations, linear and nonlinear operators do not return a pressure dimension, and the right-hand side of (2.1) has only velocity dimensions. When looping over the arrays in vector $\hat{x}$, the generalized time-steppers loop only over the number of entries corresponding to the size of the right-hand side vector, thus, skipping the last pressure `FlowField`. This avoids unnecessary loops. A vector for the right-hand side must be created by a function `createRHS` in the `NSE` class which knows the structure of the equations. The `NSE` class also provides the functions for linear and nonlinear terms, as well as the implicit solver method. Consequently, pointers of type `NSE` must be passed from `DNS` objects down to the time-stepper implementations in objects of `DNSAlgorithm`-derived types. Passing pointers to constructors of `DNSAlgorithm`-derived classes creates two copies of the pointer and requires to use the smart pointer type `shared_ptr` instead of `unique_ptr`.

2.2.2 Performance impact of the new code structure

The encapsulation of the time-stepper from the governing equations does not reduce the performance of *Channelflow* substantially. Benchmarks with a field of size $[N_x,N_y,N_z]=[128,121,128]$ indicate a performance reduction of $<5\%$ and unchanged scaling behavior (Figure 2.2). The small performance loss results from a slightly less efficient summation of the right-hand side in (2.5-2.8): Instead of summing the individual terms on the right-hand side as `ChebyCoeff`-objects at each Fourier mode, the generalized time-steppers must sum `FlowField`-objects containing the terms. Operations on `FlowField`-objects have a slightly larger overhead. Since the overhead occurs in a performance relevant part of the code, a small slow-down is observed in the benchmarks. Future development should aim to reduce the overhead produced by the algebraic operations with `FlowField`-objects. The slow-down has been compensated by additional development making iterative data access in `FlowField`-objects predictable at compile-time leading to vectorized operations and a speed-up by $\sim 20\%$. The strong-scaling behaviour of *Channelflow 2.0* is shown in Figure 2.3.

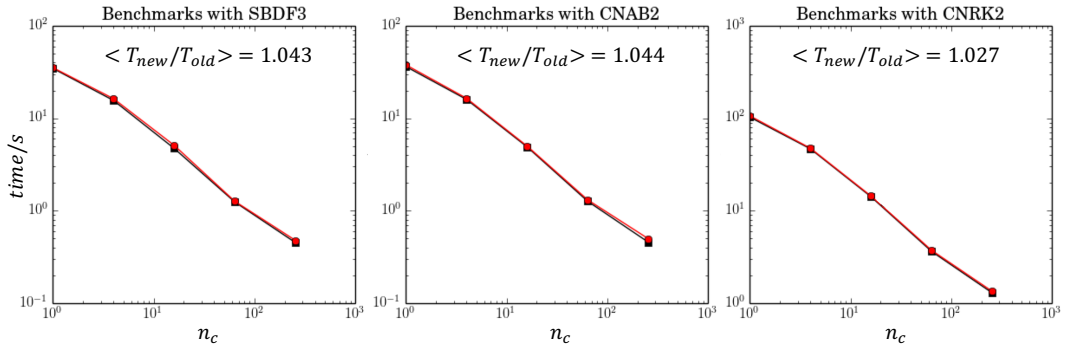

Figure 2.2 – Benchmarks of average time units during DNS using three different time-stepping algorithms before (black) and after the encapsulation of the algorithms (red). The elapsed wall-clock time is measured over the number of CPU cores n_c in a strong scaling study with `FlowField`-objects of size $[N_x, N_y, N_z] = [128, 121, 128]$. While the average relative elapsed time $\langle T_{new}/T_{old} \rangle$ differs slightly, the scaling behavior is unaffected by the new code design.

2.2.3 How to implement additional equations in the new code structure

The generalized time-steppers make implementations of additional or modified fluid flow equations in *Channelflow* more straightforward. Only few classes and functions need to be implemented. The following action items outline the general procedure that has been followed to implement ILC in *Channelflow*.

- Non-dimensionalize the new equations. In *Channelflow 2.0*, the main control parameter of the Navier-Stokes equations is a non-dimensional kinematic viscosity, denoted as $\tilde{\nu}$ here. Only for particular boundary conditions this control parameter may be interpreted as $\tilde{\nu} = 1/\mathrm{Re}$. The location of the channel walls, the velocity at the walls, and the pressure gradient along the channel can be chosen independent of $\tilde{\nu}$. The flexibility in the boundary conditions allows to simulate flows with mixed boundary conditions, e.g. required for homotopy transformations of flows. Thus, the interpretation of $\tilde{\nu}$ is left to the user. For consistency, the new governing equations are ideally non-dimensionalized such that the non-dimensional system parameters can be expressed as non-dimensional diffusion constants in the equations, and such that the interpretation of these constants depends on the specific boundary conditions. Section 2.2.4 describes how this step is carried out for ILC.

- Find a general laminar base solution and express it in terms of Chebychev coefficients. Section 2.2.5 describes how this step is carried out for ILC.

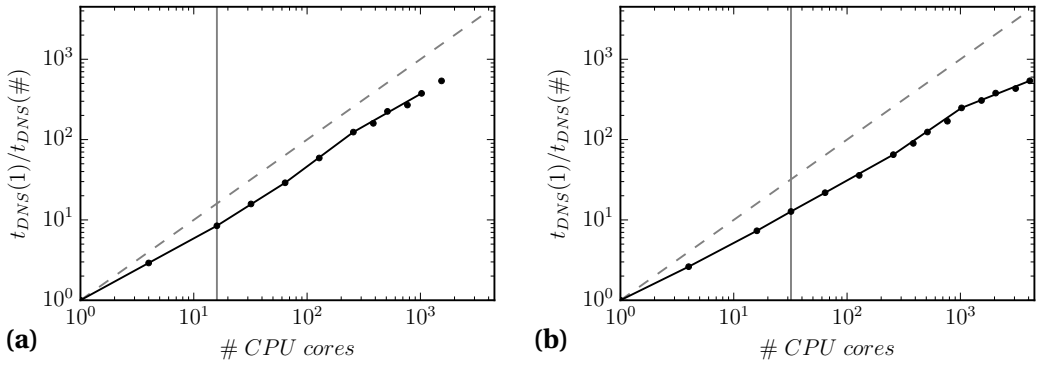

Figure 2.3 – Benchmarks of the parallel time-stepper during DNS in a strong scaling study using a `FlowField` of size $[N_x, N_y, N_z] = [682, 121, 682]$, excluding padded modes, corresponding to a file size of $1.35GB$. The DNS speed-up relative to a serial single-core computations has been measured as averaged elapsed wall-clock time on **(a)** EPFL's HPC cluster 'Fidis' (28 Intel Broadwell cores per node) and on **(b)** the CSCS cluster 'Piz Daint' (Cray XC40 with 36 cores per node). The vertical grey lines mark computations on a single node. The dashed line marks ideal speed-up.

- Implement the non-dimensionalized governing equations for fluctuations around a laminar base flow. Keep the terms for the base flow in the equations to allow a base flow that is not a solution of the equations. Derive from the existing classes in *Channelflow 2.0* to use the already implemented methods. A maximum of four derived classes need to be implemented for an extension that can use all tools and methods of *Channelflow 2.0*: One class that provides an implicit solver as well as linear and nonlinear terms of the governing equation to the time-steppers, as described in Section 2.2.1. This class is labeled `extNSE` in Figure 2.1. Two classes that allow to control a DNS (`extDNS` and `extFlags` in Figure 2.1). One dynamical systems interface class to link the time integrator to the `nsolver`-library (`extDSI` in Figure 2.1). Section 2.2.6 describes how this step is done for ILC.

- Validate the implementation. Section 2.2.7 describes how this step is carried out for ILC.

2.2.4 Non-dimensionalizing the Oberbeck-Boussinesq equations

The time-evolution of velocity $\boldsymbol{U}(x,y,z,t)$, pressure $P(x,y,z,t)$ and temperature $\mathcal{T}(x,y,z,t)$ for a three-dimensional incompressible flow in the presence of gravitational acceleration $\boldsymbol{g}$ is

described by the Oberbeck-Boussinesq equations

$$\frac{\partial \boldsymbol{U}}{\partial t} + (\boldsymbol{U}\cdot\nabla)\,\boldsymbol{U} = -\frac{1}{\rho_{ref}}\nabla P + \nu\nabla^2\boldsymbol{U} + \boldsymbol{g}\left[1-\alpha(\mathcal{T}-\mathcal{T}_{ref})\right] \tag{2.9}$$

$$\frac{\partial \mathcal{T}}{\partial t} + (\boldsymbol{U}\cdot\nabla)\,\mathcal{T} = \kappa\nabla^2\mathcal{T}\,, \tag{2.10}$$

$$\nabla\cdot\boldsymbol{U} = 0\,. \tag{2.11}$$

Bold symbols denote vector quantities. While many previous numerical studies have considered these equations for toroidal-polodial variables (Busse and Clever, 1992; Subramanian et al., 2016), the present study implements the Oberbeck-Boussinesq equations for primitive variables. The Oberbeck-Boussinesq approximation states that density ρ is the only fluid property depending on temperature, and that this dependence is linear, $\rho(\mathcal{T}) = \rho_{ref}\left[1-\alpha(\mathcal{T}-\mathcal{T}_{ref})\right]$ (Landau and Lifschitz, 1987). Accordingly, the kinematic viscosity ν, the thermal conductivity κ and the thermal expansion coefficient α of the fluid are assumed constant. Moreover, density fluctuations around the reference density $\rho_{ref}(\mathcal{T}_{ref})$ are assumed to only affect the buoyancy term $\boldsymbol{g}\rho(\mathcal{T})/\rho_{ref}$, i.e. the last term in the momentum equations (2.9). The range of validity of the Oberbeck-Boussinesq approximation is discussed e.g. by Gray and Giorgini (1976).

In ILC, the fluid resides between two parallel walls. The wall-normal direction is y. The reference frame is allowed to rotate about the z-direction by angle γ. Directions x and z are called the streamwise and the spanwise directions, respectively. The vector of gravitational acceleration is $\boldsymbol{g} = g\hat{\boldsymbol{g}} = g\left(-\sin(\gamma)\hat{\boldsymbol{e}}_x - \cos(\gamma)\hat{\boldsymbol{e}}_y\right)$. Vectors $\hat{\boldsymbol{g}}$, $\hat{\boldsymbol{e}}_x$ and $\hat{\boldsymbol{e}}_y$ are unit vectors. Note that here gravity is aligned with $-\hat{\boldsymbol{e}}_y$ for $\gamma = 0°$. This choice of coordinates makes the notation of space dimensions compatible with the notation typically used in pure shear flows with channel geometry as well as consistent with the notation implemented in *Channelflow*.

Equations (2.9-2.11) are five coupled nonlinear second-order partial differential equations for five unknowns $[\boldsymbol{U}, \mathcal{T}, P]$ with $\boldsymbol{U} = [U, V, W]$. The boundary conditions for these unknowns correspond to a flow domain with channel geometry. The fluid resides between two parallel walls at locations $y = a$ and $y = b$, respectively, moving at different fixed velocities and maintained at different fixed temperatures such that

$$U(y=a,b) = U_{1,2}\,, \tag{2.12}$$

$$V(y=a,b) = 0\,, \tag{2.13}$$

$$W(y=a,b) = W_{1,2}\,, \tag{2.14}$$

$$\mathcal{T}(y=a,b) = \mathcal{T}_{1,2}\,. \tag{2.15}$$

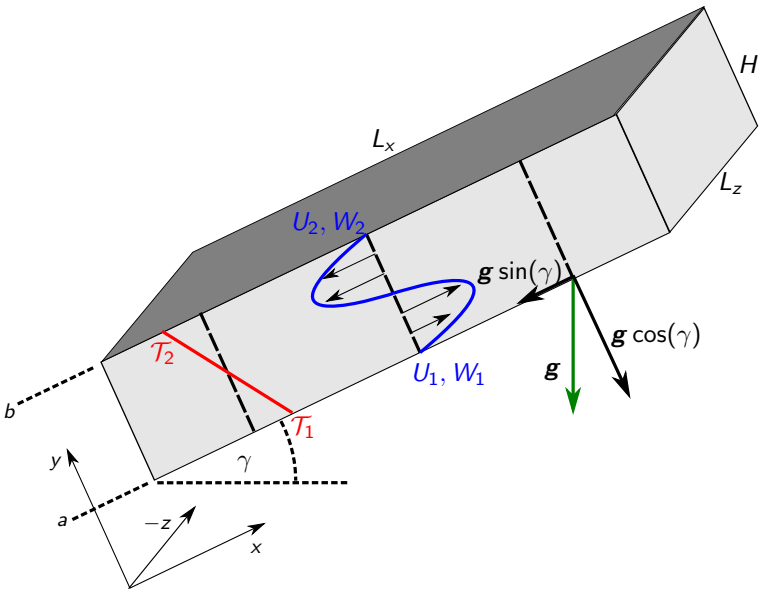

Figure 2.4 – The incompressible Oberbeck-Boussinesq equations are solved in a double-periodic channel of height H, length L_x and width L_z, inclined against gravity $\boldsymbol{g}$ at angle γ. The fluid (light grey) is confined between two walls at $y = a$ and $y = b$ (dark grey). The walls can have prescribed temperatures $\mathcal{T}_{1,2}$ and streamwise and spanwise velocities $U_{1,2}$ and $W_{1,2}$, respectively. The sketched laminar temperature profile (red) and laminar velocity profile (blue) correspond to the standard ILC-boundary conditions with wall velocities zero.

In the streamwise dimension x and and the spanwise dimension z, periodic boundary conditions are imposed

$$[\boldsymbol{U}, \mathcal{T}, \nabla P](x = 0, y, z, t) = [\boldsymbol{U}, \mathcal{T}, \nabla P](x = L_x, y, z, t)\,, \tag{2.16}$$

$$[\boldsymbol{U}, \mathcal{T}, \nabla P](x, y, z = 0, t) = [\boldsymbol{U}, \mathcal{T}, \nabla P](x, y, z = L_z, t)\,. \tag{2.17}$$

Thus, L_x and L_z are length and width of the double-periodic channel, and $H = b - a$ is the gap height between the walls. The flow domain is sketched in Figure 2.4.

The integrated flow over the full domain must satisfy a balance between the mean pressure gradient and the mean flow rate in both the streamwise and the spanwise directions. For periodic boundary conditions (2.16) and (2.16), this balance is under-determined and needs to be constrained. As an integral constraint, either the mean pressure gradient or the mean flow rate are imposed in each of the streamwise and spanwise directions. This choice affects the calculation of the pressure distribution and consequently, affects the dynamics of the flow.

A boundary condition for calculating pressure at the channel walls is

$$\frac{\partial V}{\partial y}(y=a,b)=0\,, \tag{2.18}$$

which follows implicitly from (2.11) and the imposed uniform velocities at the walls.

In order to non-dimensionalize the Oberbeck-Boussinesq equations and the boundary conditions, the dimensional scales are separated from non-dimensional numerical values, denoted by "~". Substituting, $\boldsymbol{x}=\tilde{\boldsymbol{x}}L$, $t=\tilde{t}\,\tau$, $\boldsymbol{U}=\tilde{\boldsymbol{U}}\,U$, $\mathcal{T}=\tilde{\mathcal{T}}\,\vartheta$, and $P=\tilde{P}\,\pi$ into (2.9-2.11) leads to

$$\left[\frac{U}{\tau}\right]\frac{\partial\tilde{\boldsymbol{U}}}{\partial\tilde{t}}+\left[\frac{U^2}{L}\right](\tilde{\boldsymbol{U}}\cdot\tilde{\nabla})\,\tilde{\boldsymbol{U}}=-\left[\frac{\pi}{\rho_{ref}L}\right]\tilde{\nabla}\tilde{P}+\left[\frac{\nu U}{L^2}\right]\tilde{\nabla}^2\tilde{\boldsymbol{U}}+[g]\,\hat{\boldsymbol{g}}-[g\alpha\vartheta]\,\hat{\boldsymbol{g}}(\tilde{\mathcal{T}}-\tilde{\mathcal{T}}_{ref})\,, \tag{2.19}$$

$$\left[\frac{\vartheta}{\tau}\right]\frac{\partial\tilde{\mathcal{T}}}{\partial\tilde{t}}+\left[\frac{\vartheta U}{L}\right](\tilde{\boldsymbol{U}}\cdot\tilde{\nabla})\,\tilde{\mathcal{T}}=\left[\frac{\kappa\vartheta}{L^2}\right]\tilde{\nabla}^2\tilde{\mathcal{T}}\,, \tag{2.20}$$

$$\left[\frac{U}{L}\right]\tilde{\nabla}\cdot\tilde{\boldsymbol{U}}=0\,. \tag{2.21}$$

All dimensional scales are collected in rectangular brackets. Following previous studies (Malkus, 1964; Gray and Giorgini, 1976; Chillà and Schumacher, 2012), we choose to measure the dimensional scales in units of three external scales:

- Length is measured in units of the gap height: $L=H=b-a$
- Temperature is measured in units of the temperature difference between the walls: $\vartheta=\Delta\mathcal{T}=\mathcal{T}_1-\mathcal{T}_2$
- Velocity is measured in units of the free fall velocity: $U=U_f=\sqrt{g\,\alpha\,\Delta\mathcal{T}\,H}$

Alternative sets of other external scales may be chosen (Subramanian et al., 2016). From the above choice of external scales, the units of time and pressure scales follow when collecting all scales on the right-hand side of (2.19-2.21),

$$\frac{\partial\tilde{\boldsymbol{U}}}{\partial\tilde{t}}+(\tilde{\boldsymbol{U}}\cdot\tilde{\nabla})\,\tilde{\boldsymbol{U}}=-\tilde{\nabla}\tilde{P}+\left[\frac{\nu}{\sqrt{g\,\alpha\,\Delta\mathcal{T}\,H^3}}\right]\tilde{\nabla}^2\tilde{\boldsymbol{U}}+\left[\frac{1}{\alpha\Delta\mathcal{T}}\right]\hat{\boldsymbol{g}}-\hat{\boldsymbol{g}}(\tilde{\mathcal{T}}-\tilde{\mathcal{T}}_{ref}) \tag{2.22}$$

$$\frac{\partial\tilde{\mathcal{T}}}{\partial\tilde{t}}+(\tilde{\boldsymbol{U}}\cdot\tilde{\nabla})\,\tilde{\mathcal{T}}=\left[\frac{\kappa}{\sqrt{g\,\alpha\,\Delta\mathcal{T}\,H^3}}\right]\tilde{\nabla}^2\tilde{\mathcal{T}} \tag{2.23}$$

$$\tilde{\nabla}\cdot\tilde{\boldsymbol{U}}=0 \tag{2.24}$$

Since the non-dimensional form requires $\pi=\rho_{ref}\,g\,\alpha\,\Delta\mathcal{T}\,H$, pressure is measured in units of the hydrostatic pressure exerted by a fluid of height H. Since the non-dimensional form

requires $\tau = H/U_f$, time is measured in free-fall time units. In this non-dimensional form, the dimensional scales form two dimensionless groups, the Rayleigh number Ra and the Prandtl number Pr, where

$$\mathrm{Ra} = \frac{g\,\alpha\,\Delta\mathcal{T}\,H^3}{\nu\kappa}\,, \tag{2.25}$$

$$\mathrm{Pr} = \frac{\nu}{\kappa}\,. \tag{2.26}$$

Thus, the non-dimensional Oberbeck-Boussinesq equations have the form

$$\frac{\partial \boldsymbol{U}}{\partial t} + (\boldsymbol{U}\cdot\nabla)\,\boldsymbol{U} = -\nabla P + \tilde{\nu}\nabla^2\boldsymbol{U} + \eta\hat{\boldsymbol{g}} - \hat{\boldsymbol{g}}(\mathcal{T} - \mathcal{T}_{ref})\,, \tag{2.27}$$

$$\frac{\partial \mathcal{T}}{\partial t} + (\boldsymbol{U}\cdot\nabla)\,\mathcal{T} = \tilde{\kappa}\nabla^2\mathcal{T}\,, \tag{2.28}$$

$$\nabla\cdot\boldsymbol{U} = 0\,, \tag{2.29}$$

where "˜" is omitted for all quantities except for the two parameters, $\tilde{\nu} = (\mathrm{Pr}/\mathrm{Ra})^{1/2}$ and $\tilde{\kappa} = 1/(\mathrm{Pr}\,\mathrm{Ra})^{1/2}$, to clearly denote them as non-dimensional kinematic viscosity and thermal diffusivity, respectively. The non-dimensionalization of the boundary conditions (2.12-2.17) implies $b-a=1$ and $\mathcal{T}_1 - \mathcal{T}_2 = 1$. Choosing different numerical values for gap heights or temperature differences makes the above non-dimensionalization inconsistent and the interpretation $\mathrm{Ra} = 1/\tilde{\nu}\tilde{\kappa}$ and $\mathrm{Pr} = \tilde{\nu}/\tilde{\kappa}$ does not hold anymore. In *Channelflow*, the location of the wall and the numerical values of velocities at the walls can be set by the user and are not enforced to match certain numbers. In line with this design decision, the non-dimensionalized Oberbeck-Boussinesq equations (2.27-2.29) are implemented with boundary conditions of the general form (2.12-2.17), which from now on, are considered as non-dimensional. Boundary conditions for which $b-a=1$ and $\mathcal{T}_1 - \mathcal{T}_2 = 1$ hold are suggested by the default settings of the implementation. Users that want to exploit the flexibility in the boundary conditions should be aware that deviations from the default settings may change the interpretation of $\tilde{\nu}$ and $\tilde{\kappa}$.

The above non-dimensional form of the Oberbeck-Boussinesq equations has two advantages compared to other forms. First, the dimensionless parameters Ra and Pr are combined in a non-dimensional kinematic viscosity $\tilde{\nu}$. Thus, the non-dimensional Oberbeck-Boussinesq equations share one control parameter with the non-dimensional Navier-Stokes equations, as already implemented in *Channelflow*. Second, Rayleigh numbers in studies of thermal convection often span several orders of magnitude. In (2.27) and (2.28), Ra appears as square root, which makes this form of non-dimensionalization numerically advantageous over forms where Ra directly scales non-dimensional terms in the equations (e.g. Subramanian et al., 2016).

Equations (2.27-2.29) correspond to the initially given equations (1.2-1.4) with two modifications. First, the reference temperature is chosen as $\mathcal{T}_{ref} = 0$. For non-dimensional and anti-symmetric boundary conditions $\mathcal{T}_{1,2} = \pm 0.5$, commonly used to numerically study ILC (e.g. Subramanian et al., 2016), $\mathcal{T}_{ref} = 0$ matches the laminar base state for temperature at midplane and makes the laminar velocity and temperature profiles antisymmetric. Second, (1.2-1.4) describe pressure relative to the hydrostatic pressure profile. As a result, the hydrostatic pressure term $\eta\hat{\boldsymbol{g}}$, where $\eta = 1/\alpha\Delta\mathcal{T}$, is canceled out. The laminar base state for pressure, temperature and velocity are discussed in the following section.

2.2.5 Laminar base state for general boundary conditions

To find the laminar base states of (2.27-2.29) for inclined channels, three assumptions are made:

1. The laminar base state is time independent.

2. The laminar base state is homogeneous in the x- and z-dimension, implying y-dependence only.

3. No external pressure gradients are imposed to drive a flow. The pressure base state absorbs the hydrostatic pressure.

The second assumption simplifies the continuity equation (2.29) to $\partial V(y)/\partial y = 0$. Together with boundary condition (2.13), this implies that there is no wall-normal base flow, $V_0(y) = 0$. Decomposing velocity, pressure gradient and temperature into y-dependent base profiles for the laminar solution and fluctuations read

$$\boldsymbol{U}(\boldsymbol{x},t) = U_0(y)\boldsymbol{e}_x + W_0(y)\boldsymbol{e}_z + \boldsymbol{u}(\boldsymbol{x},t)\,, \tag{2.30}$$

$$\nabla P(\boldsymbol{x},t) = \Pi_x(y)\boldsymbol{e}_x + \Pi_y(y)\boldsymbol{e}_y + \Pi_z(y)\boldsymbol{e}_z + \nabla p(\boldsymbol{x},t)\,, \tag{2.31}$$

$$\mathcal{T}(\boldsymbol{x},t) = \mathcal{T}_0(y) + \theta(\boldsymbol{x},t)\,. \tag{2.32}$$

The pressure base state is considered as gradients which can be x-z-homogeneous in a laminar flow. Inserting these decompositions into (2.27) and (2.28) and assuming the fluctuations to

be zero, the laminar base state must satisfy

$$U: \quad 0 = -\Pi_x(y) \qquad +\tilde{\nu}\frac{\partial^2}{\partial y^2}U_0(y) - \eta\sin(\gamma) + \sin(\gamma)\left(\mathcal{T}_0(y) - \mathcal{T}_{ref}\right), \tag{2.33}$$

$$V: \quad 0 = -\Pi_y(y) \qquad -\eta\cos(\gamma) + \cos(\gamma)\left(\mathcal{T}_0(y) - \mathcal{T}_{ref}\right), \tag{2.34}$$

$$W: \quad 0 = -\Pi_z(y) \qquad +\tilde{\nu}\frac{\partial^2}{\partial y^2}W_0(y), \tag{2.35}$$

$$\mathcal{T}: \quad 0 = \qquad \tilde{\kappa}\frac{\partial^2}{\partial y^2}\mathcal{T}_0(y), \tag{2.36}$$

as well as the boundary conditions (2.12-2.15). Since these boundary conditions are considered in a general form without enforcing particular numerical values, the laminar base state is calculated for three different types of boundary conditions:

- **general**: Location of the walls and the numerical boundary values at the walls (2.12-2.15) are arbitrary.

- **symmetric walls**: The location of the walls is fixed at $[a,b] = [-0.5, 0.5]$. Velocity and temperature values at these symmetrically placed walls remain arbitrary. This form of the laminar base state is the one implemented in *Channelflow* as rescaled Chebychev polynomials. In *Channelflow*, Chebychev polynomials are defined on the interval $[a,b] = [-1,1]$ and rescaled to the specific height H of the numerical domain.

- **default**: The y-symmetric boundary conditions of non-dimensional ILC are $\mathcal{T}(y = \pm 0.5) = \mp 0.5$, $\mathcal{T}_{ref} = 0$ and $U(y = \pm 0.5) = W(y = \pm 0.5) = 0$. They are defined as the default settings in *Channelflow*.

Pressure base profile

In general, the four equations (2.33-2.36) under-determine the laminar base state which consists of six unknown profiles $U_0(y)$, $W_0(y)$, $\mathcal{T}_0(y)$ and $\Pi(y)$ along all three space dimensions. In the hydrostatic case however, the number of unknowns reduces to four because $U_0(y) = W_0(y) = 0$. A hydrostatic layer requires stationary walls and may occur for two different cases of inclination angle γ. First, in a horizontal channel with $\gamma = 0$, the fluid is at rest for any $\mathcal{T}_0(y)$. The only non-zero pressure gradient in this case is $\Pi_y(y) = -\eta\cos(\gamma) + \cos(\gamma)\left(\mathcal{T}_0(y) - \mathcal{T}_{ref}\right)$, due to (2.34). Second, in an inclined channel with $\gamma \neq 0$, the fluid is at rest only if $\mathcal{T}_0(y) = \mathcal{T}_{ref}$. In this case, the non-zero pressure gradients are $\Pi_x = -\eta\sin(\gamma)$ and $\Pi_y = -\eta\cos(\gamma)$. Thus, the

laminar base state for hydrostatic pressure gradients in horizontal and inclined channels is

$$\Pi_x = -\eta \sin(\gamma) \,, \tag{2.37}$$

$$\Pi_y(y) = -\eta \cos(\gamma) + \cos(\gamma) \left(\mathcal{T}_0(y) - \mathcal{T}_{ref}\right) \,, \tag{2.38}$$

$$\Pi_z = 0 \,, \tag{2.39}$$

with $\eta = 1/\alpha\Delta\mathcal{T}$. Note that the second term in 2.38 is not part of the hydrostatic pressure at finite inclinations. These pressure base profiles apply under general, symmetric walls and default boundary conditions.

Temperature base profile

The temperature profile $\mathcal{T}_0(y)$ of the laminar base state is found by integrating (2.36) twice with respect to y:

$$C_2 + y\, C_1 = \mathcal{T}_0(y) \tag{2.40}$$

The integration constants C_1 and C_2 are determined by the general dimensionless boundary conditions (2.15)

$$C_2 + a\, C_1 = \mathcal{T}_0(a) = \mathcal{T}_1 \,, \tag{2.41}$$

$$C_2 + b\, C_1 = \mathcal{T}_0(b) = \mathcal{T}_2 \,. \tag{2.42}$$

The first constant follows from the difference (2.41) - (2.42):

$$C_1 = \frac{\mathcal{T}_2 - \mathcal{T}_1}{(b-a)} \qquad \text{(general)} \tag{2.43}$$

$$C_1 = \mathcal{T}_2 - \mathcal{T}_1 \qquad \text{(sym. walls)} \tag{2.44}$$

$$C_1 = -1 \qquad \text{(default)} \tag{2.45}$$

The second constant follows from the sum (2.41) + (2.42) with C_1:

$$C_2 = \frac{b\mathcal{T}_1 - a\mathcal{T}_2}{(b-a)} \qquad \text{(general)} \tag{2.46}$$

$$C_2 = \frac{\mathcal{T}_1 + \mathcal{T}_2}{2} \qquad \text{(sym. walls)} \tag{2.47}$$

$$C_2 = 0 \qquad \text{(default)} \tag{2.48}$$

Thus, the temperature base profile is

$$\mathcal{T}_0(y) = \frac{(b-y)\,\mathcal{T}_1 - (a-y)\,\mathcal{T}_2}{(b-a)} \qquad \text{(general)}\,, \tag{2.49}$$

$$\mathcal{T}_0(y) = (\mathcal{T}_2 - \mathcal{T}_1)\,y + \frac{\mathcal{T}_1 + \mathcal{T}_2}{2} \qquad \text{(sym. walls)}\,, \tag{2.50}$$

$$\mathcal{T}_0(y) = -y \qquad \text{(default)}\,. \tag{2.51}$$

Velocity base profile

The velocity profile $U_0(y)$ of the laminar base state must satisfy (2.33). Since the pressure base profile (2.37) cancels with the mean gravitional acceleration term, $\eta\sin(\gamma)$, the velocity base profile $U_0(y)$ must satisfy

$$\tilde{\nu}\frac{\partial^2}{\partial y^2}U_0(y) = -\sin(\gamma)\left(\mathcal{T}_0(y) - \mathcal{T}_{ref}\right)\,. \tag{2.52}$$

Inserting the temperature base profile (2.49) gives

$$\frac{H}{q}\frac{\partial^2}{\partial y^2}U_0(y) = (\mathcal{T}_2 - \mathcal{T}_1)\,y + (bT_1 - aT_2 - HT_{ref})\,, \tag{2.53}$$

with prefactor $q = -\sin(\gamma)/\tilde{\nu}$ and scale $H = (b-a)$. Integrating twice with respect to y gives

$$\frac{H}{q}\frac{\partial}{\partial y}U_0(y) = \frac{1}{2}(\mathcal{T}_2 - \mathcal{T}_1)\,y^2 + (bT_1 - aT_2 - HT_{ref})\,y + C_1\,, \tag{2.54}$$

$$\frac{H}{q}\,U_0(y) = \frac{1}{6}(\mathcal{T}_2 - \mathcal{T}_1)\,y^3 + \frac{1}{2}(bT_1 - aT_2 - HT_{ref})\,y^2 + C_1\,y + C_2\,. \tag{2.55}$$

The integration constants C_1 and C_2 are determined by the general dimensionless boundary conditions (2.12):

$$y = a: \quad \frac{H}{q}U_1 = \frac{1}{6}(\mathcal{T}_2 - \mathcal{T}_1)\,a^3 + \frac{1}{2}(bT_1 - aT_2 - HT_{ref})\,a^2 + C_1\,a + C_2 \tag{2.56}$$

$$y = b: \quad \frac{H}{q}U_2 = \frac{1}{6}(\mathcal{T}_2 - \mathcal{T}_1)\,b^3 + \frac{1}{2}(bT_1 - aT_2 - HT_{ref})\,b^2 + C_1\,b + C_2 \tag{2.57}$$

C_1 follows from the difference (2.56) - (2.57):

$$C_1 = \frac{(U_1 - U_2)H}{(a-b)q} - \frac{1}{2(a-b)}\left(\frac{1}{3}(\mathcal{T}_2 - \mathcal{T}_1)(a^3 - b^3) + (bT_1 - aT_2 - HT_{ref})(a^2 - b^2)\right) \quad \text{(general)} \quad (2.58)$$

$$C_1 = \frac{U_1 - U_2}{(a-b)q} + \frac{1}{24}(\mathcal{T}_1 - \mathcal{T}_2) \quad \text{(sym. walls)} \quad (2.59)$$

$$C_1 = \frac{1}{24} \quad \text{(default)} \quad (2.60)$$

C_2 follows from the sum (2.56) + (2.57) with C_1:

$$C_2 = \frac{H}{2q}\left[(U_1 + U_2) - (U_1 - U_2)\frac{(a+b)}{(a-b)}\right] + \frac{1}{12}(\mathcal{T}_1 - \mathcal{T}_2)\left[(a^3 + b^3) - (a^3 - b^3)\frac{(a+b)}{(a-b)}\right] - \frac{1}{4}(bT_1 - aT_2 - HT_{ref})\left[(a^2 + b^2) - (a^2 - b^2)\frac{(a+b)}{(a-b)}\right] \quad \text{(general)} \quad (2.61)$$

$$C_2 = \frac{1}{2q}(U_1 + U_2) + \frac{1}{16}(\mathcal{T}_1 + \mathcal{T}_2 - 2T_{ref}) \quad \text{(sym. walls)} \quad (2.62)$$

$$C_2 = 0 \quad \text{(default)} \quad (2.63)$$

Inserting the two coefficients into (2.55), one obtains the velocity profile $U_0(y)$ of the laminar base state:

$$\begin{aligned}
U_0(y) = & \frac{\sin(\gamma)(\mathcal{T}_1-\mathcal{T}_2)}{6\tilde{\nu}(b-a)}y^3 \\
& -\frac{\sin(\gamma)}{2\tilde{\nu}(b-a)}(bT_1-aT_2-HT_{ref})y^2 \\
& +\left(\frac{U_1-U_2}{(a-b)}-\frac{\sin(\gamma)}{2\tilde{\nu}(a-b)^2}\left(\frac{1}{3}(\mathcal{T}_2-\mathcal{T}_1)(a^3-b^3)+(bT_1-aT_2-HT_{ref})(a^2-b^2)\right)\right)y \\
& +\frac{1}{2}\left[(U_1+U_2)-(U_1-U_2)\frac{(a+b)}{(a-b)}\right] \\
& -\frac{\sin(\gamma)}{12\tilde{\nu}}(\mathcal{T}_1-\mathcal{T}_2)\left[(a^3+b^3)-(a^3-b^3)\frac{(a+b)}{(a-b)}\right] \\
& +\frac{\sin(\gamma)}{4\tilde{\nu}}(bT_1-aT_2-HT_{ref})\left[(a^2+b^2)-(a^2-b^2)\frac{(a+b)}{(a-b)}\right] \qquad \text{(general)} \qquad (2.64)
\end{aligned}$$

$$\begin{aligned}
U_0(y) = & \frac{\sin(\gamma)}{6\tilde{\nu}}(\mathcal{T}_1-\mathcal{T}_2)y^3-\frac{\sin(\gamma)}{2\tilde{\nu}}\left(\frac{\mathcal{T}_1+\mathcal{T}_2}{2}-\mathcal{T}_{ref}\right)y^2 \\
& -\frac{\sin(\gamma)}{24\tilde{\nu}}(\mathcal{T}_1-\mathcal{T}_2)y+\frac{\sin(\gamma)}{8\tilde{\nu}}\left(\frac{\mathcal{T}_1+\mathcal{T}_2}{2}-\mathcal{T}_{ref}\right) \\
& +(U_2-U_1)y \quad +\frac{U_1+U_2}{2} \qquad \text{(sym. walls)} \qquad (2.65)
\end{aligned}$$

$$U_0(y) = \frac{\sin(\gamma)}{6\tilde{\nu}}\left(y^3-\frac{1}{4}y\right) \qquad \text{(default)} \qquad (2.66)$$

The base profile $W_0(y)$ must satisfy (2.35). The problem is solved for the general boundary conditions (2.14) in analogy to the temperature base profile $\mathcal{T}_0(y)$ and thus, has the same linear form as (2.49) and (2.50):

$$W_0(y) = \frac{(b-y)\,W_1-(a-y)\,W_2}{(b-a)} \qquad \text{(general)} \qquad (2.67)$$

$$W_0(y) = (W_2-W_1)y+\frac{W_1+W_2}{2} \qquad \text{(sym. walls)} \qquad (2.68)$$

$$W_0(y) = 0 \qquad \text{(default)} \qquad (2.69)$$

Here, the spanwise velocity base profile is only wall-driven. Future development should consider inclination and buoyancy-driven flow also along the z-dimension.

Having calculated the complete laminar base state, the next step is to express this state in terms of spectral Chebychev coefficients. These coefficients are then implemented in *Channelflow*.

Chebychev coefficients of the base profiles

Wall-normal profiles are defined as series expansions with Chebyshev polynomials within the spectral data representation of *Channelflow*. The above calculated laminar base profiles are at most of cubic order. The first four Chebyshev polynomials of the first kind are

$$\mathcal{C}_0(x) = 1\,, \tag{2.70}$$
$$\mathcal{C}_1(x) = x\,, \tag{2.71}$$
$$\mathcal{C}_2(x) = 2x^2 - 1\,, \tag{2.72}$$
$$\mathcal{C}_3(x) = 4x^3 - 3x\,, \tag{2.73}$$

defined on the interval $x \in [-1,1]$ with the normalization $\mathcal{C}_j(1) = 1$. The laminar base solution profiles have been calculated in the polynomial form

$$f(y) = p_3 y^3 + p_2 y^2 + p_1 y + p_0\,. \tag{2.74}$$

In the case of general boundary conditions with symmetric walls, the calculated polynomials are defined on the interval $y\epsilon[-0.5, 0.5]$. The coefficients q_i of a Chebyshev expansion $f(y) = \sum_{i=0}^{3} q_i \mathcal{C}_i(x)$ relate to coefficients p_i as

$$q_0 = \frac{1}{8} p_2 + p_0 \tag{2.75}$$
$$q_1 = \frac{3}{32} p_3 + \frac{1}{2} p_1 \tag{2.76}$$
$$q_2 = \frac{1}{8} p_2 \tag{2.77}$$
$$q_3 = \frac{1}{32} p_3 \tag{2.78}$$

where a the stretching transformation with $y = x/2$ is considered. Using this relation, the laminar base profiles, calculated for symmetric walls at $y = \pm 0.5$, can be expressed in terms of Chebyshev coefficients. If the walls are located differently, the Chebyshev transformation in *Channelflow* transforms the functions from the interval $[-1,1]$ in the spectral representation to any chosen interval $[a,b]$ in the physical representation. The base profiles calculated for arbitrary wall locations at $y = a$ and $y = b$ (general case) provide test cases for units testing the numerical implementations of the Oberbeck-Boussinesq equations and the Chebyshev transformation.
The temperature base profile $\mathcal{T}_0(y)$, defined in (2.50), has the spectral Chebyshev coefficients:

$$q_0 = \frac{\mathcal{T}_2 + \mathcal{T}_1}{2} \tag{2.79}$$
$$q_1 = \frac{\mathcal{T}_2 - \mathcal{T}_1}{2} \tag{2.80}$$

The coefficients of the spanwise velocity profile $W_0(y)$, defined in (2.68), are found analogously:

$$q_0 = \frac{W_2 + W_1}{2} \tag{2.81}$$

$$q_1 = \frac{W_2 - W_1}{2} \tag{2.82}$$

The Chebyshev coefficients for the streamwise velocity profile $U_0(y)$, defined in (2.65), are slightly more complicated:

$$q_0 = \frac{\sin(\gamma)}{16\tilde{\nu}}\left(\frac{\mathcal{T}_1 + \mathcal{T}_2}{2} - \mathcal{T}_{ref}\right) + \frac{U_2 + U_1}{2} \tag{2.83}$$

$$q_1 = -\frac{\sin(\gamma)}{192\tilde{\nu}}(\mathcal{T}_1 - \mathcal{T}_2) + \frac{U_2 - U_1}{2} \tag{2.84}$$

$$q_2 = -\frac{\sin(\gamma)}{16\tilde{\nu}}\left(\frac{\mathcal{T}_1 + \mathcal{T}_2}{2} - \mathcal{T}_{ref}\right) \tag{2.85}$$

$$q_3 = \frac{\sin(\gamma)}{192\tilde{\nu}}(\mathcal{T}_1 - \mathcal{T}_2) \tag{2.86}$$

The pressure base profiles Π_x and $\Pi_y(y)$, defined in (2.37) and (2.38), respectively, are linearly related to $\mathcal{T}_0(y)$ and its Chebyshev coefficients.

2.2.6 Implementation of the Oberbeck-Boussinesq equations

Having non-dimensionalized the Oberbeck-Boussinesq equations and calculated the laminar base state, *Channelflow* is extended to the new governing equations. Inserting the decomposition (2.30-2.32) into the governing equations (2.27-2.28) yields the following momentum and heat equations

$$\begin{aligned}\frac{\partial \boldsymbol{u}(\boldsymbol{x},t)}{\partial t} + (\boldsymbol{U}(\boldsymbol{x},t)\cdot\nabla)\,\boldsymbol{U}(\boldsymbol{x},t) &= -\nabla p(\boldsymbol{x},t) + \tilde{\nu}\nabla^2\boldsymbol{u}(\boldsymbol{x},t) \\ &+ \left(\sin(\gamma)\boldsymbol{e}_x + \cos(\gamma)\boldsymbol{e}_y\right)\theta(\boldsymbol{x},t) \\ &+ \left[-\Pi_x - \eta\sin(\gamma) + \tilde{\nu}\frac{\partial^2 U_0(y)}{\partial y^2} + \sin(\gamma)(\mathcal{T}_0(y) - \mathcal{T}_{ref})\right]\boldsymbol{e}_x \\ &+ \left[-\Pi_y(y) - \eta\cos(\gamma) + \cos(\gamma)(\mathcal{T}_0(y) - \mathcal{T}_{ref})\right]\boldsymbol{e}_y \\ &+ \left[\tilde{\nu}\frac{\partial^2 W_0(y)}{\partial y^2}\right]\boldsymbol{e}_z\,, \end{aligned} \tag{2.87}$$

$$\frac{\partial \theta(\boldsymbol{x},t)}{\partial t} + (\boldsymbol{U}(\boldsymbol{x},t)\cdot\nabla)\,\mathcal{T}(\boldsymbol{x},t) = \tilde{\kappa}\nabla^2\theta(\boldsymbol{x},t) + \left[\tilde{\kappa}\frac{\partial^2 \mathcal{T}_0(y)}{\partial y^2}\right]. \tag{2.88}$$

The nonlinear terms on the left-hand side are not considered in decomposed form and are products of the total velocity $\boldsymbol{U}$ and the total temperature $\mathcal{T}$. In*Channelflow*, fluctuating components around any arbitrary base profile may be considered. In line with the design

decision that base profiles do not need to be a solution of the governing equations, the terms containing the base profiles are not canceled and remain in the equations. If the base profiles correspond to the laminar base state as defined in Section 2.2.5, all terms in rectangular brackets in (2.87) and (2.88) are zero. If not, these terms are added as constant profiles, denoted as $C_{\boldsymbol{u}}(y)$ or $C_\theta(y)$, to the equations.

Equations (2.87) and (2.88) are numerically implemented as a spectral Galerkin approximation using Fourier × Chebyshev × Fourier expansions in $x \times y \times z$. Velocity and temperature fluctuations are expanded as

$$[\boldsymbol{u},\theta](\boldsymbol{x},t) = \sum_{k_x=-K_x}^{K_x} \sum_{j=0}^{N_y-1} \sum_{k_z=-K_z}^{K_z} \left[\hat{\boldsymbol{u}},\hat{\theta}\right]_{k_x,j,k_z}(t)\, \mathcal{C}_j(y)\, e^{2\pi i(k_x x/L_x + k_z z/L_z)} \tag{2.89}$$

where $\mathcal{C}_j(y)$ is the j-th Chebyshev polynomial of the first kind. $[\hat{\boldsymbol{u}},\hat{\theta}]_{k_x,j,k_z}(t)$ are the time-dependent amplitudes of the discrete Fourier and Chebyshev modes, respectively. Inserting (2.89) into (2.87) and (2.88), the momentum and heat equations can be expressed in the form of a general spectral nonlinear evolution equation (2.1) for the general state vector $\hat{\boldsymbol{x}} = [\hat{\boldsymbol{u}},\hat{\theta},\hat{p}]$. Using the spectral operator $\hat{\nabla}$, given in (2.4), the components of the linear operator $\mathcal{L}_{\xi_i}\hat{\boldsymbol{x}}$ in (2.1) are defined as

$$\mathcal{L}_{\boldsymbol{u}}\hat{\boldsymbol{x}} = \tilde{\nu}\left(\hat{\nabla}\cdot\hat{\nabla}\right)\hat{\boldsymbol{u}} - \hat{\nabla}\hat{p}\,, \tag{2.90}$$

$$\mathcal{L}_{\theta}\hat{\boldsymbol{x}} = \tilde{\kappa}\left(\hat{\nabla}\cdot\hat{\nabla}\right)\hat{\theta}\,, \tag{2.91}$$

and the components of the nonlinear operator $\mathcal{N}_{\xi_i}(\hat{\boldsymbol{x}})$ in (2.1) are defined as

$$\mathcal{N}_{\boldsymbol{u}}(\hat{\boldsymbol{x}}) = \mathbb{F}\left(\mathbb{F}^{-1}(\hat{\boldsymbol{U}})\cdot\mathbb{F}^{-1}(\hat{\nabla}\hat{\boldsymbol{U}})\right) + C_{\boldsymbol{u}} - \sin(\gamma)\hat{\theta}\hat{\boldsymbol{e}}_x - \cos(\gamma)\hat{\theta}\hat{\boldsymbol{e}}_z\,, \tag{2.92}$$

$$\mathcal{N}_{\theta}(\hat{\boldsymbol{x}}) = \mathbb{F}\left(\mathbb{F}^{-1}(\hat{\boldsymbol{U}})\cdot\mathbb{F}^{-1}(\hat{\nabla}\hat{T})\right) + C_\theta\,, \tag{2.93}$$

with the Fourier-Chebyshev transform operator $\mathbb{F}$. The evaluation of nonlinear products in physical space instead of spectral space reduces the number of operations N^2 to $N\log(N)$. This approach is called pseudospectral method (Canuto et al., 2006, Section 3.4.1). The constants $\hat{C}_{\boldsymbol{u}}$ and $\hat{C}_\theta$ contain the spectral form of the constant base profiles inside the rectangular brackets in (2.87) and (2.88), respectively. The spectral base profiles are given by the Chebyshev coefficients discussed in Section 2.2.5.

The generalization of the time-stepping algorithms discussed in Section 2.1.2 allows to advance (2.87) and (2.88) in time based on the definition of the linear and nonlinear terms (2.90-2.93). The time-stepping algorithms treat the linear terms fully or semi implicitly and the nonlinear terms fully explicitly. Since the linear terms are not coupled, the two implicit problems can be solved independently from each other at the same temporal stage. For all time-stepping

algorithms (2.5-2.8), the implicit problem for time step $n+1$ reads

$$\tilde{\nu}\frac{\partial^2}{\partial y^2}\hat{\boldsymbol{u}}^{n+1} - \lambda_{\boldsymbol{u}}\hat{\boldsymbol{u}}^{n+1} - \tilde{\nabla}\hat{p}^{n+1} = \mathrm{RHS}_{\boldsymbol{u}}(\boldsymbol{u},\theta)^{n,n-1,\dots}\,, \tag{2.94}$$

$$\tilde{\kappa}\frac{\partial^2}{\partial y^2}\hat{\theta}^{n+1} - \lambda_{\theta}\hat{\theta}^{n+1} = \mathrm{RHS}_{\theta}(\boldsymbol{u},\theta)^{n,n-1,\dots}\,, \tag{2.95}$$

with

$$\lambda_{\boldsymbol{u}} = \frac{\chi}{\Delta t} + 4\pi^2\tilde{\nu}\left(\frac{k_x^2}{L_x^2} + \frac{k_z^2}{L_z^2}\right)\,, \tag{2.96}$$

$$\lambda_{\theta} = \frac{\chi}{\Delta t} + 4\pi^2\tilde{\kappa}\left(\frac{k_x^2}{L_x^2} + \frac{k_z^2}{L_z^2}\right)\,. \tag{2.97}$$

The factor χ depends on the specific time-stepping algorithm (2.5-2.8). Equation (2.95) represent a one-dimensional Helmholtz problem that is solved for boundary conditions $\theta(y=a,b)=0$ using the Chebyshev Tau method (Canuto et al., 1988, Section 5.1.2). The coupled Helmholtz problem (2.94) is solved for boundary conditions $\boldsymbol{u}(y=a,b)=0$ and $\nabla\cdot\boldsymbol{u}=0$ using the influence matrix method (Kleiser and Schumann, 1980; Canuto and Landriani, 1986). The specific Helmholtz problem also depends on the choice of the integral constraint as either mean pressure gradient or mean flow rate (see Section 2.2.4). The methods to solve (2.95) and (2.95) were already implemented in *Channelflow*.

The Oberbeck-Boussinesq equations contain the Navier-Stokes equations. See the first line in (2.87). As a consequence much of the existing implementation for the Navier-Stokes equations in *Channelflow* has been re-used for the extension module *Channelflow-ILC*. Four new classes have been implemented, all of which were derived from existing classes and override the base class methods. The class diagram in Figure 2.1 indicates the four new classes by the prefix "ext" (short for extension). The terms of the Oberbeck-Boussinesq equations and the laminar base state are implemented in the class `OBE` derived from `NSE` (see "extNSE" in Figure 2.1). Three public class methods in `OBE` provide the terms in the Oberbeck-Boussinesq equations to the generalized time-stepping algorithms in DNSAlgorithm: `linear` provides (2.90) and (2.91), `nonlinear` provides (2.92) and (2.93), and `solve` solves (2.94) and (2.95). Each of these methods takes one input and one output argument of type `vector<FlowField>&`. This vector type corresponds to $\boldsymbol{x} = [\hat{\boldsymbol{u}}, \hat{\theta}, \hat{p}]$. This order of entries is assumed at multiple locations and must be respected. The classes `ILC` and `ILCFlags` are user interfaces for running direct numerical simulations of ILC and derived from `DNS` and `DNSFlags`, respectively. The class `ilcDSI`, derived from `cfDSI`, is the dynamical systems interface to provide the time evolution of the Oberbeck-Boussinesq equations to the `nsolver` library.

2.2.7 Validation

The numerical implementation of the Oberbeck-Boussinesq equations for inclined channels has been validated by reproducing previously computed or analytic results on three different levels of importance of nonlinear effects.

Linear and weakly nonlinear instabilities. Many previous studies have accurately determined stability thresholds in thermal convection. The primary onset of convection in Rayleigh-Bénard at $Ra_c = 1707.76$ (Busse, 1978b) and the codimension-2 point in ILC at $[\gamma_{c2}, \mathrm{Ra}_{c2}] = [77.7567°, 8053.1]$ (Subramanian et al., 2016) have been successful reproduced using numerical continuation of exact invariant straight convection rolls (see Section 4.3.3 for more details). Moreover, critical thresholds of the well-known secondary wavy instability of longitudinal rolls in ILC (Clever and Busse, 1977) have been compared with recent Floquet analysis (Subramanian et al., 2016, personal communication). The wavelengths that first become unstable in the wavy instability are much larger than the gap height H of ILC. Floquet analysis of longitudinal rolls at $\gamma = 40°$, resolved by $M = 12$ wall-normal sine-modes (compare Subramanian et al., 2016, Appendix A), indicates a wavenumber of $k_x = 0.03$ at a critical Rayleigh number of $Ra_c = 2257.9$ as most unstable wavenumber. This implies a pattern wavelength of $L_x = 2\pi/k_x \approx 200$ in units of H. Smaller or larger wavelengths become unstable at higher Ra_c. *Channelflow-ILC* reproduces this result. At the wavy instability, a Ra-forward supercritical Pitchfork bifurcation creates a finite amplitude branch of exact invariant wavy rolls (see Section 5.3.3). Numerical continuation along this branch down in Ra yields the bifurcation point and the critical wavy instability threshold Ra_c. The critical thresholds Ra_c computed for different imposed domain lengths L_x coincide with the neutral stability curve obtained from Floquet analysis (Figure 2.5). Computing a long-wavelength instability, like the wavy instability, by continuing nonlinear invariant states in a fully resolved three-dimensional domain of lateral extent $[L_x, L_z] \approx [200, 2]$ and with resolution $[N_x, N_y, N_z] = [64, 17, 32]$ is numerically challenging because all modal interactions within this domain are considered. Floquet analysis considers different modal interactions only individually.

Nonlinear scaling invariance. During the scope of studying the bifurcations to invariant solutions underlying spatially periodic convection patterns in ILC (Section 5), a scaling invariance of the nonlinear Oberbeck-Boussinesq equations has been identified (Equations 5.15-5.19). The scaling invariance leads to an exact correspondence of steady and x-uniform states across Ra and γ. Numerical continuation of invariant longitudinal rolls along the scale invariant path in control parameters reproduces this analytic result (see Figure 5.4 and Section 5.3).

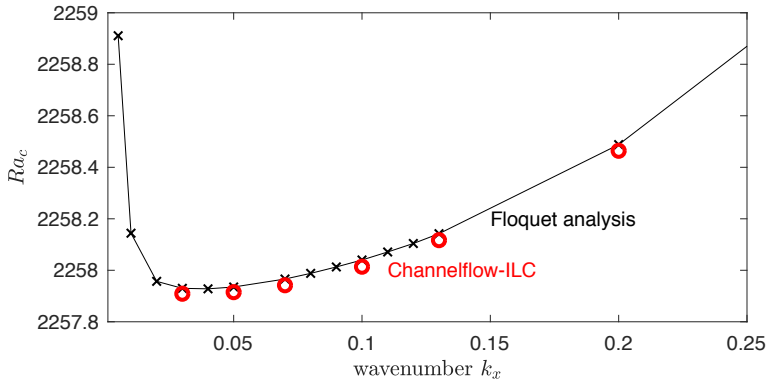

Figure 2.5 – Agreement between results of *Channelflow-ILC* and recent Floquet analysis. Critical thresholds in Rayleigh number Ra_c for the secondary wavy instability of longitudinal straight convection rolls in ILC at inclination angle $\gamma = 40°$ and Prandtl number Pr = 1.07. The Floquet analysis is described in Subramanian et al. (2016) and the data was communicated with the leading author.

Fully turbulent thermal convection. The MPI parallelization of *Channelflow-ILC* allows performant DNS of fully turbulent thermal convection. Previous statistical results on the Nusselt number scaling Nu ~ Ra for fully turbulent Rayleigh-Bènard convection by (Kerr, 1996) have been reproduced.

The DNS are for Pr = 0.7 and Ra $\in (5e4, 2e7)$ in a periodic domain of size $[L_x, L_y, L_z] = [6, 6, 1]$, discretized by 288 × 288 × 96 gird points (Figure 2.6a). Nu is calculated at midplane and averaged over $T = 2500$ free fall time units. The present simulated data follows the scaling of Kerr (1996) (Figure 2.6b). The DNS at Ra = $2e7$ used $11.6e3\,CPUh$ requiring a runtime of approximately 1 week using 64 cores in parallel.

2.2.8 The NetCDF file format an parallel input/output

Prior to the numerical research on turbulent patterns in wall-bounded shear flows, a new file format, *NetCDF-4*, has been implemented in *Channelflow*. This part of code development was motivated by

- improving visual post-processing analysis of three-dimensional field data.
- improving the performance of input/output operations.

Numerical studies of turbulent patterns in wall-bounded shear flows are often interactive. Preliminary data is computed and decisions how to proceed need to be based on a post-processing analysis of the preliminary data. This includes a visual inspection of the three-

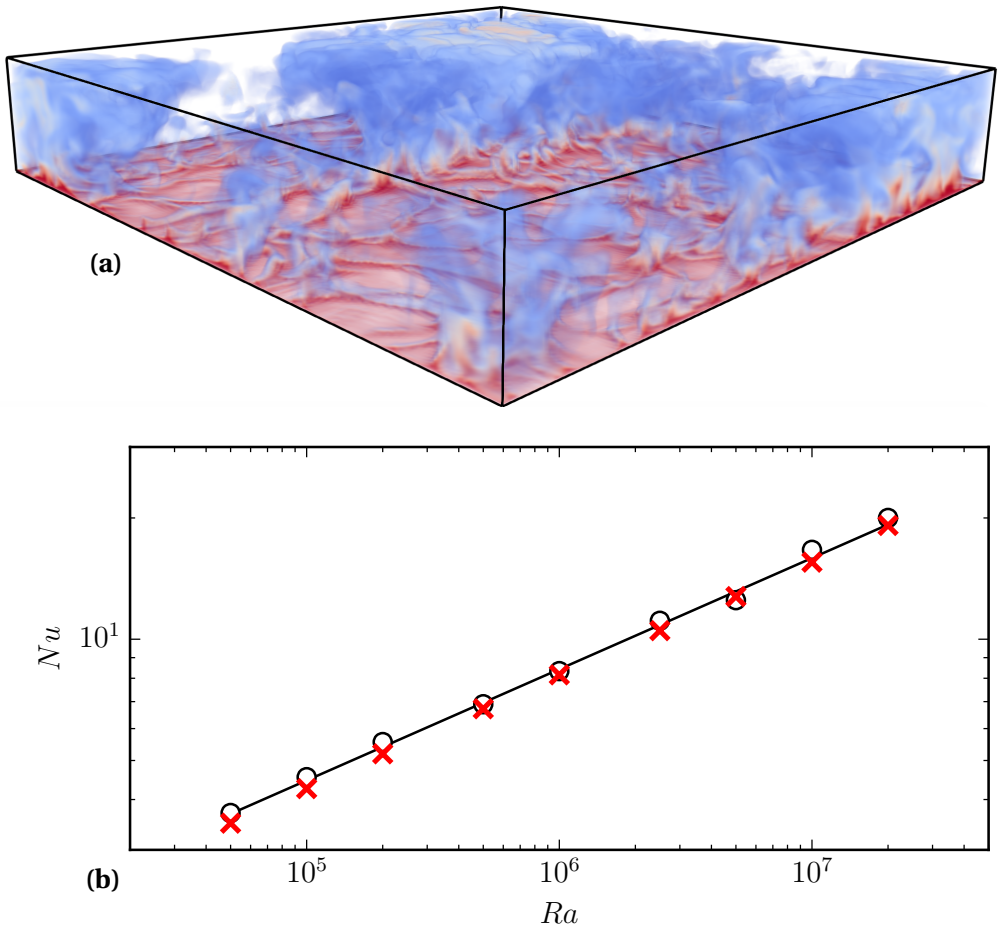

Figure 2.6 – DNS of turbulent convection in Rayleigh-Bénard convection at Pr = 0.7 using *Channelflow-ILC*. **(a)** Volumetric rendered temperature field of positive temperatures at Ra = $1e7$ illustrates range of scales of turbulent convection plumes. **(b)** Scaling of Nusselt number Nu with Rayleigh number Ra of the present DNS statistics (×) compare well to the DNS statistics of Kerr (1996) (∘) which fit to $\mathrm{Nu} = 0.186\,\mathrm{Ra}^{0.276}$ (−).

dimensional raw data of velocity or temperature fields in physical space. *NetCDF-4* simplifies such an analysis. The description of metadata in the file is chosen according to the "climate and forecast" conventions (CF). These convections are supported by many standard visualization tools like *Paraview* or *VisIt* and allow to directly import the data. The file formats that were already implemented in *Channelflow* before are the original binary format (extension `.ff`) and the *HDF5* format (extension `.h5`). These formats cannot be directly imported into standard visualization tools without additional conversions.

Turbulent patterns in wall-bounded shear flows can be of large spatial extent. Hence, the file size with the corresponding field data can be large. Advancing spatially extended turbulent patterns has become feasible with the MPI parallel time-stepping algorithms in *Channelflow*. However, the input/output of data files, in *HDF5* or binary format, was previously not parallelized. In addition, the communication protocol to collect (or distribute) the data on (or from) the single process that performs the I/O was inefficient. Data was not communicated in the largest possible chunks of the data array but rather entry by entry. For the implementation of the *NetCDF* file format, the communication protocol has been optimized by sending/receiving the largest possible chunks of the data array. This step in the code development improved the performance of serial input/output operations for MPI applications by three orders of magnitude (Figure 2.7). Moreover, the *NetCDF* interfaces for parallel I/O have been implemented. On HPC clusters with a parallel file system hardware, parallel I/O allows all processors to access storage. This avoids expensive communication between processors and, typically more costly, between compute nodes. The performance improvement due to parallel I/O becomes significant only for very large data files on very large distributions (Figure 2.7).

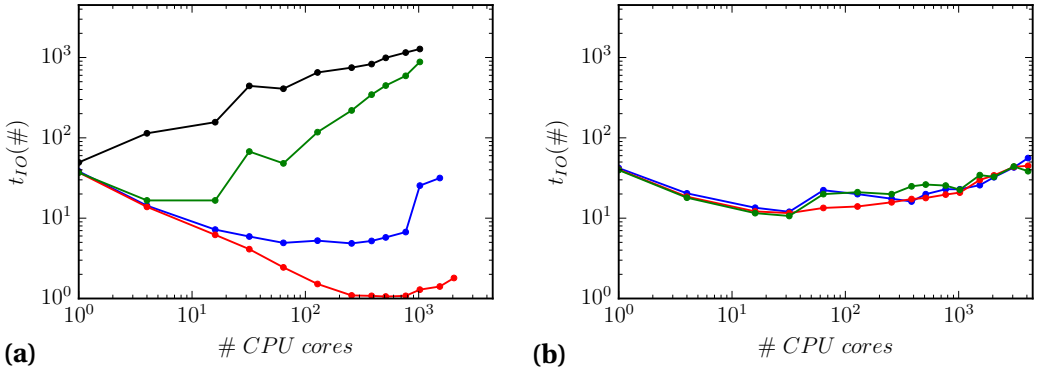

Figure 2.7 – Benchmarks of the newly implemented file Input/Output (I/O) in a strong scaling study using a `FlowField` of size $[N_x, N_y, N_z] = [682, 121, 682]$, excluding padded modes, corresponding to a file size of $1.35GB$. The averaged elapsed wall-clock time per I/O operation is measured for varying numbers of CPU cores on **(a)** EPFL's HPC cluster 'Fidis' (28 Intel Broadwell cores per node) and on **(b)** the CSCS cluster 'Piz Daint' (Cray XC40 with 36 cores per node). The performance of the previously existing I/O protocol using the HDF-5 format (black) is compared to the serial (blue) and parallel I/O protocol (red/green) using the NetCDF-4 format. On 'Fidis', parallel I/O performs better using the 'collective' (red) than the 'independent' access mode (green). On 'Piz Daint', the HDF-5 I/O protocol is not working for `FlowFields` of this size. The performance difference between the three different I/O protocols using NetCDF-4 is negligible. Serial and parallel I/O protocols using NetCDF-4 were implemented during the scope of the present thesis and improved the I/O performance by up to three orders of magnitude for MPI applications.

Part I

Spatio-temporal patterns in inclined layer convection

3 Invariant states in inclined layer convection: An overview

In this part of the thesis, we investigate spatially periodic convection patterns in inclined layer convection. We construct and analyze invariant solutions underlying all observed basic pattern motifs when changing Rayleigh number and inclination at a Prandtl number of 1.07. Figure 3.1 provides an overview of the main invariant solutions in the considered parameter space.

This part differs from the remaining parts of this thesis in notation and terminology in that

- we refer to the wall-normal direction in inclined layer convection as the z-direction and to the spanwise direction as the y-direction. This is the common choice in thermal convection studies.
- we refer to "invariant solutions" as "invariant states". This is convenient because the terminology of "primary state" and "secondary state" is often used to describe convection patterns that emerge sequentially when control parameters are varied.

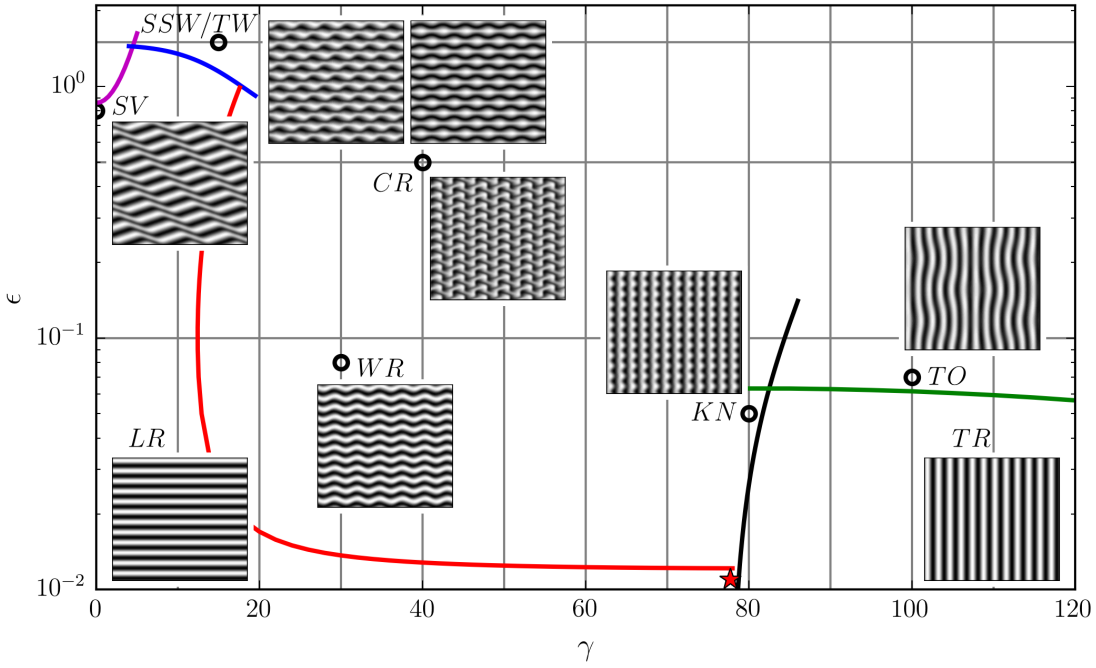

Figure 3.1 – This part of the thesis considers a parameter space of inclined layer convection over inclination angle γ and normalized Rayleigh number $\epsilon = (Ra - Ra_c)/Ra_c$ at $Pr = 1.07$. Thick lines indicate critical thresholds of secondary instabilities (Subramanian et al., 2016) explaining the onset of spatio-temporal convection patterns observed by Daniels et al. (2000). Here, we identified invariant solutions capturing the full variety of previously analyzed spatio-temporal convection patterns. Panels show the midplane temperature contours of these invariant solutions with gravity pointing from right to left. Circular markers point to the control parameters where their relevance for the temporal dynamics is studied in Chapter 4. Thin grey lines indicate the sections along which these invariant states are numerically continued for a bifurcation analysis (Chapter 5). Results about individual convection patterns are found in the following specific sections: Skewed varicose pattern (SV) in Sections 4.4.3 and 5.3.1. Subharmonic standing waves (SSW) and traveling waves (STW) in Sections 4.4.2 and 5.3.2. Wavy rolls (WR) in Sections 4.4.1 and 5.3.3. Crawling rolls (CR) in Chapter 6. Knot pattern (KN) in Sections 4.4.1 and 5.3.4. Transverse oscillations (TO) in Sections 4.4.2 and 5.3.5.

4 Temporal transitions along dynamical connections between invariant states

Remark This chapter is largely inspired by a pre-print of the name "Invariant states in inclined layer convection. Part 1. Temporal transitions along dynamical connections between invariant states".

Florian Reetz[1] and Tobias M. Schneider[1]

[1]Emergent Complexity in Physical Systems Laboratory (ECPS),
École Polytechnique Fédérale de Lausanne, CH 1015 Lausanne, Switzerland

Under consideration for publication in *Journal of Fluid Mechanics*

Chapter summary

Thermal convection in an inclined layer between two parallel walls kept at different fixed temperatures is studied for fixed Prandtl number Pr = 1.07. Depending on the angle of inclination and the imposed temperature difference, the flow exhibits a large variety of self-organized spatio-temporal convection patterns. Close to onset, these patterns have been explained in terms of linear stability analysis of primary and secondary flow states. At larger temperature difference, far beyond onset, experiments and simulations show complex, dynamically evolving patterns that are not described by stability analysis and remain to be explained. Here we employ a dynamical systems approach. We construct stable and unstable exact invariant states, including equilibria and periodic orbits of the fully nonlinear three-dimensional Oberbeck-Boussinesq equations. These invariant states underlie the observed convection

patterns beyond their onset. We identify state-space trajectories that, starting from the unstable laminar flow, follow a sequence of dynamical connections between unstable invariant states until the dynamics approaches a stable attractor. Together, the network of dynamically connected invariant states mediates temporal transitions between coexisting invariant states and thereby supports the observed complex time-dependent dynamics in inclined layer convection.

4.1 Introduction

Fluids in spatially extended wall-bounded domains can form regular flow patterns when driven by external forces (Cross and Hohenberg, 1993). Even when the flow exhibits spatio-temporal chaos or is weakly turbulent, regular patterns may form. Prominent examples are chaotic spirals in thermal convection (Morris et al., 1993), or oblique turbulent-laminar stripes in shear flows (Prigent et al., 2002). These patterns emerge in dissipative systems that are not in thermodynamic equilibrium. Consequently, the formation of sustained patterns depends crucially on the strength and nature of the energy supplying external driving forces.

A fluid system where not only the strength but also the nature of the driving force can be controlled and changed smoothly is inclined layer convection (ILC), the flow between two parallel walls maintained at different temperatures and inclined against gravity. Here, the angle of inclination defines the ratio between the wall-normal and the wall-parallel buoyancy force. The former drives a lift-up mechanism, by which buoyancy may directly destabilize the flow as in the non-inclined Rayleigh-Bénard system. The latter generates shear forces between upward and downward driven flow, leading to shear instabilities. Many different convection patterns have been observed in ILC by systematically changing the angle of inclination from horizontal layer convection to vertical layer convection and beyond (Daniels et al., 2000). These observations also reveal complex spatio-temporal dynamics of convection patterns, such as intermittent bursting (Busse and Clever, 2000; Daniels et al., 2003) or spatial competition between patterns (Daniels and Bodenschatz, 2002; Daniels et al., 2008). While the onset of several convection patterns has been explained using stability analysis, the mechanisms underlying the complex dynamics far above onset are not well understood.

First experiments on ILC focused on heat transfer properties in an inclined layer of air at Prandtl number $\mathrm{Pr} \approx 0.7$ (Nusselt, 1908; de Graaf and van der Held, 1953; Hollands and Konicek, 1973; Ruth et al., 1980b). Qualitative changes in the heat transfer were related to instabilities in the flow. Early linear stability analysis of laminar ILC at different Pr found two different primary instabilities (Gershuni and Zhukhovitskii, 1969; Chen and Pearlstein, 1989). Depending on the angle of inclination, laminar flow becomes unstable to convection rolls with either longitudinal orientation, at small inclinations, or with transverse orientation, at large inclinations. This result was confirmed by systematic experimental surveys using water at $\mathrm{Pr} \approx 7$ (Hart, 1971a) as

well as experiments using liquid crystals at high Pr (Shadid and Goldstein, 1990). Observations of modulated longitudinal rolls (Hart, 1971a,b) were compared and related to secondary instabilities of longitudinal rolls calculated using stability analysis (Clever and Busse, 1977). Similar primary and secondary instabilities have also been found in other shear flows with imposed temperature gradients (see Kelly, 1994, for a review).

Systematic experimental explorations of self-organized patterns in large aspect ratio domains of ILC under changing control parameters report on ten different convection patterns in compressed CO_2 at Pr = 1.07 (Daniels et al., 2000; Daniels and Bodenschatz, 2002; Daniels et al., 2003, 2008). While some of the observed patterns are sufficiently regular to resemble patterns linked to instabilities that had been described previously for other Pr, most observations indicate complex dynamics including spatio-temporal chaos. Exploring the same parameter space studied by Daniels, Bodenschatz, Pesch and collaborators, Subramanian et al. (2016) identified five secondary instabilities using Floquet analysis. These instabilities were calculated at the critical control parameters for the onset of the pattern and related to the dynamics observed in experiments and numerical simulations above these critical parameters using Galerkin methods (Subramanian et al., 2016). In summary, pattern formation in ILC has been studied extensively at different control parameters using experiments, numerical simulations, and stability analysis.

Relating a pattern forming instability identified by stability analysis at a critical control parameter to experimental or numerical observations above the critical control parameter requires a particular underlying bifurcation structure: At a critical control parameter, attracting state A loses stability to a forward bifurcating stable branch B. Above the critical control parameter, the unstable pattern A has lost dynamical relevance and the dynamics approaches the attracting state B that has emerged at the critical control parameter. Attracting state B remains observable in the flow until it undergoes another bifurcation and itself loses stability. Explaining the succession of patterns observed in ILC and other flows based on stability analysis thus relies on two conditions: First, a forward bifurcating stable branch continues to the control parameters where the pattern is observed without undergoing another bifurcation. Second, there is a single attracting state that describes the asymptotic dynamics both before and after the bifurcation. Under these conditions, a sequence of patterns can be described by a succession of single-state attractors arranged in a forward bifurcation sequence. However, such a 'sequence of bifurcations'-approach (Busse and Clever, 1996), envisioning a forward bifurcating scenario, is not applicable *a priori*. Rather, in order to describe observed patterns via sequences of forward bifurcations, the bifurcation structure needs to be confirmed by following the fully nonlinear bifurcation branches. Moreover there might not be a single attracting state as evidenced by observations of complex non-saturated temporally evolving dynamics in large domains. The time-dependent, complex dynamics was speculated to be a consequence of experimental imperfections (Clever and Busse, 1995; Busse and Clever,

1996) but have also been observed in direct numerical simulations in the absence of such imperfections (Subramanian et al., 2016). Consequently, an alternative approach is required to explain those complex patterns beyond onset.

Recent studies of subcritical shear flows have demonstrated the dynamical relevance of unstable exact invariant states, also called exact coherent states (Kawahara et al., 2012, and references therein). Invariant states are numerically fully resolved exact solutions of the governing nonlinear Navier-Stokes equations representing non-trivial flow structures or patterns in the flow as either steady equilibrium states or exact periodic orbits. The dynamical relevance of weakly unstable invariant states follows from their ability to transiently attract and repel the dynamics along their stable and unstable manifolds (Gibson et al., 2008b; Halcrow et al., 2009; Chandler and Kerswell, 2013; Suri et al., 2017; Farano et al., 2019). Whenever invariant states are transiently approached by the dynamics, they become transiently observable in the flow (Hof et al., 2004). These results support a dynamical systems description of turbulent flow where invariant states and their stable and unstable manifolds form a dynamical network embedded in the 'strange' state space attractor generating the complex turbulent dynamics (Lanford, 1982). Likewise, within this nonlinear dynamical systems approach, we expect unstable invariant states in ILC representing pattern motifs to support the complex pattern dynamics observed in experiments and simulations.

Shortly after the discovery of the first unstable invariant state in Couette flow (Nagata, 1990; Clever and Busse, 1992; Waleffe, 1998), invariant states were also identified in ILC. Busse and Clever (1992) revisited their analysis of the wavy instability of longitudinal rolls (Clever and Busse, 1977), and constructed stable and unstable finite amplitude states corresponding to wavy rolls combining a Galerkin method with Newton-Raphson iteration. Clever and Busse (1995) applied the same approach to tertiary and quarternary states for convection in a vertical layer, where shear forces dominate over buoyancy. Since then, invariant states have not been studied in ILC. In pure shear flows however, the significance of invariant states for the temporal transition between subcritical laminar and turbulent shear flows was extensively investigated (Kerswell, 2005; Eckhardt et al., 2007; Kawahara et al., 2012). In linearly stable shear flows, the transition to turbulence requires finite amplitude perturbations of the stable laminar flow that cross the edge of chaos between laminar and turbulent attractors in state space. This edge is spanned by the stable manifold of invariant states with a single unstable direction, a so-called edge state (Skufca et al., 2006; Schneider et al., 2007), such that the edge separates the coexisting attractors of turbulent and laminar flow (Schneider et al., 2008). Consequently, invariant edge states guide the transition to turbulence for linearly stable flows. In contrast to canonical subcritical shear flows, the laminar flow in ILC undergoes a linear instability so that infinitesimal perturbations are sufficient to trigger temporal transitions away from laminar flow. The role of invariant states for the dynamics leaving the unstable laminar flow and their

significance for the observed complex dynamics has not been investigated in ILC. They may act as transiently visited unstable states or serve as asymptotic attractors.

In the present chapter we numerically study ILC at Pr = 1.07 in minimal periodic domains and identify stable and unstable invariant states underlying different convection patterns at selected control parameters where these basic convection patterns are observed in simulations and experiments. Temporal transitions from unstable laminar flow are characterized using a phase portrait analysis of the state space trajectories describing the temporal evolution. For seven different combinations of inclination angle and imposed temperature difference transient visits to unstable invariant states are observed before the dynamics approaches attracting stable invariant states.

Depending on the inclination angle, the instability of the laminar flow is either driven by buoyancy or shear (Chen and Pearlstein, 1989; Daniels et al., 2000). At small inclinations, shear forces are negligible in the laminar state so that the emerging longitudinal convection rolls are associated with a buoyancy driven instability. At large inclinations, the wall-normal lift-up mechanism due to buoyancy is negligible so that the instability giving rise to transverse convection rolls is shear driven. Disentangling the role of buoyancy and shear for higher order instabilities driving the dynamics away from non-trivial unstable states is not straightforward as even at low inclinations, the flow field of any type of convection roll will produce significant shear, and at any inclination, temperature gradients aligned with gravity will lead to buoyant forcing. We demonstrate that phase portraits based on energy transport rates provide a systematic approach for clearly characterising any instability of an equilibrium state as either shear or buoyancy driven.

The chapter has the following structure. Section 4.2 introduces the governing equations for ILC, symmetries of the system and equations for energy transfer. Numerical methods for a dynamical systems description are introduced in Section 4.3. Temporal transitions between invariant states are presented in seven phase portraits in Section 4.4 and discussed in Section 4.5.

4.2 Oberbeck-Boussinesq equations for inclined layers

We consider thermal convection of a Newtonian fluid in an infinite layer of thickness H confined between a hot and a cold wall at prescribed temperatures $\mathcal{T}_1$ and $\mathcal{T}_2$, respectively. The fluid layer is inclined against the vector of gravitational acceleration $\boldsymbol{g}$ by angle γ (Figure 4.1). The dynamics of the incompressible flow with velocity vector $\boldsymbol{U} = [U, V, W](x, y, z, t)$, temperature $\mathcal{T} = \mathcal{T}(x, y, z, t)$, and pressure $p = p(x, y, z, t)$ relative to the hydrostatic pressure $P = P(x, y, z, t)$, where $\nabla P = \hat{\boldsymbol{g}}$, is given by the nondimensionalised Oberbeck-Boussinesq

equations

$$\frac{\partial \boldsymbol{U}}{\partial t} + (\boldsymbol{U}\cdot\nabla)\,\boldsymbol{U} = -\nabla p + \tilde{\nu}\nabla^2\boldsymbol{U} - \hat{\boldsymbol{g}}\,\mathcal{T}\,, \tag{4.1}$$

$$\frac{\partial \mathcal{T}}{\partial t} + (\boldsymbol{U}\cdot\nabla)\,\mathcal{T} = \tilde{\kappa}\nabla^2\mathcal{T}\,, \tag{4.2}$$

$$\nabla\cdot\boldsymbol{U} = 0\,, \tag{4.3}$$

with $\tilde{\nu} = (\mathrm{Pr}/\mathrm{Ra})^{1/2}$ and $\tilde{\kappa} = (\mathrm{Pr}\,\mathrm{Ra})^{-1/2}$. This set of nonlinear partial differential equations has three control parameters: the angle of inclination γ against the gravitational unit vector $\hat{\boldsymbol{g}} = -\sin(\gamma)\boldsymbol{e}_x - \cos(\gamma)\boldsymbol{e}_z$, the Prandtl number $\mathrm{Pr} = \nu/\kappa$, the ratio between kinematic viscosity ν and thermal diffusivity κ, and the Rayleigh number $\mathrm{Ra} = g\,\alpha\,\Delta T\,H^3/(\nu\kappa)$ where $\Delta\mathcal{T} = \mathcal{T}_1 - \mathcal{T}_2$ and α is the thermal expansion coefficient.

In the nondimensionalised equations (4.1-4.3), temperature is measured in units of $\Delta\mathcal{T}$ and lengths in units of H. To describe convective fluid motion with an appropriate scale, we choose to measure velocity in units of the free fall velocity $U_f = (g\,\alpha\,\Delta\mathcal{T}\,H)^{1/2}$ that has also been used in previous studies of Rayleigh-Bénard convection at control parameters above convection onset (e.g. Gray and Giorgini, 1976; Chillà and Schumacher, 2012). The free fall velocity scale implies a free-fall time unit $T_f = (H/g\,\alpha\,\Delta\mathcal{T})^{1/2}$. Note that an alternative nondimensionalisation using the heat diffusion time scale $T_d = H^2/\kappa$ is also common in thermal convection studies (e.g. Subramanian et al., 2016). The conversion factor is $T_f = T_d/\sqrt{\mathrm{Ra}\,\mathrm{Pr}}$.

The nondimensionalised boundary conditions at the walls are

$$\boldsymbol{U}(z = \pm 0.5) = 0\,, \tag{4.4}$$

$$\mathcal{T}(z = \pm 0.5) = \mp 0.5\,. \tag{4.5}$$

4.2.1 Laminar base flow

Equations (4.1-4.3) with boundary conditions (4.4-4.5) admit a laminar solution that only depends on the wall-normal coordinate z and is spatially uniform in x and y

$$\boldsymbol{U}_0(z) = \frac{\sin(\gamma)}{6\,\tilde{\nu}}\left(z^3 - \frac{1}{4}z\right)\boldsymbol{e}_x\,, \tag{4.6}$$

$$\mathcal{T}_0(z) = -z\,, \tag{4.7}$$

$$p_0(z) = \Pi - \cos(\gamma)z^2/2\,, \tag{4.8}$$

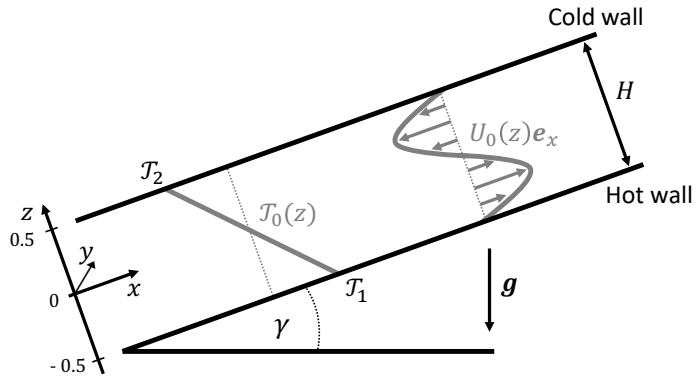

Figure 4.1 – Schematic of inclined layer convection. Streamwise, spanwise and wall-normal dimensions are indicated by x, y and z, respectively. A layer of an incompressible Newtonian fluid is confined between a lower hot and an upper cold wall. The layer is inclined against gravity $\boldsymbol{g}$ at angle γ. Hot fluid flows up the hot wall while cold fluid descends along the cold wall generating a laminar base flow (4.6-4.7) with linear temperature profile $\mathcal{T}_0(z)$ and cubic velocity profile $U_0(z)$, as outlined by grey lines. The competition of buoyancy and shear gives rise to a variety of intricate convection patterns when the three control parameters, inclination γ, thermal driving Ra and Prandtl number Pr are varied.

with arbitrary pressure constant Π. The linear temperature profile and the cubic velocity profile of this laminar base flow are sketched in Figure 4.1 (grey lines). Within the laminar solution, buoyancy forces caused by the linear temperature profile as well as shear forces due to the velocity gradients in the buoyancy driven cubic velocity profile are present. The former is destabilizing for $-90° < \gamma < 90°$ while shear can lead to instabilities at all non-zero inclination angles. At sufficiently strong driving, instabilities create overturning convective motion so that the laminar solution is no longer observed and the symmetries of ILC are broken.

4.2.2 Symmetries

ILC at zero inclination ($\gamma = 0°$) corresponds to Rayleigh-Bénard convection with isotropy and homogeneity in the x-y-plane. At all inclinations $0° \neq \gamma \neq 180°$, the isotropy of the horizontal layer is broken by the wall-parallel component of gravity, driving the laminar flow along the x-dimension. The laminar flow in ILC is still homogeneous and thereby invariant under continuous translations

$$\tau'(\Delta x, \Delta y)[U, V, W, \mathcal{T}](x, y, z) = [U, V, W, \mathcal{T}](x + \Delta x, y + \Delta y, z) \,. \tag{4.9}$$

Moreover, ILC is invariant under discrete reflections

$$\pi_y[U,V,W,\mathcal{T}](x,y,z) = [U,-V,W,\mathcal{T}](x,-y,z)\,, \tag{4.10}$$

$$\pi_{xz}[U,V,W,\mathcal{T}](x,y,z) = [-U,V,-W,-\mathcal{T}](-x,y,-z)\,. \tag{4.11}$$

The symmetry group of ILC consists of all products of the generators $\{\pi_y, \pi_{xz}, \tau'(\Delta x, \Delta y)\}$. We indicate this group by $S_{ilc} = \langle \pi_y, \pi_{xz}, \tau'(\Delta x, \Delta y)\rangle$, where angle brackets $\langle\rangle$ imply all products of elements given in the brackets. ILC has the same symmetries as plane Couette flow where analogous notation is commonly used (e.g Gibson and Brand, 2014).

Instead of considering an infinite fluid layer, we consider a finite periodic fluid layer by imposing periodic boundary conditions in x and in y, $[U,V,W,\mathcal{T}](x,y,z) = [U,V,W,\mathcal{T}](x+L_x,y,z)$ and $[U,V,W,\mathcal{T}](x,y,z) = [U,V,W,\mathcal{T}](x,y+L_y,z)$, respectively. Due to the periodic boundary conditions, we express continuous translations as

$$\tau(a_x,a_y)[U,V,W,\mathcal{T}](x,y,z) = [U,V,W,\mathcal{T}](x+a_xL_x,y+a_yL_y,z)\,, \tag{4.12}$$

with shift factors $a_x, a_y \in [0,1)$ scaling the spatial periods L_x and L_y of the periodic domain. Continuous translations in periodic domains are cyclic and shifts by L_x or L_y correspond to the identity operator $\tau(0,0)$. Since the streamwise direction x and the spanwise direction y of ILC can be rotated and reflected, the symmetry group of ILC in x-y-periodic domains is $O(2)_x \times O(2)_y$, where $\times$ is the direct product.

The relevance of the system's symmetries for the dynamics is that once a state is invariant under a symmetry transformation of the equivariance group S_{ilc}, $[\boldsymbol{U},\mathcal{T}] = \sigma[\boldsymbol{U},\mathcal{T}]$ with $\sigma \in S_{ilc}$, the evolution under the full nonlinear governing equations (4.1-4.3) will preserve the symmetry and the evolving trajectory will remain in the symmetry subspace of all possible states invariant under σ (e.g. Cvitanović et al., 2017). Consequently, trajectories and invariant states of the infinitely extended system without any symmetry constraints can be computed in symmetry subspaces, including those defined by the discrete translation symmetries imposed by periodic boundary conditions. To compute states in symmetry subspaces defined by a discrete symmetry $\sigma \in S_{ilc}$ satisfying $\sigma^2 = 1$, we impose σ using a projection $([\boldsymbol{U},\mathcal{T}] + \sigma[\boldsymbol{U},\mathcal{T}])/2$ during simulations. Any exact solution in a symmetry subspace remains a valid solution of the full unconstrained infinite system. Imposing symmetries does not affect the state but may disallow instabilities breaking the imposed symmetries and thereby simplifies numerical access to invariant state with symmetries.

All invariant states discussed in the present chapter are invariant under transformations of subgroups of $S_{ilc} = \langle \pi_y, \pi_{xz}, \tau(a_x,a_y)\rangle$. We will specify the generators of the symmetry group S of invariant states in terms of the combinations of π_y, π_{xz} and $\tau(a_x,a_y)$. The choice of generators is not unique because translations $\tau(a_x,a_y)$ define conjugacy classes of group

elements, corresponding to the free choice of the spatial phase of invariant states in x and y. We choose the spatial phase such that three-dimensional inversion $\pi_{xyz} = \pi_y \pi_{xz}$, where applicable to invariant states, applies with respect to the domain origin at $(x, y, z) = (0, 0, 0)$.

4.2.3 Energy transfer

ILC is a thermally driven dissipative system. The externally imposed temperature difference results in the thermal energy flux that is required to sustain those temperature gradients that, together with gravity, generate buoyancy forces driving fluid flow. Thereby thermal energy is converted to kinetic energy, that is eventually dissipated by viscosity. The kinetic energy balance is obtained by multiplying (4.1) with $\boldsymbol{U}$ and space averaging equations (4.1) over the entire domain volume Ω, denoted by $\langle\rangle_\Omega$,

$$\frac{1}{2}\frac{\partial}{\partial t}\left\langle U^2\right\rangle_\Omega = \qquad \left\langle \hat{\boldsymbol{g}}\,\boldsymbol{U}\,\mathcal{T}\right\rangle_\Omega - \tilde{\nu}\left\langle(\nabla\times\boldsymbol{U})^2\right\rangle_\Omega \qquad = (I-D)\,I_0\,. \tag{4.13}$$

The rate of change of kinetic energy in Ω is given by the difference between energy input I, the work due to buoyancy forces, and viscous dissipation D (Malkus, 1964). These rates are measured in units of the laminar transfer rate

$$I_0 = D_0 = \sin^2(\gamma)/(720\,\tilde{\nu})\,. \tag{4.14}$$

Since the kinetic energy of all equilibrium states remains constant, energy transfer rates need to be balanced, implying $I = D$. A periodic orbit will be characterized by instantaneously unbalanced rates but the net energy transfer integrated over one period T of the orbit vanishes, $\int_0^T (I-D)\,dt = 0$. For equilibria with relative dissipation $D/I = 1$, Equation (4.13) allows to distinguish two destabilising mechanisms. When buoyancy forces drive an instability of an equilibrium state, I increases over D implying $D/I < 1$ for the initial dynamics triggered by the instability. A shear driven instability of an equilibrium leads initially to $D/I > 1$ because rising shear increases D over I. Local oscillatory instabilities of equilibrium states discussed in the present chapter cause oscillation amplitudes to grow symmetrically around $D/I = 1$ with an exponential growth rate. The symmetry around $D/I = 1$ suggests that buoyancy and shear forces contribute equally to the destabilising mechanism underlying an oscillatory instability. We will characterize all invariant states and their instabilities in terms of energy transfer.

On average, the thermal heat flux through any plane parallel to the walls is independent of the height z. At the walls, the transport is purely diffusive but in the center of the domain convective heat transport can be significant. To quantify the instantaneous, time-dependent, heat transport due to convective effects, we formulate the energy balance equation for heat not averaged over the full but over the lower half of the domain. This generates boundary flux

terms at the midplane between the walls, where convective transport is expected to be largest. The volume average of (4.2) over the lower half of the domain volume $\Omega/2$, yields

$$\frac{\partial}{\partial t}\langle\mathcal{T}\rangle_{\Omega/2} = \quad \left\langle -\tilde{\kappa}\frac{\partial}{\partial z}\mathcal{T}\right\rangle_{A(-0.5)} - \left\langle W\mathcal{T} - \tilde{\kappa}\frac{\partial}{\partial z}\mathcal{T}\right\rangle_{A(0)} \quad = (J - \mathrm{Nu})\, J_0 \,. \tag{4.15}$$

Here $\langle\rangle_{A(z)}$ denote averages over planes at height z parallel to the walls. The rate of change of thermal energy averaged over the lower half of the domain $\Omega/2$ is given by the diffusive boundary heat flux J at the lower wall and the instantaneous Nusselt number Nu at the midplane. J_0 is the laminar diffusive heat flux

$$J_0 = \mathrm{Nu}_0 = \tilde{\kappa}\,. \tag{4.16}$$

As for the kinetic energy balance, equilibrium states imply $J = \mathrm{Nu}$. Periodic orbits will have unbalanced instantaneous fluxes that average to vanishing net thermal energy change over one period.

4.3 Numerical approach

We perform direct numerical simulations of (4.1-4.3) in x-y-periodic domains and compute invariant states using matrix-free Newton methods. The evolution of simulated state trajectories is studied relative to invariant states in 'phase portraits' defined by the net kinetic energy transfer rates in (4.13). The technical details are introduced in the following sections, and the approach is demonstrated by explaining the transition dynamics from laminar flow to straight convection rolls.

4.3.1 Direct numerical simulations

The Oberbeck-Boussinesq equations for inclined layers (4.1-4.3) in a x-y-periodic domain are solved using a pseudo-spectral method (Canuto et al., 2006, p.133ff), fully resolving all dissipative scales in a direct numerical simulations (DNS). After substituting the base-fluctuation decomposition $[\boldsymbol{U},\mathcal{T}] = [\boldsymbol{U}_0,\mathcal{T}_0] + [\boldsymbol{u},\theta]$ into (4.1-4.3), the continuous field variables of the fluctuations $[\boldsymbol{u},\theta](x,y,z,t)$ are numerically approximated by Fourier and Chebychev expansions of the form

$$[\boldsymbol{u},\theta](\boldsymbol{x},t) = \sum_{k_x=-K_x}^{K_x}\sum_{k_y=-K_y}^{K_y}\sum_{j=0}^{N_z-1}\left[\hat{\boldsymbol{u}},\hat{\theta}\right]_{k_x,k_y,j}(t)\,\mathcal{C}_j(z)\,e^{2\pi i\left(k_x x/L_x + k_y y/L_y\right)} \tag{4.17}$$

where $\mathcal{C}_j(z)$ is the j-th Chebyshev polynomial of the first kind, linearly rescaled to the interval $z\in[-0.5,0.5]$. Velocity and temperature are fixed at the walls of the domain at $\boldsymbol{u}(z=\pm 0.5) =$

0 and $\theta(z = \pm 0.5) = 0$, as the inhomogeneous boundary conditions are absorbed in $T_0(z)$. Owing to incompressibility, pressure p is a dependent variable and fully determined by $\boldsymbol{u}$. Pressure is obtained by solving a τ-problem with the influence matrix method (Kleiser and Schumann, 1980; Canuto and Landriani, 1986). To completely specify the problem with periodic boundary conditions, an integral constraint on either pressure gradient or mean flux is required. We keep the mean-pressure gradient along the x- and the y-direction constant, specifically $\int_0^{L_y}\int_0^{L_x}\nabla p\,\mathrm{d}x\mathrm{d}y = 0$. Technically, we modify pressure as $p = p' + \boldsymbol{U}^2/2$ which allows expressing the nonlinear term in (4.1) in rotational form $\boldsymbol{U}\times(\nabla\times\boldsymbol{U}) = (\boldsymbol{U}\cdot\nabla)\boldsymbol{U} - \boldsymbol{U}^2/2$. After evaluation of the nonlinear terms in (4.1) and (4.2) in physical space, the products are transformed to a spectral representation using the FFTW library (Frigo and Johnson, 2005) and dealiased using the 2/3 rule (Canuto et al., 2006, p.133f). Due to dealiasing, a grid of size $N_x \times N_y \times N_z$ in physical space implies spectral summation bounds of $K_x = N_x/3 - 1$ and $K_y = N_y/3 - 1$ in (4.17). We use e.g. $[N_x, N_y, N_z] = [32, 32, 25]$ to resolve a single pair of convection rolls in a domain of extent $[L_x, L_y] = [2.2211, 2.0162]$. This choice is discussed in Section 4.3.3. For time-marching, an implicit-explicit multistep algorithm of 3rd order is implemented solving the diffusion terms and the pressure term fully implicitly, and the nonlinear terms and the buoyancy term explicitly. See Section 2.2.6 for the details of the time-stepping algorithm. The code is written in *C++* as an extension module to the MPI-parallel software *Channelflow 2.0* (Gibson et al., 2019).

The numerical implementations in *Channelflow-ILC* has been validated by reproducing three key results with different levels of importance of nonlinear effects. First, a highly resolved critical threshold for the linear onset of convection in Subramanian et al. (2016) is accurately reproduced (see Section 4.3.3). Second, numerical continuations in γ and Ra of invariant states underlying longitudinal convection rolls reproduce an analytic scaling invariance of the nonlinear Oberbeck-Boussinesq equations (4.1-4.3), as discussed in Section 5.3 (Equations 5.15-5.19). Third, the statistics of fully turbulent Rayleigh-Bénard convection match previous results on the scaling of Nu ~ Ra (Section 2.2.7).

4.3.2 Computation of invariant states

We not only simulate the time evolution of ILC but also compute invariant states. Any state of ILC can be expressed as a state vector $\boldsymbol{x}(t) = [\boldsymbol{u}, \theta](x, y, z, t)$ in a state space of ILC for given boundary conditions. The unique time evolution of state vectors $\boldsymbol{x}(t)$ is computed using DNS. Invariant states are defined as particular state vectors $\boldsymbol{x}^*$ such that

$$\mathcal{G}(\boldsymbol{x}^*) = \sigma\mathcal{F}^T(\boldsymbol{x}^*) - \boldsymbol{x}^* = 0\,, \tag{4.18}$$

where $\mathcal{F}^T$ is the evolution operator for equations (4.1-4.3) over a finite time period T defining a dynamical system for ILC. Operator σ is an element of the symmetry group S_{ilc} and applies a

discrete coordinate transformation in terms of (4.10-4.12). Since equations (4.1-4.3) are partial differential equations, the state space of this dynamical system is of infinite dimension. The numerical representation of ILC discussed in Section 4.3.1 renders the state space dimension finite. The spatially discretised partial differential equations correspond to a set of coupled ordinary differential equations, one for each of the four fields $[u, v, w, \theta]$ at each spatial collocation point. Thus, the dynamical system has a state space with $N = 4 \times N_x \times N_y \times N_z \times 4/9$ dimensions. The factor $4/9$ accounts for the cut-off wavenumbers due to dealiasing. To solve (4.18) efficiently in an N-dimensional state space, *Channelflow-ILC* employs a matrix-free Newton-Raphson iteration, based on GMRES to construct a Krylov subspace, together with a Hookstep trust region optimization (Viswanath, 2007). The trust region optimization increases the radius of convergence. To be within a radius of convergence of the Newton-Raphson method, the initial state of the iteration must be close to an invariant state. Full convergence within double-precision arithmetic requires the residual of (4.18) to be $||\mathcal{G}(\boldsymbol{x})||_2 = \mathcal{O}(10^{-16})$. Here, we define the normalized L_2-norm of state vectors as $||\boldsymbol{x}||_2 = (L_x L_y)^{-1/2}(\int [\boldsymbol{u}, \theta] dx dy dz)^{1/2}$. Once invariant states have converged in a Newton iteration, their spectrum of eigenvalues can be computed using Arnoldi iteration (Viswanath, 2007) and bifurcation branches can be computed using continuation methods (see Dijkstra et al., 2014, for a review).
We distinguish two types of invariant states, namely equilibrium states (EQ) and periodic orbits (PO). If the period T in (4.18) can be arbitrarily chosen *a priori*, then invariant states are steady states or EQs. We use $T = 20$ to compute an EQ. If invariant states require T to match a specific time period, the state is unsteady but exactly recurrent over T and the invariant state is a PO. The period T of a PO is determined in the Newton iteration. There are additional classifications of EQs and POs. If $\sigma \in S_{ilc}$ in (4.18) with $\sigma \neq 1$, the invariant state is a *relative* invariant state. Relative EQs are traveling wave states (TW) that are steady states in a co-moving frame of reference. TWs satisfy (4.18) with $\sigma = \tau(a_x, a_y)$, where shift factors a_x and a_y must be determined in the Newton iteration. A relative PO might also travel over its period T requiring a specific $\sigma = \tau(a_x, a_y)$. Some periodic orbits that have $\sigma = 1$ after a full period T still may exploit a discrete symmetry operation $\sigma \neq 1$ after a relative period $T' = T/n$ with $n \in \mathbb{N}$. This type of relative PO is a 'pre-periodic orbit' (see e.g. Budanur and Cvitanović, 2017).

Where possible, we name invariant states according to the existing names of observed convection patterns and instabilities in Subramanian et al. (2016). We will show that specific nonlinear invariant states underlie specific convection patterns and that the specific states can be linked, in most cases, to bifurcation points corresponding to specific instabilities. To reflect the link between observed patterns, invariant states and instabilities but also to clearly distinguish between the three distinct objects, we use different symbols/fonts to indicate: An observed "pattern X" as $\mathcal{PX}$, instabilities linked to this pattern as PX_i, and exact invariant states underlying the pattern as PX.

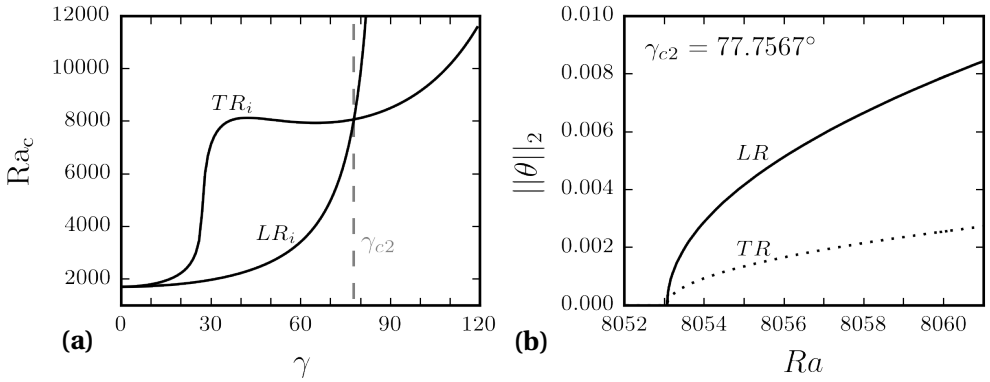

Figure 4.2 – **(a)** Critical thresholds $\mathrm{Ra}_c(\gamma)$ for the instabilities to longitudinal rolls (LR_i) and transverse rollse (TR_i) from linear stability analysis of B at Pr = 1.07 (Subramanian et al., 2016). **(b)** Bifurcation branches of invariant states LR and TR at γ_{c2} bifurcate together from B at $\mathrm{Ra}_{c2} = 8053.1$. When computing LR and TR in a minimal domain of size $[L_x, L_y] = [\lambda_x, \lambda_y]$, LR is stable (solid line) and TR is unstable (dotted line).

4.3.3 Straight convection rolls as equilibrium states

The simplest invariant state in ILC is the laminar base flow (4.6-4.8), denoted as B and representing a zero-state for the fluctuations $[\boldsymbol{u}, \theta] = 0$. When B becomes dynamically unstable, straight convection rolls may form. In ILC at $\gamma = 0°$, the case equal to Rayleigh-Bénard convection, the critical threshold for the onset of convection is $\mathrm{Ra}_c(\gamma = 0°) = 1707.76$ (Busse, 1978b). In ILC at $\gamma \neq 0°$, two types of straight rolls can emerge from the primary instability, either longitudinal rolls (LR), with orientation along x, or transverse rolls (TR), with orientation along y. The type of rolls to which B becomes first unstable when Pr is fixed and Ra is increased depends on γ (Gershuni and Zhukhovitskii, 1969; Hart, 1971a). Figure 4.2a shows the curves for critical thresholds $\mathrm{Ra}_c(\gamma)$ at Pr = 1.07. The point in the γ-Ra-plane where LR_i and TR_i have the same critical threshold is a condimension-2 point. We reproduce this point at $\gamma = 77.7567° \equiv \gamma_{c2}$ and $\mathrm{Ra}_c(\gamma_{c2}) = 8053.1 \equiv \mathrm{Ra}_{c2}$ via numerical continuation of equilibrium states LR and TR down in Ra to their exact bifurcation point from B (Fig. 4.2b). LR is invariant under the symmetry group $S_{\mathrm{lr}} = \langle \pi_{xz}\tau(0, 0.5), \pi_y\tau(0, 0.5), \tau(a_x, 0)\rangle$, and TR is invariant under $S_{\mathrm{tr}} = \langle \pi_{xz}, \pi_y, \tau(0, a_y)\rangle$. Both equilibrium states, LR and TR, are numerically fully converged to satisfy (4.18). Useful initial states for the Newton iteration are obtained from a 'phase portrait' analysis as explained in the following section.

Floquet analysis suggests streamwise and spanwise wavelengths for the primary instability to longitudinal and transverse rolls at the codimension-2 point (Subramanian et al., 2016). Accordingly we choose the periodic domain to match wavelengths $\lambda_x = 2.2211$ and $\lambda_y = 2.0162$ of instabilities TR_i and LR_i, respectively. For the domain size $[L_x, L_y] = [\lambda_x, \lambda_y]$, we have

reproduced the codimension-2 point at $[\gamma_{c2}, \mathrm{Ra}_{c2}] = [77.7567°, 8053.1]$. We confirmed that all given digits are significant. The step-size of the continuation was chosen sufficiently small to indicate the bifurcation point at this accuracy. Moreover, increasing the grid resolution beyond $[n_x, n_y, n_z] = [32, 32, 25]$ does not change the result. We fix $\lambda_x = 2.2211$ and $\lambda_y = 2.0162$ as constants in this chapter, and choose all periodic domains to be periodic over $[L_x, L_y] = [l\,\lambda_x, m\,\lambda_y]$ and to be discretised with $[N_x, N_y, N_z] = [l\,n_x, m\,n_y, n_z]$ with $l, m \in \mathbb{N}$. Thus, the invariant states discussed here have prescribed pattern wavelengths, unlike pattern forming instabilities calculated using a Floquet analysis.

4.3.4 Phase portrait analysis

Temporal transitions from laminar flow to longitudinal or transverse rolls are studied by initialising a simulation with small perturbations around the dynamically unstable base state B and visualizing the time evolution in a state space projection representing a 'phase portrait'. Two state vector trajectories $\boldsymbol{x}(t)$ are simulated just above the codimension-2 point, at γ_{c2} and $\mathrm{Ra} = 8500 > \mathrm{Ra}_{c2}$. Each trajectory starts from B perturbed by small amplitude noise of $\mathcal{O}(10^{-5})$. The evolution of $\boldsymbol{x}(t)$ is simulated in the symmetry subspace of (λ_x, λ_y)-periodicity, corresponding to the domain size, and either S_{lr} or S_{tr}. Imposing either S_{lr} or S_{tr} causes $\boldsymbol{x}(t)$ to remain in the symmetry subspace since (4.1-4.3) are equivariant under S_{lr} and S_{tr}. Each symmetry subspace contains only one type of straight convection rolls. Thus, the choice of either S_{lr} or S_{tr} selects whether longitudinal or transverse rolls emerge.
The longitudinal and the transverse state trajectories are analysed in a 'phase plane' spanned by kinetic energy input I and relative viscous dissipation D/I defined in (4.13). The D/I-axis allows to distinguish two types of instabilities of equilibrium states in ILC satisfying $D = I$. The transition towards LR is triggered by a buoyancy driven instability of B that initially increases I over D. The transition towards TR is triggered by a shear driven instability of B that initially increases D over I. The phase portrait illustrates that the state LR is reached via a temporal transition from a buoyancy driven instability of B, and TR is reached via a temporal transition from a shear driven instability of B (Figure 4.3a).
The phase portrait analysis not only characterises the forces driving an instability but also helps to identify good initial guesses for Newton iterations that may converge to invariant states. After a stage of exponential growth in the transition from B, the two state trajectories saturate and the dynamics slows down exponentially (Figure 4.3a). Exponential slow-down near $D/I = 1$ suggests the presence of an equilibrium state, and indeed, the two final state vectors $\boldsymbol{x}(t = 1000)$ are close to invariant states and good initial guesses for a Newton iteration. They converge to LR and TR, respectively, and provide the starting point for the numerical continuation shown in Figure 4.2b. Consequently, the phase portrait analysis is useful for finding invariant states during temporal transitions. Moreover, the phase portrait clearly illustrates how the dynamics follow dynamical connections between invariant states, in this

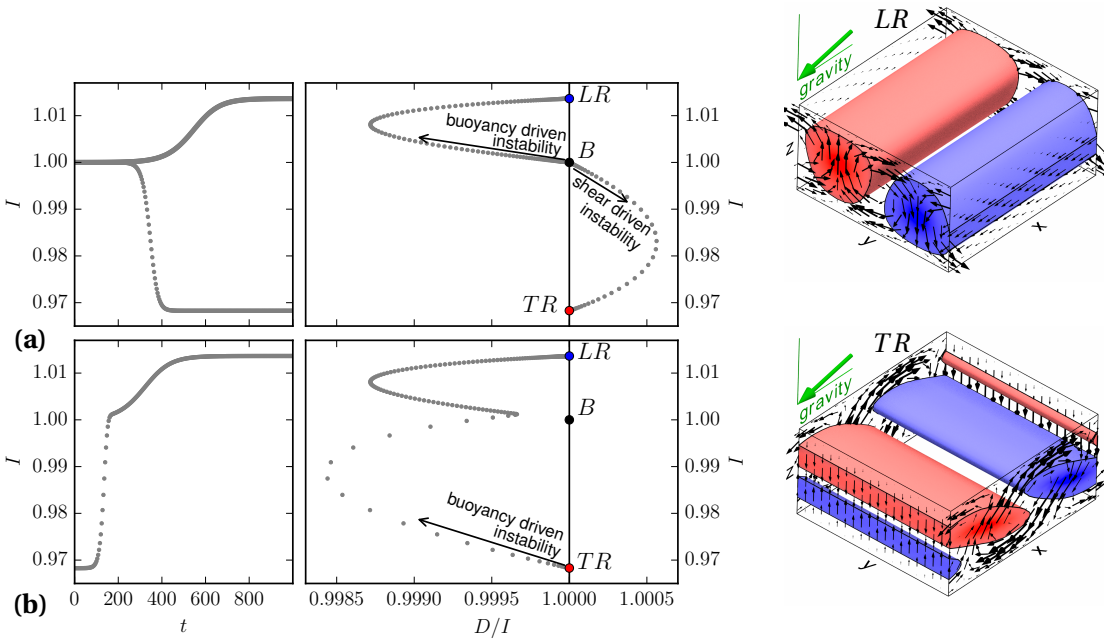

Figure 4.3 – **(a)** Simulated state trajectories (grey dots) evolving from noise around the unstable laminar base flow B at γ_{c2} and Ra = 8500 over time t (left), and plotted as phase portraits in a plane of kinetic energy input I and relative dissipation D/I (right). The DNS is confined to either S_{lr} and S_{tr}, allowing either a buoyancy driven instability to initiate a temporal transition to LR or a shear driven instability to initiate a temporal transition to TR. Arrows indicate the direction of the evolution. Exact equilibrium states LR and TR are visualized by 3D contours at $1/3[\min(\theta),\max(\theta)]$ and the inplane components of $\boldsymbol{u}$ at the domain sides. **(b)** Without imposing discrete symmetries, TR is dynamically unstable. Perturbing TR initiates a dynamical connection to LR with fast dynamics near the unstable manifold of TR and slow dynamics near the stable manifold of LR.

case $B \rightarrow LR$ and $B \rightarrow TR$. We use the term 'dynamical connection' for state trajectories connecting the state space neighborhood of two invariant states in a finite time. Dynamical connections indicate the existence of a nearby heteroclinic connection requiring infinite time to be traversed (e.g. Farano et al., 2019).
The dynamical stability of LR and TR at γ_{c2} and Ra = 8500 is characterised using Arnoldi iteration in the symmetry subspace of the (λ_x, λ_y)-periodic domain. LR is stable and TR is weakly unstable with respect to two shift-symmetry related three-dimensional, longitudinally oriented, eigenmodes with linear growth rate of $\omega_r = 0.044$. These unstable eigenmodes of TR do not exist in the symmetry subspace defined by S_{tr} where the temporal transition to stable TR was simulated. However, the simulated dynamical connection $B \rightarrow TR$ also exists in the larger subspace where S_{tr} is not imposed and $B \rightarrow TR$ connects two unstable invariant states. When perturbing unstable TR, a buoyancy driven instability triggers a dynamical connection $TR \rightarrow LR$. Along this connection the dynamics undergo a rapid slow-down suggesting a transition from the fast unstable manifold of TR to the slow stable manifold of LR whose leading eigenvalue is $\omega_r = -0.016$ (Figure 4.3b).
In summary, the phase portrait analysis serves three purposes. First, high-dimensional state space trajectories can be visualised in a two-dimensional projection. Second, close approaches to invariant states and a slow-down of the dynamics provide useful initial guesses for Newton iterations to converge. Thus, the phase portrait analysis gives access to invariant states. Third, the type of instability triggering a transition from an equilibrium state can be characterized as either buoyancy driven or shear driven via the departure from the $D/I = 1$ line in the phase portrait.

4.4 Transitions to tertiary states

On increasing Ra, secondary patterns of regular straight convection rolls give way to five different tertiary convection patterns (Daniels et al., 2000). These patterns have been associated with five different secondary instabilities (Subramanian et al., 2016). The type of convection pattern emerging when increasing Ra depends on the inclination angle γ. Following the cited work, we study the five tertiary convection patterns in ILC at Pr = 1.07. In the parameter space $\gamma \in [0°, 120°]$ and $\epsilon \in [0, 2]$, where $\epsilon = (\mathrm{Ra} - \mathrm{Ra}_c)/\mathrm{Ra}_c$ is a normalized Rayleigh number relative to the critical threshold $\mathrm{Ra}_c(\gamma)$ for convection onset (Figure 4.2a). We select specific control parameters where the patterns have been observed.
The following sections apply the phase portrait analysis outlined in Section 4.3.4 to each convection pattern individually. Instead of discussing the five patterns in order of increasing angle of inclination γ, we choose to order the patterns in terms of the complexity of the transition dynamics towards the attractive invariant state underlying the pattern: first, transitions to equilibrium states (Section 4.4.1), second, transitions to periodic orbits (Section 4.4.2), and third, transition dynamics in the absence of an attractive tertiary state (Section 4.4.3).

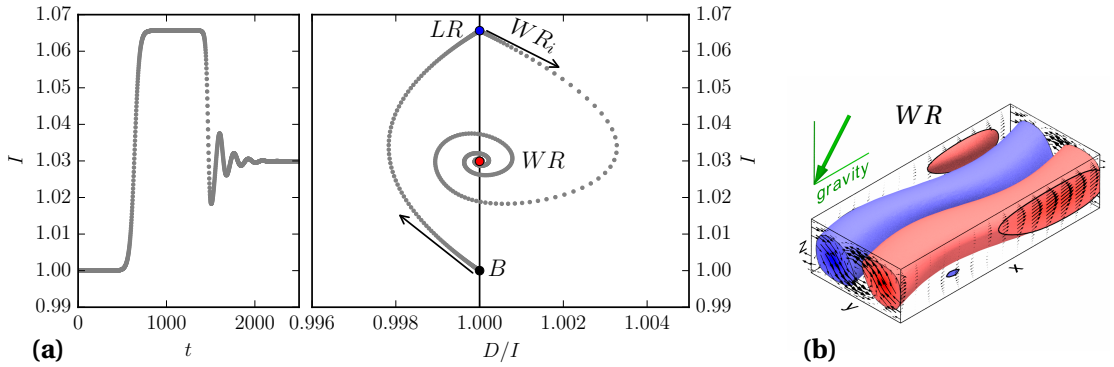

Figure 4.4 – **(a)** State trajectory evolution from the unstable base state B at $\gamma = 40°$ and Ra = 2385 ($\epsilon = 0.07$). After a transient in the vicinity of LR, the shear driven instability WR_i of LR makes the trajectory follow a stable spiral towards equilibrium state WR. **(b)** Flow structure of WR in a periodic domain of size $[2\lambda_x, \lambda_y]$.

4.4.1 Transitions with equilibrium state attractor

Wavy rolls

The convection pattern of wavy rolls ($\mathcal{WR}$) has been observed in early experiments (Hart, 1971a) and associated to the wavy instability WR_i of LR (Clever and Busse, 1977), also found for longitudinal rolls in Benard-Couette flow (Clever et al., 1977). Hart (1971b) already hypothesised a relation between $\mathcal{WR}$ and wavy vortex flow in Taylor-Couette experiments (Coles, 1965). Such a relation was later found to exist, and exploited in the first constructions of invariant states underlying wavy velocity streaks in subcritical shear flows (Nagata, 1990; Clever and Busse, 1992). $\mathcal{WR}$ are observed in ILC at control parameters $[\gamma, \epsilon, \mathrm{Pr}] = [40°, 0.07, 1.07]$ (Daniels et al., 2000). We simulate a temporal transition starting from small-amplitude noise around the unstable base flow at these control parameters. The size of the periodic domain is $[2\lambda_x, \lambda_y]$ and no additional discrete symmetries are imposed.

The phase portrait reveals a two-stage transition form the base flow B to wavy rolls. First, a buoyancy driven instability of B leads to a slow transient over $700 < t < 1\,400$ in the vicinity of LR. Second, a shear driven instability of LR leads to a spiraling trajectory on which the dynamics approach the equilibrium state WR (Figure 4.4). The spectrum of eigenvalues of WR has the complex pair $(\omega_r, \pm\omega_i) = (-0.007, \pm 0.039)$ closest to the imaginary axis. The imaginary part suggests an oscillation period on the spiraling trajectory of $T = 2\pi/\omega_i = 161$. The decaying oscillations of the trajectory for $t > 1\,500$ match this period. The flow structure of equilibrium state WR shows the characteristic wavy modulations observed in experiments and simulations (Figure 4.4b). WR are invariant under shift-reflect and shift-rotate symmetries

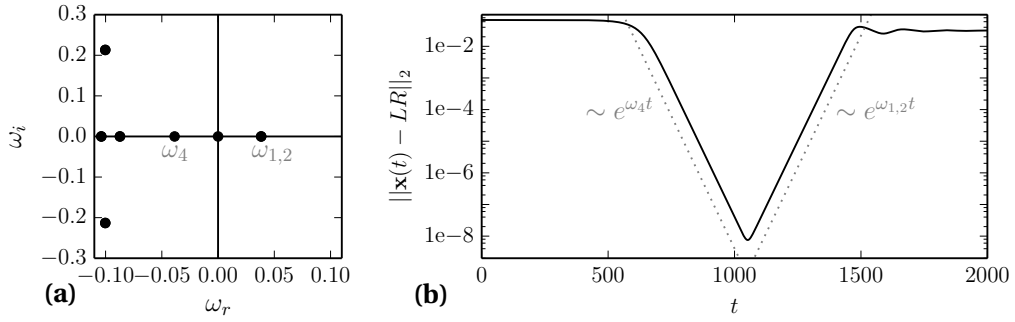

Figure 4.5 – **(a)** Spectrum of leading eigenvalues of LR explains exponential approach and escape rates relative to LR. **(b)** L_2-distance between LR and the state trajectory shown in Figure 4.4 illustrates exponential approach and escape dynamics in the state space neighborhood of LR. The dotted line marks the exponential rates given by the leading stable and unstable eigenvalues of LR.

$S_{\mathrm{wr}} = \langle \pi_y \tau(0.5, 0.5), \pi_{xz} \tau(0.5, 0.5) \rangle$. These symmetries are analogous to the symmetries of wavy velocity streaks in plane Couette flow (e.g. Gibson et al., 2008b).

The state trajectory follows a sequence of dynamical connections $B \rightarrow LR \rightarrow WR$. The transient close to LR, a saddle point with stable and unstable eigendirections, follows exponential dynamics. The leading eigenvalues of LR are real, $[\omega_{1,2}, \omega_3, \omega_4] = [0.038, 10^{-9}, -0.039]$, and define the exponential rate of approach, $\sim e^{\omega_4 t}$, and escape, $\sim e^{\omega_{1,2} t}$ (Figure 4.5). The double multiplicity of the positive eigenvalue is a result of the continuous translation symmetry $\tau(a_x, 0)$ of LR allowing two orthonormal eigenmodes of arbitrary x-phase. Continuous translations $\tau(0, a_y)$ are not an invariance of LR but change the y-phase of LR and generate a continuum of equivalent states. The Goldstone mode corresponding to the translation invariance of LR is the marginally stable eigenmode with eigenvalue ω_3. Therefore, the pitchfork bifurcation creating LR is a circle pitchfork bifurcation(Crawford and Knobloch, 1991). The non-zero finite value of ω_3 is a measure for the accuracy of the Arnoldi iteration. The minimal distance of the state trajectory to LR is $||\boldsymbol{x}(t = 1050) - LR||_2 / ||LR||_2 \approx 10^{-8}$. Consequently, the transition dynamics from B generate a trajectory transiently visiting the state space neighborhood of the unstable equilibrium state LR, as already suggested by the phase portrait.

When increasing thermal driving, the $\mathcal{WR}$ pattern is succeeded by weakly turbulent wavy rolls, also called 'crawling rolls' (Daniels et al., 2000). A DNS at $\epsilon = 0.5$ leads to a much more complicated phase portrait than at $\epsilon = 0.07$. At these control parameters, the state trajectory initially still undergoes the transition sequence $B \rightarrow LR \rightarrow WR$. However, WR is now unstable. After a transient visit close to WR at $t = 500$, a buoyancy driven instability of WR leads to a sequence of large-amplitude, fast oscillations before the state trajectory is attracted to a small-amplitude, slow bursting cycle (Figure 4.6). The fast transient oscillations have clockwise

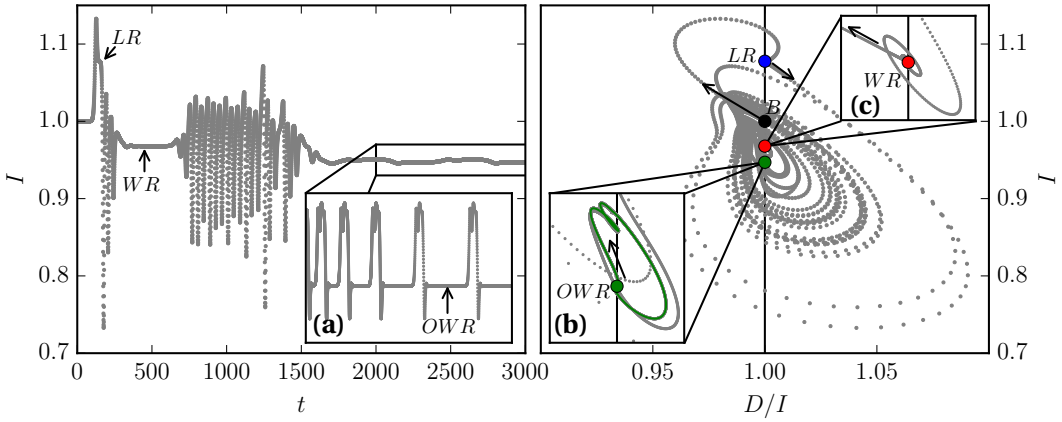

Figure 4.6 – State trajectory evolution from the unstable base state B at $\gamma = 40°$ and Ra = 3344 ($\epsilon = 0.5$). The trajectory visits unstable LR, followed by a transient visit of WR (inset **(c)**). Subsequently, the trajectory undergoes a sequence of rapid oscillations and is finally attracted to a heteroclinic cycle between equilibrium state OWR and a symmetry related equilibrium. The time series for $2000 < t < 10000$ in inset **(a)** indicates the increasing time spent near the equilibrium states. The phase portrait of the heteroclinic cycle is magnified in inset **(b)**. Since the energy transfer rates do not differ for symmetry related states, the heteroclinic cycle appears as a homoclinic cycle. See Figure 4.7a for a projection that distinguishes the two equilibrium states.

revolving trajectories in the D/I-I-plane and dominate the phase portrait. We suspect the existence of an unstable periodic orbit with similar shaped phase portrait underlying the transient oscillations. Finding and analysing this periodic orbit is beyond the scope of this work and discussed elsewhere (Chapter 6). Here, we discuss the slow dynamical attractor at these control parameters.

The temporal dynamics of ILC at $[\gamma, \epsilon, \mathrm{Pr}] = [40°, 0.5, 1.07]$ in a periodic domain of size $[2\lambda_x, \lambda_y]$ is attracted to a heteroclinic cycle. The cycle dynamically connects an equilibrium state, which we name oblique wavy rolls (OWR), with a symmetry related equilibrium state $\tau_{xy}OWR$ (Figure 4.7). Here, $\tau_{xy} = \tau(0.25, 0.25)$ is a shift operator translating the wavy flow structure by half a pattern wavelength in the direction of the domain diagonal along which the wavy convection rolls of OWR are aligned. OWR and $\tau_{xy}OWR$ show two spatial periods of the wavy pattern along the domain diagonal and both are invariant under transformations of $S_{\mathrm{owr}} = \langle \pi_{xyz}, \tau(0.5, 0.5) \rangle$. Without imposing the symmetries in S_{owr}, OWR and $\tau_{xy}OWR$ have each a single purely real unstable eigenmode, denoted as state vector $\boldsymbol{e}^u$ and $\tau_{xy}\boldsymbol{e}^u$, respectively, that breaks the $\tau(0.5, 0.5)$-symmetry by having only one spatial period along the domain diagonal (Figure 4.7c). Perturbing OWR with $\boldsymbol{e}^u$ initiates the temporal transition $OWR \rightarrow \tau_{xy}OWR$. Perturbing $\tau_{xy}OWR$ with $\tau_{xy}\boldsymbol{e}^u$ initiates the temporal transition $\tau_{xy}OWR \rightarrow OWR$.

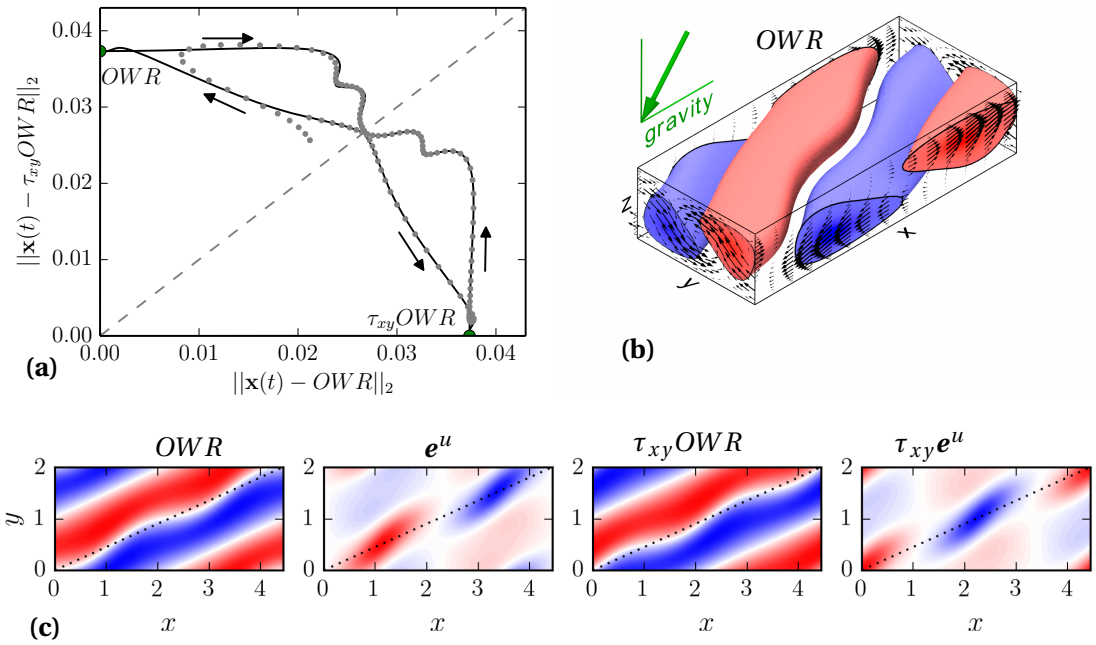

Figure 4.7 – Robust heteroclinic cycle between two symmetry related equilibrium states at $\gamma = 40^\circ$ and Ra = 3344 ($\epsilon = 0.5$). **(a)** L_2-distance relative to the two symmetry related equilibrium states, OWR and $\tau_{xy}OWR$, visualises how the simulated state trajectory (grey dots) approaches the heteroclinic cycle (black line). The direction of the dynamics is indicated by black arrows. **(b)** Flow structure of OWR in a periodic domain of size $[2\lambda_x, \lambda_y]$. **(c)** Temperature contours at midplane illustrate the spatial phase of OWR, $\tau_{xy}OWR$, and their unstable eigenmodes $\boldsymbol{e}^u$ and $\tau_{xy}\boldsymbol{e}^u$, respectively, along the diagonal of the domain (dotted line). The pattern wavenumbers of equilibria and unstable eigenmodes along the domain diagonals suggest a nearby 1:2 resonance.

Together, the two dynamical connections form a heteroclinic cycle. The two involved unstable eigenmodes $\boldsymbol{e}^u$ and $\tau_{xy}\boldsymbol{e}^u$ preserve the symmetries π_{xyz} and $\pi_{xyz}\tau(0.5,0.5)$, respectively. Thus, they are analogous to *sine*- and *cosine*-eigenmodes in that they first, are orthogonal such that the L_2 inner product is $\langle \boldsymbol{e}^u, \tau_{xy}\boldsymbol{e}^u \rangle = 0$ and second, have a reflection symmetry with respect to different reflection points, namely π_{xyz} and $\pi_{xyz}\tau(0.5,0.5)$ (Figure 4.7c). When imposing π_{xyz}-symmetry, the unstable eigenmode $\tau_{xy}\boldsymbol{e}^u$ is disallowed, $\tau_{xy}OWR$ becomes dynamically stable, and the associated symmetry subspace Σ_1 contains only the dynamical connection $OWR \to \tau_{xy}OWR$. When imposing $\pi_{xyz}\tau(0.5,0.5)$-symmetry, the unstable eigenmode $\boldsymbol{e}^u$ is disallowed, OWR becomes dynamically stable, and the associated symmetry subspace Σ_τ contains only the dynamical connection $\tau_{xy}OWR \to OWR$. Hence, the heteroclinic cycle satisfies all three conditions for the existence of a robust heteroclinic cycle between two symmetry related equilibrium states (Krupa, 1997):

(i) OWR is a saddle and $\tau_{xy}OWR$ is an attractor (or sink) in a symmetry subspace Σ_1 of the entire state space of the $[2\lambda_x, \lambda_y]$-periodic domain.

(ii) There is a saddle-attractor connection $OWR \to \tau_{xy}OWR$ in Σ_1.

(iii) There is a symmetry relation between the two equilibrium states, mediated by $\tau_{xy} \in S_{\mathrm{ilc}}$.

Robust heteroclinic cycles of this type have been previously described in systems with $O(2)$-symmetry that are near a codimension-2 point where bifurcating eigenmodes show a spatial 1:2 resonance (Armbruster et al., 1988; Proctor and Jones, 1988; Mercader et al., 2002; Nore et al., 2003). In the present case, the existence of OWR with wavenumber $m = 2$ along the domain diagonal and with an instability of wavenumber $m = 1$ suggests a nearby codimension-2 point where oblique straight rolls become simultaneously unstable to $m = 1$ and $m = 2$ wavy modulations. Oblique straight rolls are not discussed here but are a known instability of laminar ILC (Gershuni and Zhukhovitskii, 1969). In Section 5.3.3, we demonstrate that OWR of both wavenumbers, $m = 1$ and $m = 2$, indeed bifurcate off oblique straight rolls in two pitchfork bifurcations at only slightly different control parameters, suggesting a 1:2 resonance.

The robust heteroclinic cycle is numerically identified as an attractor of the dynamics suggesting its dynamical stability. The stability of robust heteroclinic cycles depends on the leading eigenvalues of the involved equilibrium states (Krupa and Melbourne, 1995). The leading eigenvalues of OWR without imposing additional discrete symmetries are $[\omega_1, \omega_2, \omega_{3,4}] = [0.016, -0.023, -0.037 \pm 0.050]$. When imposing π_{xyz}, the contracting eigenvalue ω_2 vanishes. When imposing $\pi_{xyz}\tau(0.5,0.5)$, the expanding eigenvalue ω_1 vanishes. Thus, the leading expanding and contracting eigenvalues belong to two different symmetry subspaces. The complex eigenvalue $\omega_{3,4}$ is radial as it belongs to both subspaces and does not influence the stability of the cycle. Since $|\omega_1|/|\omega_2| < 1$, the heteroclinic cycle is dynamically stable (Krupa and Melbourne, 1995).

We do not expect this heteroclinic cycle to be stable in larger domains. However, oblique wavy rolls are observed to evolve slowly in experiments and simulations at lower thermal driving (Daniels et al., 2008). At the control parameters selected here, observations in larger domains indicate chaotic dynamics on a faster time scale than the time scale of the approach to the heteroclinic cycle (Chapter 6). The time period Δt over which the state trajectory remains close to an equilibrium increases with time (Figure 4.6a). It should eventually diverge but here saturates at $\Delta t \approx \mathcal{O}(10^3)$. This saturation effect is due to the numerical double-precision of the DNS. The unstable eigenvalue $\omega_1 = 0.016$ of OWR amplifies the numerical noise on a time scale of $\log(10^{16})/\omega_1 = \mathcal{O}(10^3)$.

Knots

The convection pattern of knots ($\mathcal{KN}$) is experimentally observed as 'knotted' superposition of $\mathcal{TR}$ and $\mathcal{LR}$ just above inclination γ_{c2} (Daniels et al., 2000). Stability analysis confirms the existence of a KN_i instability of TR (Fujimura and Kelly, 1993). We refer to experimental and numerical observations of $\mathcal{KN}$ at $[\gamma, \epsilon, \mathrm{Pr}] = [80°, 0.05, 1.07]$ (Subramanian et al., 2016). At these control parameters, a temporal transition from the noise-perturbed unstable base flow is simulated in a periodic domain of size $[\lambda_x, \lambda_y]$. No additional discrete symmetries are imposed.

After the initially shear driven transition $B \rightarrow TR$, the buoyancy driven instability KN_i of TR leads to a stable spiral approaching KN, an equilibrium state underlying the observed $\mathcal{KN}$ pattern (Figure 4.8). The spectrum of eigenvalues of stable KN has a complex pair $(\omega_r, \omega_i) = (-0.0085, \pm 0.0304)$ closest to the imaginary axis. The linear period of $T = 2\pi/\omega_i = 207$ matches the simulated oscillations on the stable spiral trajectory. The flow structure of KN shows the characteristic bimodal mix of longitudinal and transverse modes, here, with a stronger transverse contribution (Figure 4.8b). KN is invariant under symmetries $S_{\mathrm{kn}} = \langle \pi_y \tau(0, 0.5), \pi_{xyz} \rangle$.

Close to the control parameters where stationary $\mathcal{KN}$ are observed, Daniels et al. (2000) report on bursting dynamics. When simulating a transition at increased $\epsilon = 0.15$ ($\mathrm{Ra} = 9338$), the state trajectory, after transiently visiting TR, does not approach KN that has become unstable. Instead, the trajectory visits again the laminar base flow ($TR \rightarrow B$) from where it approaches a stable periodic orbit with period $T = 251$ and S_{kn} symmetries. We call this orbit bursting knots (BKN). The BKN orbit describes a bursting cycle with slow dynamics near B and fast dynamics along a clockwise revolving trajectory in the D/I-plane (Figure 4.9). The fast stage shows growth of a transient $\mathcal{KN}$ pattern that ultimately forms decaying longitudinal plumes (Figure 4.9b). Longitudinal modes decay because LR_i exists only at higher ϵ at $\gamma = 80°$. During the slow stage, the phase portrait of the orbit shows sharp turns near B suggesting an influence of the stable and unstable manifold of B on the orbit (inset in Figure

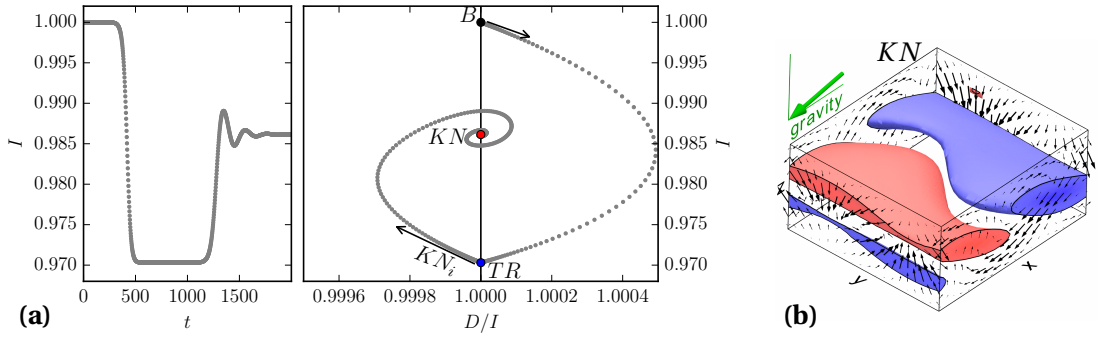

Figure 4.8 – **(a)** State trajectory evolution from the unstable base state B at $\gamma = 80°$ and $\epsilon = 0.05$ (Ra = 8525). After a transient in the vicinity of TR, the buoyancy driven instability KN_i causes the trajectory to follow a stable spiral towards equilibrium state KN. **(b)** Flow structure of KN in a periodic domain of size $[\lambda_x, \lambda_y]$.

4.9). The bursting dynamics of this specific periodic orbit appears similar to a nonlinear limit cycle found in natural doubly diffusive convection (Bergeon and Knobloch, 2002) but does not match the traveling dynamics of the longitudinal bursts observed in ILC at these control parameters Daniels et al. (2000). The next section discusses two periodic orbits clearly underlying experimental observations.

4.4.2 Transitions with periodic attractors

Subharmonic oscillations

An oscillatory instability of LR at small inclinations gives rise to a convection pattern of spatially subharmonic oscillations observed in experiments at Pr = 1.07 (Daniels et al., 2000) and studied using Floquet analysis at Pr = 0.71 (Busse and Clever, 2000). Here, we depart from our convention to follow the naming of Subramanian et al. (2016) and name this pattern subharmonic standing wave ($\mathcal{SSW}$) instead of longitudinal subharmonic oscillations to stress the standing wave nature of the pattern. We refer to observations of $\mathcal{SSW}$ at $[\gamma, \epsilon, \mathrm{Pr}] = [17°, 1.5, 1.07]$ (Daniels et al., 2000; Subramanian et al., 2016). A temporal transition is simulated in a periodic domain of size $[2\lambda_x, 2\lambda_y]$, well matching the results of the Floquet analysis in Subramanian et al. (2016). Unexpectedly, the dynamics transiently exhibits spatially subharmonic oscillations but does not saturate at a stable oscillatory pattern at these control parameters. Therefore, we reduce the angle of inclinations to $\gamma = 15°$. No additional discrete symmetries are imposed.

After a rapid transient visit near LR, the dynamics along a drifting spiral trajectory is attracted to a stable limit cycle, a periodic orbit named SSW (Figure 4.10). The initial part of the transition

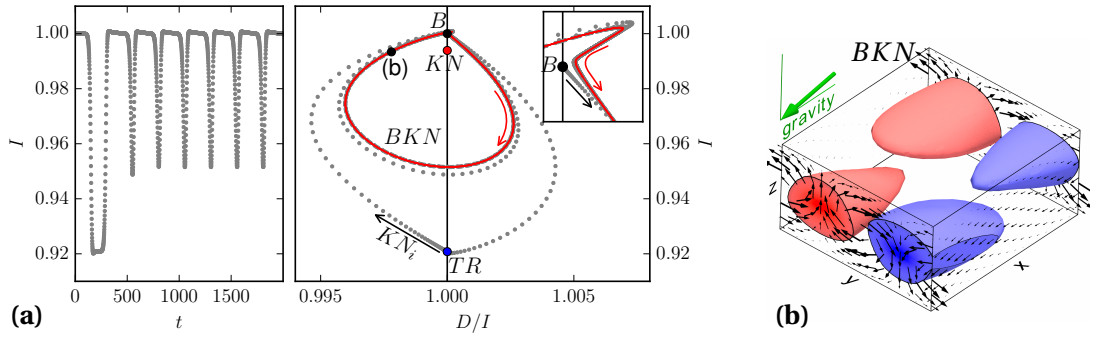

Figure 4.9 – **(a)** State trajectory evolution from the unstable base state B at $\gamma = 80°$, like in Figure 4.8, but at increased $\epsilon = 0.15$ (Ra = 9338). Instead of terminating in a stable spiral, the trajectory returns to laminar flow from where it approaches the stable periodic orbit BKN along which knots emerge as bursts. The inset magnifies the phase portrait close to the laminar base state B. **(b)** Flow structure of an instance along the periodic orbit BKN illustrates decaying longitudinal plumes that bring the state trajectory close to laminar flow.

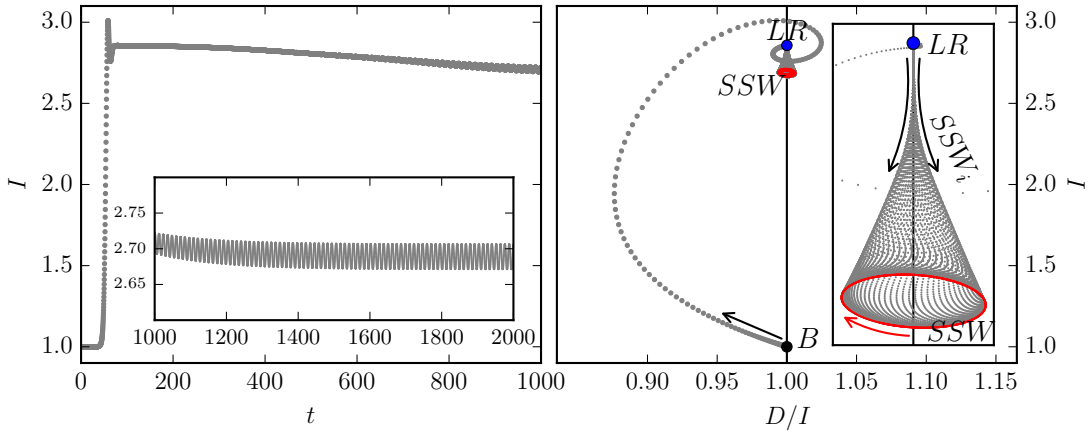

Figure 4.10 – State trajectory evolution from the unstable base state B at $\gamma = 15°$ and $\epsilon = 1.5$ (Ra = 4420). The phase portrait illustrates how the instability SSW_i leads to an oscillatory transition $LR \rightarrow SSW$ along a symmetric unstable spiral approaching periodic orbit SSW (red solid line). The inset magnifies the phase portrait of the transition $LR \rightarrow SSW$.

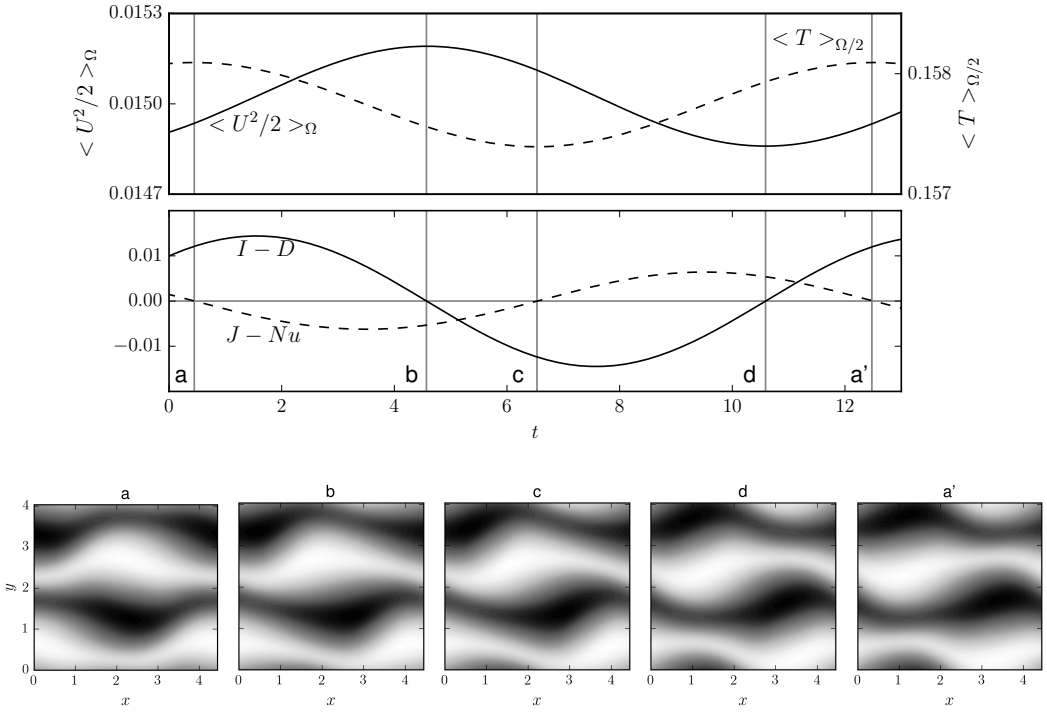

Figure 4.11 – Transfer rates of kinetic energy (solid) and thermal energy (dashed) over one relative period $T'_{\mathrm{ssw}} = 12.03$ of the *SSW* orbit at $\gamma = 15°$ and $\epsilon = 1.5$ (Ra = 4420). Temperature contours at midplane show instances of kinetic energy balance $I - D = 0$ (b,d) or thermal energy balance $J - \mathrm{Nu} = 0$ (a,c,a') along the orbit. States a and a' are related by symmetry transformation $\sigma = \pi_y \tau(0.25, 0.25)$.

$LR \to SSW$ is symmetric around $D/I = 1$ indicating that buoyancy and shear forces equally drive this instability. The periodic orbit *SSW* revolves clockwise in the D/I-plane. *SSW* is also a pre-periodic orbit satisfying condition (4.18) with $\sigma_{\mathrm{ssw}} = \pi_y \tau(0.25, 0.25)$ and a pre-period of $T'_{\mathrm{ssw}} = 12.03$. The local oscillatory instability of *LR* suggests $T = 2\pi/\omega_i = 45.11$, close to the observed full orbit period of $T_{\mathrm{ssw}} = 4T'_{\mathrm{ssw}} = 48.12$. After $2T'_{\mathrm{ssw}}$, condition (4.18) requires $\sigma = \tau(0.5, 0)$. The orbit is invariant under inversion and half-box shifts $S_{\mathrm{ssw}} = \langle \pi_{xyz}, \tau(0.5, 0.5) \rangle$.

Periodic orbits in ILC must exactly balance net transfer of kinetic energy and heat over one period $\int_0^{T'_{\mathrm{ssw}}} (I - D)\, dt = 0$. The terms in the energy equations (4.13-4.15) oscillate approximately harmonically with one relative period of *SSW*. Instances of $I - D = 0$ or $J - \mathrm{Nu} = 0$ correspond to local extrema of $< U^2/2 >_\Omega$ and $< T >_{\Omega/2}$, respectively. The phase lag between kinetic energy and heat phase is $0.37\, T'_{\mathrm{ssw}}$ (Figure 4.11). The Nusselt number varies between $1.88 \leq \mathrm{Nu} \leq 1.90$, close but below the convective heat transfer of *LR* with Nu = 1.98. The pattern of *SSW* over one period can be described as standing wave modulation (panels in Figure 4.11), a consequence of counter-propagating traveling waves along the hot and cold

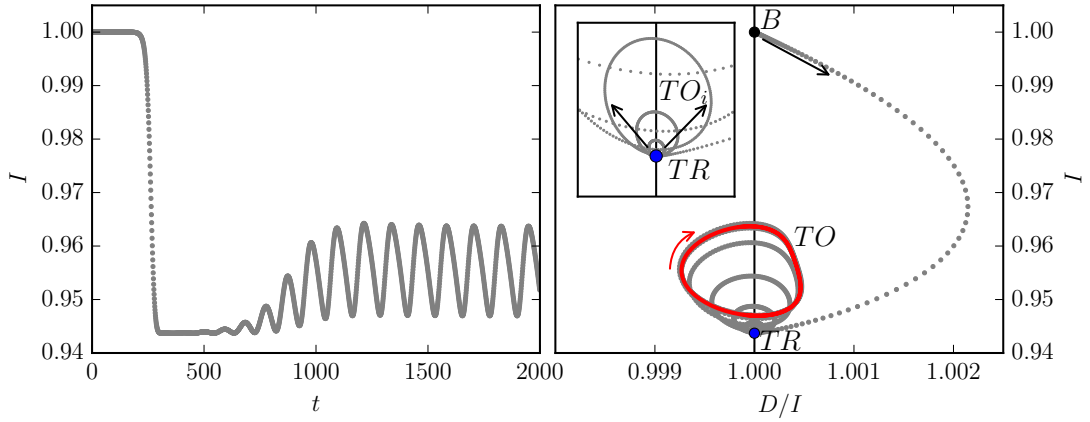

Figure 4.12 – State trajectory evolution from the unstable base state B at $\gamma = 100°$ and $\epsilon = 0.1$ (Ra = 10050). The phase portrait illustrates how the TO instability leads to an oscillatory transition $LR \rightarrow TO$ along an unstable spiral approaching periodic orbit TO (red solid line). Initial oscillations triggered by TO_i are symmetric with respect to $D/I = 1$. The inset magnifies the initial symmetric trajectory from TR.

plumes of LR (Busse and Clever, 2000).

Transverse oscillations

Transverse oscillations ($\mathcal{TO}$) are observed experimentally as chaotic bending modulations of $\mathcal{TR}$, a pattern also named 'switching diamond panes' (Daniels et al., 2000). An oscillatory TO_i instability is found as a secondary instability of TR in the interval $83.2° < \gamma \leq 120°$ for Pr = 1.07 (Subramanian et al., 2016). We refer to observations of $\mathcal{TO}$ at $[\gamma, \epsilon, \mathrm{Pr}] = [100°, 0.1, 1.07]$ (Daniels et al., 2000; Subramanian et al., 2016), and simulate a temporal transition at these control parameters in a periodic domain of size $[12\lambda_x, 6\lambda_y]$, close to the pattern wavelengths used to simulate TO in Subramanian et al. (2016). Without imposing additional discrete symmetries, no stable periodic orbit is found. Therefore, a transition is simulated in a symmetry subspace defined by $S_{\mathrm{to}} = \langle \pi_y, \pi_{xz}, \tau(0.5, 0.5) \rangle$.

The transition $B \rightarrow TR$ gives rise to 12 pairs of straight transverse rolls before slow and weak bending modulations set in. Like SSW_i, the instability TO_i of TR generates a state trajectory that is initially symmetric around $D/I = 1$ suggesting that buoyancy and shear forces drive this instability equally. The state trajectory from TR approaches the stable periodic orbit TO within a few oscillation periods (Figure 4.12). TO is a pre-periodic orbit solving condition (4.18) with $\sigma_{\mathrm{to}} = \tau(0.5, 0)$ and a pre-period of $T'_{\mathrm{to}} = 122.1$, i.e. half of the full period. As observed experimentally (Daniels et al., 2000), the oscillation period is on the order of one diffusion

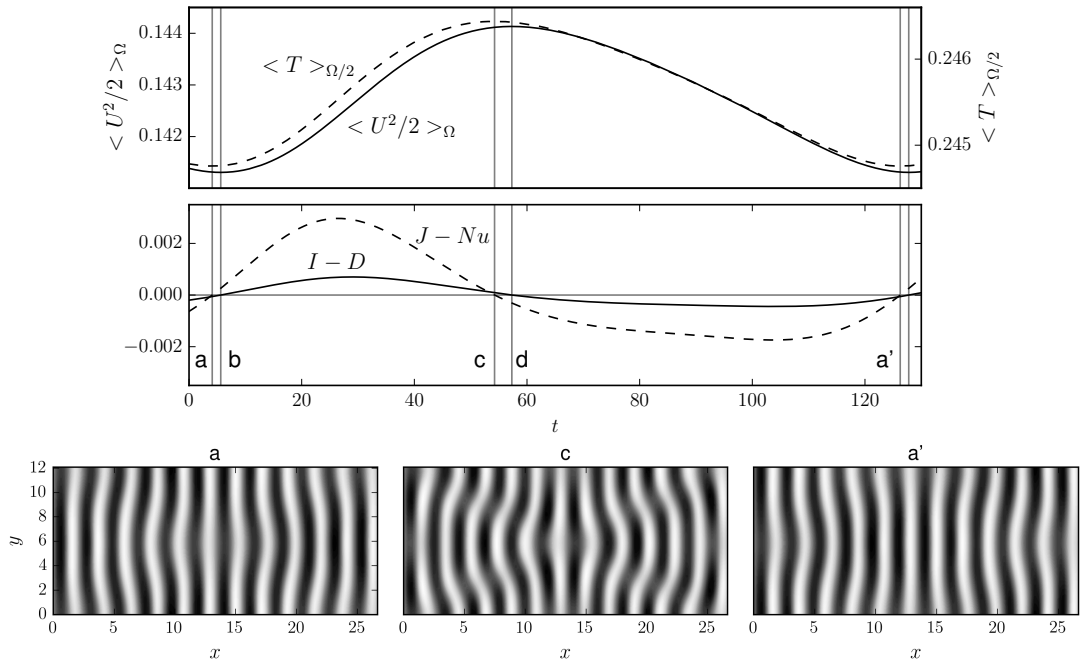

Figure 4.13 – Transfer rates of kinetic (solid) and thermal energy (dashed) over one relative period $T'_{\mathrm{to}} = 122.1$ of the TO orbit at $\gamma = 100°$ and $\epsilon = 0.1$ (Ra = 10050). Temperature contours at midplane show instances of thermal energy balance $J - \mathrm{Nu} = 0$. States a and a' are related by symmetry transformation $\sigma = \tau(0.5, 0)$.

time scale $\mathcal{O}(T_d) = \mathcal{O}(\sqrt{\mathrm{Ra}\,\mathrm{Pr}}\,T_f)$. Without the imposed discrete symmetries S_{to}, TO has six eigenvalues with positive real part at the given parameters. The associated eigenmodes break all symmetries in S_{to}.

Heat and kinetic energy oscillate non-harmonically and almost in phase over a relative period of TO at these control parameters. The pattern of TO resembles TR at the kinetic energy minimum. Near the energy maximum, the transverse rolls are maximally bent (Figure 4.13). The weak subharmonic varicose oscillations have a much larger pattern wavelength than all other invariant states discussed in the present work. In very large domains, observations show spatial-temporal chaos at these control parameters (Daniels et al., 2000; Subramanian et al., 2016), suggesting that the periodic orbit TO in larger domains is embedded in a chaotic attractor.

4.4.3 Transient dynamics of the skewed varicose pattern in Rayleigh-Bénard convection

Various secondary instabilities are known in Rayleigh-Bénard convection, namely Eckhaus, zigzag, knot, skewed varicose, cross rolls, and oscillatory instability (Busse, 1978b). At Pr = 1.07, the skewed varicose instability SV_i is the first to destabilise convection rolls as demonstrated by experiments (Bodenschatz et al., 2000) and stability analysis (Subramanian et al., 2016). We refer to observations of the skewed varicose pattern ($\mathcal{SV}$) at $[\gamma, \epsilon, \mathrm{Pr}] = [0°, 2.26, 1.07]$ (Bodenschatz et al., 2000, Fig.7). A normalised Rayleigh number of $\epsilon = 2.26$ is far above the critical threshold for SV_i. Here, we simulate a temporal transition at $\epsilon = 1.05$, much closer to threshold. The periodic domain is of size $[4\lambda_x, 4\lambda_y]$, and no additional discrete symmetries are imposed.

The conducting state of the Rayleigh-Bénard system before convection onset is isotropic in the x-y-plane and rolls have no preferred orientation in the infinite system. Therefore, we denote straight convection rolls in the isotropic system as R_λ with a subscript indicating the approximate pattern wavelength λ if $\gamma = 0°$. The attributes 'longitudinal' and 'transverse' relate to the direction of rolls relative to the base flow and are only used in the inclined case. At control parameters $[\gamma, \epsilon, \mathrm{Pr}] = [0°, 1.05, 1.07]$, rolls of various wavelengths are unstable. To promote the growth of rolls at λ_y, we perturb the base state with small-amplitude rolls at λ_y and aligned with the x-dimension. In addition, we add small-amplitude noise to break the translational symmetries. This perturbation of B triggers the growth of four pairs of convection rolls $R_{\lambda 2}$, comparable to the pattern of LR at $\gamma \neq 0$ in the present study. After a rapid transition $B \rightarrow R_{\lambda 2}$ over $\Delta t = 40$, the shear driven instability SV_i generates a slow departure from $R_{\lambda 2}$ over $\Delta t = 20\,000$. The exponential escape rate from LR is given by the only positive real eigenvalue of LR, $\omega_r = 3.8 \cdot 10^{-4}$, with quadruple multiplicity. The associated eigenmodes show the characteristic three-dimensional oblique pattern of the skewed varicose instability (Busse and Clever, 1979). While escaping from LR, the convection rolls $R_{\lambda 2}$ start tilting and form a thin skewed region along the domain diagonal where rolls become strongly sheared ($t_1 = 20\,680$), pinch off ($t_2 = 20\,782$), reconnect and form rolls $R_{\lambda 3}$ at increased wavelength $\lambda = 2.5731$ and rotated by 16.8° against the x-direction (Figure 4.14). $R_{\lambda 3}$ are linearly stable at these control parameters.

The simulated sequence of dynamical connections $B \rightarrow R_{\lambda 2} \rightarrow R_{\lambda 3}$ is invariant under $S_{\mathrm{sv}} = \langle \pi_{xyz}, \tau(0.25, 0.25) \rangle$ and at t_2, resembles the experimentally observed SV pattern (Figure 7 in Bodenschatz et al., 2000). However, the phase portrait does not indicate a transiently visited invariant state. The state trajectory crosses $D/I = 1$ without slow-down (Figure 4.14). Simulating the instability SV_i at other control parameters does not change this observation. Thus, the transient dynamics of the $\mathcal{SV}$ pattern seems to occur in the absence of an underlying invariant state.

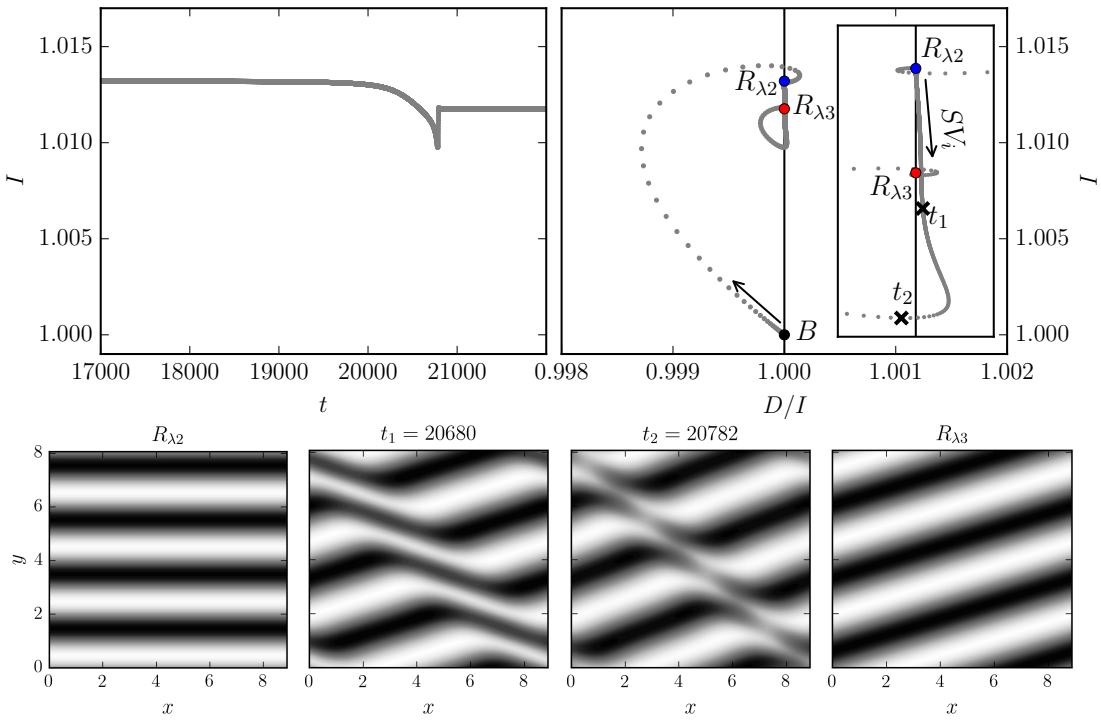

Figure 4.14 – State trajectory evolution from the unstable base state B at $\gamma = 0$ and $\epsilon = 1.05$ (Ra = 3500). Initially for $0 < t < 40$, a fast transition along $B \rightarrow R_{\lambda 2}$ gives rise to straight convection rolls at wavelength λ_y (not shown). After a very long transient close to $R_{\lambda 2}$, the shear driven instability SV_i of straight convection rolls $R_{\lambda 2}$ leads to rolls $R_{\lambda 3}$ at increased wavelength. The inset magnifies the phase portrait of the transition $R_{\lambda 2} \rightarrow R_{\lambda 3}$. During the transition $R_{\lambda 2} \rightarrow R_{\lambda 3}$ around $t_1 = 20\,680$, a skewed varicose pattern emerges transiently. The midplane temperature contours (bottom) illustrate different instances along the state trajectory (cross markers).

Table 4.1 – Summary of temporal transitions sequences identified at selected control parameters where complex convection patterns are observed. For each transition along a dynamical connection, denoted by →, we list the initial driving force of the instability (B: buoyancy, S: shear, E: equally).

γ	Ra	ϵ	temporal transition sequence	driving forces	figure
0°	3500	1.05	$B \rightarrow R_{\lambda 2} \rightarrow R_{\lambda 3}$	B, S	4.14
15°	4420	1.5	$B \rightarrow LR \rightarrow SSW$	B, E	4.10
40°	2385	0.07	$B \rightarrow LR \rightarrow WR$	B, S	4.4
40°	3344	0.5	$B \rightarrow LR \rightarrow WR \rightarrow OWR \rightarrow \tau_{xy} OWR \rightarrow ...$	B, S, B, S, S, ...	4.6
80°	8525	0.05	$B \rightarrow TR \rightarrow KN$	S, B	4.8
80°	9338	0.15	$B \rightarrow TR \rightarrow B \rightarrow BKN$	S, B, S	4.9
100°	10050	0.1	$B \rightarrow TR \rightarrow TO$	S, E	4.12

4.5 Discussion

In this study, we identify exact invariant states of the fully nonlinear three-dimensional Oberbeck-Boussinesq equations that underlie the various convection patterns observed in ILC. At control parameters where tertiary convection patterns have been observed in experiments and simulations, we numerically study the temporal dynamics from a perturbed unstable base flow. Table 4.1 summarises all cases studied. Except for the transient skewed varicose pattern at $\gamma = 0°$, the dynamics asymptotically approaches stable invariant states underlying observed convection patterns. Temporal dynamics approaching attractive invariant states has been suggested by earlier works Daniels et al. (2008); Subramanian et al. (2016). In these previous studies, numerical simulations close to known secondary instabilities, and in parts constrained to specific modal interactions, are found to approach nonlinear states emerging from the instabilities. Here, we find both stable and unstable invariant states as fixed points of a Newton iteration, numerically fully resolved and converged to machine precision. Details of the transition from the laminar state to transiently visited unstable invariant states are discussed.

State trajectories are never found to directly approach a stable tertiary or higher order state, but the dynamics first transiently visits unstable invariant states underlying the secondary convection pattern of straight convection rolls, as shown in Table 4.1. Approach to and escape from unstable invariant states follow the exponential dynamics along their stable and unstable manifolds, well described by the eigenvalues of the invariant states. This observation strongly suggests the existence of nearby heteroclinic connections between invariant states, located within the intersection of the unstable manifold of the initial state and the stable manifold of the final state. In one case at $\gamma = 40°$, a robust heteroclinic cycle between two symmetry-related

unstable equilibrium states underlying oblique wavy rolls has been found. Thus, the present results demonstrate the dynamical relevance not only of stable but also of coexisting unstable invariant states and their dynamical connections. The network of dynamically connected invariant states clearly supports complex temporal dynamics in ILC.

Invariant states and their dynamical connections have been computed in minimal periodic domains matching single pattern wavelengths but they also exist in larger domains. The size of the domain does however change the stability properties of the invariant states. States that are stable in small domains can be unstable in larger domains (Ahlers and Behringer, 1978; Melnikov et al., 2014). Consequently, the sequences of temporal transitions between invariant states observed here may also be observed in larger domains, but not necessarily with the same stable terminal state as in the present study. In the small domains, most transitions are unidirectional, from the base state B, via a secondary roll (LR, TR) to a tertiary state (Table 4.1). In larger domains, unstable tertiary states are expected to allow dynamical cycles that visit the same states multiple times. Examples of such cycles observed in the small domains include the robust heteroclinic cycle ($OWR \rightarrow \tau_{xy} OWR \rightarrow OWR \rightarrow ...$) and the dynamics leading to the periodic orbit of bursting knots (BKN): After escaping from unstable laminar flow and transiently visiting TR, the state trajectory returns to the state space neighborhood of laminar flow B (Figure 4.9). Together, the connections may form a dynamical network supporting the spatio-temporally chaotic dynamics observed in experiments and large-domain simulations.

We characterise the instabilities of equilibrium states that trigger temporal transitions as buoyancy driven, shear driven or equally buoyancy-shear driven, by analysing the temporal transitions in phase portraits defined by kinetic energy input and dissipation. We thereby confirmed that $\mathcal{LR}$ emerge from a buoyancy driven instability and $\mathcal{TR}$ emerge from a shear driven instability of the base state. Secondary instabilities are never driven by the same force as the associated primary instability. If the primary instability is buoyancy dominated, the secondary one will involve shear and *vice versa* (Table 4.1). Consequently, the temporal dynamics in ILC at all angles of inclinations may involve instabilities driven by buoyancy and shear.

We find seven invariant states that participate in sequences of temporal transitions that may be described as *primary state* → *secondary state* → *tertiary state*. Here, the terminology refers to the order of states visited in transition sequences such that *primary* transitions to *secondary*, *secondary* transitions to *tertiary*. We expect that this order reflects the order of bifurcations that create these invariant states. However, generically the sequence of bifurcations will not prescribe the order in which states, coexisting at the same control parameters, are visited during temporal evolution. An example for this is the temporal evolution triggered by the skewed varicose instability of straight convection rolls. The transition $R_{\lambda 2} \rightarrow R_{\lambda 3}$ cannot result from bifurcations of $R_{\lambda 3}$ from $R_{\lambda 2}$ because both types of straight convection rolls must bifurcate

Table 4.2 – Summary of invariant states underlying observed convection patterns (EQ: equilibrium, PPO: pre-periodic orbit). The symmetries of the invariant states are given by the size of the periodic domain ($\lambda_x = 2.2211$, $\lambda_y = 2.0162$) and the generators of the symmetry group.

convection pattern	invariant state	type	domain	symmetry group generators
laminar flow	B	EQ	-	π_y, π_{xz}, $\tau(a_x, a_y)$
isotropic rolls	R_λ	EQ	$[4\lambda_x, 4\lambda_y]$	π_y, π_{xz}, $\tau(a_x, a_y(a_x))$
long. rolls	LR	EQ	$[1\lambda_x, 1\lambda_y]$	π_y, π_{xz}, $\tau(a_x, 0)$
trans. rolls	TR	EQ	$[1\lambda_x, 1\lambda_y]$	π_y, π_{xz}, $\tau(0, a_y)$
skewed varicose	-	-	$[4\lambda_x, 4\lambda_y]$	π_{xyz}, $\tau(0.25, 0.25)$
subharmonic standing wave	SSW	PPO	$[2\lambda_x, 2\lambda_y]$	π_{xyz}, $\tau(0.5, 0.5)$
wavy rolls	WR	EQ	$[2\lambda_x, 1\lambda_y]$	$\pi_y\tau(0.5, 0.5)$, $\pi_{xz}\tau(0.5, 0.5)$
oblique wavy rolls	OWR	EQ	$[2\lambda_x, 1\lambda_y]$	π_{xyz}, $\tau(0.5, 0.5)$
knots	KN	EQ	$[1\lambda_x, 1\lambda_y]$	$\pi_y\tau(0, 0.5)$, $\pi_{xz}\tau(0, 0.5)$
trans. oscillations	TO	PPO	$[12\lambda_x, 6\lambda_y]$	π_y, π_{xz}, $\tau(0.5, 0.5)$

from B. To understand the relation between the complex temporal dynamics reported here and the corresponding bifurcation structure, the bifurcations of the invariant states visited by the dynamics must be computed. We list all invariant states found to underlie observed convection patterns in the present study in Table 4.2. This collection represents the starting point for subsequent work where invariant states are numerically continued under changing control parameters to compute bifurcation diagrams in ILC (Chapter 5).

In conclusion, temporal transitions from unstable laminar flow in ILC are found to follow sequences of dynamical connections between unstable invariant states until the dynamics approaches a stable invariant state. The stable invariant state underlies the basic pattern observed in experiments and simulations. Existence and dynamical influence of the dynamical connections between unstable invariant states support the complex dynamics observed in large domains.

5 Bifurcations and connections between branches of invariant states

Remark This chapter is largely inspired by a pre-print of the name "Invariant states in inclined layer convection. Part 2. Bifurcations and connections between branches of invariant states".

Florian Reetz[1], Priya Subramanian[2,3] and Tobias M. Schneider[1]

[1] Emergent Complexity in Physical Systems Laboratory (ECPS),
École Polytechnique Fédérale de Lausanne, CH 1015 Lausanne, Switzerland
[2] School of Mathematics, University of Leeds, Leeds LS2 9JT, UK
[3] Mathematical Institute, University of Oxford, Woodstock Road, Oxford OX2 6GG, UK

Under consideration for publication in *Journal of Fluid Mechanics*

Chapter summary

Convection in a layer inclined against gravity is a thermally driven non-equilibrium system, in which both buoyancy and shear forces drive spatio-temporally complex flow. As a function of the strength of thermal driving and the angle of inclination, a multitude of convection patterns is observed in experiments and numerical simulations. Several observed patterns have been linked to exact invariant states of the fully nonlinear 3D Oberbeck-Boussinesq equations. These exact equilibria, traveling waves and periodic orbits reside in state space and, depending on their stability properties, are transiently visited by the dynamics or act as attractors. To explain the dependence of observed convection patterns on control parameters, we study the

parameter dependence of the state space structure. Specifically, we identify the bifurcations that modify the existence, stability and connectivity of invariant states. We numerically continue exact invariant states underlying spatially periodic convection patterns at Pr = 1.07 under changing control parameters for temperature difference between the walls and inclination angle. The resulting state branches cover various inclinations from horizontal layer convection to vertical layer convection and beyond. The collection of all computed branches represents an extensive bifurcation network connecting 16 different invariant states across control parameters. Individual bifurcation structures are discussed in detail and related to the observed complex dynamics of individual convection patterns. Together, the bifurcations and associated state branches indicate at what control parameters which invariant states coexist. This provides a nonlinear framework to explain the multitude of complex flow dynamics arising in inclined layer convection.

5.1 Introduction

Thermal convection in a gap between two parallel infinite walls maintained at different fixed temperatures, a system known as Rayleigh-Bénard convection, is a thermally driven nonequilibrium system that exhibits many different complex convection patterns (e.g. Cross and Greenside, 2009). When inclining the walls against gravity, hot and cold fluid flows up and down the incline, respectively, creating a cubic laminar flow that breaks the isotropy of a horizontal layer and produces shear forces. This system is known as inclined layer convection (ILC). ILC has three control parameters: the temperature difference between the walls, the Prandtl number Pr parametrising the diffusive properties of the fluid, and the angle of inclination against gravity.

Recent experiments of ILC using compressed CO_2 (Pr = 1.07) have systematically varied the temperature difference and the inclination angle over a wide range, and report ten different spatio-temporal convection patterns (Daniels et al., 2000). In these experiments, the flow domain has a lateral extent much larger than the gap height and thereby allows large-scale patterns to form. The observed convection patterns show spatio-temporally complex dynamics. This includes intermittent temporal bursting of spatially localized convection structures, observed both at small angles of inclination (Busse and Clever, 2000; Daniels et al., 2000) as well as at large angles of inclination (Daniels et al., 2003). Other examples include transient oblique patterns forming unsteady interfaces between spatial domains of differently oriented wavy roll patterns (Daniels and Bodenschatz, 2002; Daniels et al., 2008), bimodal patterns, turbulent patterns like crawling rolls at intermediate inclinations (Daniels et al., 2008) and chaotically switching diamond panes. These convection patterns have also been reproduced in direct numerical simulations of ILC (Subramanian et al., 2016). How the large variety of

patterns at different control parameters emerges from the nonlinear equations describing the flow is however not completely understood.

Theoretical approaches towards explaining spatio-temporal convection patterns in ILC can be described as either an approach 'close to thresholds' or an approach 'far above thresholds'. Approaches 'close to thresholds' include linear stability analysis and the construction of weakly nonlinear amplitude equations. At critical stability thresholds, flow states become unstable and give rise to new pattern motifs. Linear stability analysis of laminar ILC (Gershuni and Zhukhovitskii, 1969; Vest and Arpaci, 1969; Hart, 1971b; Ruth et al., 1980a; Chen and Pearlstein, 1989; Fujimura and Kelly, 1993) identified two different types of primary instabilities. A buoyancy driven instability gives rise to straight convection rolls oriented along the base flow at small inclinations. A shear driven instability gives rise to straight convection rolls oriented transverse to the base flow at large inclinations. Secondary instabilities of finite amplitude straight convection rolls and subsequent tertiary instabilities at increased temperature difference and certain angles of inclination have been investigated using Floquet analysis of two- and three-dimensional states (Clever and Busse, 1977; Busse and Clever, 1992; Clever and Busse, 1995; Busse and Clever, 1996; Subramanian et al., 2016). Such stability analysis can only explain the onset of convection patterns at, or very close, to the critical stability thresholds in control parameters.

Theoretical approaches to convection patterns 'far above thresholds' include the construction of finite amplitude states within a nonlinear analysis at control parameters far above the critical stability thresholds. Finite amplitude states can be constructed by choosing a Galerkin projection for the governing equations of ILC, often motivated by pattern motifs and their symmetries as identified in a stability analysis at critical stability thresholds (Busse and Clever, 1996; Golubitsky and Stewart, 2002). Galerkin approximations can then be evolved in time under the fully nonlinear governing equations until their amplitudes saturate at finite values with either steady or periodic time evolution (Subramanian et al., 2016). Alternative to forward time integration, finite amplitudes of a Galerkin projection may also be calculated using a Newton-Raphson iteration giving access also to dynamically unstable finite amplitude states (Busse and Clever, 1992; Fujimura and Kelly, 1993; Subramanian et al., 2016). If Galerkin projections invoke a complete basis and fully resolve all spatial scales and modal interactions in the three-dimensional flow, exact finite-amplitude states with steady or periodic time evolution can be found. These so-called invariant states are time-invariant exact solutions of the full nonlinear partial differential equations governing the flow. Depending on their temporal dynamics, invariant states are steady equilibrium states, traveling waves or periodic orbits, all of which capture particular structures in the flow. Invariant states can either be dynamically stable or dynamically unstable. In subcritical shear flows like pipe or Couette flow, the construction and analysis of unstable invariant states has lead to significant progress in understanding the complex dynamics of weakly turbulent flow by describing chaotic state

space trajectories relative to invariant states (Kerswell, 2005; Eckhardt et al., 2007; Kawahara et al., 2012, and references therein).

In ILC, only few highly resolved three-dimensional invariant states had been constructed (Busse and Clever, 1992; Clever and Busse, 1995) before in Chapter 4 (referred to as RS19 in the following), we identified stable and unstable invariant states underlying various convection patterns at Pr = 1.07 observed in experiments (Daniels et al., 2000) and simulations (Subramanian et al., 2016). These invariant states are found to transiently attract and repel the dynamics of ILC that is numerically simulated in minimal periodic domains. Minimal periodic domains accommodate only a single spatial period of a periodic convection pattern. Any invariant state computed in minimal periodic domains is also an invariant state in larger extended domains where the pattern of the state periodically repeats in space. To capture a specific pattern with an invariant state in a minimal periodic domain, the size of the domain must be chosen appropriately to match the wavelengths of the pattern. A suitable domain size for a specific pattern can be suggested by Floquet analysis which determines the most unstable pattern wavelength of an instability. At the critical thresholds of instabilities, invariant states emerge in bifurcations and may continue as state branches far above critical thresholds. Thus, bifurcations provide a connection between instabilities 'at thresholds' and invariant states 'far above thresholds'.

In general, bifurcations are structural changes in a system's state space across which the dynamics of the system changes qualitatively (Guckenheimer and Holmes, 1983). Emerging stable invariant states that may continue 'far above thresholds' correspond to a supercrtical, forward bifurcation leading to continuous changes in the dynamics. Subcritical bifurcations however, create discontinuous changes in the dynamics allowing for sudden transitions from one state of the system to a very different state. Prominent and potentially harmful examples of such bifurcations, also called tipping points, have been identified in the earth's climate system (Lenton et al., 2008) or in combustion chambers (Juniper and Sujith, 2018). In low-dimensional nonlinear model systems, like the three-dimensional Lorenz model for thermal convection (Lorenz, 1963), various types of bifurcations have been found and related to different routes to chaos (see Argyris et al., 1993, for a review). Thus, different types of bifurcations change the dynamics in different ways. Complex temporal dynamics may be observed where invariant states coexist at equal control parameters (RS19). Complex spatial dynamics, like spatial coexistence of different states in a non-conservative system as ILC, suggests that the spatially coexisting states also coexist as individual states at equal control parameters (Knobloch, 2015). Coexistence of invariant states at equal control parameters is a consequence of bifurcations creating these invariant states. Thus, bifurcations creating invariant states that underlie observed convection patterns in ILC not only provide a parametric connection between invariant states and instabilities, but may also explain the state space structure underlying the spatio-temporally complex dynamics observed in spatially extended domains.

Computing bifurcation diagrams in nonlinear dynamical systems requires in practice to numerically continue branches of stable and unstable invariant states under changes of control parameters (see Dijkstra et al., 2014, for a review). Numerically fully resolved invariant states in minimal periodic domains of ILC have between $\sim 10^4$ and $\sim 10^6$ degrees of freedom (RS19), fewer than the earth's climate system but much more than the Lorenz equations. Due to the numerically demanding size of the state space, not many prior studies have computed bifurcation diagrams in ILC. Using 4 degrees of freedom, Fujimura and Kelly (1993) traced states of mixed longitudinal and transverse modes in almost vertical fluid layers. Using $\sim 10^3$ degrees of freedom, Busse and Clever (1992) continued invariant states underlying three-dimensional wavy rolls at selected Pr and angles of inclinations, and Clever and Busse (1995) followed a sequence of supercritical bifurcations in vertical fluid layers. Bifurcation diagrams of two-dimensional invariant states have been computed in vertical convection (Mizushima and Tanaka, 2002b,a) and horizontal convection (Waleffe et al., 2015), not addressing three-dimensional dynamics. Recent advances in matrix-free algorithms and computer hardware allow to efficiently construct and continue fully resolved three-dimensional invariant states in double-periodic domains with channel geometry (Viswanath, 2007; Gibson et al., 2008b). We use an extension to the existing numerical framework of the MPI-parallel code *Channelflow 2.0* (Gibson et al., 2019) that also handles ILC (RS19).

The aim of this chapter is to systematically compute and describe bifurcations in ILC. These bifurcations explain the spatio-temporal complexity observed both experimentally and numerically. Using numerical continuation, we trace invariant states that have been constructed in RS19 and that underlie the observed basic convection patterns. The analysis covers the same range of system parameters as recent experimental (Daniels et al., 2000) and theoretical work (Subramanian et al., 2016) at Pr = 1.07 and leads to an extensive network of bifurcating branches across control parameters. To understand how temporal and spatio-temporal complexity arises in ILC, we specifically address the following three questions:

Q1 *Bifurcation types*: Complex temporal dynamics between coexisting invariant states is a result of bifurcations creating the associated invariant states. Different bifurcation types change the dynamics in different ways. What types of bifurcations create invariant states underlying the observed convection patterns in ILC?

Q2 *Connection to instabilities*: Floquet analysis characterises instabilities at critical control parameters. Results from such an analysis are valid close to the critical thresholds for small amplitude solutions. Do the fully nonlinear invariant states, found in RS19 to underlie the observed convection patterns far from critical thresholds in ILC, bifurcate at the corresponding secondary instabilities reported from a Floquet analysis in Subra-

manian et al. (2016)?

Q3 *Range of existence*: Spatio-temporally complex dynamics suggests existence of invariant states at the associated control parameters. How do the bifurcation branches of invariant states in ILC continue across control parameters and what are the limits of their existence?

The present chapter is structured in the following way. Section 5.2 describes the numerical methods and outlines the systematic bifurcation analysis. The results of the bifurcation analysis are stated in Section 5.3. In five subsections, we report in detail on selected bifurcation diagrams explaining individual convection patterns. The results are discussed in response to *Q1*-*Q3* in Section 5.4.

5.2 Bifurcation analysis of invariant states

Before introducing the approach of the bifurcation analysis in Section 5.2.3, we summarize the basic numerical concepts underlying direct numerical simulations of ILC (Section 5.2.1), and describe the invariant states that capture relevant convection patterns (Section 5.2.2). More details on the direct numerical simulations and identified invariant states are described elsewhere (RS19).

5.2.1 Direct numerical simulation of inclined layer convection

ILC is studied by numerically solving the nondimensionalised Oberbeck-Boussinesq equations for the velocity $\boldsymbol{U}$, temperature $\mathcal{T}$ and pressure p relative to the hydrostatic pressure

$$\frac{\partial \boldsymbol{U}}{\partial t} + (\boldsymbol{U}\cdot\nabla)\,\boldsymbol{U} = -\nabla p + \tilde{\nu}\nabla^2\boldsymbol{U} - \hat{\boldsymbol{g}}\,\mathcal{T}\,, \tag{5.1}$$

$$\frac{\partial \mathcal{T}}{\partial t} + (\boldsymbol{U}\cdot\nabla)\,\mathcal{T} = \tilde{\kappa}\nabla^2\mathcal{T}\,, \tag{5.2}$$

$$\nabla\cdot\boldsymbol{U} = 0\,, \tag{5.3}$$

in numerical domains with x, y and z indicating the streamwise, the spanwise and the wall-normal dimension. The domains are bounded in z by two parallel walls at $z = \pm 0.5$. In the streamwise dimension x and the spanwise dimension y periodic boundary conditions are imposed at $x = [0, L_x]$ and $y = [0, L_y]$, respectively. The walls are stationary with $\boldsymbol{U}(z = \pm 0.5) = 0$, have prescribed temperatures $\mathcal{T}(z = \pm 0.5) = \mp 0.5$, and are inclined against the gravitational unit vector $\hat{\boldsymbol{g}} = -\sin(\gamma)\boldsymbol{e}_x - \cos(\gamma)\boldsymbol{e}_z$ by inclination angle γ. With these boundary conditions,

Equations (5.1-5.3) admit the laminar solution

$$\boldsymbol{U}_0(z) = \frac{\sin(\gamma)}{6\tilde{\nu}}\left(z^3 - \frac{1}{4}z\right)\boldsymbol{e}_x\,, \tag{5.4}$$

$$\mathcal{T}_0(z) = -z\,, \tag{5.5}$$

$$p_0(z) = \Pi - \cos(\gamma)z^2/2\,, \tag{5.6}$$

with arbitrary pressure constant Π. Equations (5.1-5.3) are nondimensionalised by three characteristic scales of the system. We have chosen the temperature difference $\Delta\mathcal{T}$ between the walls, the gap height H, and the free-fall velocity $U_f = (g\,\alpha\,\Delta\mathcal{T}\,H)^{1/2}$ as characteristic scales. This nondimensionalisation defines the parameters $\tilde{\nu} = (\mathrm{Pr}/\mathrm{Ra})^{1/2}$ and $\tilde{\kappa} = (\mathrm{Pr}\,\mathrm{Ra})^{-1/2}$ in terms of the Rayleigh number $\mathrm{Ra} = g\,\alpha\,\Delta T\,H^3/(\nu\kappa)$ and the Prandtl number $\mathrm{Pr} = \nu/\kappa$. Here, α is the thermal expansion coefficient, ν is the kinematic viscosity, and κ is thermal diffusivity. Thus, ILC has three control parameters, γ, Ra, and Pr, of which we fix $\mathrm{Pr} = 1.07$.

Time is measured in free-fall units H/U_f but will also be compared with other relevant time scales of ILC, like the heat diffusion time H^2/κ, and the laminar mean advection time $L_x/\bar{U}_0$. The latter follows from the laminar velocity profile (5.4) integrated over the lower half of the domain where $-0.5 \le z \le 0$, that is $\bar{U}_0 = \sin(\gamma)/384\tilde{\nu}$.

The pseudo-spectral code *Channelflow 2.0* (Gibson et al., 2019) has been extended to solve (5.1-5.3) using Fourier-Chebychev-Fourier expansions with N spectral modes in space and a 3rd order implicit-explicit multistep algorithm to march forward in time (see RS19; and references therein). Any time evolution computed with *Channelflow-ILC* represents a unique state vector trajectory $\boldsymbol{x}(t) = [\boldsymbol{u},\theta](x,y,z,t)$ in a state space with N dimensions. This state space contains all solenoidal velocity fluctuations $\boldsymbol{u} = \boldsymbol{U} - \boldsymbol{U}_0$ and temperature fluctuations $\theta = \mathcal{T} - \mathcal{T}_0$.

5.2.2 Computing invariant states

Invariant states are particular state vectors $\boldsymbol{x}^*(t)$ representing roots of a recurrent map

$$\mathcal{G}(\boldsymbol{x}^*,\mu) = \sigma\mathcal{F}^T(\boldsymbol{x}^*,\mu) - \boldsymbol{x}^* = 0\,. \tag{5.7}$$

Here, $\mathcal{F}^T(\boldsymbol{x},\mu)$ is the dynamical map integrating (5.1-5.3) from state $\boldsymbol{x}$ over time period T at system parameter $\mu \in [\gamma, \mathrm{Ra}, \mathrm{Pr}]$. The invariant state is either an equilibrium state if T is a free parameter, or a periodic orbit if T must match a specific period. Definition (5.7) includes a symmetry transformation $\sigma \in S_{ilc}$. The symmetry group $S_{ilc} = O(2)_x \times O(2)_y$, where $\times$ is the direct product, is an equivariance of Equations (5.1-5.3) in x-y-periodic domains. S_{ilc} is generated by spanwise y-reflection π_y, streamwise x-z-reflection π_{xz}, and x- and

y-translations $\tau(a_x, a_y)$ such that

$$\pi_y[u,v,w,\theta](x,y,z) = [u,-v,w,\theta](x,-y,z)\,, \tag{5.8}$$

$$\pi_{xz}[u,v,w,\theta](x,y,z) = [-u,v,-w,-\theta](-x,y,-z)\,, \tag{5.9}$$

$$\tau(a_x,a_y)[u,v,w,\theta](x,y,z) = [u,v,w,\theta](x+a_xL_x, y+a_yL_y, z)\,, \tag{5.10}$$

with shift factors $a_x, a_y \in [0,1)$ scaling the spatial periods L_x and L_y of the periodic domain. All invariant states discussed here are invariant under transformations within subgroups of $S_{ilc} = \langle \pi_y, \pi_{xz}, \tau(a_x,a_y)\rangle$, where angle brackets $\langle\rangle$ imply all products of elements given in the brackets. The specific coordinate transformations for reflection symmetries depend on the spatial phase of the flow structure relative to the origin. We choose the spatial phase such that three-dimensional inversion $\pi_{xyz} = \pi_y\pi_{xz}$, where applicable to invariant states, applies with respect to the domain origin at $(x,y,z) = (0,0,0)$.

If $\sigma \neq 1$ in (5.7), the invariant state is a *relative* invariant state. A traveling wave state, where $\sigma = \tau(a_x,a_y)$ with specific shift factors a_x and a_y, is a relative equilibrium state. A relative periodic orbit is either traveling, where $\sigma = \tau(a_x,a_y)$ must be applied after period T, or is 'pre-periodic' if $\sigma = 1$ after a full period T but $\sigma \neq 1$ after time interval $T' = T/n$ with $n \in \mathbb{N}$.

Invariant states are computed by solving (5.7) with a Newton-Raphson iteration using matrix-free Krylov methods (Gibson et al., 2019). Practically, we stop iterations if $||\mathcal{G}(\boldsymbol{x},\mu)||_2 < 10^{-13}$ where

$$||\boldsymbol{x}||_2 = \left(\frac{1}{L_xL_y} \int_0^{L_x}\int_0^{L_y}\int_{-0.5}^{0.5} u^2+v^2+w^2+\theta^2\, dx\, dy\, dz \right)^{1/2}. \tag{5.11}$$

A residual of $< 10^{-13}$ is sufficiently close to double machine precision to consider the iteration as fully converged.

Invariant states may be dynamically stable or unstable. The dynamical stability is characterised by the eigenvalues and eigenmodes of the linearised equations computed using Arnoldi iteration (Gibson et al., 2019) and depends on the specific symmetry subspace defined by size $[L_x, L_y]$ of the periodic domain and potentially imposed discrete symmetries $\sigma \in S_{ilc}$. We impose σ on a state vector $\boldsymbol{x}(t)$ using a projection $(\boldsymbol{x}(t) + \sigma\boldsymbol{x}(t))/2$ which requires $\sigma^2 = 1$. We will specify the considered symmetry subspace for each computation of the eigenvalue spectrum.

Previously, invariant states underlying observed convection patterns in ILC have been identified by combining direct numerical simulations in small periodic domains with Newton-Raphson iteration (RS19). There, simulations from unstable laminar flow perturbed by small-

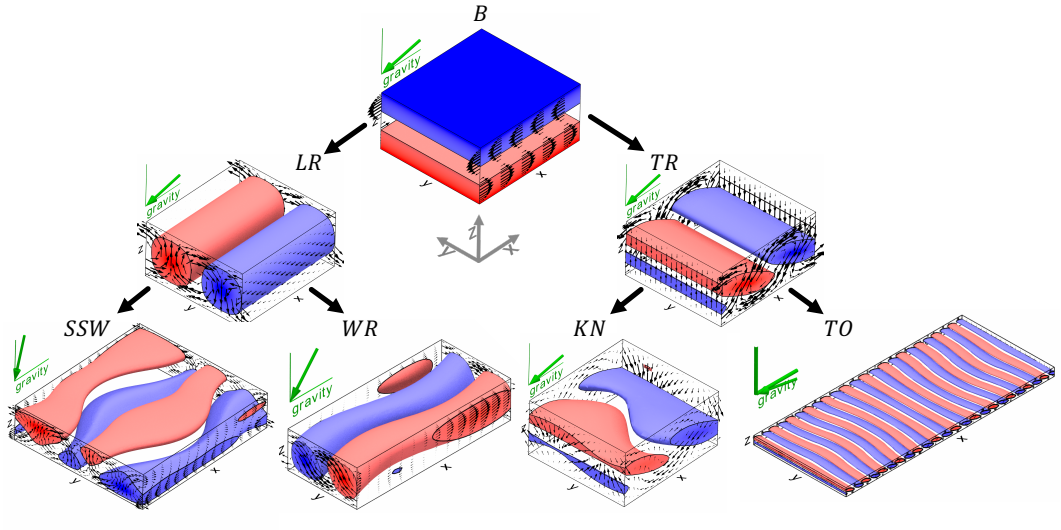

Figure 5.1 – Invariant states found as sequentially visited states in temporal transitions at selected control parameters (RS19). Black arrows indicate the direction of temporal transitions, starting from laminar base flow B, via longitudinal and transverse rolls (equilibria LR and TR), to four different tertiary invariant states representing the convection patterns of subharmonic standing waves (periodic orbit SSW), wavy rolls (equilibrium WR), knots (equilibrium KN) and transverse oscillations (periodic orbit TO). While B is shown as the vector fields of total velocity $\boldsymbol{U}$ at the box sides and 3D contours of total temperature $\mathcal{T}$, all other states are shown in terms of velocity and temperature fluctuations, $\boldsymbol{u}$ and θ, around B. Iso-contours of temperature are at $1/3[\min(\theta), \max(\theta)]$. The states are computed at different inclinations of the domain (green gravity vectors): B, LR and TR at γ_{c2}, and the four tertiary states at the system parameters marked in Figure 5.2.

amplitude noise lead to temporal transitions between seven invariant states. All of these seven invariant states are either stable or weakly unstable, depending on the symmetry subspace corresponding to the chosen periodic domain, control parameters and potentially imposed discrete symmetries. As a consequence, the temporal dynamics is either asymptotically or transiently attracted to these invariant states. Moreover, the temporal dynamics is found to visit these invariant states in a specific sequential order. Figure 5.1 summarizes the observed transition sequences and visualises the flow structures of all seven invariant states. Which invariant state is visited by the dynamics depends on the control parameters. Following Daniels et al. (2000) and Subramanian et al. (2016), we explore the two-dimensional parameter space of inclination angle γ and Rayleigh number Ra at fixed Pr = 1.07. Here, a codimension-2 point at $[\gamma_{c2}, \mathrm{Ra}_{c2}]$ determines the type of primary instability and visited secondary state. In general, at any Prandtl number, the transition from a laminar base flow (B) leads to longitudinal rolls (LR) for angles of $\gamma < \gamma_{c2}$, while for angles with $\gamma > \gamma_{c2}$ the transition from B leads to transverse rolls (TR). At Pr = 1.07, we determine the codimension-2 point accurately at $[\gamma_{c2}, \mathrm{Ra}_{c2}] = [77.7567°, 8053.1]$ when computing LR and TR in a domain with periodicity $[L_x, L_y] = [\lambda_x, \lambda_y]$ where $[\lambda_x, \lambda_y] = [2.2211, 2.0162]$ and grid size $[n_x, n_y, n_z] = [32, 32, 25]$. Wavelengths λ_x and λ_y are suggested by Floquet analysis (Subramanian et al., 2016). As in RS19, we fix the domain periodicity $[\lambda_x, \lambda_y]$ and the grid resolution $[n_x, n_y, n_z]$ throughout this study and choose all computational domains as multiples of this minimal periodic box. Subharmonic standing waves (SSW) are computed in a domain with periodicity $[L_x, L_y] = [2\lambda_x, 2\lambda_y]$, wavy rolls ($WR$) with $[L_x, L_y] = [2\lambda_x, \lambda_y]$, knots ($KN$) with $[L_x, L_y] = [\lambda_x, \lambda_y]$, and transverse oscillations (TO) with $[L_x, L_y] = [12\lambda_x, 6\lambda_y]$. The grid size is scaled accordingly. Choosing all domains as integer multiples of the same minimal box ensures commensurable wavelengths and thus allows for potential bifurcation between invariant states.

The approach of combining direct numerical simulations from unstable laminar flow with Newton-Raphson iteration allows to determine all of the above invariant states. However, this approach fails in the case of the pattern emerging from the skewed varicose instability at $\gamma = 0°$ (RS19). There, the dynamics does not asymptotically approach or transiently visit an invariant state underlying the pattern, suggesting that no associated invariant state exists above thresholds. Therefore, we search for the bifurcating branch below critical parameters of the skewed varicose instability by taking the following steps. The bifurcating eigenmode that destabilizes x-aligned straight convection rolls at wavelength λ_y ($R_{\lambda 2}$) in a domain of periodicity $[L_x, L_y] = [4\lambda_x, 4\lambda_y]$ is computed using Arnoldi iteration. Different finite amplitude perturbations of $R_{\lambda 2}$ with the bifurcating eigenmode are integrated forward in time to generate a large set of initial states for brute-force Newton-Raphson iterations below critical threshold parameters of the instability. Using this approach we identified an unstable equilibrium state that underlies the skewed varicose pattern and is described in Section 5.3.1. Consequently, invariant states in thermal convection cannot be assumed to generically exist above critical control parameters, but may also be found below thresholds suggesting a backward bifurcation.

Whether bifurcations are forward or backward in control parameters, is studied in the present bifurcation analysis.

5.2.3 Bifurcation analysis

The general approach of our bifurcation analysis is to compute bifurcation branches of invariant states in ILC and to characterize the resulting bifurcation diagrams. Branches of invariant states are computed using continuation methods to solve (5.7) under a changing control parameter μ (Dijkstra et al., 2014). There are two iterative predictor-corrector schemes for numerical continuation implemented in *Channelflow-ILC*. The control parameter continuation uses quadratic extrapolation to predict a state vector $\boldsymbol{x}$ for some value of μ which is fixed in the following Newton-Raphson iteration, the corrector step. The pseudo-arclength continuation does not prescribe μ in the corrector step but solves for μ as additional unknown entry in state vector $\boldsymbol{x}$ under an additional arclength constraint. Depending on the shape of the continued state branch, one continuation scheme might outperform the other (Gibson et al., 2019). Continuation of periodic orbits with long periods may require a multi-shooting method to converge (Gibson et al., 2019). Where invariant states have discrete reflection symmetries π_y or π_{xz} (5.8-5.9) we impose reflections during numerical continuation because they fix the spatial phase of the flow relative to the x- or y-coordinates. If the spatial phase is free, states may translate under numerical continuation reducing the computational efficiency. Since both continuation schemes solve (5.7) and the algorithmic details do not change the resulting bifurcation diagrams, we use the better performing scheme for each branch.

Continuations of the invariant states cover *a priori* chosen sections across the considered parameter space at Pr = 1.07 covering $0^\circ \leq \gamma < 120^\circ$ and $0 \leq \epsilon \leq 2$, as illustrated by thin grey lines in Figure 5.2. The control parameter $\epsilon = (\mathrm{Ra} - \mathrm{Ra}_c(\gamma))/\mathrm{Ra}_c(\gamma)$ indicates Ra normalised by a critical threshold function $\mathrm{Ra}_c(\gamma)$ which here, approximates the true critical control parameters $\mathrm{Ra}'_c(\gamma)$ of the primary instability in ILC (see Figure 2a in RS19). Thus, the primary instability defining the onset of convection is always at $\epsilon \approx 0$, independent of the inclination angle. Critical thresholds of bifurcation points are denoted as ϵ_c. To continue invariant states in γ at ϵ = const., also Ra needs to be adjusted accounting for variations in $\mathrm{Ra}_c(\gamma)$. Since the true critical $\mathrm{Ra}'_c(\gamma)$ cannot be expressed in closed-form, we define the function

$$\mathrm{Ra}_c(\gamma \leq \gamma_{c2}) = \frac{\mathrm{Ra}'_c(\gamma = 0^\circ)}{\cos(\gamma)} \tag{5.12}$$

$$\mathrm{Ra}_c(\gamma > \gamma_{c2}) = \frac{1}{41}(\gamma - \gamma_{c2})^3 + \frac{5}{14}(\gamma - \gamma_{c2})^2 + 29(\gamma - \gamma_{c2}) + \mathrm{Ra}'_{c2} \tag{5.13}$$

to keep $\epsilon = (\mathrm{Ra} - \mathrm{Ra}_c(\gamma))/\mathrm{Ra}_c(\gamma)$ = const. under γ-continuations. The definition of function $\mathrm{Ra}_c(\gamma)$ has three precise coefficients, namely the critical parameters for horizontal convection $\mathrm{Ra}'_c(\gamma = 0^\circ) = 1707.76$ (Busse, 1978a) and the codimension-2 point $[\gamma_{c2}, \mathrm{Ra}'_{c2}] = [77.7567^\circ, 8053.1]$.

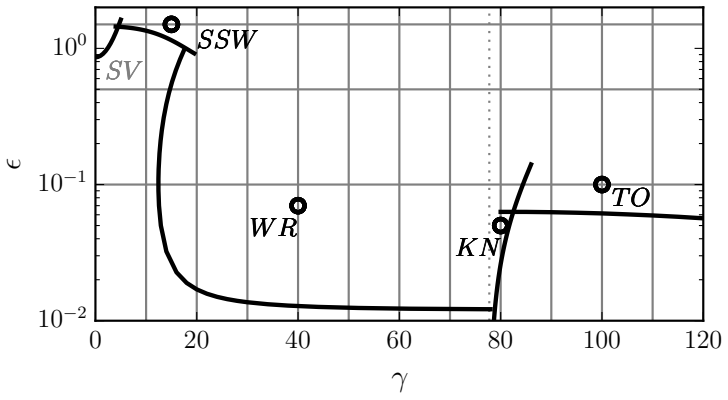

Figure 5.2 – The considered parameter space is spanned by inclination angle γ and $\epsilon = (\mathrm{Ra} - \mathrm{Ra}_c)/\mathrm{Ra}_c$ at Pr = 1.07. The parameters at which invariant states have been identified in RS19 (Figure 5.1) are marked by circles. The invariant state underlying skewed varicose pattern (*SV*) is not described in RS19 but identified in this work. Thick solid lines indicate critical thresholds in control parameters of the five secondary instabilities determined by Subramanian et al. (2016). Bifurcations between invariant states are computed along 15 sections across the parameter space (grey solid lines). The thin grey dotted line marks the inclination angle of the codimension-2 point at $\gamma_{c2} = 77.7567°$.

Relation (5.12), already found by Gershuni and Zhukhovitskii (1969), is a geometric consequence of the linear laminar temperature profile. Polynomial (5.13) is a least-square-fit of the empirical critical thresholds for $\gamma_{c2} < \gamma < 120°$ reported in Subramanian et al. (2016), and is an approximation of the true $\mathrm{Ra}'_c(\gamma) \approx \mathrm{Ra}_c(\gamma)$. The purpose of defining $\mathrm{Ra}_c(\gamma)$ in (5.12-5.13) is not to most accurately capture the true $\mathrm{Ra}'_c(\gamma)$ but to provide a closed-form function for converting values between Ra and ϵ. The conversion allows γ-continuations at ϵ = const. and a comparison of the present results with other work reported in terms of a similar ϵ', based on the empirically determined primary instabilities.

Linear stability analysis of invariant states is performed at selected points along continued branches. Under continuation, we consider invariant states in their minimal periodic domain capturing only one spatial period of the pattern. In order to compare the dynamical stability between different invariant states, Arnoldi iterations must be performed in identical symmetry subspaces. This implies using the same periodic domains and imposing the same discrete symmetries for all considered states. Wherever we compute the dynamical stability along selected bifurcation branches, we specifically choose and report the symmetry subspace for the full branch.

Many bifurcation types of vector fields are known (e.g. Guckenheimer and Holmes, 1983). The most common bifurcations we encounter in ILC are pitchfork bifurcations, Hopf bifurcations,

saddle-node bifurcation and mutual annhilation of two periodic orbits, all of which are also well-known bifurcations in ordinary differential equations (e.g. Schaeffer and Cain, 2016). The two latter types we simply refer to as 'folds'. If bifurcations are not one of these four common types, we provide explicit references that discuss the bifurcation type in detail, as such discussions would be beyond the scope of the present work. When discussing symmetry-breaking bifurcations, the classification into supercritical/subcritical bifurcations refers to a 'more stable'/'less stable' bifurcating branch in comparison to the stability of the coexisting parent branch (Tuckerman and Barkley, 1990). The orientation of symmetry-breaking bifurcations along a control parameter μ is given specifically as μ-forward or μ-backward.

5.3 Results

We first provide an overview of the results from the bifurcation analysis. Considering twelve sections at constant γ and three sections at $\epsilon = \text{const.}$ (Figure 5.2), we present 15 bifurcation diagrams here in Figures 5.3 and 5.4. A complete analysis of all branches in these diagrams is beyond the scope of this chapter. Instead in this section, we first summarise the bifurcation diagrams and then focus on selected state branches covering the control parameters where spatio-temporally complex convection patterns are observed and temporal dynamics between invariant states has been studied (RS19). We specifically discuss the branches that bifurcate from straight convection rolls via the five secondary instabilities that were identified by Subramanian et al. (2016). These are, skewed-varicose instability, longitudinal subharmonic oscillatory instability, wavy roll instability, knot instability and transverse oscillatory instability. Branches of equilibrium and travelling wave states are plotted in terms of the norm of the temperature fluctuations,

$$||\theta||_2 = \left(\frac{1}{L_x L_y} \int_0^{L_x} \int_0^{L_y} \int_{-0.5}^{0.5} \theta^2(x,y,z,t_\pm)\, dx\, dy\, dz \right)^{1/2}, \tag{5.14}$$

as a function of the bifurcation parameter. Periodic orbits are illustrated by a pair of branches indicating the minimum and maximum of $||\theta||_2$ over one orbit period, at instances $t_\pm$. Bifurcation branches are labeled inside the diagram with the name of the invariant state. We recommend reading each diagram panel by first identifying the branches of LR and/or TR. In most cases, LR or TR have the largest $||\theta||_2$ and tertiary branches bifurcate to lower $||\theta||_2$. See Figure 5.3 for bifurcations while varying ϵ and Figure 5.4 for bifurcations while varying γ.

The ϵ-bifurcations at fixed γ, confirm the common observation that LR and TR always bifurcate in supercritical, ϵ-forward pitchfork bifurcations from the laminar base state. At $\gamma = 0$, longitudinal and transverse rolls are related via symmetries, and we refer to both of them as R_λ, where the subscript indicates the wavelength of the roll pattern. At $0 < \gamma \leq 20^\circ$, branches

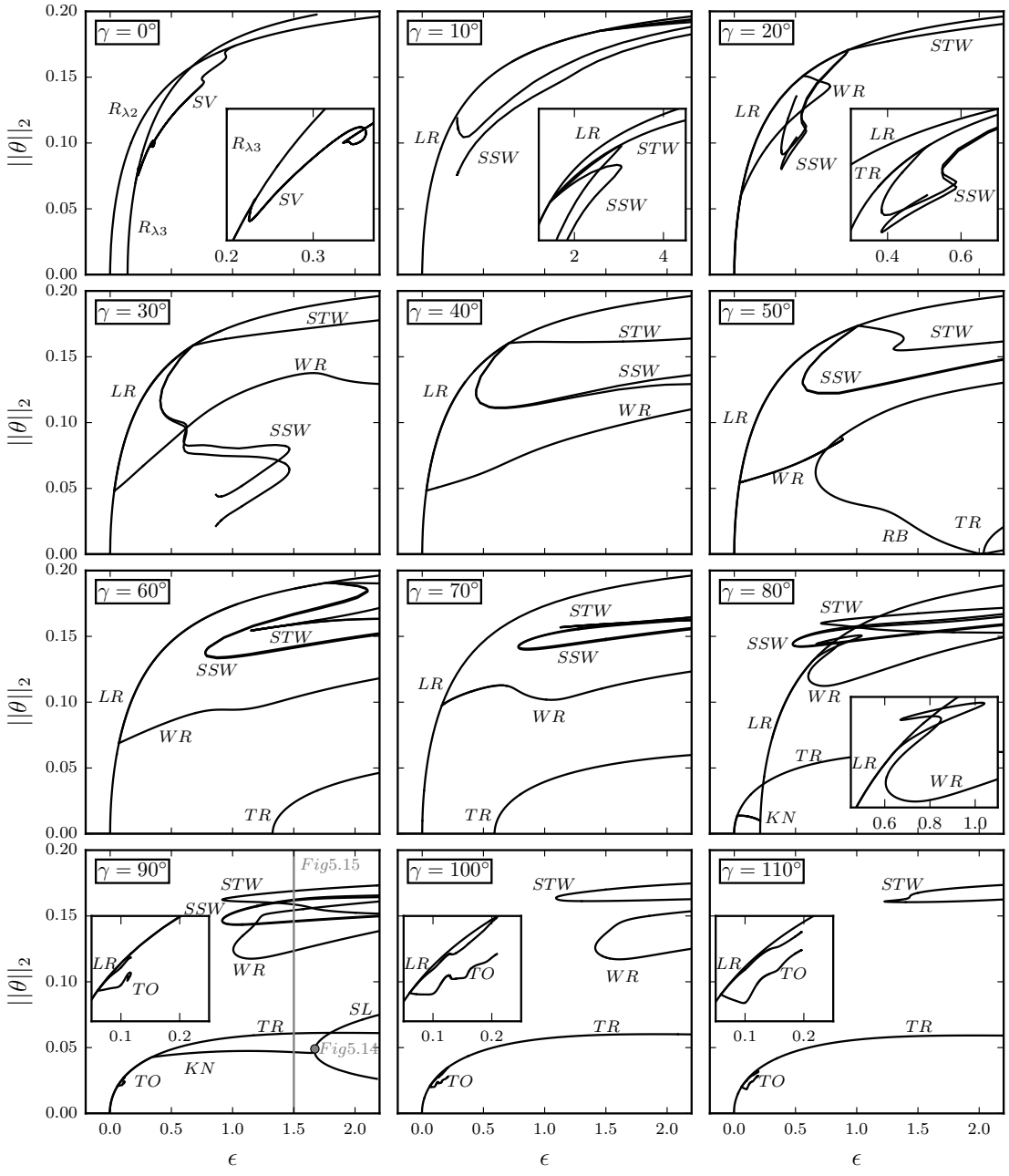

Figure 5.3 – Summary of all bifurcation branches of invariant states continued in ϵ at constant $\gamma \in \{0°, 10°, 20°, ..., 110°\}$. Each branch is plotted in terms of $||\theta||_2$ (Equation 5.14) and is labeled by the name of the invariant state to which the branch belongs. Insets enlarge or isolate features of the bifurcations diagrams. All panels are labeled by the angle of inclination and share the same axes. TR is left out in panels $\gamma \in \{0°, 10°, 20°\}$ to avoid clutter. In panel $\gamma = 90°$, the grey vertical line crosses the bifurcation branches where invariant states are shown in Figure 15 and discussed in Section 5.7. KN at $\gamma = 90°$ connect to equilibrium state SL showing a subharmonic lambda pattern (Figure 14), discussed in Section 5.6.

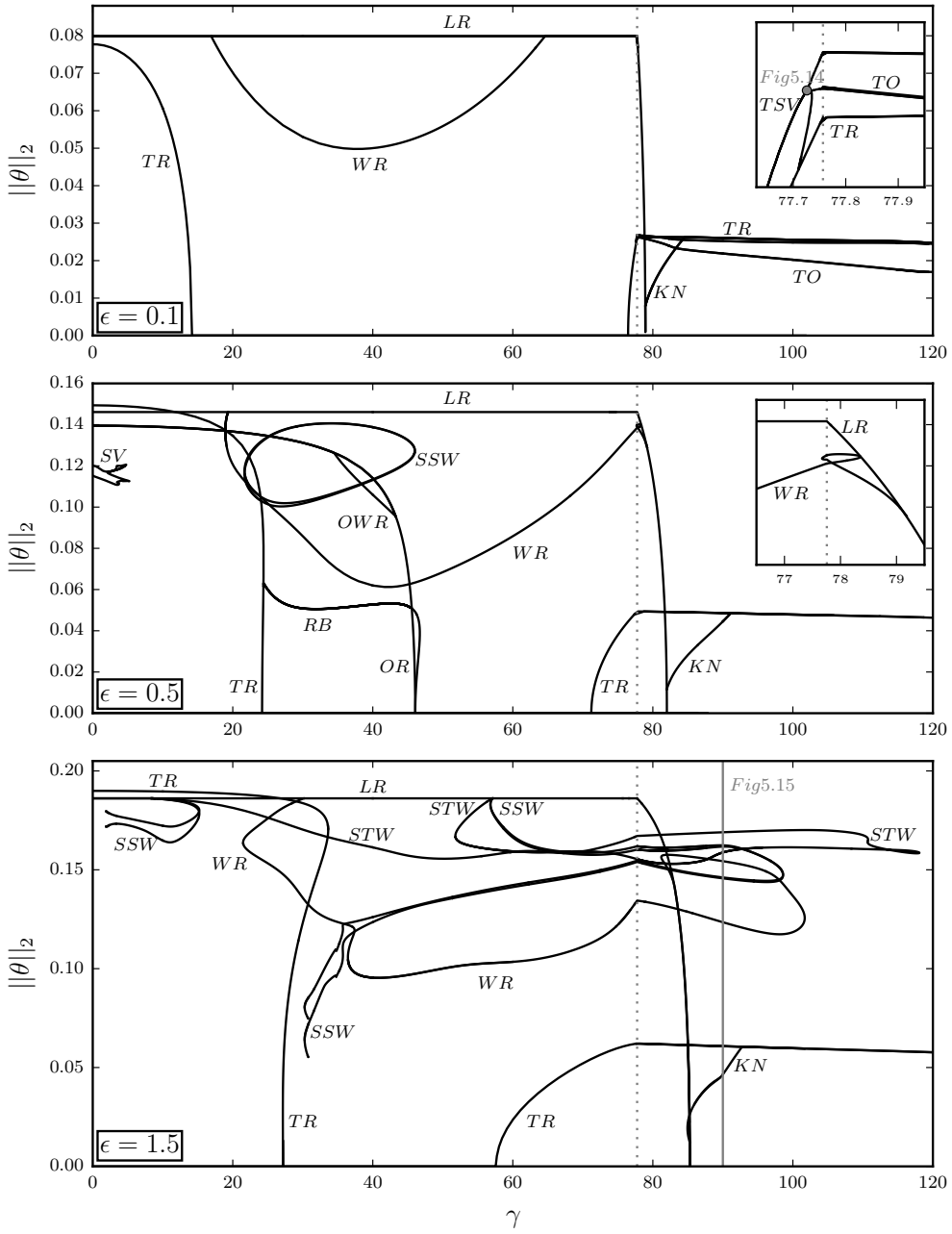

Figure 5.4 – Summary of all bifurcation branches of invariant states continued in γ at constant $\epsilon \in \{0.1, 0.5, 1.5\}$. Each branch is plotted in terms of $||\theta||_2$ (Equation 5.14) and is labeled by the name of the invariant state to which the branch belongs. All panels are labeled by the ϵ value and share the same axes. Grey dotted lines mark the inclination angle of the codimension-2 point. Insets enlarge features of the bifurcations diagrams around the inclination angle of the codimension-2 point. In panel $\epsilon = 1.5$, the grey vertical line crosses the bifurcation branches where invariant states are shown in Figure 15 and discussed in Section 5.7. TO at $\epsilon = 0.1$ (inset) connect to equilibrium state TSV showing a transverse subharmonic varicose pattern (Figure 14), discussed in Section 5.6.

of LR and TR still are very close to each other. Only the LR-branches, defining the onset of convection, are plotted to avoid clutter. At $30° \leq \gamma \leq 40°$, TR bifurcates outside the considered interval of $0 \leq \epsilon \leq 2$. At $\gamma \geq 50°$, the branches of TR and LR bifurcate again closer to each other. The branches however differ significantly in amplitude and functional form. TR-branches show non-monotonic behaviour in $||\theta||_2$, e.g., a local maximum at $\epsilon = 1.8$ and $\gamma = 90°$. Non-monotonic branches of TR were also computed in vertical convection at Pr = 0.71 (Mizushima and Tanaka, 2002b,a).

LR-branches monotonically increase in $||\theta||_2$ with ϵ. For further increasing ϵ, LR appears to eventually approach the same ϵ-scaling law as reported for invariant states underlying straight convection rolls in horizontal convection at $\gamma = 0°$ (Waleffe et al., 2015). The large-ϵ behaviour is observed for all γ. The observation that a scaling law of straight convection rolls at $\gamma = 0°$ also describes LR-branches at $\gamma \neq 0°$ suggests a particular scaling invariance of the nonlinear Oberbeck-Boussinesq equations under changes of inclination angle γ. This scaling invariance is discussed in the following paragraph.

At fixed ϵ, all γ-continuations of LR result in horizontal lines in $||\theta||_2$ for $0° \leq \gamma \leq \gamma_{c2}$ (Figure 5.4). These horizontal lines are a remarkable feature of the bifurcation diagrams and can be explained as a consequence of a scaling invariance of the nonlinear Oberbeck-Boussinesq equations, that holds for patterns or states that are steady in time and uniform in x, like LR: For $\gamma < \gamma_{c2}$, keeping $\epsilon = \text{const.}$ implies $\text{Ra} \sim 1/\cos(\gamma)$ (5.12). The laminar solution thus scales with γ as $U_0 \sim \sin(\gamma)/\sqrt{\cos(\gamma)}$ and $\mathcal{T}_0 \sim 1$. Here, Pr is constant. Inserting the base-fluctuation decomposition $\boldsymbol{U} = \boldsymbol{U}_0 + \boldsymbol{u}$ and $\mathcal{T} = \mathcal{T}_0 + \theta$ into (5.1-5.3) and assuming $\partial_t[\boldsymbol{u}, \theta] = 0$ and $\partial_x[\boldsymbol{u}, \theta] = 0$ for steady stripe/roll states, the governing equations for each component scale with a global γ-dependent factor, provided that temperature and velocity fluctuations scale as $u(y,z) \sim \sin(\gamma)/\sqrt{\cos(\gamma)}$, $v(y,z) \sim w(y,z) \sim \sqrt{\cos(\gamma)}$, and $\theta(y,z) \sim 1$:

$$
\begin{aligned}
u: \quad & v\partial_y u + w\partial_z(u + U_0(z)) &&= -\partial_x p + (\text{Pr}/\text{Ra})^{1/2}\nabla^2 u + \sin(\gamma)\theta && \sim \sin(\gamma) && (5.15)\\
v: \quad & v\partial_y v + w\partial_z v &&= -\partial_y p + (\text{Pr}/\text{Ra})^{1/2}\nabla^2 v && \sim \cos(\gamma) && (5.16)\\
w: \quad & v\partial_y w + w\partial_z w &&= -\partial_z p + (\text{Pr}/\text{Ra})^{1/2}\nabla^2 w + \cos(\gamma)\theta && \sim \cos(\gamma) && (5.17)\\
\theta: \quad & v\partial_y \theta + w\partial_z(\theta + \mathcal{T}_0(z)) &&= (\text{PrRa})^{-1/2}\nabla^2\theta && \sim \sqrt{\cos(\gamma)} && (5.18)\\
c: \quad & \partial_y v + \partial_z w &&= 0 && \sim \sqrt{\cos(\gamma)} && (5.19)
\end{aligned}
$$

This scaling implies that any equilibrium at one value of γ corresponds to a whole family of equilibria for $0° \leq \gamma \leq 90°$. The temperature scaling $\theta(y,z) \sim 1$ directly implies that $||\theta||_2$ of LR remains invariant under changes in γ with $\epsilon = \text{const.}$ This leads to self-similar curves under ϵ-continuation at fixed γ (Figure 5.3) and horizontal lines under γ-continuation at fixed ϵ (Figure 5.4). Moreover, any x-uniform and steady invariant state for $0 < \gamma \leq 90°$ corresponds to a specific invariant state in the horizontal Rayleigh-Bénard case at $\gamma = 0°$. A similar relation has previously been reported for the infinite Pr limit only (Clever, 1973). The scaling relation

provided here is valid for all Pr and a property of the full nonlinear Oberbeck-Boussinesq equations.

In the limit of a vertical gap ($\gamma \to 90°$), the $\cos^{-1}(\gamma)$-scaling implies diverging Ra. In this limit, the amplitude of the fixed $u(y,z)$-profile diverges and the cross-flow components vanish, $v, w \to 0$. The temperature field $\theta(y,z)$ remains fixed. Consequently in a vertical gap, hot and cold streamwise jets without cross flow and diverging streamwise velocity amplitude are invariant states in the Ra $\to \infty$ limit. Any temperature field of LR found at $\gamma < 90°$ is a valid temperature field for these jets at infinite Ra.

The subsequent sections discuss selected bifurcation diagrams covering the parameters where temporal dynamics between invariant states has been studied (RS19). We do not systematically explain the bifurcations at all control parameters but rather highlight important features of the bifurcations at selected control parameters. In each section we summarise key features of the bifurcation structure and relate those to observed spatio-temporally complex dynamics of the flow. The sections are ordered by increasing values of the angle of inclination.

5.3.1 Skewed varicose state - subcritical connector of bistable rolls

The skewed varicose instability of Rayleigh-Bénard convection, first found as spatially periodic instability at Pr = 7 (Busse and Clever, 1979), is experimentally observed to trigger a spatially localized transient pattern at Pr = 1.07 with very subtle varicose features (Bodenschatz et al., 2000, Figure 7). This section reports on a bifurcation from straight convection rolls to an equilibrium state capturing the observed skewed varicose pattern in a periodic domain. The bifurcating branch is subcritical, exists only below ϵ_c of the skewed varicose instability, and connects two bistable straight convection rolls at different wavelengths and orientations. The subcritical coexistence of the skewed varicose equilibrium with bistable straight convection rolls may explain the spatial localization of the transiently observed pattern.

Bifurcation branch of skewed varicose states

When convection patterns in experiments or numerical simulations exhibit complex dynamics, we expect the existence of invariant states underlying the pattern dynamics. For the pattern dynamics emerging from the skewed varicose instability of straight convection rolls R_λ at $\gamma = 0°$ we however do not find invariant states at the control parameters where the dynamics is observed. Direct numerical simulations in a minimal periodic domain can reproduce the transient dynamics of the skewed varicose pattern, but previous analysis of the temporal dynamics did not yield an underlying invariant state (RS19).

An equilibrium state resembling the observed skewed varicose pattern (SV) is identified below ϵ_c of the skewed varicose instability, as described in Section 5.2.2. Numerical continuation of SV reveals a subcritical ϵ-backward pitchfork bifurcation from $R_{\lambda 2}$ at $\epsilon_c = 1.019$. The bifurcation breaks the continuous translation symmetry $\tau(a_x, 0)$ of straight convection rolls $R_{\lambda 2}$. Here we consider the rolls to be x-aligned and periodic with wavelength λ_y. The bifurcating eigenmode shows a skewed three-dimensional flow structure. The bifurcating equilibrium SV is $[4\lambda_x, 4\lambda_y]$-periodic and invariant under transformations of the symmetry group $S_{sv} = \langle \pi_{xyz}, \tau(0.25, 0.25) \rangle$. From the bifurcation point, the SV-branch continues down in ϵ, undergoes a sequence of folds, and terminates at $\epsilon = 0.206$ in a bifurcation from straight convection rolls $R_{\lambda 3}$ with wavelength $\lambda = 2.8$ (panel $\gamma = 0°$ in Figure 5.3). Thus, the equilibrium state SV connects two equilibrium states representing straight convection rolls at different wavelengths. SV exists only below the critical threshold parameter ϵ_c. The pure subcritical existence of SV explains why no temporal transition to an underlying invariant state at $\epsilon > \epsilon_c$ has been found in RS19.

Since the bifurcation branches are very cluttered at $\gamma = 0°$ in Figure 5.3, we reproduce the bifurcation diagram schematically. In Figure 5.5, the bifurcation branches are plotted in terms of their approximate dominating pattern wavelength λ_p as a function of ϵ. Along the SV-branch, convection rolls develop skewed relative orientations (Figure 5.5b) until the rolls pinch-off and reconnect at an oblique orientation (Figure 5.5c). At the bifurcation point, $R_{\lambda 3}$ is rotated by 74.6° against the orientation of $R_{\lambda 2}$ (Figure 5.5a,c). To link these two different roll orientations, the continuous deformations in the skewed varicose pattern skip two instances for potential reconnection to straight rolls with orientations in between. Each of the potential reconnection points corresponds to a pair of folds along the SV-branch. Here, three pairs of folds are observed but this number is specific to the chosen domain size. In between the first two folds at $0.94 < \epsilon < 0.95$, the SV-branch is bistable with $R_{\lambda 2}$ and $R_{\lambda 3}$ in a symmetry subspace of S_{sv}. The stability of all branches is indicated by the linestyle. Overall, the bifurcation diagram indicates coexistence of stable (or weakly unstable) SV with stable $R_{\lambda 2}$ and $R_{\lambda 3}$ over a range of ϵ. The coexistence of invariant states suggests spatial coexistence of straight convection rolls and the skewed varicose patterns.

The convection pattern along the SV-branch at $\epsilon < \epsilon_c$ may be compared to the convection pattern observed transiently in time along a simulated transition at $\epsilon = 1.05 > \epsilon_c$ (dashed line in Figure 5.5d and Section 4.3 in RS19). The midplane temperature contours of SV along its subcritical bifurcation branch partly match the transient patterns along the supercritical temporal transition. We find matching patterns at initial instances in time when straight convection rolls are observed (Figure 5.5c,g), and at intermediate time when the transient pattern of skewed varicose pattern emerges (Figure 5.5b,f). Thus, SV indeed captures the observed transient pattern triggered by the skewed varicose instability, but the comparison is for different ϵ. This observation raises the question how the transient temporal dynamics

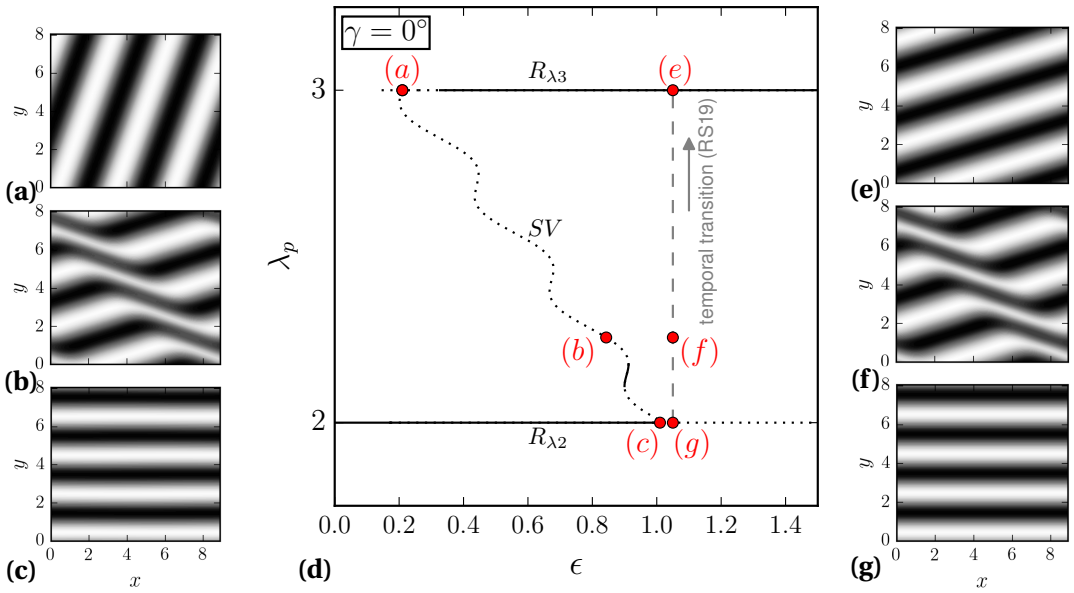

Figure 5.5 – For $\gamma = 0°$ (Rayleigh-Bénard), the subcritical bifurcation of the skewed varicose state (SV) connects two equilibrium states of straight convection rolls at different wavelength and orientation. Midplane temperature fields of equilibrium states **(a-c)** are chosen along the SV-branch, plotted here in a schematic bifurcation diagram in terms of an approximate dominating pattern wavelength λ_p over ϵ in **(d)**. A simulated temporal transition from unstable $R_{\lambda 2}$ to stable $R_{\lambda 3}$ at supercritical $\epsilon > \epsilon_c$ (RS19) is indicated by the dashed line. Snapshots from the temporal transition **(g,f,e)** show matching skewed varicose patterns between the equilibrium state **(b)** for $\epsilon < \epsilon_c$ and the transient state **(f)** at $\epsilon > \epsilon_c$. The orientation of $R_{\lambda 3}$ differs between the terminating bifurcation branch at $\epsilon = 0.2$ **(a)** and the attracted temporal dynamics at $\epsilon = 1.05$ **(e)**.

observed above critical thresholds can be related to an equilibrium state existing only below critical thresholds.

5.3.2 Subharmonic oscillations - standing and traveling waves

Subharmonic oscillations are observed as standing wave patterns emerging in spatially localized patches that may travel across extended domains (Daniels et al., 2000; Subramanian et al., 2016). Here, the periodic orbit SSW, underlying the standing wave, is found to coexist with a traveling wave state. Standing and traveling wave states always bifurcate together in equivariant Hopf bifurcations. Both, standing and traveling waves capture observed patterns

of spatially subharmonic oscillations. The existence of a traveling wave state explains the observed traveling dynamics of the pattern.

Equivariant Hopf bifurcation from longitudinal rolls

Starting from the periodic orbit SSW, found at $[\gamma,\epsilon] = [15°, 1.5]$ in RS19, we continue the branch down in γ. The SSW-branch bifurcates from LR at $[\gamma_c,\epsilon_c] = [8.5°, 1.5]$. This bifurcation is a γ-forward, supercritical Hopf bifurcation with a critical orbit period of $T_{\mathrm{ssw}} = 80.2$. The bifurcation corresponds to four complex eigenvalues crossing the imaginary axis at $\omega_i = \pm 0.078$ controlling the period $T_{\mathrm{ssw}} = 2\pi/|\omega_i|$. The Hopf bifurcation to SSW accounts only for one pair of complex neutral eigenmodes. The other pair gives rise to a traveling wave state that we term longitudinal subharmonic wave (STW) with a critical phase speed of $c = L_x/T_{\mathrm{lsw}} = 0.055$ where $T_{\mathrm{lsw}} = T_{\mathrm{ssw}}$. Both invariant states, the π_y-symmetric STW and the π_{xyz}-symmetric SSW (shown in left panels of Fig. 5.6(a) and (b)), each have a counter-propagating sibling state obtained via π_{xz}-transformation. Both invariant states capture a subharmonic oscillatory convection pattern invariant under $\tau(0.5, 0.5)$. An equilibrium pattern very close to STW can be observed in spatially forced horizontal convection (Weiss et al., 2012). STW also resembles the subharmonic "sinucose" state arising from an instability of longitudinal streaks in pure shear flow (Waleffe, 1997).

At parameters where SSW and STW bifurcate locally from LR, they share the same bifurcation point (see panels for $10° \leq \gamma \leq 60°$ in Figure 5.3. This robust feature in the bifurcation diagram is a consequence of equivariant Hopf bifurcations. It is known that Hopf bifurcations that break the $O(2)$-symmetry of a flow must result in two branches originating from the bifurcation: A standing wave branch and a traveling wave branch (Knobloch, 1986). At most one of the two branches is stable. In the present case, the Hopf bifurcation breaks the $O(2)_x$-symmetry of LR. The bifurcation at $[\gamma_c,\epsilon_c] = [8.5°, 1.5]$ (inset panel in Figure 5.6c) has both the branches bifurcating supercritically. SSW is initially stable and STW is unstable. This corresponds to one specific of six discussed cases in Knobloch (1986). However, here the bifurcation is secondary. While in Knobloch (1986), bifurcations from a non-patterned two-dimensional primary state with a spatial $O(2)$-symmetry are discussed, here, the bifurcating secondary equilibrium state LR is a three-dimensional state that is symmetric under transformations of $O(2) \times Z_2$. The additional third dimension and the additional reflection symmetry do not affect the conditions necessary for equivariant Hopf bifurcations (Knobloch, 1986).

Continuations of SSW and STW in γ reveal their existence over a large range of inclination angles γ, including $\gamma > 90°$ where their parent state LR does not exist anymore (Figure 5.6c). Over this range in γ, the orbit period of SSW and the propagation time $T_{\mathrm{lsw}} = L_x/c$ of STW with phase velocity c and $L_x = 2\lambda_x$ follow approximately the mean laminar advection time $L_x/\bar{U}_0$ (Figure 5.6d). While the state branch of STW at $\epsilon = 1.5$, shown as light grey line in Figure

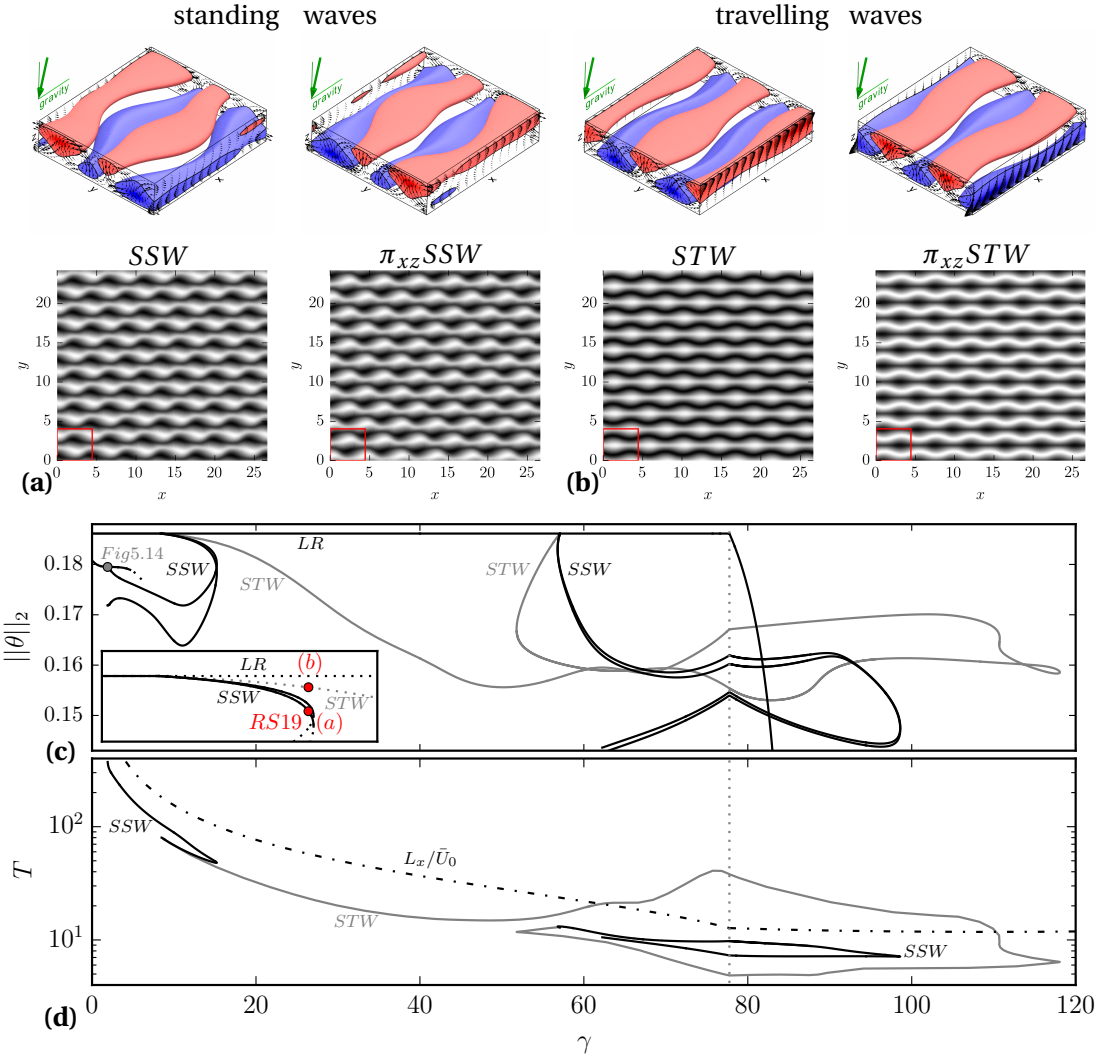

Figure 5.6 – Symmetry-related pairs of standing wave states SSW **(a)** and traveling wave states STW **(b)** bifurcate together in equivariant Hopf-bifurcations from LR. The pattern of SSW and STW is visualised by temperature contours in three and two dimensions (midplane). The bifurcation diagram in **(c)** shows the branches of SSW (black) and STW (grey) at $\epsilon = 1.5$. Other branches shown in Figure 5.4 for $\epsilon = 1.5$ are suppressed for clarity. The inset indicates stable (solid) and unstable (dotted) branches close to the bifurcation at $\gamma = 8.5°$ giving rise to the states in **(a)** and **(b)** at $\gamma = 15°$. 'RS19' labels the control parameter where temporal dynamics has been studied in RS19. Panel **(d)** illustrates how the orbit period T_{ssw} of SSW and the travel time T_{lsw} of STW across L_x approximately follow the mean advection time $L_x/\bar{U}_0$ of the laminar base flow B (dashed-dotted line). Note the 'hydrolic jumps' where phase and advection velocity match at $\gamma = 65°$ and at $\gamma = 110°$ of the STW-branch.

5.6c, connects two Hopf bifurcations, one at small and one at large γ, the SSW branches at $\epsilon = 1.5$, shown as black lines in Figure 5.6c, originating from these two bifurcations remain disconnected. The branch bifurcating forward at $\gamma_c = 8.5°$ undergoes a fold at $\gamma = 15.2°$ (Figure 5.6c) explaining why no temporal state transition from LR to SSW was found at $\gamma = 17°$ in RS19. The fold destabilizes SSW and connects to a state branch reaching to subcritical parameters where LR is linearly stable. Similar folds occur under ϵ-continuations at $\gamma = 10°$ and $\gamma = 20°$. Beyond these folds, SSW state branches terminate and show 'loose ends' in the bifurcation diagrams. These terminations correspond to global bifurcations which we explain in the next subsection.

Global bifurcation to longitudinal subharmonic oscillations

The global bifurcation at $\gamma = 10°$ occurs at $\mathrm{Ra}_c = 2230.25$ ($\epsilon_c = 0.286$) where the pre-periodic orbit SSW, satisfying (5.7) with $\sigma_{\mathrm{ssw}} = \pi_y \tau(0.25, 0.25)$ and a pre-period of $T' = T/4$, collides with a heteroclinic cycle between two symmetry related saddle states TR and $\sigma_{\mathrm{ssw}} TR$ (Figure 5.7). At the global bifurcation point, the spectrum of eigenvalues of TR is computed in a symmetry subspace Σ_0 given by the $[2\lambda_x, 2\lambda_y]$-periodic domain with imposed symmetries of SSW, namely $\tau(0.5, 0.5)$ and π_{xyz}. The five leading eigenvalues are real and read $[\omega_1, \omega_2, \omega_3, \omega_4, \omega_5]$ $= [0.048, 0.045, -0.090, -0.120, -0.138]$. The midplane temperature contours of the associated eigenmodes $[\boldsymbol{e}_1^u, \boldsymbol{e}_2^u, \boldsymbol{e}_3^s \boldsymbol{e}_4^s, \boldsymbol{e}_5^s]$ are given in Figure 5.7h. Eigenvalues and eigenmodes of TR do not change significantly when Ra crosses Ra_c. In contrast to the heteroclinic cycle discussed in RS19, where each of the two symmetry related instances of OWR has a single unstable eigenmode, the present cycle connects symmetry related instances of TR with two unstable eigenmodes each. Perturbations of TR with the eigenmode $\boldsymbol{e}_1^u$ trigger a state transition $TR \to \sigma_{\mathrm{ssw}} TR$ while perturbations with $\boldsymbol{e}_2^u$ lead to LR which is dynamically stable in Σ_0 at these control parameters. The symmetry relation between TR and $\sigma_{\mathrm{ssw}} TR$ guarantees that $\sigma_{\mathrm{ssw}} TR$ has the same eigenvalues as TR and symmetry related eigenmodes $\sigma_{\mathrm{ssw}}[\boldsymbol{e}_1^u, \boldsymbol{e}_2^u, \boldsymbol{e}_3^s, \boldsymbol{e}_4^s, \boldsymbol{e}_5^s]$ allowing for the returning transition $\sigma_{\mathrm{ssw}} TR \to TR$ to close the heteroclinic cycle.

Direct numerical simulations indicate that states close to the heteroclinic cycle are eventually attracted to LR. To show that this heteroclinic cycle is dynamically unstable but structurally stable, we identify two symmetry subspaces of Σ_0 in which either $TR \to \sigma_{\mathrm{ssw}} TR$ or $\sigma_{\mathrm{ssw}} TR \to TR$ exists as heteroclinic connection between an equilibrium with a single unstable eigenmode and a dynamically stable equilibrium. By doing so, the heteroclinic cycle is shown to satisfy all conditions of a structurally stable, or robust, heteroclinic cycle between two symmetry related equilibrium states (Krupa, 1997), also discussed in RS19. Subspace Σ_1 is given by imposing the symmetries in the group $\langle \pi_y, \pi_{xz}, \tau(0.5, 0.5) \rangle$ and contains the connection $TR \to \sigma_{\mathrm{ssw}} TR$. Of the five initially considered eigenmodes in Σ_0, TR in Σ_1 has still $[\boldsymbol{e}_1^u, \boldsymbol{e}_3^s, \boldsymbol{e}_5^s]$ and $\sigma_{\mathrm{ssw}} TR$ in Σ_1 has still $\sigma_{\mathrm{ssw}}[\boldsymbol{e}_4^s, \boldsymbol{e}_5^s]$. Subspace Σ_τ is given by imposing the symmetries in the group

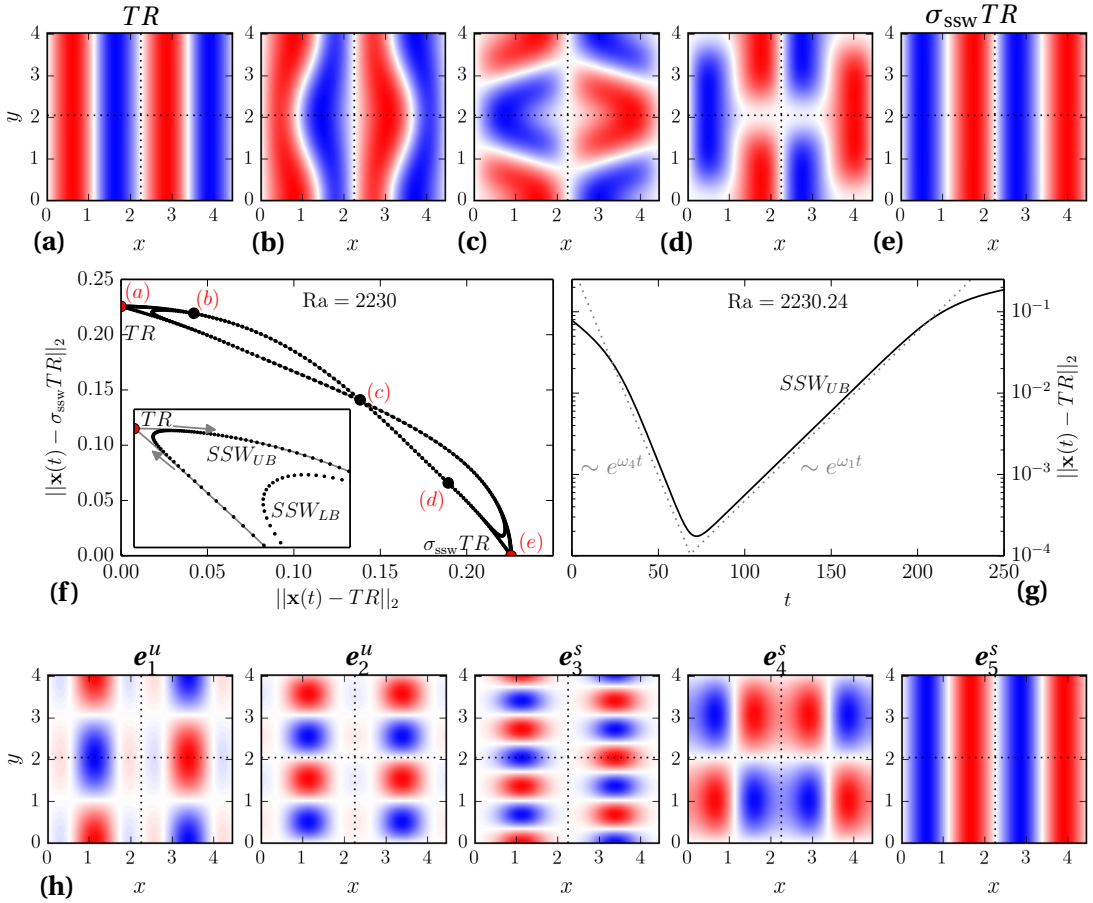

Figure 5.7 – The pre-periodic orbit SSW approaches a global bifurcation at $\gamma = 10°$ and $\mathrm{Ra}_c = 2230.25$ ($\epsilon_c = 0.286$) where it collides with a robust heteroclinic cyle between TR and the symmetry related equilibrium $\sigma_{ssw}TR$ with $\sigma_{\mathrm{ssw}} = \pi_y\tau(0.25, 0.25)$. **(a-e)** Sequence of midplane temperature contours along the dynamical connection $TR \rightarrow \sigma_{ssw}TR$ at $\mathrm{Ra} = 2230$. **(f)** State space projection of the lower (LB) and the upper branch (UB) of SSW (cf. Figure 5.8a). Inset enlarges the orbit trajectories (black dots) near TR and the heteroclinic cycle (grey lines). **(g)** L_2-distance of the SSW_{UB} orbit trajectory from TR at $\mathrm{Ra} = 2230.24$ very close to Ra_c. The dynamics of SSW_{UB} is exponential for most of the pre-period and governed by two eigenvalues of TR. **(h)** Midplane temperature contours of two unstable and three stable eigenmodes $\boldsymbol{e}_i^{u/s}$ of TR associated to the five leading eigenvalues $[\omega_1, \omega_2, \omega_3, \omega_4, \omega_5] = [0.048, 0.045, -0.090, -0.120, -0.138]$ of TR.

$\langle \pi_y\tau(0.5,0), \pi_{xz}\tau(0.5,0), \tau(0.5,0.5)\rangle$ and contains the connection $\sigma_{\text{ssw}}TR \to TR$. Of the five initially considered eigenmodes in Σ_0, $\sigma_{\text{ssw}}TR$ in Σ_τ has still $\sigma_{\text{ssw}}[\boldsymbol{e}_1^u, \boldsymbol{e}_3^s, \boldsymbol{e}_5^s]$ and TR in Σ_τ has still $[\boldsymbol{e}_4^s, \boldsymbol{e}_5^s]$. Using the classification of eigenvalues and associated stability theorem in Krupa and Melbourne (1995), we identify ω_1 as expanding, ω_2 as transverse, ω_4 as contracting and ω_5 as radial eigenvalue. Eigenvalue ω_3 exists in the same subspace as the expanding eigenvalue ω_1 and therefore does not affect the dynamical stability. Since $\min(-\omega_4, \omega_1 - \omega_2) \not> \omega_1$, the heteroclinic cycle is not asymptotically stable (Krupa and Melbourne, 1995, Theorem 2.7).

Before SSW disappears in the global bifurcation at Ra_c, the solution branch undergoes a fold at $\text{Ra} < \text{Ra}_c$ (Figure 5.8a). The existence of such a fold near a global bifurcation follows from the dynamical stability of the bifurcating periodic orbit relative to the dynamical stability of the heteroclinic cycle. To analyse the stability, we consider the linearised dynamics around the heteroclinic cycle $TR \to \sigma_{\text{ssw}}TR \to TR$ at Ra_c and obtain the following Poincaré map (see Bergeon and Knobloch, 2002, for a derivation)

$$\zeta_{i+1} = c\zeta_i^\rho + \mu, \quad \rho = -\frac{\omega_4}{\omega_1} = 2.51\,, \tag{5.20}$$

with constant $c > 0$ and control parameter $\mu \propto \text{Ra}_c - \text{Ra}$. Variable $\zeta_i \ll 1$ describes a local coordinate in a Poincaré section located at a distance $\varepsilon \ll 1$ from TR and defining a small perturbation around the state vector of TR as $\boldsymbol{x}' = \boldsymbol{x}_{TR} + \zeta_i \boldsymbol{e}_1^u + \varepsilon \boldsymbol{e}_4^s$. The heteroclinic cycle corresponds to $\zeta_i = 0$ and is reached at $\mu = 0$. The bifurcating periodic orbit is a fixed point $\bar{\zeta}$ of the map such that $\bar{\zeta} = c\bar{\zeta}^\rho + \mu$. Since $\rho > 1$, a nearby fixed point $\bar{\zeta}$ exists only for $\mu > 0$ and $\text{Ra} < \text{Ra}_c$, respectively. The graph in Figure 5.8b illustrates the map (5.20) and shows that the fixed point $\bar{\zeta}$ is dynamically stable. The stability of $\bar{\zeta}$ assumes that no additional transverse eigendirections are unstable. However, the symmetry subspace that contains SSW also contains $\boldsymbol{e}_2^u$ which must be taken into account. Thus, the above analysis predicts that SSW bifurcates with a single unstable eigendirection from the heteroclinic cyle, namely $\boldsymbol{e}_2^u$. Since SSW for $\text{Ra} > \text{Ra}_c$ has two unstable eigenmodes, the periodic orbit must undergo a fold prior to the global bifurcation to stabilise the extra unstable eigendirection. Such a fold also exists at $\gamma = 20^\circ$ (Figure 5.3) but further away from the global bifurcation. Note that unlike the global bifurcation discussed in Bergeon and Knobloch (2002), the present bifurcation involves first, a heteroclinic cycle between two symmetry related equilibrium states and second, a dynamically unstable periodic orbit such that the fold may have a stabilising effect.

The period of SSW must increases towards an infinite time period as the periodic orbit approaches the heteroclinic cycle. The map (5.20) suggests a scaling law for $T \sim \text{Ra}$ close to the global bifurcation. Since $\zeta \ll 1$ and $\rho > 1$, the periodic orbit is given by the approximation $\bar{\zeta} \approx \mu$. Over a full period of SSW, the orbit trajectory visits both TR and $\sigma_{\text{ssw}}TR$ twice. The time the orbit trajectory spends in the ε-neighborhood of TR or $\sigma_{\text{ssw}}TR$ dominates the entire orbit period T (Figure 5.7g) such that T satisfies the approximation $\bar{\zeta} \approx \varepsilon \exp(-\omega_1 T/4)$. Hence,

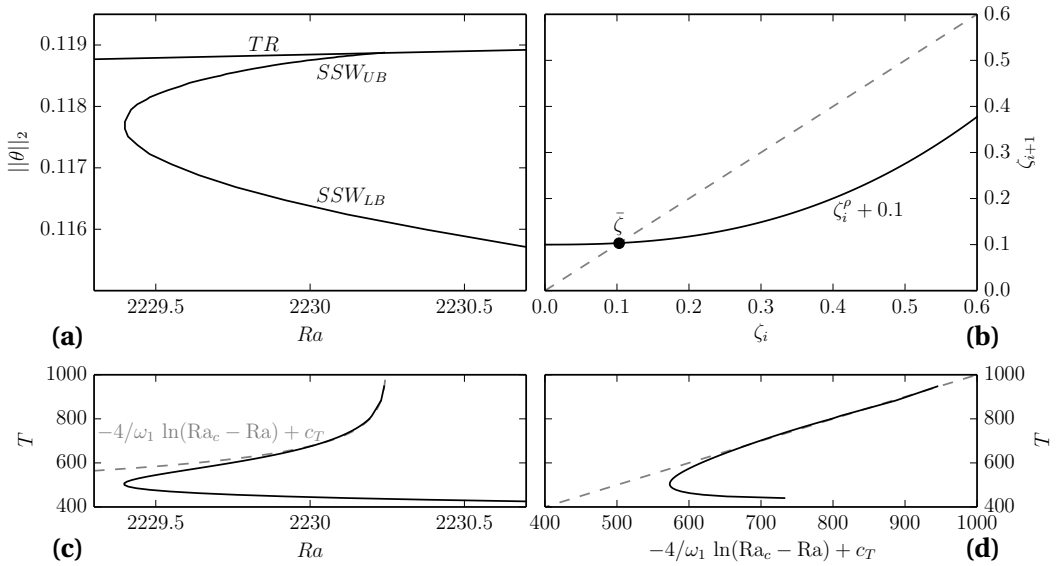

Figure 5.8 – Before SSW disappears in a global heteroclinic bifurcation at $\gamma = 10°$ and $\mathrm{Ra}_c = 2230.25$ ($\epsilon_c = 0.286$), the branch undergoes a saddle node bifurcation. **(a)** Enlarged bifurcation diagram showing the branch of SSW indicating the maximum $||\theta||_2$ over one cycle (cf. panel $\gamma = 10°$ in Figure 5.3). **(b)** Graphical representation of the linearised Poincaré map (5.20) for $\mu = 0.1$ around the heteroclinic cycle between symmetry related instances of TR. The fixed point $\bar{\zeta}$ is stable as the slope of the map at $\bar{\zeta}$ is less than one (dashed line). **(c,d)** Towards the global bifurcation, the orbit period of SSW approaches an infinite period according to a logarithmic scaling law shown as a function of Ra in **(c)** and for rescaled Ra in **(d)**. This law follows from the linearised map (5.20). Here, the constant is $c_T = 560$.

the period of SSW is expected to increase with $T \sim -4/\omega_1 \ln(\mathrm{Ra}_c - \mathrm{Ra})$. Using a mutli-shooting method, SSW is continued close to the global bifurcation. The increasing orbit period confirms the predicted scaling law (Figure 5.8c,d).

5.3.3 Wavy rolls with defects - connecting coexisting state branches

Convection patterns of wavy rolls are observed to quickly incorporate defects in large experimental domains (Daniels and Bodenschatz, 2002; Daniels et al., 2008). These defects may form interfaces between spatially coexisting wavy rolls at different orientations against the base flow. Here, a bifurcation and stability analysis of WR reveals four new equilibrium states, including obliquely oriented states and rolls with defects, that all coexist with WR for the same control parameters. The multiple states can give rise to the observed spatial coexistence.

Pitchfork bifurcations from longitudinal rolls

Equilibrium states WR emerge either in pitchfork bifurcations from LR at inclinations $20^\circ \leq \gamma \leq 80^\circ$ or in saddle-node bifurcations in the absence of LR at $90^\circ \leq \gamma \leq 100^\circ$. The fact that WR can exist without bifurcating from LR is known from thermal Couette flow (Clever and Busse, 1992). Almost all computed pitchfork bifurcations from LR to WR are either ϵ-forward or γ-backward. This observation holds even when the WR-branches develop additional folds, like in the bifurcation diagrams at $\gamma = 80^\circ$ or at $\epsilon = 1.5$. The only γ-forward bifurcation of WR from LR is observed at $\epsilon = 0.1$ (Figure 5.4, $\epsilon = 0.1$).

Additional bifurcations from wavy rolls

In most cases, WR-branches continue to large ϵ. This does not imply the absence of connections to other invariant states. When WR lose stability, additional bifurcations occur. We demonstrate the increasing number of invariant states and their patterns by following the higher order instabilities of WR at $\gamma = 40^\circ$. Arnoldi iteration for WR indicates the stability of the WR-branch up to $\epsilon = 0.256$ in a $[2\lambda_x, \lambda_y]$-periodic domain (Figure 5.9f). At this point, a subcritical pitchfork bifurcation breaks the π_{xz}- and π_y-symmetry and gives rise to an equilibrium state showing disconnected wavy rolls and named DWR. DWR is invariant under π_{xyz}. Following the DWR-branch from the pitchfork bifurcation, it undergoes a saddle-node bifurcation at $\epsilon = 0.254$, becomes bistable with WR and connects to an equilibrium state of oblique rolls (OR) that continues as a stable branch to larger values of ϵ. DWR represents stationary roll defects that along its branch breaks the topology of rolls in a double periodic domain (Figure 5.9b), and connects convection rolls at different orientations.

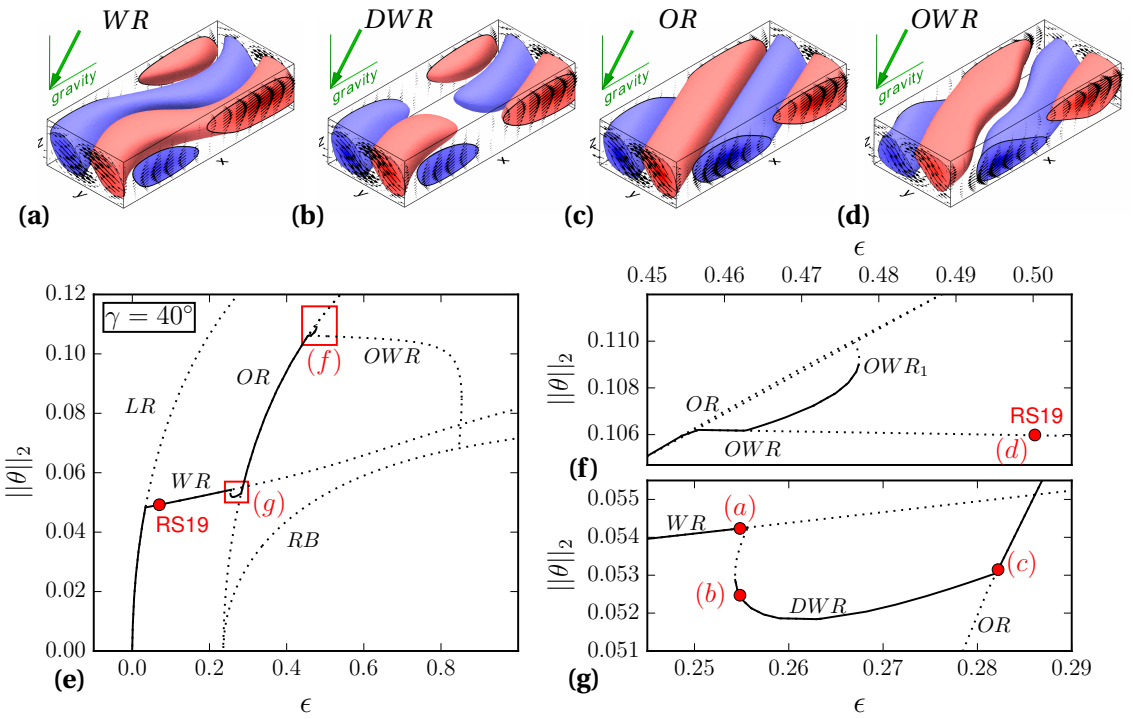

Figure 5.9 – Bifurcation sequence from wavy rolls to oblique wavy rolls **(a-d)**. Bifurcation diagram **(e)** shows how seven equilibrium states are connected over ϵ and indicates stable (solid) and unstable (dotted) parts of the branches. Dynamical stability is computed by Arnoldi iteration in a $(2\lambda_x, \lambda_y)$-periodic domain. Panel **(g)** enlarges the parameter region where DWR connects WR with OR. Panel **(f)** enlarges the parameter region where OWR_1 with pattern wavenumber $m = 1$ connects OWR with pattern wavenumber $m = 2$ with OR. 'RS19' labels the control parameter values at which temporal dynamics have been studied in RS19.

OR is a secondary state bifurcating from the laminar flow B. The oblique orientation at angle $\tan^{-1}(\lambda_y/2\lambda_x)$ against the laminar flow direction coincides with the diagonal of the $[2\lambda_x, \lambda_y]$-periodic domain (Figure 5.9c). OR is invariant under transformations of $S_{\mathrm{or}} = \langle \pi_{xyz}, \tau(a_x, \pm a_x) \rangle$ corresponding to an $O(2)$-symmetric state. The sign of continuous shift factor a_x differs between left (+) and right (−) oblique rolls, with $OR^l = \pi_y OR^r$. When OR becomes unstable, an ϵ-forward pitchfork bifurcation at $\epsilon = 0.456$ gives rise to stable oblique wavy rolls (OWR), see Figure 5.9d. As OR, OWR can have left or right orientation. The symmetry group of OWR is $S_{\mathrm{owr}} = \langle \pi_{xyz}, \tau(0.5, \pm 0.5) \rangle$. Equilibrium OWR with a wavy pattern of wavenumber $m = 2$ along the domain diagonal loses stability at $\epsilon = 0.463$ to an equilibrium OWR_1 with a pattern wavenumber of $m = 1$ and broken $\tau(0.5, \pm 0.5)$-symmetry. The branch of OWR_1 undergoes a saddle-node bifurcation at $\epsilon = 0.477$ and terminates on OR at $\epsilon = 0.476$ (Figure 5.9f). The small ϵ-range with $\Delta\epsilon = 0.476 - 0.456 = 0.02$ between the two symmetry-breaking bifurcations of OWR_1 with $m = 1$ and OWR with $m = 2$ from OR suggests a nearby codimension-2 point with spatial 1:2 resonance. When stable OWR_1 disappear in the saddle-node bifurcation, the temporal dynamics becomes attracted to a robust heteroclinic cycle between unstable instances of OWR that is discussed in RS19. The branch of OWR continues as unstable branch until it terminates at $\epsilon = 0.8$ on ribbons (RB), an unstable equilibrium state bifurcating together with OR from B in an equivariant pitchfork bifurcation (Figure 5.9e). The detailed properties of RB are discussed in the following section, but we already note that RB shows disconnected rolls or plumes, similar to DWR. Thus, we find two instances of bifurcation sequences that may be described as “straight rolls bifurcate to wavy rolls, wavy rolls bifurcate to disconnected rolls”. In one instance the sequence happens for longitudinal orientation and in the other instance for oblique orientation. The fact that all of the above states coexist with the WR branch at equal control parameters explains that all patterns represented by the invariant states can spatially coexist with wavy rolls in large domains.

5.3.4 Knots and ribbons - two different types of bimodal states

Observations of knot patterns exist in horizontal convection (Busse and Whitehead, 1974; Busse and Clever, 1979) and inclined layer convection (Daniels et al., 2000). They have been described as ‘bimodal convection’ in both cases. Here, the properties of equilibrium states for knots are compared to ribbons, a bimodal state identified in the previous section. A decomposition along their bifurcation branches implies that knots and ribbons are bimodal states that fundamentally differ in their bifurcation structure.

Bifurcations to states for knots and ribbons

KN at $\gamma = 80°$ bifurcates ϵ-forward from TR. At smaller $||\theta||_2$ than TR, KN continues without folds and terminates in ϵ-backward bifurcations from LR (Figure 5.3, $\gamma = 80°$). This bifurcation sequence requires $\gamma > \gamma_{c2}$ and was previously analysed using two-mode interactions (Fujimura and Kelly, 1993). At $\gamma = 90°$, LR does not exist at finite ϵ and the KN-branch terminates in a bifurcation from an equilibrium state we term subharmonic lambda plumes (SL) and briefly discuss in Section 5.6.

RB is an equilibrium state found via continuing the state branches of OWR and WR that terminate in ϵ-bifurcations from RB at $\gamma = 40°$ and $\gamma = 50°$, respectively (Figure 5.3). RB is invariant under transformations of $S_{\mathrm{rb}} = \langle \pi_y, \pi_{xz}, \tau(0.5, 0.5) \rangle$. Neither experiments nor simulations of ILC observe the pattern of RB as dynamically stable pattern at the considered parameters. However, we refer to experimental observations of "ribbons" in Taylor-Couette flow (Tagg et al., 1989). Ribbons in Taylor-Couette flow are analogous to ribbons in ILC. In Taylor-Couette flow, they bifurcate together with oblique spirals (Chossat and Iooss, 1994) and are connected via oblique wavy cross-spirals (Pinter et al., 2006), two states that are comparable to OR and OWR in ILC. As in the Taylor-Couette flow, OR and RB in ILC bifurcate robustly together in equivariant bifurcations (Knobloch, 1986) and are connected via OWR. However, OR and RB are stationary states and their bifurcation is an equivariant pitchfork bifurcation, unlike equivariant Hopf bifurcations such as those found in Taylor-Couette flow, and those discussed in Section 5.3.2.

Decomposition in terms of straight convection rolls

As a consequence of the stationary equivariant bifurcation, the linear relation $\boldsymbol{x}_{RB} = \alpha \boldsymbol{x}^l_{OR} + \beta \boldsymbol{x}^r_{OR}$ with $\alpha = \beta$ holds at the bifurcation points, where $\boldsymbol{x}_{RB}$ indicates the state space vector of RB, and $\boldsymbol{x}^l_{OR}$ and $\boldsymbol{x}^r_{OR}$ are the state space vectors of OR^l and OR^r, respectively. This linear decomposition is valid for all parameters, where RB and OR bifurcate from laminar flow B. Since RB emerges as linear superposition of two differently oriented straight convection rolls, we call RB a 'bimodal state'. The term 'bimodal' has been used previously to describe knot patterns of straight convection rolls at orthogonal orientations in experiments of Rayleigh-Bénard convection (Busse and Whitehead, 1974) and in experiments of ILC for $\gamma > \gamma_{c2}$ (Daniels et al., 2000). In line with previously used terminology, we describe KN and RB both as bimodal states. However, there are fundamental differences between KN and RB bimodal states that are illustrated by the subsequently discussed decomposition analysis.

We consider a bimodal equilibrium state vector $\mathbf{b}(\epsilon)$ depending on continuation parameter ϵ as decomposition

$$\mathbf{b}(\epsilon) = \alpha(\epsilon)\,\mathbf{m}_1(\epsilon) + \beta(\epsilon)\,\mathbf{m}_2(\epsilon) + \mathbf{d}(\epsilon) \tag{5.21}$$

where $\alpha, \beta \in \mathbb{R}$ and $\mathbf{m}_1, \mathbf{m}_2$ are state vectors of two differently oriented straight convection rolls. $\mathbf{d}$ is the difference vector that is necessary to create the composite state $\mathbf{b}$. We simplify the notation by suppressing the dependence of the decomposition on ϵ. We seek the optimal bimodal decomposition (5.21)

$$\langle \alpha\mathbf{m}_1 + \beta\mathbf{m}_2, \mathbf{d}\rangle = 0, \tag{5.22}$$

with $||\mathbf{d}||_2$ minimal. The minimal $\mathbf{d}$ measures nonlinear and non-bimodal effects. The corresponding optimal coefficients α and β may be found via the inner product of (5.21) with $\mathbf{m_1}$ and $\mathbf{m_2}$, respectively,

$$\alpha = \frac{\langle \mathbf{m}_1, \mathbf{b}\rangle}{\langle \mathbf{m}_1, \mathbf{m}_1\rangle} - \beta\frac{\langle \mathbf{m}_1, \mathbf{m}_2\rangle}{\langle \mathbf{m}_1, \mathbf{m}_1\rangle}, \quad \beta = \frac{\langle \mathbf{m}_2, \mathbf{b}\rangle}{\langle \mathbf{m}_2, \mathbf{m}_2\rangle} - \alpha\frac{\langle \mathbf{m}_2, \mathbf{m}_1\rangle}{\langle \mathbf{m}_2, \mathbf{m}_2\rangle}, \tag{5.23}$$

where we assume $\langle \mathbf{m}_1, \mathbf{d}\rangle = 0$ and $\langle \mathbf{m}_2, \mathbf{d}\rangle = 0$ to satisfy (5.22). The inner product $\langle , \rangle$ is induced by the full norm (5.11). (5.23) with (5.21) is a coupled system of equations for the optimal coefficients α and β that we solve iteratively.

The optimal bimodal decomposition (5.21) with (5.23) is calculated for $\mathbf{b} = \boldsymbol{x}_{RB}$ and $\mathbf{m}_{1,2} = \boldsymbol{x}_{OR}^{l,r}$ along the ϵ-bifurcation branches at $\gamma = 40°$. The coefficients are found to be equal at all ϵ, and to decrease linearly from $\alpha = \beta = 0.3291$ at the bifurcation point (Figure 5.10). The difference vector $\mathbf{d}$ increases linearly in $||\theta||_2$ and mostly accounts for corrections to the flow at the streamwise interfaces between hot and cold plumes (Figure 5.10d).

The optimal bimodal decomposition (5.21) with (5.23) is calculated again for $\mathbf{b} = \boldsymbol{x}_{KN}$ along the KN-branch at $\gamma = 80°$. Since LR does not coexist with most of the KN-branch (Figure 5.11), the state vectors $\boldsymbol{m}_1 = \boldsymbol{x}_{TR}$ and $\boldsymbol{m}_2 = \boldsymbol{x}_{LR}$ in the decomposition are not considered as ϵ-dependent. We choose the decomposition $\boldsymbol{x}_{KN}(\epsilon) = \alpha(\epsilon)\boldsymbol{x}_{TR}(\epsilon = 0.024) + \beta(\epsilon)\boldsymbol{x}_{LR}(\epsilon = 0.22) + \boldsymbol{d}(\epsilon)$. Here, ϵ parametrises linear interpolation between two bifurcation points. The resulting optimal coefficients α and β in general differ. While the contribution of the longitudinal rolls monotonically increases, the contribution of the transverse rolls decreases (Figure 5.11). A decomposition with $\alpha = \beta$ is found at $\epsilon = 0.095$, approximately half-way between the bifurcation points and close to the maximum of $||\mathbf{d}||_2$. Note that $\mathbf{d}$ at the maximum amplitude resembles a ribbon pattern (Figure 5.11d). Towards the bifurcation points, $\mathbf{d}$ decreases parabolically to zero. Since $\mathbf{d}$ combines nonlinear and non-bimodal effects, as well as effects due to interpolation between TR and LR at fixed values of ϵ, the dominant source for the large values of $\partial||\boldsymbol{d}||_2/\partial\epsilon$ at the bifurcations is unclear. Stability analysis of the knot instability indicates a three-mode inter-

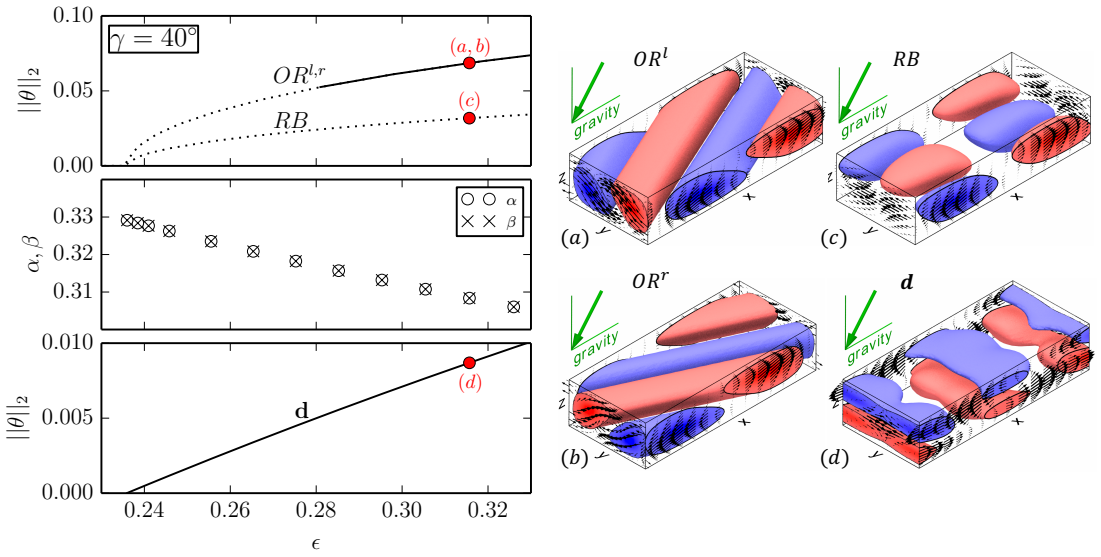

Figure 5.10 – Decomposition of bimodal ribbons (RB) into left and right oriented oblique rolls ($OR^{l,r}$). The bifurcation diagram with details of the decomposition (left) is shown together with visualisations of the temperature and velocity fields on the right (red labels in the diagram indicate panels on the right). RB bifurcates together with $OR^{l,r}$ in equivariant pitchfork bifurcations from the laminar base flow. At $\gamma = 40°$, RB emerges with one additional unstable eigendirection, and $OR^{l,r}$ become dynamically stable in a $[2\lambda_x, \lambda_y]$-periodic domain at $\epsilon = 0.282$ (solid line in top left panel). The optimal decomposition $\boldsymbol{x}_{RB}(\epsilon) = \alpha(\epsilon)\,\boldsymbol{x}^l_{OR}(\epsilon) + \beta(\epsilon)\,\boldsymbol{x}^r_{OR}(\epsilon) + \mathbf{d}(\epsilon)$ implies linearly decreasing equal coefficients $\alpha = \beta$ along the branches (middle panel). The difference vector $\mathbf{d}$ grows linearly in $||\theta||_2$ from zero at the bifurcation point (bottom panel). Thus, RB can be viewed as a bimodal state combining two equally contributing oblique rolls.

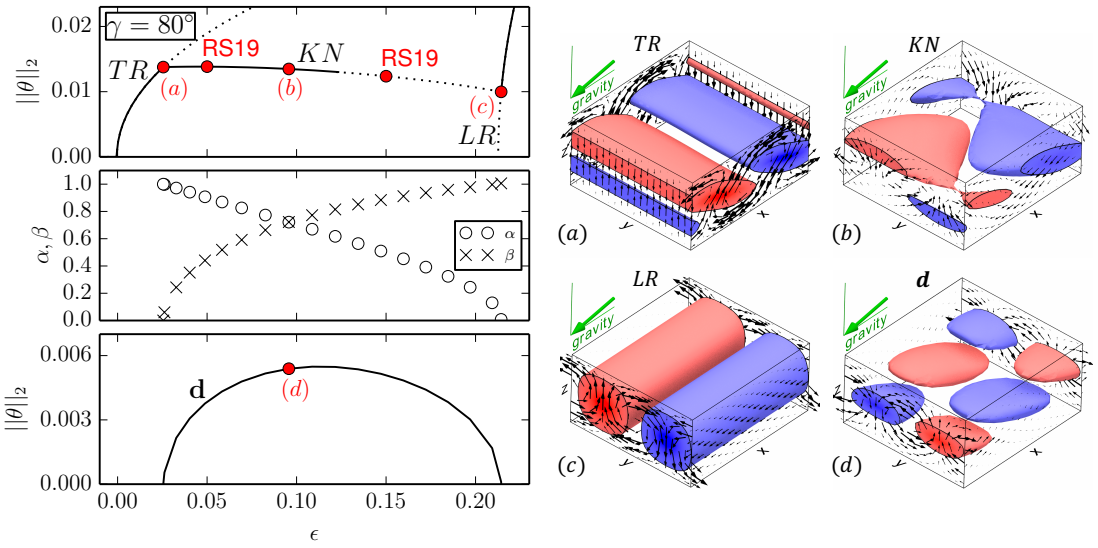

Figure 5.11 – Decomposition of knots (KN) into longitudinal and transverse oriented rolls, LR and TR, respectively. The bifurcation diagram with details of the decomposition (left) is shown together with visualisations of the temperature and velocity fields on the right (red labels in the diagram indicate panels on the right). KN connect TR and LR at $\gamma = 80°$ (top). Dynamical stability in a $[\lambda_x, \lambda_y]$-periodic domain is indicated by the solid lines. 'RS19' labels the control parameter where temporal dynamics has been studied in RS19. Between the bifurcation points, the optimal decomposition $KN(\epsilon) = \alpha(\epsilon)\, TR(\epsilon = 0.024) + \beta(\epsilon)\, LR(\epsilon = 0.22) + \mathbf{d}(\epsilon)$ results in decreasing α, increasing β (middle), and parabolically varying $\mathbf{d}$ (bottom). Thus, KN can be viewed as a bimodal state combining transverse and longitudinal rolls with monotonically changing relative contributions.

action(Fujimura and Kelly, 1993; Subramanian et al., 2016), suggesting that a third state is involved as evidenced by the significant contribution of $\boldsymbol{d}$.

KN and RB differ in their bifurcation structure. KN is a connecting state between TR and LR, while RB bifurcates together with $OR^{l,r}$ in an equivariant pitchfork bifurcation. As a consequence, their bimodal decomposition into two composing straight convection rolls differs significantly. RB is composed of an equal weight superposition of two symmetry related oblique rolls $OR^l = \pi_y OR^r$. KN in ILC at $\gamma \neq 0°$ is a mixed mode state, composed of transverse and longitudinal rolls that are not symmetry related and whose weight continuously changes along the branch. At $\gamma = 0°$ however, TR and LR become symmetry related via rotation. The knot patterns observed in Rayleigh-Benard convection (Busse and Whitehead, 1974) are thus expected to bifurcate in equivariant pitchfork bifurcations, like RB in ILC .

5.3.5 Transverse oscillations - continuation towards a chaotic state space

The pattern of obliquely modulated transverse rolls, called 'switching diamond panes', shows complex dynamics with chaotically switching pattern orientations (Daniels et al., 2000). A periodic orbit TO underlying transverse oscillations has been identified in RS19 at moderate ϵ. The pattern of transverse oscillations seems to capture some aspects of the observed complex dynamics. ϵ-continuations of TO show that the orbit period of TO is subject to large and non-monotonic changes, and the number of unstable eigendirections of TO increases quickly with ϵ. This suggests the existence of complex state space structures that support the chaotic dynamics of switching diamond panes.

Bifurcations to transverse oscillations

In all but one analysed parameter continuations, the pre-periodic orbit TO bifurcates from TR in a supercritical Hopf bifurcation. The bifurcations are either ϵ-forward at $\epsilon \approx 0.07$, found at inclination angles $\gamma = [80°, 90°, 100°, 110°]$, or γ-backward, found at $\epsilon = 0.1$ and $\gamma = 132.2°$. The latter case represents the upper inclination limit of existence of TO at $\epsilon = 0.1$. At the lower limit, just below γ_{c2}, TO bifurcates as quaternary state from the transverse subharmonic varicose state TSV (see inset panel in Figure 5.4). TSV is an equilibrium state discussed briefly in Section 5.6. A common feature of all TO-branches is that the $||\theta||_2$-maximum over the orbit period remains close to the $||\theta||_2$-value of TR. This agrees with the observation that TO modulations are sinusoidal oscillations around strictly transverse rolls with the maximum deflection associated to the minimum in $||\theta||_2$ over the orbit period (RS19).

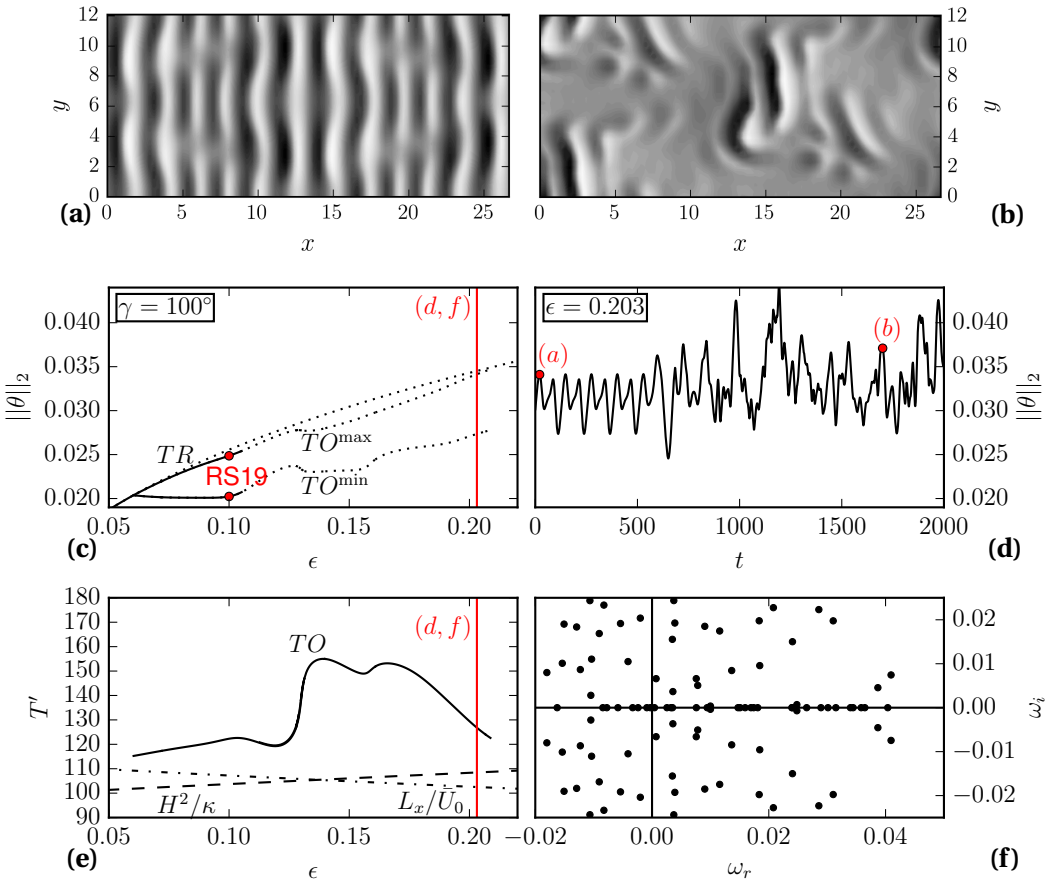

Figure 5.12 – Continuation of TO at $\gamma = 100°$ towards a chaotic state space. **(a)** Midplane temperature of TO at Ra = 11 000 ($\epsilon = 0.203$) before instabilities create a turbulent flow **(b)**. The corresponding simulated time series of TO **(d)** shows the transition from a periodic to a turbulent signal. The transition is a consequence of the many linear instabilities of TO **(f)** that have emerged along the bifurcation branch **(c)**. Solid/dotted bifurcation branches indicate stable and unstable states in the symmetry subspace of $S = \langle \pi_y, \pi_{xz}, \tau(0.5, 0.5) \rangle$. 'RS19' labels the control parameter value at which temporal dynamics has been studied in RS19. The changing relative period T' of TO along the bifurcation branch is shown in **(e)** and compared to the time scale of thermal diffusion H^2/κ and laminar mean advection $L_x/\bar{U}_0$ (dashed and dashed-dotted lines).

Numerical continuation of transverse oscillations

γ-continuation of TO at $\epsilon = 0.1$ is numerically straight forward and yields periodic orbits showing weak bending modulations around a purely transverse orientation (RS19, Section 4.2.2). ϵ-continuations are found to be numerically challenging for increasing ϵ. We could not continue TO much beyond $\epsilon = 0.2$ (Figure 5.12c). The reason for the computational difficulty is two-fold. First, the time period of the orbit drastically changes with ϵ, which causes challenges for our shooting method. The pre-periodic orbit TO satisfying (5.7) with $\sigma = \tau(0.5, 0)$ oscillates slowly with a relative period $T' \sim \mathcal{O}(10^2)$ close to the heat diffusion time H^2/κ and the laminar mean advection time $L_x/\bar{U}_0$. Along the continuation, the large orbit period is subject to significant and non-monotonic changes over small ϵ-intervals (Figure 5.12e). These changes in the orbit period are numerically difficult to trace. Secondly, the iterative solver of the Newton algorithm converges better if the target state is dynamically stable or weakly unstable (Sanchez et al., 2004). Computing the spectrum of eigenvalues of TO in the symmetry subspace of $[12\lambda_x, 6\lambda_y]$-periodicity indicates that the state branch at $\gamma = 100^\circ$ and $\epsilon = 0.203$ has collected 63 unstable eigenvalues with a broad range of frequencies ω_i (Figure 5.12f). At these parameters, the single-shooting Newton algorithm converged TO to a residual of $||\mathcal{G}(\mathbf{x})||_2 < 3 \times 10^{-11}$ (see Equation 5.7). When integrating the converged orbit forward in time, unstable directions trigger a transition to a turbulent state after $t = 500$ (Figure 5.12d). This turbulent state has been described as longitudinal bursts within switching diamond panes (Daniels et al., 2000). We conclude that continuation of TO for $\epsilon > 0.2$ is challenging due to the numerical condition of a temporally slow, spatially large and very unstable periodic orbit that competes with many fast and small-scale modes in a chaotic turbulent state space.

5.4 Discussion

Towards understanding how temporal and spatio-temporally complex dynamics arises in ILC, we have computed three-dimensional invariant states underlying several observed spatially periodic convection patterns in ILC at Pr = 1.07. Numerical continuation of these invariant states in two control parameters, the normalised Rayleigh number ϵ and the inclination angle γ, yields 15 bifurcation diagrams covering systematically selected parameter sections in the intervals $\epsilon \in [0, 2]$ and $\gamma \in [0, 120)$. For some selected bifurcating state branches, we have characterised their stability properties and pattern features along the branches. These state branches were selected for a more detailed discussion in the present chapter for two reasons. First, each selected branch bifurcates at a different secondary instability. Second, they cover the control parameters at which the temporal dynamics along dynamical connections between stable and unstable invariant states have previously been described (RS19).

The relevance of the computed invariant states for observed spatio-temporally complex dynamics in ILC depends in general on the type of bifurcation creating the states, the range in control parameters over which state branches exist, and the stability properties of the invariant states along their branches. The dynamical relevance of invariant states in the context of the entire bifurcation structure is discussed below by answering the three specific questions posed in the introduction ($Q1$-$Q3$). To describe the role of individual invariant states for temporal pattern dynamics, we can distinguish three different cases:
In case 1, a stable invariant state represents a dynamical attractor at specific control parameters. This case corresponds for example to supercritical ϵ-forward bifurcations where the stable bifurcating invariant state is an attractor for the dynamics above the critical control parameters for the bifurcation. For invariant states that have been identified because they represent dynamical attractors at specific control parameters (RS19), the present bifurcation analysis indeed confirms supercritical ϵ-forward bifurcations (Sections 5.3.2-5.3.5).
In case 2, invariant states exist at specific control parameters but are dynamically unstable. State branches are only stable over a finite range in control parameters. This range is limited by instabilities along state branches. Invariant states which the present study indicates as dynamically unstable at specific control parameters, may still be relevant for the observed temporal dynamics at these control parameters. One reason is that the range of stability along state branches depends on the considered pattern wavelength. Thus, invariant states might be dynamically stable at other pattern wavelengths not considered here. Another reason is that weakly unstable invariant states may be building blocks for the dynamics supported by a more complex state space attractor. Here, the evolving state vector may transiently visit weakly unstable invariant states by approaching and escaping along their stable and unstable manifolds, respectively (e.g. Suri et al., 2017). The simplest example for such complex state space attractors is the robust heteroclinic cycle between two weakly unstable instances of symmetry related OWR described in RS19.
In case 3, invariant states do not exist at specific control parameters but their pattern is reminiscent in some state space regions that may be transiently visited by the dynamics. Folds or symmetry-breaking bifurcations may limit the existence of invariant states in parameter space. However, the pattern of the invariant state may still emerge transiently at control parameters beyond the existence limits. We have observed this case for the transient skewed varicose pattern along a dynamical connection from unstable to stable straight convection rolls in Rayleigh-Bénard convection (Section 5.3.1), as well as for transient subharmonic oscillations at $[\epsilon, \gamma] = [1.5, 17°]$ (see Section 4.4.2) where the SSW-branch does not exist anymore due to a fold (Figure 5.6). The state space structure supporting such transient dynamics seems related to a state space structure supporting intermittency (Pomeau and Manneville, 1980).

Consequently, the patterns of invariant states are often observed because invariant states are stable and attracting, but neither stability nor existence of invariant states is required for observing their pattern.

5.4.1 Bifurcation types (Q1)

Bifurcations create or destroy invariant states and change the stability along state branches. Thus, bifurcation structures describe how state space structures change across control parameters. In response to question $Q1$, stated in the introduction, we list all the different types of bifurcations found in the present study and refer to particular examples. Identified bifurcation types include:
Pitchfork bifurcation, e.g. from TR or LR to KN along ϵ at $\gamma = 80°$ (Figure 5.11). Equivariant pitchfork bifurcation, e.g. from B to RB and OR along ϵ at $\gamma = 40°$ (Figure 5.10). Hopf bifurcation, e.g. from TR to TO along ϵ at $\gamma = 100°$ (Figure 5.12). Equivariant Hopf bifurcation, e.g. from LR to SSW and STW along γ at $\epsilon = 1.5$ (Figure 5.6). Saddle-node bifurcation, e.g. WR along ϵ at $\gamma = 90°$ (Figure 5.3, panel $\gamma = 90°$). Mutual annihilation of two periodic orbits, e.g. the two folds bounding the SSW isola along γ at $\epsilon = 0.5$ (Figure 5.4). The global bifurcation of a periodic orbit colliding with a structurally robust heteroclinic cycle, e.g. the SSW collision with $TR \to \tau_x TR \to TR$ along Ra at $\gamma = 10°$ (Figure 5.8).
The symmetry-breaking pitchfork and Hopf bifurcations are found as ϵ- or γ-forward or backward bifurcations. The orientation of bifurcations can change when control parameters are changed, e.g. WR bifurcates γ-forward from LR at $\epsilon = 0.1$, but γ-backward at $\epsilon = 0.5$ (Figure 5.4). Moreover, pitchfork and Hopf bifurcations can be supercritical or subcritical independent of their orientation. The ϵ-backward pitchfork bifurcation from $R_{\lambda 2}$ to SV at $\gamma = 0°$ is subcritical (Figure 5.5) but the ϵ-backward pitchfork bifurcation from OR to DWR at $\gamma = 40°$ is supercritical (Figure 5.9f).
The sequential order in which bifurcations occur may depend on the considered path through parameter space. RB at $\epsilon = 0.5$ for example can bifurcate in primary or secondary bifurcations along γ. When decreasing γ towards $\gamma = 46°$, RB bifurcate from B in a primary bifurcation. When increasing γ towards $\gamma = 24°$, RB bifurcate from TR in a secondary bifurcation (Figure 5.4, panel $\epsilon = 0.5$). Thus, describing for example WR as tertiary state implies a particular parameter path. Since WR can bifurcate from RB that may be described as tertiary state (Figure 5.3, panel $\gamma = 50°$), WR may also be described as quartenary state.

The relation between bifurcation structures and spatio-temporally complex dynamics is in general complicated. The various local and global bifurcations can modify the coexisting invariant states and their dynamical connections in various ways. Coexistence of invariant states may result from supercritical or subcritical bifurcations as well as from folds. These bifurcation types exist in ILC at all angles of inclinations. For example, the subcritical coexistence of stable straight convection rolls with unstable SV (Figure 5.5) or with unstable SSW (Figure 5.3, panels $\gamma = 10°, 20°$), supports the experimental observation of spatially localized variants of these spatially periodic states (Bodenschatz et al., 2000; Daniels et al., 2000). The supercritical coexistence of WR with DWR, OR or OWR (Figure 5.9) supports the observed pattern defects within the spatially coexisting wavy rolls of different orientations (Daniels and

Table 5.1 – Comparison between critical thresholds of secondary instabilities determined by Floquet analysis (Subramanian et al., 2016) and the critical bifurcation points determined by the present bifurcation analysis. The comparison requires to state all critical frequencies $\omega_c^\dagger$ in diffusion time scales. Frequencies in free fall time units, used throughout this chapter, are obtained via $\omega = \omega^\dagger/\sqrt{PrRa}$.

	Floquet analysis				**bifurcation analysis**			
γ	instability	(L_x, L_y)	ϵ_c	$\omega_c^\dagger$	invariant state	(L_x, L_y)	ϵ_c	$\omega_c^\dagger$
0°	skewed varicose	(10.6, 8.07)	1.100	0	SV	(8.88, 8.06)	1.020	0
10°	long. subh. oscil.	(4.89, 4.03)	1.360	6.211	SSW/TW	(4.44, 4.03)	1.454	6.269
20°	long. subh. oscil.	(4.89, 4.03)	0.900	11.66	SSW/TW	(4.44, 4.03)	0.929	11.64
20°	wavy	(62.8, 2.02)	0.018	0	WR	(4.44, 2.02)	0.054	0
30°	wavy	(62.8, 2.02)	0.014	0	WR	(4.44, 2.02)	0.033	0
40°	wavy	(62.8, 2.02)	0.013	0	WR	(4.44, 2.02)	0.034	0
50°	wavy	(62.8, 2.02)	0.013	0	WR	(4.44, 2.02)	0.043	0
60°	wavy	(62.8, 2.02)	0.013	0	WR	(4.44, 2.02)	0.072	0
70°	wavy	(62.8, 2.02)	0.013	0	WR	(4.44, 2.02)	0.159	0
80°	knot	(2.23, 2.03)	0.026	0	KN	(2.22, 2.02)	0.024	0
90°	trans. oscil.	(26.9, 13.4)	0.063	1.733	TO	(26.7, 12.1)	0.061	2.527
100°	trans. oscil.	(27.2, 15.7)	0.060	1.484	TO	(26.7, 12.1)	0.060	2.776
110°	trans. oscil.	(27.4, 17.0)	0.057	1.312	TO	(26.7, 12.1)	0.059	3.043

Bodenschatz, 2002). The details of these relations are non-trivial as they require to consider spatial dynamics (e.g. Knobloch, 2015).

For a specific bifurcation structure we see a generic relation to complex temporal dynamics. All computed sequences of primary and secondary supercritical ϵ-forward pitchfork or Hopf bifurcations give rise to one of the four sequences of dynamical connections. These are $B \to LR \to SSW, WR$ and $B \to TR \to KN, TO$ as observed in RS19 and illustrated in Figure 5.2. Consequently, a 'sequence of bifurcations' (Busse and Clever, 1996), that consists of supercritical ϵ-forward bifurcations, gives rise to a corresponding 'sequence of dynamical connections'.

5.4.2 Connection to instabilities (Q2)

The patterns of the tertiary invariant states SV, SSW/W, WR, KN and TO are similar to the pattern motifs associated to the five secondary instabilities in ILC at Pr = 1.07 (Subramanian et al., 2016). The similarity suggests that the invariant states bifurcate at corresponding secondary instabilities. To confirm this, we compare the bifurcation points of the nonlinear state branches with the critical threshold parameters of the secondary instabilities determined by Subramanian et al. (2016) using Floquet analysis (compare with question $Q2$ stated in the introduction). Floquet analysis solves for the pattern wavelengths that first become unstable at

the critical threshold ϵ_c when ϵ is increased towards ϵ_c for fixed γ. For numerical continuation of invariant states, the pattern wavelength is prescribed. The critical threshold ϵ_c is determined by continuing the state branch down in ϵ towards the bifurcation at ϵ_c for fixed γ. Consequently, Floquet analysis yields the minimal ϵ_c of the instability, while branches of invariant states at prescribed wavelengths bifurcate at higher ϵ_c. We expect comparable critical thresholds between the two methods if the associated pattern wavelengths are comparable.

Table 5.1 compares the results of Floquet analysis and bifurcation analysis in terms of pattern wavelengths L_x and L_z, critical thresholds ϵ_c, and critical frequency ω_c for Hopf bifurcations. We find clear agreement between the results for skewed varicose, longitudinal subharmonic oscillatory, and knot instabilities. Note that Floquet analysis finds the skewed varicose instability for $\gamma = 0°$ at a slightly higher ϵ_c than the bifurcation analysis. This suggests that the Floquet analysis did not capture the most unstable wavelengths of the skewed varicose instability.
For the wavy instabilities, the ϵ_c obtained from the bifurcation analysis is significantly larger. This discrepancy results from the difference in wavelength L_x. Floquet analysis indicates L_x one order of magnitude larger than the L_x prescribed in the bifurcation analysis. We confirmed that WR bifurcates at identical ϵ_c when identical pattern wavelengths are prescribed. Thus, the equilibrium state WR bifurcates at the previously characterised wavy instability.
For the transverse oscillatory instability, the two methods agree in ϵ_c but differ in the critical frequency ω_c. The reasons for this discrepancy are not clear. Continuing the periodic orbit TO to identical pattern wavelengths does not change the critical frequency much. Thus, we hypothesise that the instability characterised by Floquet analysis corresponds to a different bifurcating periodic orbit as TO. This hypothesis is supported by two observations. First, a weakly nonlinear analysis of the normal form near the transverse oscillatory instability suggests a subcritical ϵ-backward bifurcation. TO however, is always found to bifurcate supercritically and ϵ-forward. Second, the pattern of TO can be described as spatially subharmonic standing wave oscillations. Like the subharmonic standing wave state SSW, also TO oscillates on the time scale of the laminar mean advection across the pattern $L_x/\bar{U}_0$ (Section 5.2.1). Thus, these subharmonic standing waves satisfy the approximate resonance condition

$$m\, L_x\, \omega_c \approx n\, \bar{U}_0 2\pi\ , \tag{5.24}$$

with $(m,n) \in \mathbb{N}$. For bifurcations to SSW at small γ, this approximation holds for $(m,n) = (2,1)$ with relative errors of about $\pm 15\%$. The nonlinear time scales along the SSW-branch are shown in Figure 5.6d. For bifurcations to TO, this approximation holds for $(m,n) = (2,1)$ with relative errors of less than $\pm 10\%$. The nonlinear time scales along the TO-branch are shown in Figure 5.12e. The transverse oscillatory instability from Floquet analysis however satisfies (5.24) best for $(m,n) = (4,1)$. Due to the different resonance numbers, we suspect other physics than those of subharmonic standing waves to govern the instability described by Floquet analysis. Future research should investigate the possibility for other periodic orbits than TO

to bifurcate, possibly subcritically, at or near the transverse oscillatory instability. Except in the case of TO, the bifurcating invariant states match the characteristics of the secondary instabilities described previously in Subramanian et al. (2016).

5.4.3 Range of existence (Q3)

The third specific question is about the limits of existence of invariant solutions as control parameters are varied (*Q3* state in the introduction). This problem has been approached by continuing invariant states as far as possible along *a priori* defined sections across the $[\gamma, \epsilon]$-parameter space at Pr = 1.07. Since the continuation methods allow tracing invariant states beyond critical threshold parameters of additional instabilities, it was possible to follow bifurcation branches over large intervals of control parameters. The travelling wave STW, for example, is found to exist over a large range of inclinations $10° \leq \gamma \leq 110°$, covering different flow regimes with small and large laminar shear forces. We identify three invariant states SSW/W and WR whose solution branches persist across the angle of the codimension-2 point γ_{c2}, and for $\gamma > 90°$ where their parent state LR has disappeared. With the exception of SV, all tertiary invariant states are found to exist for the case of vertical convection with $\gamma = 90°$. All invariant states existing at $[\gamma, \epsilon] = [90°, 1.5]$ are briefly discussed and compared with turbulent vertical convection in Section 5.7. We visually summarise the regions of existence and coexistence of the computed invariant states in Figure 5.13.

Continuation and stability analysis along state branches revealed bifurcations to or from other invariant states. These states are neither clearly observed in experiments or simulations, nor do they correspond to instabilities found by Floquet analysis. The stability analysis along the branch of WR (Section 5.3.3) introduced four additional equilibrium states, namely DWR, OR, OWR, and RB. Other invariant states were obtained because continuations terminated at bifurcations from these states. Specifically, TO may bifurcate from the TSV equilibrium (Figure 5.4, $\epsilon = 0.1$), KN may bifurcate from SL (Figure 5.3, $\gamma = 90°$), and a global bifurcation of SSW may involve LSV as parent state (Figure 5.6c). These three additional states are described in Section 5.6. We do not distinguish invariant states connected via folded bifurcation branches as upper and lower branch states. Folds exist at all angles of inclinations. See e.g., the bifurcation branches of SV at $\gamma = 0°$, and of STW at $\gamma = 110°$. However, we observe that state branches tend to become more folded towards inclinations around vertical (compare panels in Figure 5.3).

5.5 Conclusions

The present bifurcation analysis has identified an extensive network of parametrically connected invariant state branches in inclined layer convection. Overall, 16 different nonlinear

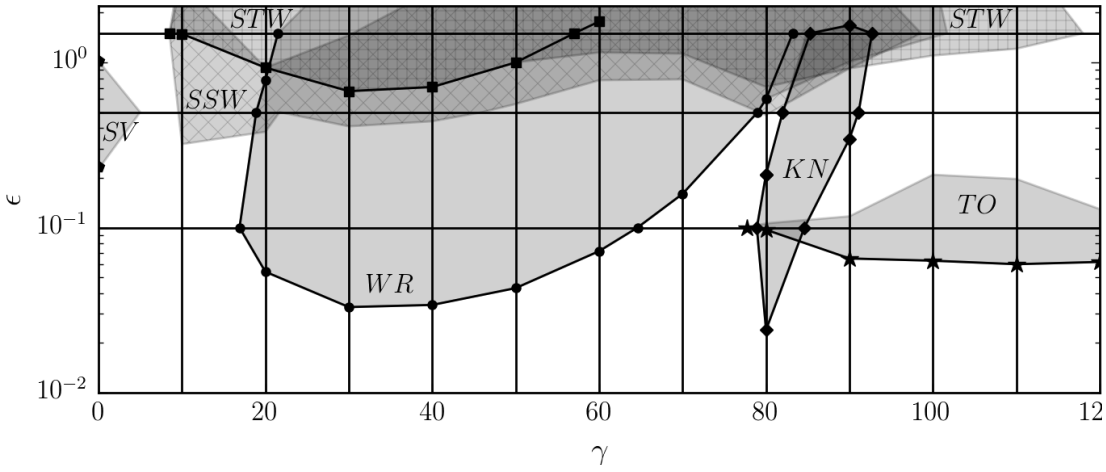

Figure 5.13 – Existence regions of invariant states in the considered parameter space at Pr = 1.07. Local symmetry breaking bifurcations are marked and connected to guide the eye: SV (⬠), WR (∘) and KN (◇) bifurcate in pitchfork bifurcations. SSW/STW (□) and TO (⋆) bifurcate in Hopf bifurcations. Where existence is not limited by symmetry breaking bifurcations, the limits are due to folds, global bifurcations or, in the case of TO, due to numerical challenges. Hatched regions of existence allow to better distinguish SSW (×) and STW (+).

three-dimensional invariant states have been discussed in the present chapter. Many of them are related to spatio-temporally complex dynamics observed in experiments and simulations. Seven different types of bifurcations were found, including common types like Hopf bifurcations or saddle-node bifurcations, and including less common types like equivariant bifurcations or global collisions between periodic orbits and robust heteroclinic cycles. Computing this many different invariant states and branches just for this work and RS19 has been straightforward relative to recent integrated efforts of the research community to compute similar numbers of invariant states and branches in other canonical shear flows like plane Couette or pipe flow. Inclined layer convection covers flows from horizontal Rayleigh-Bénard convection to vertical layer convection which are relevant for engineering applications and which have been widely studied using experiments and simulations. This chapter demonstrates that these flows are numerically accessible to nonlinear dynamical systems concepts.

5.6 Additional invariant states participating in bifurcations

This section briefly discusses three additional invariant states that do not represent previously observed convection patterns at Pr = 1.07 but that participate in the bifurcation network by bifurcating to the above discussed invariant states.

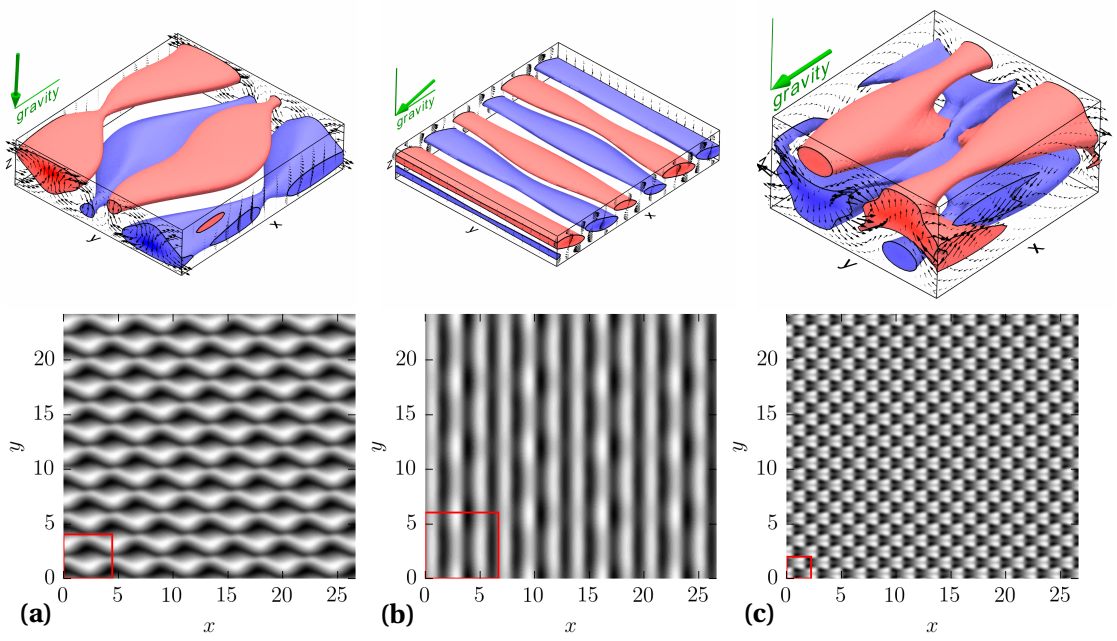

Figure 5.14 – 3D flow structure and midplane temperature contours of three steady equilibrium states participating in bifurcations. **(a)** longitudinal subharmonic varicose LSV, **(b)** transverse subharmonic varicose TSV, **(c)** subharmonic lambda plumes SL.

The γ-continuation of SSW at $\epsilon = 1.5$ approaches an equilibrium state at $\gamma = 1.9°$ that we name LSV, short for longitudinal subharmonic varicose state. The pattern of the equilibrium resembles an instance in time along the orbit SSW at $\gamma = 15°$ (Figure 5.14a). LSV is invariant under transformations of $S_{\text{ssw}} = \langle \pi_{xyz}, \tau(0.5, 0.5) \rangle$ and can be continued from $\gamma = 0°$ to $\gamma = 30°$ along which the relative position of the hot and cold plumes changes continuously.

Just below γ_{c2}, a γ-forward Hopf bifurcation generates TO from an equilibrium state, previously named transverse subharmonic varicose (TSV), at $\epsilon = 0.1$ (inset panel in Figure 5.4). This invariant state represents stationary varicose modulations of the TR pattern with $[3\lambda_x, 3\lambda_y]$-periodicity and invariance under transformations of $S_{\text{tv}} = \langle \pi_{xz}, \pi_y \rangle$ (Figure 5.14b). TSV are similar to the state discussed in Clever and Busse (1995) but have different periodicity.

Due to the absence of LR at finite Ra at $\gamma = 90°$, KN do not terminate in a bifurcation from LR as described in Section 5.3.4 but from SL, an equilibrium that we name subharmonic lambda plumes. The $[\lambda_x, \lambda_y]$-periodic SL emerges in a saddle-node bifurcation at $\epsilon = 1.670$. From the upper branch of SL, KN bifurcate ϵ-backward at $\epsilon = 1.672$ (Figure 5.3). The subharmonic flow structure of SL is invariant under transformations of $S_{\text{sl}} = \langle \pi_{xz}\tau(0, 0.5), \pi_y\tau(0.5, 0), \tau(0.5, 0.5) \rangle$ and resembles lambda-shaped plumes at scales of half the gap height (Figure 5.14c).

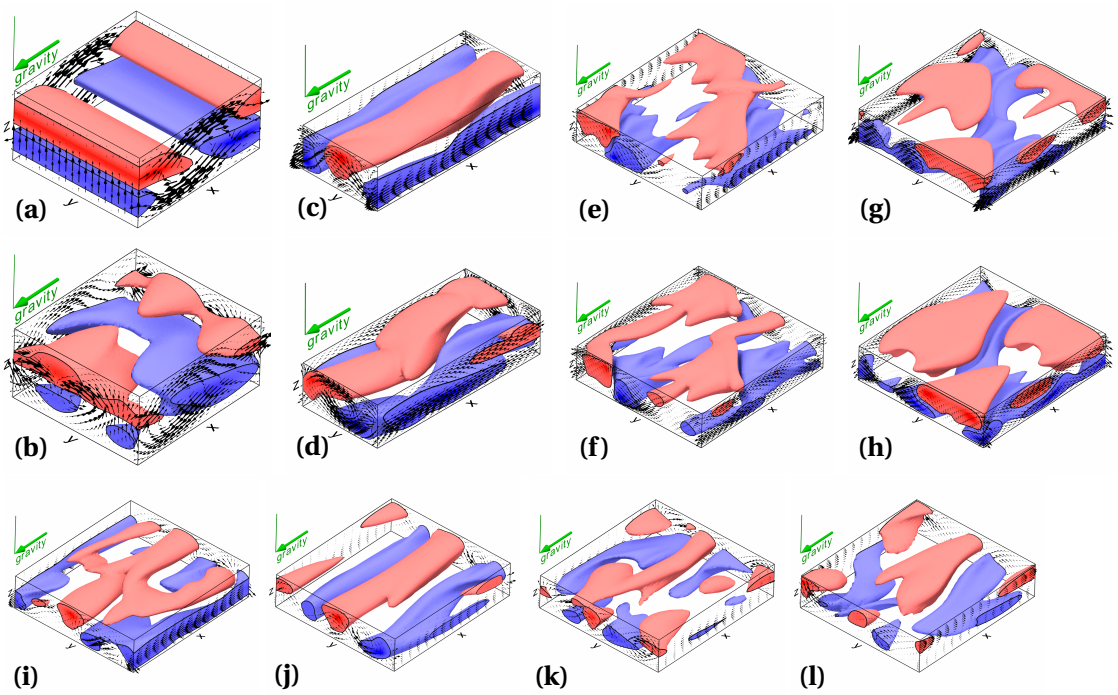

Figure 5.15 – Continuation yields eight invariant states in vertical layer convection ($\gamma = 90°$) at $\epsilon = 1.5$ (Ra = 21 266). **(a)** TR, **(b)** KN, **(c/d)** upper/lower branch of WR, **(e/f)** upper/lower branch of SSW, **(g/h)** upper/lower branch of STW. The distinction between upper/lower branches refers to $||\theta||_2$. The upper branches of WR and SSW are closer to bifurcations from LR than the lower branches, for STW *vice versa*. **(i)-(l)** Snapshots from a DNS at $\gamma = 90°$ and $\epsilon = 1.5$ show transiently emerging structures resembling the invariant states above.

5.7 Invariant states in vertical layer convection

ILC at $\gamma = 90°$ is a particular case because vertical layer convection has the largest laminar shear forces of all inclinations and can be considered a pure shear flow. Here, buoyancy provides a body force along the channel domain, acting like a pressure gradient in pressure-driven channel flow. Despite the absence of a wall-normal buoyancy force, all main invariant states considered in the present study were numerically continued to $\gamma = 90°$, with the exception of LR existing only at Ra $= \infty$ due to (5.15-5.19) and SV. The flow structures of the invariant states at $\gamma = 90°$ and $\epsilon = 1.5$ show sharper interfaces and more pointed convective plumes than at the parameters where these states were initially found (Figure 5.15).

6 Turbulent wavy rolls in inclined layer convection: An outlook

The invariant states discussed in the previous two chapters underlie spatially periodic patterns whose temporal dynamics is observed to be spatio-temporally complex only in large flow domains. Here, we provide an outlook to invariant states in ILC that capture chaotic dynamics in a small flow domain (Section 6).

Inclining a Rayleigh-Bénard convection cell against gravity creates a shear flow between hot and cold fluid, driven up and down the inclined plates by buoyancy force. Experiments on so-called inclined layer convection (ILC) find turbulent wavy convection rolls (Daniels et al., 2000, 2008), reminiscent of wavy velocity streaks in weakly turbulent subcritical shear flows. Turbulent ILC is observed close above the onset of convection where a turbulent attractor can be expected to have a much simpler structure than in subcritical shear flows. However, turbulent inclined layer convection has not been studied using exact invariant solutions.
This outlook reports on an exact periodic orbit (EPO) forming the obvious 'backbone' structure of turbulent ILC studied in direct numerical simulations (DNS). The EPO is found via stepwise reducing the complexity of the flow by reducing the domain size, from spatio-temporal chaos in a large numerical domain, via temporal chaos in an intermediate size domain, to an attractive EPO in a small minimal domain. The EPO captures the bursting dynamics and the mean statistics of turbulent ILC, and defines the onset of chaos.

Numerical dynamical systems approach. We consider ILC as a dynamical system with the fully resolved three-dimensional velocity field $\boldsymbol{U}(x,y,z)$ and temperature field $\mathcal{T}(x,y,z)$ evolving under the nonlinear incompressible Oberbeck-Boussinesq equations (4.1-4.3). The flow domain is bounded by two plates at temperature difference $\Delta\mathcal{T}$, seperated by H, and inclined by angle γ against the unit vector of gravity $\hat{\boldsymbol{g}} = -\sin(\gamma)\boldsymbol{e}_x - \cos(\gamma)\boldsymbol{e}_z$. Along the plates in the streamwise and spanwise dimensions, the domain is periodic over L_x and L_y. The characteristic time scale is the free-fall time unit $(H/g\,\alpha\,\Delta\mathcal{T})^{1/2}$. The nondimensional parameters are $\tilde{\nu} = (Pr/Ra)^{1/2}$ and $\tilde{\kappa} = (Pr\,Ra)^{-1/2}$ with Rayleigh number $Ra = g\,\alpha\,\Delta T\,H^3/(\nu\kappa)$ and Prandtl

number $Pr = \nu/\kappa$. Here, α is the thermal expansion coefficient, ν is the kinematic viscosity, and κ is thermal diffusivity. Turbulent ILC is studied at the control parameters $Ra = 3344$, $Pr = 1.07$ and $\gamma = 40°$.

DNS of the governing equations are done using the ILC extension module to the code *Channelflow 2.0* (Section 2). Matrix-free algorithms allow the construction, parametric continuation and stability analysis of invariant solutions, as described in Gibson et al. (2019). Numerical domains are discretized using N Fourier and Chebychev modes, implying a phase space with N dimensions. We consider numerical domains of three different sizes: the large domain $\Omega_1 : (L_x, L_y, H) = (26.7, 24.2, 1)$ with $N_x \times N_y \times N_z = 256 \times 256 \times 25 = 1.6 \cdot 10^6$, the intermediate domain $\Omega_2 : (L_x, L_y, H) = (4.4, 4.0, 1)$ with $N_x \times N_y \times N_z = 42 \times 42 \times 25 = 4.4 \cdot 10^4$, and the small domain $\Omega_3 : (L_x, L_y, H) = (4.4, 2.0, 1)$ with $N_x \times N_y \times N_z = 42 \times 20 \times 25 = 2.1 \cdot 10^4$. Domains Ω_2 and Ω_3 have been used recently to study invariant solutions in ILC at different control parameters (Reetz et al., 2019b). The choice of the numerical domain determines the observed level of dynamical complexity in DNS, namely spatio-temporal chaos in Ω_1, temporal chaos in Ω_2, and periodic bursting in Ω_3.

Spatio-temporal chaos in a large domain. DNS in Ω_1 reproduces a convection pattern first observed in experiments on ILC with large aspect ratio (Daniels et al., 2000, 2008) and described as crawling rolls or undulation chaos. If a domain is large enough, the bursting cycle of crawling rolls may be observed at different locations in space. Thus, a single snapshot from DNS in Ω_1 suffices to show the different stages of the bursting cycle at different locations at the same time (Fig. 6.1A-D). The spatial pattern at each location is compared with the spatial pattern at temporal instances along an unstable EPO found at the considered control parameters (Fig. 6.1a-d).

Temporal chaos in a small domain. DNS in Ω_2 shows chaotic dynamics suggesting the existence of a chaotic attractor. A phase portrait of the chaotic attractor together with the unstable EPO reveals a characteristic shape in the plane of kinetic energy and dissipation (Figure 6.2). The chaotic trajectory clearly resembles the shape of the EPO in this projection. Moreover, the EPO captures the dominant frequency of the dynamics and the mean statistics of the chaotic attractor (Figure 6.2).

This unstable periodic orbit is a paradigm of how unstable invariant solutions may be highly relevant for observed chaotic dynamics. Studying this periodic orbit allows furthermore to characterize the onset of turbulent crawling rolls in ILC.

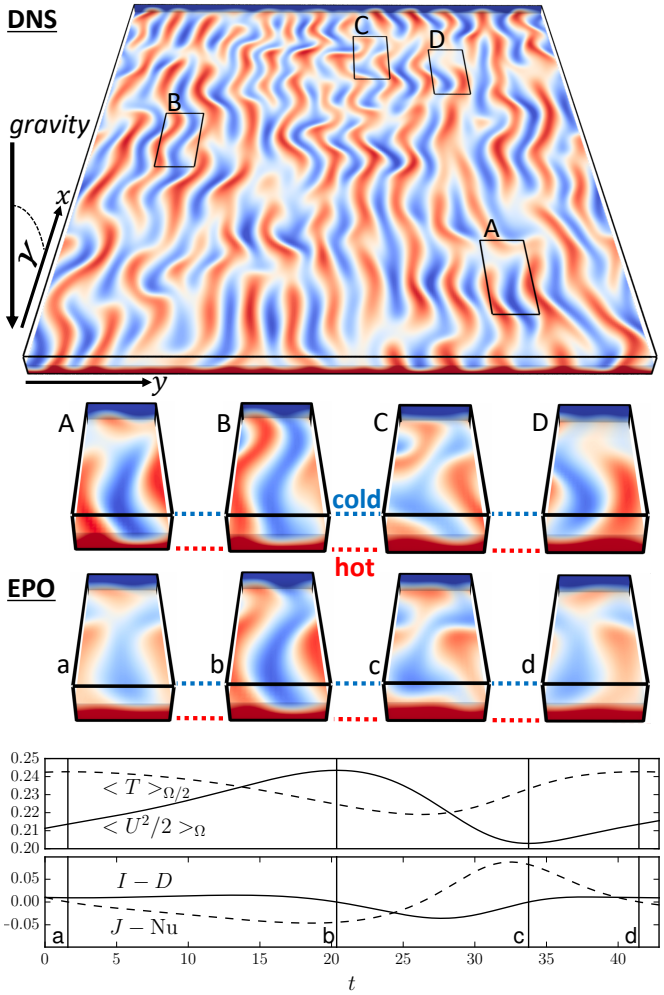

Figure 6.1 – Exact periodic orbit (EPO) captures a characteristic bursting cycle of turbulent inclined layer convection at $\gamma = 40°$ observed in direct numerical simulations (DNS). Instantaneous temperature patterns at different locations (A-D) in the large domain Ω_1 match the patterns of the EPO at different timings (a-d) in a small minimal domain Ω_3. The timings are indicated in the time series (vertical lines) of terms in the energy equations (4.13-4.15) over one orbit period. The EPO undergoes a nonlinear cycle of slow formation of wavy rolls (a-b), followed by a rapid burst of spanwise roll break-up (b-c), and regeneration of rolls with a defect at a different spatial phase (c-d). This nonlinear bursting cycle is also observed over time in the large domain turbulence.

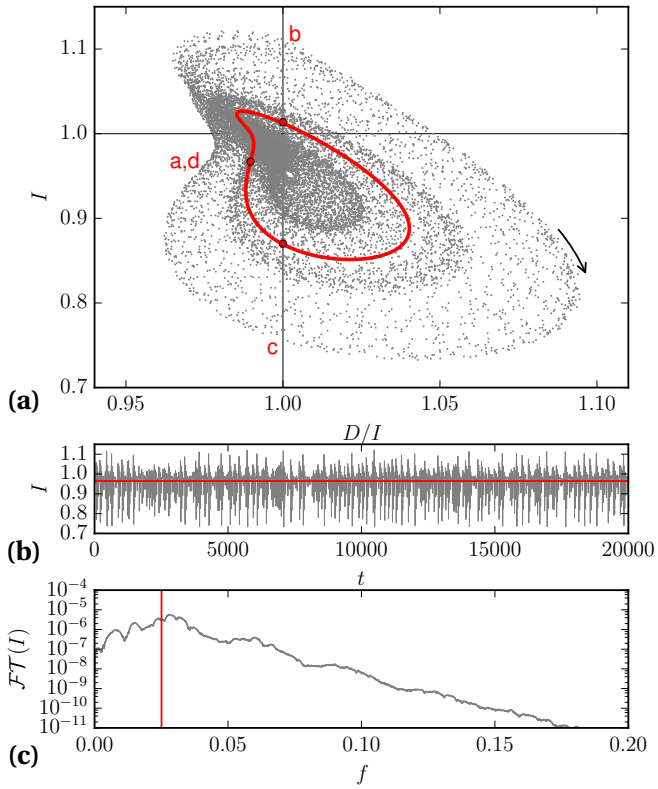

Figure 6.2 – **(a)** 'Phase portrait' of the chaotic attractor (grey dots) illustrates how chaotic inclined layer convection in the intermediate domain Ω_2 shadows the unstable EPO (red orbit with points referring to instances a-d in Fig. 6.1). The cloud of $20k$ dots represents $20k$ simulated time units. The chaotic time series from DNS **(b)** has the same mean energy input as the EPO, and the Fourier spectrum **(c)** peaks at the inverse pre-period of the EPO (red lines). Thus, the statistics of chaotic inclined layer convection is centered around the unstable EPO.

Part II
Oblique stripe patterns in plane Couette flow

7 Constructing invariant solutions with oblique patterns

Plane Couette flow (PCF) and inclined layer convection (ILC) are both shear flows between two extended parallel walls with a laminar flow that is anti-symmetric in the wall-normal direction. However, the physics of PCF are very different compared to ILC. ILC is driven by buoyancy forces which are absent in PCF. PCF is driven by moving the walls against each other. The laminar flow is linearly stable at all driving forces (Bayly et al., 1988). Other dynamical attractors are not known in PCF, except for a short range of wall velocities (Clever and Busse, 1997; Kreilos and Eckhardt, 2012). Thus, the approach to identify invariant solutions by following the temporal dynamics towards an attractor, as applied to ILC (Section 4), does not work in PCF. Various other approaches (see e.g. Kawahara et al., 2012, for a review) lead to a large collection of unstable invariant solutions in PCF (Gibson et al., 2009). None of the known invariant solutions captures the spatial features of oblique turbulent-laminar stripes (Section 1.3).

The starting point for finding an invariant solution that captures the spatial features of oblique turbulent-laminar stripes is the well-known Nagata equilibrium (Nagata, 1990; Clever and Busse, 1992; Waleffe, 1997). This equilibrium solution is the first invariant solution found in PCF. Two branches of the Nagata equilibrium emerge in a saddle-node bifurcation. The so-called 'upper branch' is connected to the dynamical attractor mentioned above. The 'lower branch' is always dynamically unstable. At control parameters where oblique stripe patterns are observed, the Nagata equilibrium in a minimal periodic domain has only a single unstable eigendirection and is thus an 'edge state' (Skufca et al., 2006; Schneider et al., 2007). In spanwise extended periodic domains of PCF, the 'edge states' are spanwise localized variants of the Nagata equilibrium that coexist with laminar flow (Schneider et al., 2010b) and may bifurcate from the spatially periodic Nagata equilibrium (Schneider et al., 2010a; Salewski et al., 2019). These and other localized invariant solutions have been proposed to represent the turbulent-laminar coexistence of transitional PCF (e.g. Brand and Gibson, 2014). These previous results motivate the following

Hypothesis: Spatially modulated variants of the Nagata equilibrium capture turbulent-laminar coexistence over a specific oblique period in space, thereby suggesting how weakly turbulent PCF selects wavelength and orientation for a regular oblique stripe pattern.

As for the turbulent patterns in ILC (Chapter 4), a minimal periodic domain is chosen to search for invariant solutions underlying the oblique stripe pattern in PCF. A suitable minimal domain is suggested by Barkley and Tuckerman (2005) who performed first DNS of oblique turbulent-laminar stripes. Their minimal periodic domain is tilted against the streamwise direction to align the domain orientation with the typically arising oblique orientation of stripes in experiments, i.e. $\theta = 24°$ against the streamwise direction. Along the statistically homogeneous direction of stripes, the domain is short with $L_x = 10$. Across the pattern, the domain is long with $L_z = 120$ (Barkley and Tuckerman, 2005) or $L_z = 40$ (Barkley and Tuckerman, 2007) and matches a typically observed pattern wavelength of $\lambda = 40$. Like for the turbulent patterns in ILC, the choice of a minimal domain is motivated by observations or analysis of patterns whose spatial features emerge under less constrained conditions. This is important because the analysis in a specific minimal domain prescribes the spatial features of the pattern. Nevertheless, a minimal domain representation is needed to reduce the size of the state space. Throughout this section, the analysis focuses on oblique stripe patterns in a minimal periodic domain of extent $[L_x, H, L_z] = [10, 2, 40]$ and tilted against the streamwise direction by $\theta = 24°$.

Invariant solutions have previously not been studied in tilted periodic domains. To construct a variant of the Nagata equilibrium in a tilted periodic domain, the following shear transformation is applied to the velocity field of the 'lower branch'-Nagata equilibrium at Re = 350 in a non-tilted domain of extent $[L_x, H, L_z] = [10, 2, 40/9]$ (Figure 7.1a):

$$\mathcal{S}_n[u, v, w](x, y, z) = \left[u, v, w + u\left(\frac{L_z}{L_x}\right)\right]\left(x, y, z + x\left(\frac{L_z}{L_x}\right)\right) . \tag{7.1}$$

Using the resulting velocity field as initial guess for a Newton-Krylov iteration in a tilted domain of extent $[L_x, H, L_z] = [10, 2, 40/9]$ and orientation $\theta = \tan^{-1}(L_x/L_z) = 24°$, the algorithm converges on a new invariant solution. This equilibrium solution has wavy velocity streaks aligned with the domain diagonal (Figure 7.1b). We refer to this equilibrium as the *tilted Nagata equilibrium*. It differs from the standard Nagata equilibrium in its symmetries. The tilted Nagata equilibrium has broken the shift-reflect and shift-rotate symmetries of the Nagata equilibrium (Gibson et al., 2008b) and is only invariant under three-dimensional inversion symmetry

$$\pi_i[u, v, w](x, y, z, t) = [-u, -v, -w](-x, -y, -z, t) . \tag{7.2}$$

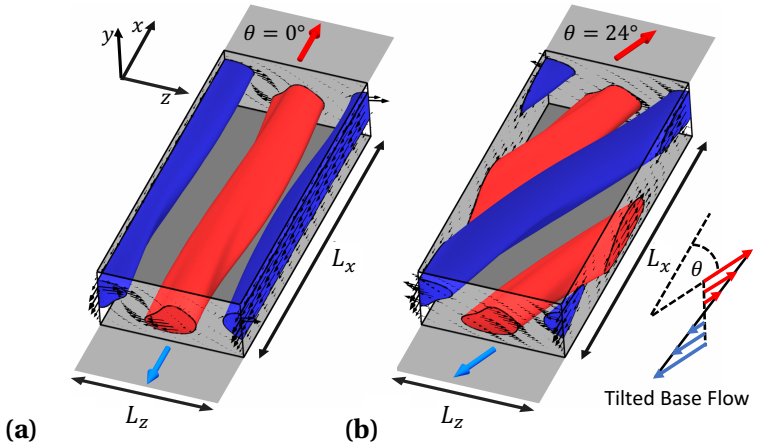

Figure 7.1 – Iso-surface in 3D of downstream velocity fluctuations around the base flow (red/blue: $u_s = \pm 0.3$) of the well-known Nagata equilibrium **(a)** and the constructed tilted Nagata equilibrium **(b)** at Re = 350. Both invariant solutions are x-z-periodic with $L_x = 10$ and $L_z = 40/9$, respectively. Boundary conditions at the lower and upper wall differ in the orientation of velocities. The tilted Nagata equilibrium requires tilted wall velocities with $\theta = \arctan(\lambda_z/\lambda_x) = 24°$. The corresponding tilted laminar base flow is sketched on the right.

Thus, the tilted Nagata equilibrium is an equilibrium solution that has not been described previously.

The tilted Nagata equilibrium is not only a solution in a periodic domain of extent $[L_x, H, L_z] = [10, 2, 40/9]$ but also in a domain of extent $[L_x, H, L_z] = [10, 2, 40]$ where nine copies of the flow structure repeat in space. Thus, a first invariant solution has been found that respects the same boundary conditions as oblique turbulent-laminar stripes. However, the tilted Nagata equilibrium is still spatially periodic on a scale of the gap height rather than of oblique stripes. A spatially modulated variant of the tilted Nagata equilibrium is obtained by applying a particular windowing function (Gibson and Brand, 2014; Beaume et al., 2016). Attempts using analytically defined windowing functions failed due to not capturing the intricate three-dimensional structure of the oblique turbulent-laminar interfaces (Barkley and Tuckerman, 2007; Duguet and Schlatter, 2013). Therefore, a statistically defined windowing function is used. The three-dimensional mean field of turbulent kinetic energy $\langle \boldsymbol{u}^2 \rangle_t(x, y, z) = 1/T \int_0^T \boldsymbol{u}^2(x, y, z, t)\, dt$ of a single stripe period is computed via DNS in a tilted minimal domain with $\theta = 24°$ and $[L_x, H, L_z] = [10, 2, 40]$ over a period of $T = 5500$. Additionally, the DNS are confined to the symmetry subspace of π_i (7.2) which is found to still allow the formation of self-organized turbulent-laminar stripes. In this subspace, the envelope of the stripe pattern cannot drift in the x- or z-dimension, as observed by Barkley and Tuckerman (2007), because the inversion symmetry fixes the spatial phase of the pattern envelope. Simulating patterns with a fixed spatial phase allows us to combine mean energy fields of turbulent-laminar stripes from several

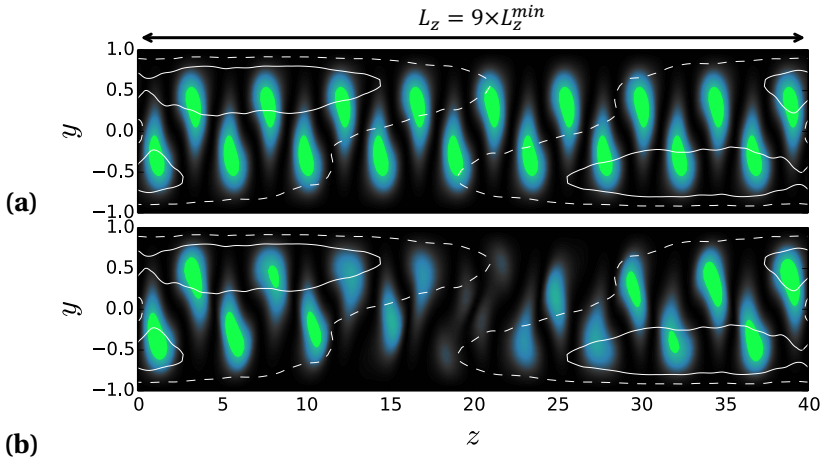

Figure 7.2 – Contours of the statistical window function $W(x,y,z)$ (white lines, solid: $W = 1$, dashed: $W = 0.25$), defined in (7.3), overlying the contours of kinetic energy of periodically extended tilted Nagata equilibrium **(a)** and the converged modulated equilibrium solution in **(b)**, all in a y-z-cross-section at $x = 0$.

DNS runs in an ensemble average. The window function is given by the three-dimensional scalar field

$$W(x,y,z) = 1.4\langle \boldsymbol{u}^2 \rangle_t / \max(\langle \boldsymbol{u}^2 \rangle_t) \; . \tag{7.3}$$

The product of W with the tilted Nagata equilibrium in the domain $[L_x, H, L_z] = [10, 2, 40]$ represents an initial guess for a Newton-Krylov iteration with Hookstep optimization that yields an obliquely patterned equilibrium solution (Figure 7.2). We refer to this equilibrium as *stripe equilibrium*.

The windowing approach discussed above may yield a second, in some sense complementary, stripe equilibrium. The tilted Nagata equilibrium is invariant under π_i with respect to two different symmetry points along one streamwise wavelength of its wavy velocity streaks. Shifting the tilted Nagata equilibrium by half a streamwise wavelength results in a velocity field that is again invariant under π_i. Thus, the π_i-symmetric windowing function $W(x,y,z)$ can be multiplied with two different π_i-symmetric velocity fields of the tilted Nagata equilibrium such that the symmetry points of velocity field and of windowing function $W(x,y,z)$ coincide. Newton-Krylov iteration converges for both initial guesses to a π_i-symmetric stripe equilibrium. The spatial structure of the two different stripe equilibria is visualized in Figure 7.3. The mean amplitude modulation along the z-dimension indicates that the two stripe equilibria have the same large-scale modulation but 'opposite' small-scale modulation (Figure 7.3e). Velocity and vorticity contours at midplane of the two stripe equilibria and the two differently tilted Nagata equilibria illustrate different internal 'topological' structures (Figure 7.3a-d). The green lines

connect vorticity maxima or minima with each other and guide the eye along wavy velocity streaks of equal streamwise phase. These green lines have the same topology in panels (b-d) but a different one in panel (a), showing the tilted Nagata equilibrium that has been combined with the windowing function $W(x, y, z)$ to construct the stripe equilibrium. The following section discusses how the stripe equilibrium in panel (d) can be connected via a bifurcation to the Nagata equilibrium in a tilted domain, having the same internal topological structure as the equilibrium in panel (b). The stripe equilibrium in panel (c) cannot be connected via a bifurcation to an equilibrium like in panel (b). The reason is that this stripe equilibrium has 10 vorticity minima, like the equilibrium solutions in panel (b) and (d), but only 9 vorticity maxima. This structural difference was not found to change under numerical continuations.

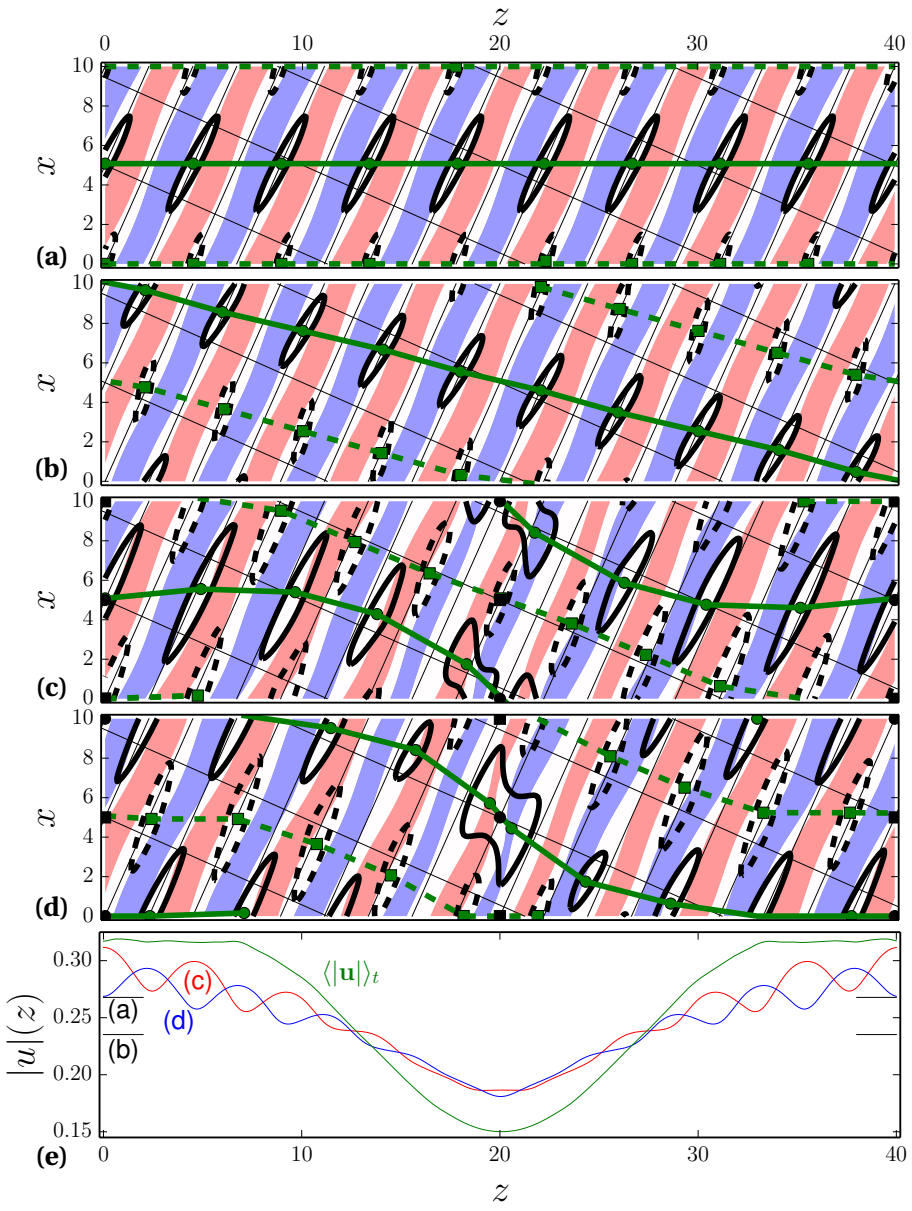

Figure 7.3 – Four different equilibrium solutions of PCF at Re = 350 in a tilted periodic domain with $\theta = 24°$ and $[L_x, H, L_z] = [10, 2, 40]$. Figure **(a-d)** show contours of streamwise velocity and vorticity at midplane ($y = 0$). The grey grid indicates streamwise and spanwise directions. Green lines connect neighboring vorticity maxima or minima to guide the eye along wave fronts of the wavy velocity streaks with equal streamwise phase. Panel **(e)** shows the amplitude modulation of the two stripe equilibria in panel **(c)** and **(d)** and of the mean kinetic energy field of stripes, used to define the windowing function in (7.3), in terms of $|u|(z) = (2L_x)^{-1/2}(\int \mathbf{u}^2 dxdy)^{1/2}$. The unpatterned tilted Nagata equilibrium solutions in panel **(a)** and **(b)** are shown in terms of the total velocity norm $||u||_2 = (2L_xL_z)^{-1/2}(\int \mathbf{u}^2 dxdydz)^{1/2}$.

8 Equilibrium solution underlying oblique turbulent-laminar stripes

Remark This chapter is largely inspired by the publication of the name "Exact invariant solution reveals the origin of self-organized oblique turbulent-laminar stripes".

Florian Reetz[1], Tobias Kreilos[1] and Tobias M. Schneider[1]

[1]Emergent Complexity in Physical Systems Laboratory (ECPS),
École Polytechnique Fédérale de Lausanne, CH 1015 Lausanne, Switzerland

Nature Communications **10**, Article number: 2277 (2019)

Chapter summary

Wall-bounded shear flows transitioning to turbulence may self-organize into alternating turbulent and laminar regions forming a stripe pattern with non-trivial oblique orientation. Different experiments and flow simulations identify oblique stripe patterns as the preferred solution of the well-known Navier-Stokes equations, but the origin of stripes and their oblique orientation remains unexplained. In concluding his lectures, Feynman highlights the unexplained stripe pattern hidden in the solution space of the Navier-Stokes equations as an example demonstrating the need for improved theoretical tools to analyze the fluid flow equations. Here we exploit dynamical systems methods and demonstrate the existence of an exact equilibrium solution of the fully nonlinear 3D Navier-Stokes equations that resembles oblique stripe patterns in plane Couette flow. The stripe equilibrium emerges from the well-studied

Nagata equilibrium and exists only for a limited range of pattern angles. This suggests a mechanism selecting the non-trivial oblique orientation angle of turbulent-laminar stripes.

8.1 Introduction

The complex laminar-turbulent transition in wall-bounded shear flows is one of the least understood phenomena in fluid mechanics. In the simple geometry of plane Couette flow (PCF), the flow in a gap between two parallel plates moving in opposite directions, the transitional flow spontaneously breaks the translational symmetries in both the streamwise and the spanwise direction causing regions of turbulent and laminar flow to coexist in space (Lundbladh and Johansson, 1991; Tillmark and Alfredsson, 1992; Daviaud et al., 1992; Lemoult et al., 2016; Couliou and Monchaux, 2017). Remarkably, the flow may further self-organize into a regular pattern of alternating turbulent and laminar stripes (Prigent et al., 2002; Barkley and Tuckerman, 2005, 2007; Duguet et al., 2010; Tuckerman and Barkley, 2011; Philip and Manneville, 2011; Ishida et al., 2017) also observed in Taylor-Couette (Coles, 1965; Andereck et al., 1986; Hegseth et al., 1989; Prigent et al., 2002; Meseguer et al., 2009; Dong, 2009) and channel flow (Tsukahara et al., 2005; Hashimoto et al., 2009; Aida et al., 2011; Tuckerman et al., 2014; Xiong et al., 2015). The wavelength of these stripes or bands is much larger than the gap size, the only characteristic scale of the system, and they are oblique with respect to the streamwise direction. Consequently, both the large-scale wavelength and the oblique orientation of turbulent-laminar stripes must directly follow from the flow dynamics captured by the governing Navier-Stokes equations. Experiments and numerical flow simulations reliably generate stripe patterns but a theory explaining the origin of the pattern characteristics is still missing. This is related to the Navier-Stokes equations being highly nonlinear partial differential equations, whose theoretical analysis remains challenging.

It was the early observation that an oblique turbulent-laminar pattern can be the preferred solution of the Navier-Stokes equations that motivated R. Feynman to stress the lack of "mathematical power [of his time] to analyze [the Navier-Stokes equations] except for very small Reynolds numbers" (Feynman et al., 1964). Recent advances in numerical methods not only allow the simulation of flows but also the construction of exact equilibria, traveling waves and periodic orbits of the fully nonlinear 3D Navier-Stokes equations. These exact invariant solutions are believed to be embedded in a strange invariant set generating the chaotic dynamics of turbulent flow in the system's state space (Lanford, 1982). Consequently, a picture emerges where turbulent flow is described as a chaotic walk between dynamically unstable invariant solutions which together with their entangled stable and unstable manifolds support the turbulent dynamics (Gibson et al., 2008b). Exact invariant solutions are thus 'building blocks' which resemble characteristic flow structures that are observed in flow simulations and experiments, when the dynamics transiently visits the exact invariant solution. A theoretical

explanation of oblique stripe patterns within this dynamical systems description requires the as yet unsuccessful identification of exact invariant solutions resembling the detailed spatial structure of turbulent-laminar stripes, including their oblique orientation and large-scale periodicity.

Nagata discovered the first invariant solution of PCF (Nagata, 1990; Clever and Busse, 1992; Waleffe, 1998). Like most invariant solutions of PCF found since then (Gibson et al., 2009), this so-called Nagata equilibrium is periodic in the streamwise and spanwise directions, repeating on the scale of the gap height. Such periodic solutions do not capture the coexistence of turbulent and laminar flow on scales much larger than the gap height and consequently cannot underly oblique stripes. Spanwise localized invariant solutions (Schneider et al., 2010a; Gibson and Brand, 2014) and doubly localized invariant solutions in extended periodic domains (Brand and Gibson, 2014) show nonlinear flow structures coexisting with laminar flow but no known invariant solution captures oblique orientation or suggests a pattern wavelength matching oblique stripe patterns.

We present a fully nonlinear equilibrium solution of PCF (Fig. 8.1b), resembling the oblique stripe pattern observed in direct numerical simulations (Fig. 8.1a). Parametric continuation demonstrates that this stripe equilibrium is connected to the well-studied Nagata equilibrium via two successive symmetry-breaking bifurcations, and that its existence is limited to oblique orientations.

8.2 Results

8.2.1 Simulating stripe patterns

For direct numerical simulations (DNS) of oblique stripe patterns in PCF we use a parallelized version of the pseudo-spectral code CHANNELFLOW (Gibson et al., 2008b, 2019). The numerical domain is periodic in two perpendicular dimensions along the plates (x and z) with periods of $(L_x, L_z) = (10, 40)$ in units of half the gap height. No-slip boundary conditions are imposed at the moving plates located at $y = \pm 1$. Inversion symmetry with respect to the domain center is enforced. The relative plate velocity and the associated base flow are tilted against the periodic domain dimensions at an angle of $\theta = 24°$ following Barkley and Tuckerman (2005). At Reynolds number $\mathrm{Re} = Uh/\nu = 350$, with the relative plate velocity $2U$, gap height $2h$ and kinematic viscosity ν the flow organizes into self-sustained turbulent-laminar stripes, as shown in Fig. 8.1a, where we periodically repeat the computational domain to highlight the large-scale structure of the pattern.

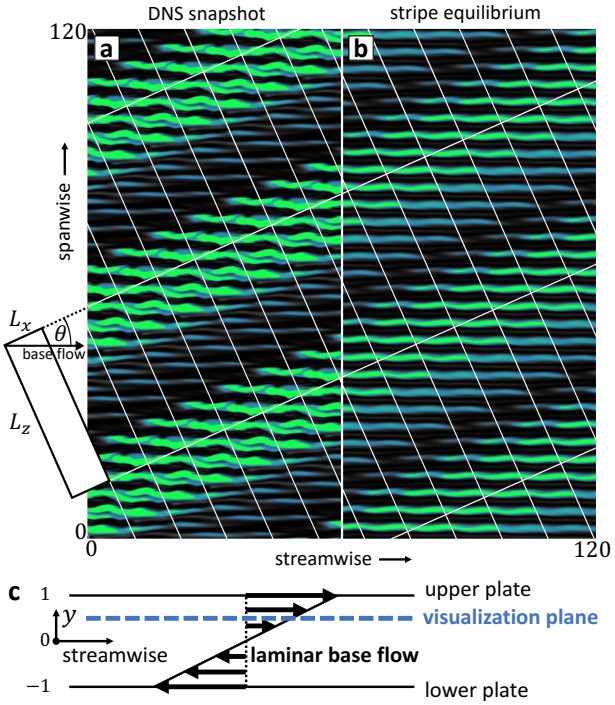

Figure 8.1 – Equilibrium solution underlies turbulent-laminar stripes. **a** The self-organized pattern of oblique turbulent-laminar stripes is observed in direct numerical simulations of plane Couette flow at Re = 350. Following Barkley and Tuckerman (2005) a tilted x-z-periodic domain outlined on the left side with $(\theta, L_x, L_z) = (24°, 10, 40)$ is used for computations. **b** The observed stripe pattern is captured by an exact invariant equilibrium solution of the fully nonlinear 3D Navier-Stokes equations. The contours are turbulent kinetic energy saturating at $\mathbf{u}^2 = 0.25$ (green), where $\mathbf{u}$ is the velocity fluctuation field around the laminar base flow (**c**). The plane of visualization is at 3/4 of the gap height.

8.2.2 Equilibrium resembling stripes

An invariant equilibrium solution capturing the stripes was found by introducing a large-scale amplitude modulation to a known spatially periodic equilibrium using a suitable window function, similar to Gibson and Brand (2014). Specifically, the Nagata equilibrium was periodically extended in the spanwise direction for $n = 9$ periods, then sheared to align the velocity streaks with the base flow in the tilted domain and finally multiplied with a scalar window function equal to a scaled mean field of turbulent kinetic energy of the oblique stripe pattern from several DNS runs. Using the constructed velocity field as initial guess, Newton iteration yields the stripe equilibrium (Fig. 8.1b).

The stripe equilibrium shares the small-scale wavy modulation with the Nagata equilibrium but also shows the large-scale oblique amplitude modulation of the turbulent-laminar stripe

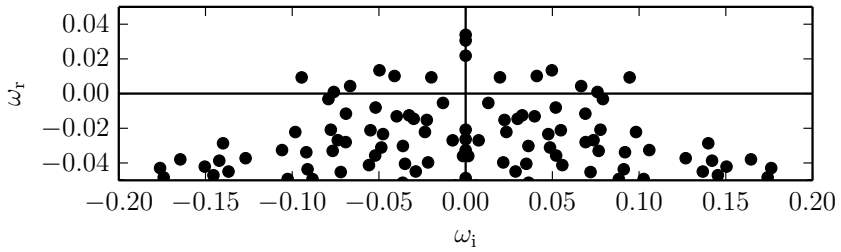

Figure 8.2 – Eigenvalue spectrum characterising the linear stability of the stripe equilibrium. Shown are the 100 leading eigenvalues in the complex plane $(\omega_\mathrm{r}, \omega_\mathrm{i})$, computed by Arnoldi iteration at Re = 350 (Gibson et al., 2019). 15 eigenvalues with a positive real part $\omega_\mathrm{r} > 0$ quantify the exponential growth rate ω_r along the unstable directions in the linear eigenspace of the stripe equilibrium. The imaginary parts ω_i quantify the oscillatory frequencies in the eigenspace and the absolute values indicate typical turbulent time scales in the flow in units of U/h. The wide aspect ratio of the spectrum (uniform axes) graphically illustrates that the maximum growth rate $\omega_r = 0.034$ is small compared to the typical turbulent time scales. The stripe equilibrium shown in Fig. 1b is thus weakly unstable.

pattern. The amplitude modulation between the high-amplitude turbulent region and the low-amplitude laminar region of the equilibrium on average follows a sinusoidal profile closely resembling the pattern mean flow found in DNS at identical boundary conditions (Barkley and Tuckerman, 2007). The stripe equilibrium moreover captures detailed features of the turbulent-laminar interfaces. A base flow directed into a turbulent region leads to a sharper 'upstream' interface than a base flow directed out of a turbulent region at a 'downstream' interface. The direction of the base flow is reversed for $y \to -y$. An upstream interface in the upper half thus corresponds to a downstream interface in the lower one. This gives rise to so-called overhang regions (Lundbladh and Johansson, 1991; Duguet and Schlatter, 2013) and an asymmetry between the left and right interface in Fig. 8.1 where turbulent kinetic energy is visualized at $y = 0.5$ above the midplane. Finally, the stripe equilibrium is symmetric under inversion $\sigma_\mathrm{i}[u, v, w](x, y, z) = [-u, -v, -w](-x, -y, -z)$, a symmetry also found for the mean flow of stripe patterns (Barkley and Tuckerman, 2007). The sinusoidal amplitude modulation, the captured overhang regions and the inversion symmetry, all characteristic of the pattern's mean flow, together with the visual comparison in Fig. 8.1 show that the stripe equilibrium has the spatial features of the oblique stripe pattern. We have thus identified a first exact invariant solution underlying oblique turbulent-laminar patterns.

The unstable eigenspace of the evolution operator linearized around the equilibrium is spanned by 15 directions. The remaining $\sim 10^6$ directions are attracting. Consequently, the dynamics is attracted towards the stripe equilibrium from almost all directions. The exponential growth rates ω_r along the unstable directions are small compared to typical turbulent time scales in the flow, given by the oscillatory frequencies ω_i in the spectrum of eigenvalues

(Fig. 8.2). The low dimensional unstable eigenspace and the small exponential growth rates suggest a weakly unstable exact invariant solution that is a dynamically relevant transiently visited 'building block' of the chaotic saddle underlying the turbulent flow.

8.2.3 Origin of the equilibrium

At small scales the stripe equilibrium reflects the wavy streak structure of the spatially periodic Nagata equilibrium. This suggests that the stripe equilibrium emerges from the Nagata equilibrium in a bifurcation creating oblique long-wavelength modulations. To identify this pattern-forming bifurcation numerically, the Nagata equilibrium needs to 'fit' in an extended tilted periodic domain aligned with the wave-vector of the neutral mode creating the oblique long-wavelength modulation. The Nagata equilibrium indeed not only satisfies the stream- and spanwise periodic boundary conditions of the commonly studied minimal flow domain but may also be periodic with respect to selected larger tilted domains. The symmetry group of the Nagata equilibrium, including all combined discrete translations over streamwise-spanwise periods $(\lambda_{\mathrm{st}}, \lambda_{\mathrm{sp}})$, intersects with the group of translations of a tilted rectangular domain, with periodicity (L_x, L_z), if

$$L_x = \frac{k\,\lambda_{\mathrm{st}}}{\cos\theta} = \frac{l\,\lambda_{\mathrm{sp}}}{\sin\theta}\,, \quad L_z = \frac{m\,\lambda_{\mathrm{st}}}{\sin\theta} = \frac{n\,\lambda_{\mathrm{sp}}}{\cos\theta} \tag{8.1}$$

is satisfied for $(k,l,m,n) \in \mathbb{N}$ and $0 < \theta < \pi/2$. Geometrically, condition (8.1) describes how the x-z coordinate lines of the tilted domain wind on a torus defined by the streamwise-spanwise periodic minimal domain. The condition is satisfied if the coordinate lines are closed curves (Fig. 8.3a). For the domain $(\theta, L_x, L_z) = (24^\circ, 10, 40)$ considered so far, the geometric condition (8.1) implies wavelengths $(\lambda_{\mathrm{st}}, \lambda_{\mathrm{sp}}) = (1.02, 4.06)$ at which the Nagata equilibrium does not exist. Keeping $L_z = 40$ and choosing winding numbers $(k,l,m,n) = (1,1,1,9)$ however leads to a slightly modified domain $(\theta, L_x, L_z) = (18.4^\circ, 40/3, 40)$ in which the Nagata equilibrium with $(\lambda_{\mathrm{st}}, \lambda_{\mathrm{sp}}) = (12.65, 4.22)$ exists, as displayed in Fig. 8.3b. On the lower branch of the Nagata equilibrium close to the saddle-node bifurcation, there is a pitchfork bifurcation at $\mathrm{Re}_{\mathrm{I}} = 164$. Its neutrally stable long-wavelength eigenmode, whose eigenvalue changes sign at Re_{I}, is plotted in Fig. 8.3c. This is the initial pattern-forming bifurcation creating oblique amplitude modulations on the Nagata equilibrium.

Using parametric continuation we follow both the periodic Nagata equilibrium (named $\mathcal{A}$ hereafter) and the emerging modulated equilibrium solution ($\mathcal{B}$) from its primary bifurcation point at $(\mathrm{Re}, \theta, L_x)_{\mathrm{I}} = (164, 18.4^\circ, 40/3)$ to the parameters $(\mathrm{Re}, \theta, L_x)_{\mathcal{C}} = (350, 24^\circ, 10)$ of the stripe equilibrium ($\mathcal{C}$). In the three-dimensional parameter space we choose a continuation path parametrized by tilt angle θ with the Reynolds number linear in θ, such that $\mathrm{Re}(\theta) = (\mathrm{Re}_{\mathrm{I}}(\theta_{\mathcal{C}} - \theta) + \mathrm{Re}_{\mathcal{C}}(\theta - \theta_{\mathrm{I}}))\,/\,(\theta_{\mathcal{C}} - \theta_{\mathrm{I}})$ and domain length $L_x(\theta) = L_z/(n\tan(\theta))$ for $n = 9$ and

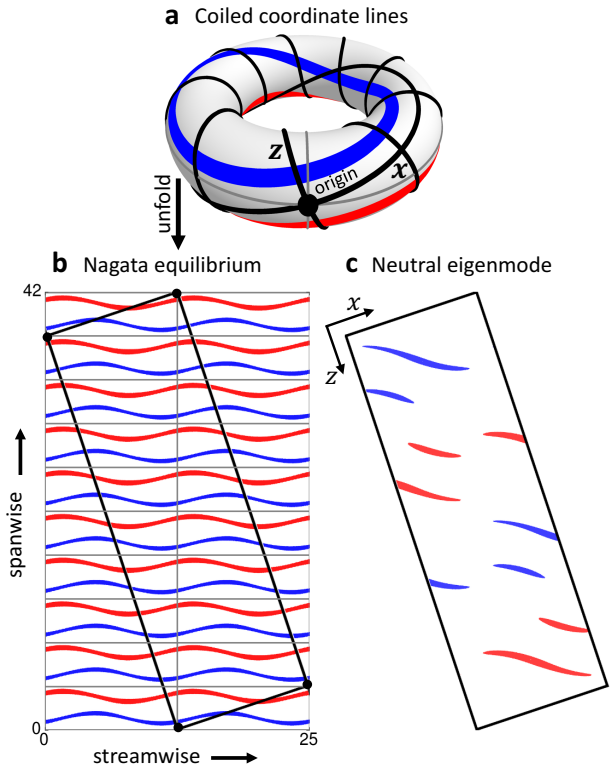

Figure 8.3 – Instability of the Nagata equilibrium creates oblique amplitude modulations. **a** Torus representing a streamwise-spanwise periodic domain. If tilted rectangular coordinate lines x and z (black) close on themselves, all solutions on the torus also respect the periodicity of a domain spanned by those lines. Specifically, the Nagata equilibrium with streamwise-spanwise periodicity $(\lambda_{st}, \lambda_{sp}) = (12.65, 4.22)$ (grey lines) is also periodic with respect to the tilted domain (black) with $(\theta, L_x, L_z) = (18.4°, 40/3, 40)$, shown in **b** for $\mathrm{Re}_I = 164$. In this tilted domain, a bifurcation with neutral eigenmode (**c**) can be detected at Re_I. This bifurcation introduces oblique long-wavelength amplitude modulations on the Nagata equilibrium. Red (blue) contours represent positive (negative) streamwise velocity in the midplane.

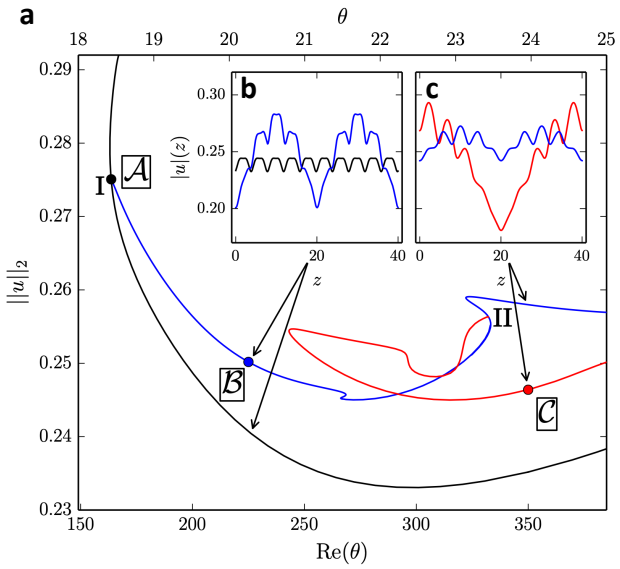

Figure 8.4 – Pattern forming bifurcations give rise to the stripe equilibrium. **a** A sequence of pattern-forming bifurcations from the small-scale periodic Nagata equilibrium $\mathcal{A}$ (Fig. 8.3b) leads to the large-scale modulated stripe equilibrium $\mathcal{C}$ (Fig. 8.1b). The solution branches are plotted in terms of the domain averaged velocity square $||u||_2 = (2L_xL_z)^{-1/2}(\int \mathbf{u}^2 dxdydz)^{1/2}$ over linearly coupled bifurcation parameters θ (top axis) and $\mathrm{Re}(\theta)$ (see text). A primary pattern-forming bifurcation on $\mathcal{A}$ at $(\mathrm{Re},\theta,L_x)_{\mathrm{I}} = (164, 18.4°, 40/3)$ creates equilibrium $\mathcal{B}$ with double-pulse profile of x-y averaged squared velocity $|u|(z) = (2L_x)^{-1/2}(\int \mathbf{u}^2 dxdy)^{1/2}$ (inset panel **b**). A secondary pattern-forming bifurcation at $(\mathrm{Re},\theta,L_x)_{\mathrm{II}} = (332, 23.4°, 10.3)$ creates the single-pulse solution branch of equilibrium $\mathcal{C}$ (inset panel **c**). Points mark the exact invariant solutions shown in Fig. 8.5.

constant domain width of $L_z = 40$. The resulting bifurcation diagram demonstrates that the Nagata equilibrium $\mathcal{A}$, is connected to the stripe equilibrium $\mathcal{C}$ (Fig. 8.4).

The primary bifurcation is of pitchfork type, subcritical, forward in Re and breaks the streamwise-spanwise translation symmetry of $\mathcal{A}$. Along the bifurcating branch of $\mathcal{B}$ significant amplitude modulations of the small scale periodic signal form with period $L_z/2$ along z, as indicated by the double-pulse profile of the z-dependent and x-y-averaged fluctuations $|u|(z)$ at $\mathrm{Re} = 225$ in Fig. 8.4b. The modulation period reflects a discrete translation symmetry $\sigma_{\mathcal{B}}$ over half the domain diagonal, $\sigma_{\mathcal{B}}[u,v,w](x,y,z) = [u,v,w](x+L_x/2, y, z+L_z/2)$. Equilibrium $\mathcal{B}$ inherits this symmetry from $\mathcal{A}$ because $\sigma_{\mathcal{B}}$ is not broken by the neutral mode of the primary bifurcation (Fig. 8.3c).

A secondary pattern-forming bifurcation occurs at $(\mathrm{Re},\theta,L_x)_{\mathrm{II}} = (332, 23.4°, 10.3)$ along solution branch $\mathcal{B}$ (blue line in Fig. 8.4). This subcritical pitchfork bifurcation breaks the translation symmetry $\sigma_{\mathcal{B}}$. The spatial period of the amplitude modulation is doubled and gives

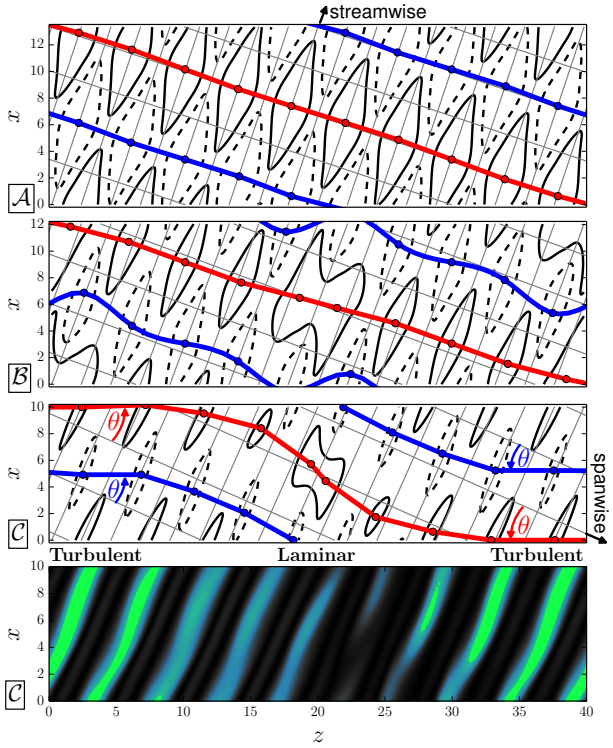

Figure 8.5 – Phase modulations along the bifurcation sequence. Streamwise vorticity $\omega_{\text{st}} = (\cos(\theta)\mathbf{e}_x + \sin(\theta)\mathbf{e}_z)\cdot\nabla\times\mathbf{u}$ at the midplane (black solid/dashed contours at $\omega_{\text{st}} = \pm 0.12$) encodes streamwise phase information of wavy streak modulations for equilibria $\mathcal{A}$, $\mathcal{B}$ and $\mathcal{C}$ along the bifurcation sequence (points in Fig. 8.4). Red (blue) lines connecting vorticity maxima (minima) represent wave fronts of constant streamwise phase. The Nagata equilibrium $\mathcal{A}$ has wave fronts oriented in the spanwise direction. The stripe equilibrium $\mathcal{C}$ has sigmoidal wave fronts. In the turbulent region the wave fronts are oriented at $\theta = 24°$ (red/blue arrows), and align with the pattern wave vector (in the z-direction). Bottom panel indicates turbulent and laminar regions in $\mathcal{C}$ (see also Fig. 8.1b).

rise to solution branch $\mathcal{C}$ forming a single-pulse equilibrium. Solution branch $\mathcal{C}$ (red line in Fig. 8.4) reaches $\text{Re}_{\mathcal{C}} = 350$ after undergoing an additional saddle-node bifurcation at $(\text{Re}, \theta, L_x) = (243, 20.8°, 11.7)$. The amplitude profiles of single- and double-pulse equilibria show that the single-pulse with period $L_z = 40$ has large modulations at $\text{Re} = 350$ and $\theta = 24°$, while the modulations in the double-pulse equilibrium are reduced (Fig. 8.4c). This agrees with the observations that stripes tend to have pattern wavelengths λ in the range of $40 \le \lambda \le 60$ at Re around 350 (Prigent et al., 2002; Tuckerman and Barkley, 2011). In summary, two bifurcations successively break discrete translation symmetries of the Nagata equilibrium to create the stripe equilibrium solution.

Small-scale velocity streaks carry a wavy modulation which has a streamwise phase that is clearly evident when plotting the streamwise vorticity at the midplane. We illustrate streamwise wave fronts by lines connecting vorticity maxima or minima in the spanwise direction (red/blue lines in Fig. 8.5). Straight and strictly spanwise oriented wave fronts indicate a constant streamwise phase of all streaks of the (spanwise periodic) Nagata equilibrium $\mathcal{A}$. The primary pattern forming bifurcation from $\mathcal{A}$ to $\mathcal{B}$ introduces local phase shifts which dislocate vorticity extrema away from a straight alignment and bend the wave front. The dislocations introduced into $\mathcal{B}$ are symmetric with respect to half-domain translations $\sigma_{\mathcal{B}}$ and centered at $z = 0$ and $z = 20$. For the stripe equilibrium $\mathcal{C}$ formed from $\mathcal{B}$ in the second pattern forming bifurcation, the topology of the wave fronts is preserved but they are geometrically deformed into sigmoidal structures.

In the turbulent region of equilibrium $\mathcal{C}$, the wave fronts of the wavy streaks are skewed at $\theta = 24°$ against the spanwise direction and oriented exactly along the pattern wave vector ($\mathcal{C}$ in Fig. 8.5). Assuming that all exact invariant solutions underlying stripe patterns show this alignment of wave fronts in the turbulent region with the pattern orientation, we conjecture that the range of possible skewing angles Nagata-type equilibria can sustain (Gibson and Schneider, 2016) limits the range of angles at which oblique stripe patterns can exist.

8.2.4 Pattern angle selection

We identified equilibrium $\mathcal{C}$ at pattern angle $\theta = 24°$. Continuation in θ for fixed pattern wavelength $\lambda = 40$ determines the range in θ for which the stripe equilibrium exists. At Re = 350, the equilibrium exists in the range $16.5° \leq \theta \leq 26.1°$ before it undergoes saddle-node bifurcations (Fig. 8.6). Outside this range the stripe equilibrium is not sustained. The range of orientation angles over which the stripe equilibrium exists agrees with the range over which oblique stripe patterns of wavelength $\lambda = 40$ are observed in simulations (Barkley and Tuckerman, 2007). At lower Re, the range of allowed pattern angles shrinks and shifts towards larger values (Fig. 8.6). This trend of allowed θ for varying Re aligns with simulations and experiments of turbulent-laminar stripes (Barkley and Tuckerman, 2007). The finite existence range of the fully nonlinear exact equilibirum solution of the 3D Navier-Stokes equations thus appears to select the non-trivial angle at which self-organized turbulent-laminar stripes emerge in transitional shear flows.

8.3 Discussion

Experimental and numerical observations of self-organized oblique turbulent-laminar stripes in wall-bounded extended shear flows suggest the existence of exact invariant solutions

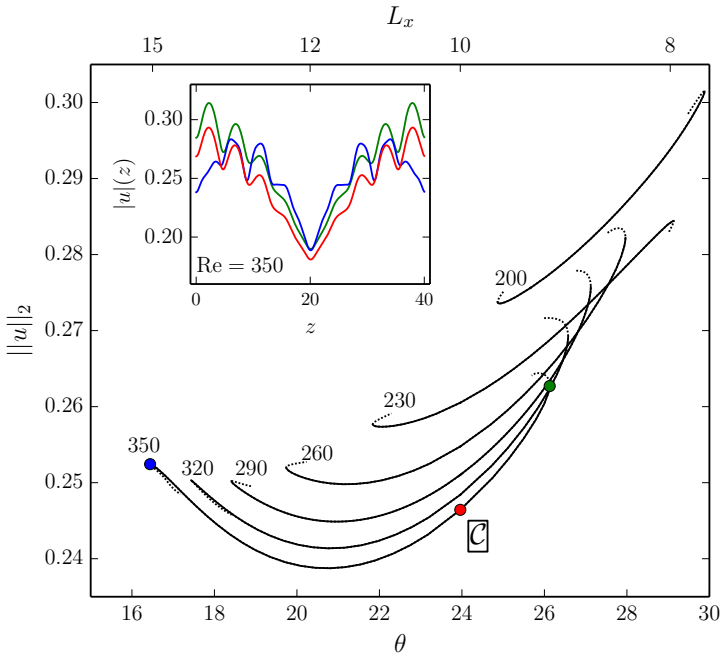

Figure 8.6 – Range of pattern orientation angle θ for which the stripe equilibrium $\mathcal{C}$ exists. Parametric continuations in θ at constant $L_z = 40$ implying $L_x \sim \tan^{-1}(\theta)$ (top axis). The solution branches are labeled by Re which remains fixed for each continuation. Beyond saddle-node bifurcations only the initial part of the branches are plotted (dotted lines). Along the remaining parts of the branches (not shown), the equilibrium solutions no longer represent the stripe pattern. The inset displays the amplitude profiles at selected points along the branch (like in Fig. 8.4). For θ increasing towards the upper saddle-node the amplitude of the profile $|u|(z)$ rises globally at all z; for θ decreasing towards the lower saddle-node the amplitude maximum decreases. At intermediate angles close to $\theta = 24°$ the equilibrium best represents turbulent-laminar stripes.

underlying these patterns. We present the first such invariant solution of the fully nonlinear 3D Navier-Stokes equations in plane Couette flow that captures the detailed spatial structure of oblique stripe patterns. The stripe equilibrium emerges from the known Nagata equilibrium via a sequence of two pattern-forming bifurcations with long-wavelength oblique neutral modes. The existence of the stripe equilibrium at wavelength $\lambda = 40$ is limited to oblique orientations in a finite range of pattern angles around $\theta = 24°$. The existence range agrees with simulations and experimental observations of turbulent-laminar stripes. This suggests a selection mechanism for the pattern angle and provides a route towards explaining why turbulent-laminar stripes are oblique.

9 Periodic orbits with oblique patterns in the edge of chaos

Remark This chapter is largely inspired by a pre-print of the name "Periodic orbits with oblique patterns in transitional plane Couette flow".

Florian Reetz[1] and Tobias M. Schneider[1]

[1]Emergent Complexity in Physical Systems Laboratory (ECPS),
École Polytechnique Fédérale de Lausanne, CH 1015 Lausanne, Switzerland

Under consideration for publication in *Physical Review Fluids*

9.1 Introduction

Transitional turbulence in linearly stable wall-bounded shear flows may segregate into laminar and turbulent regions. The spatial coexistence of turbulent and laminar flow has been observed in pipes with one extended space dimension (Barkley, 2016) and in planar shear flows with two extended space dimensions (Tuckerman et al., 2020). The properties of turbulent-laminar coexistence have been studied extensively, both, in terms of statistical laws describing a non-equilibrium phase transition (Lemoult et al., 2014; Chantry et al., 2017) and in terms of the dynamics at the interfaces between laminar and turbulent regions (Barkley, 2011; Duguet and Schlatter, 2013). For intermediate strength of driving, turbulent and laminar regions in wall-bounded shear flows may self-organize into a regular pattern of spatially periodic stripes or bands oriented obliquely relative to the laminar flow direction. Oblique stripe patterns have been observed experimentally and numerically in various wall-bounded shear flows suggesting universal mechanisms that create a regular pattern in a turbulent flow (Manneville,

2017). How turbulent-laminar stripes emerge at particular pattern wavelengths and particular oblique orientations remains an open problem.

This chapter discusses oblique stripe patterns in plane Couette flow (PCF) where two extended parallel walls slide into opposite directions and drive an incompressible flow in the gap between the walls. First experimental observations of oblique stripe patterns in spatially extended PCF report a regular pattern at a Reynolds numbers of $\mathrm{Re} = U_w h/\nu = 358$ (Prigent et al., 2002, 2003). In PCF, Re is the single control parameter of the flow where $2U_w$ is the relative wall velocity, $2h$ is the gap-height and ν is the kinematic viscosity. The wavelength of the stripe pattern λ is large compared to the gap height, $40h \lessapprox \lambda \lessapprox 60h$, and the orientation angle θ against the streamwise direction of the walls is observed in the interval $20° \lessapprox \theta \lessapprox 40°$. Oblique stripe patterns with similar ranges of λ and θ have also been reproduced in direct numerical simulations of PCF at $330 \leq \mathrm{Re} \leq 380$ (Duguet et al., 2010). Both, experiments and simulations indicate a coupling of λ, θ and Re, such that the pattern wavelength λ and the orientation angle θ tend to increase with decreasing Re. A simple approximate relation, $\mathrm{Re}\sin(\theta) \approx \pi\lambda$, has been proposed based on a mean flow analysis of the stripe pattern (Barkley and Tuckerman, 2007). Further empirical and theoretical studies are needed to more precisely describe the coupling of λ, θ and Re.

Oblique turbulent-laminar stripes are statistically symmetric under continuous translations in the direction along the oblique stripes and under discrete translations with periodicity λ across the pattern. These translation symmetries in two orthogonal space dimensions have been exploited in direct numerical simulations of oblique stripes in minimal periodic domains (Barkley and Tuckerman, 2005, 2007). In general, minimal periodic domains treat dimensions with translation symmetries as periodic. This minimizes the computational cost to study complex patterns and may reduce the level of complexity of the underlying dynamics (Golubitsky and Stewart, 2002). The size of a minimal domain capturing the pattern must be chosen such that it contains a single period of the sustained periodic flow structure (Jiménez and Moin, 1991). To capture oblique turbulent-laminar stripe patterns, the two lateral dimensions of a periodic domain must be chosen to coincide with the translation invariant directions of the pattern implying that the domain is tilted against the wall-velocity by angle θ. One side of the domain has to reflect the wavelength λ (Barkley and Tuckerman, 2005). Thus in this minimal domain approach, not only Re but also θ and λ are imposed parameters. This is in contrast to experiments and simulations in large extended domains where the angle θ and the wavelength λ are unconstrained and can be freely selected by the flow. By choosing a tilted minimal periodic domain matching experimental observations, Barkley and Tuckerman (2007) obtained well-converged temporal statistics of a stripe pattern at $\mathrm{Re} = 350$, $\theta = 24°$ and $\lambda = 40$. They find the pattern's mean flow to be well-approximated by few harmonic functions with centro-symmetry about the center points of either the laminar or the turbulent flow

region. Recently, tilted minimal domains have also been used to study oblique stripe patterns in other shear flows (Tuckerman et al., 2014).

When lowering Re from the turbulent regime towards the parameters where stripes are observed, the oblique pattern emerges from statistically homogeneous turbulence. Some studies have suggested that turbulent-laminar stripes are the consequence of a large-wavelength instability of unpatterned turbulence, in analogy to linear instabilities forming steady patterns in non-linear amplitude equations (Prigent et al., 2002; Manneville, 2012). The identification of such large-wavelength instabilities is however challenging because the nonlinear dynamics of turbulent flows are chaotic in time and space (Philip and Manneville, 2011). One way to disentangle the temporal dynamics from the spatial structure of the flow is to study exact equilibrium solutions of the governing equations with steady, time-invariant dynamics that capture the coexistence of different pattern motifs in space (Knobloch, 2015). If an exact equilibrium solution of the fully nonlinear Navier-Stokes equations captures the spatial coexistence of non-trivial 'turbulent' flow structures and the laminar solution, then the turbulent-laminar coexistence may be described as homoclinic connections in space between laminar and turbulent flow. This description assumes that the spatial coordinate across a one-dimensional pattern is treated as a time-like variable (Burke and Knobloch, 2006). Such spatial homoclinic orbits have been identifed in PCF between laminar flow and spanwise localized wavy-streaky structures (Schneider et al., 2010a; Gibson and Schneider, 2016; Salewski et al., 2019). However, these time-invariant solutions do not capture the oblique orientation of the stripe pattern nor do they suggest any particular pattern wavelength because they represent localized states of various spanwise extent. Recently, an equilibrium solution of PCF has been found to capture the pattern of oblique turbulent-laminar stripes (Reetz et al., 2019a). This stripe equilibrium is computed at Re = 350 in the same tilted minimal periodic domain with $\theta = 24°$ and $\lambda = 40$ used to simulate oblique stripes (Barkley and Tuckerman, 2007). The stripe equilibrium bifurcates first with a period of $\lambda = 20$ from the well-known 'unpatterned' equilibrium with wavy-streaky flow structures (Nagata, 1990; Busse and Clever, 1992; Waleffe, 1997), and second, increases the spatial period to $\lambda = 40$ in a spatial period-doubling bifurcation. This bifurcation sequence confirms the existence of a large-wavelength instability creating the oblique stripe patterns in PCF at a particular wavelength. Despite capturing the spatial structure of stripes the stripe equilibrium is time-independent. Thus, it does not capture the temporal dynamics of turbulent-laminar stripe patterns.

The temporal dynamics of weakly turbulent shear flows has been extensively studied by numerically constructing invariant solutions, also called 'exact coherent states' (Kerswell, 2005; Eckhardt et al., 2007; Kawahara et al., 2012). Since invariant solutions in shear flows are typically dynamically unstable, the spatial structure and the recurrent dynamics of individual invariant solutions may only be observed transiently in a turbulent flow (Hof et al., 2004). Moreover, transitional turbulence in small domains of PCF is itself transient. The statistical

life-time of a turbulent state depends on Re and suggests to be supported by a saddle structure in state space (Hof et al., 2006; Kreilos et al., 2014), the space spanned by all solenoidal velocity fields (Cvitanović et al., 2016). Laminar PCF is linearly stable and state space trajectories are thus either attracted to the laminar equilibrium solution or visit the turbulent saddle. Trajectories approaching the laminar attractor and trajectories approaching the turbulent saddle are separated in state space by the *edge of chaos*, a codimension-1 manifold locally formed by the stable manifold of invariant solutions with a single unstable eigendirection, known as *edge states* (Schneider et al., 2007). These edge states guide the transition to turbulence and might also be relevant for spontaneous decay of turbulence (de Lozar et al., 2012). Edge states can be identified using a method known as *edge-tracking* (Skufca et al., 2006). Many spatially localized invariant solutions in subcritical shear flows have been found because they are edge states for appropriately chosen flow parameters (Schneider et al., 2010b; Avila et al., 2013; Khapko et al., 2013). The stripe equilibrium is not an edge state (Reetz et al., 2019a) and the edge of chaos for turbulent-laminar stripes has not been studied.

Turbulent flows show characteristic recurrent motion where flow approximately repeats after some time (Jiménez, 2018). Unstable periodic orbits (UPO) are a particular type of invariant solutions with exact periodic time evolution. These orbits capture recurrent motion of the flow and are thus particular interesting building blocks of the temporal dynamics (Cvitanović, 2013). Knowing sufficiently many relevant UPOs allows one to predict turbulent statistics (Cvitanović and Eckhardt, 1991; Chandler and Kerswell, 2013) but individual UPOs also can be instructive by capturing important temporal features of the flow (Kreilos et al., 2013). To capture the temporal dynamics of oblique stripe patterns in PCF, periodic orbits are needed that both show temporal dynamics and capture the spatial characteristics of the pattern. Such orbits have not been identified yet.

Following the recent construction of an equilibrium solution capturing the spatial structure of oblique turbulent-laminar stripes in PCF (Reetz et al., 2019a), in this chapter we construct UPOs underlying oblique stripe patterns. Imposing discrete symmetries allows to identify one UPO in the edge of chaos at Re = 350 in a tilted domain. Continuation reveals two additional UPOs at the same Re connected via fold bifurcations. The UPOs represent standing wave oscillations with a wavelength of $\lambda = 20$ and an oblique orientation at $\theta = 24°$. We describe the transient turbulent dynamics at Re = 350 relative to the three identified UPOs.

This chapter is structured as follows. To identify the symmetry subspace in which edge-tracking yields an UPO, we step-wise reduce the complexity of the spatio-temporal dynamics by imposing symmetries (Section 9.2). Confining the temporal dynamics in two symmetry subspaces additionally to the edge of chaos, reduces the complexity even more (Section 9.3), and leads to almost periodic dynamics near one UPO that is connected to two other UPOs at

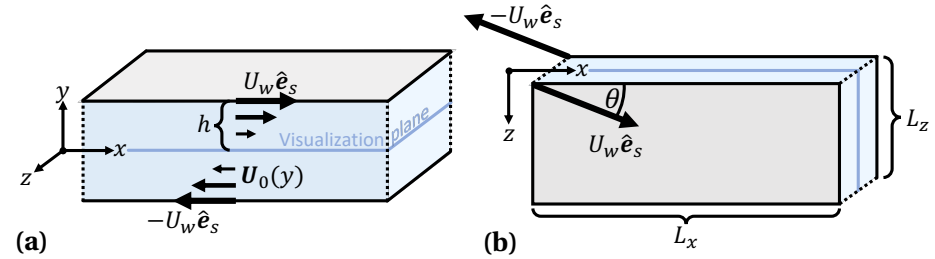

Figure 9.1 – Geometry of plane Couette flow (PCF). A Newtonian fluid (light blue) is studied numerically in x-z-periodic domains, bounded in y by two parallel walls (light grey). The walls move with a relative velocity of $2U_w$ in opposite directions and thereby drive a flow. The unit vector $\hat{\boldsymbol{e}}_s$ indicates the streamwise direction. In the present chapter, PCF is studied in both, non-tilted domains **(a)**, where $\hat{\boldsymbol{e}}_s$ is aligned with x, and in tilted domains **(b)**, where $\hat{\boldsymbol{e}}_s$ is oriented at a non-zero angle θ relative to the x-dimension. For all values of θ, the nondimensionalized laminar flow profile is $\boldsymbol{U}_0(y) = y\hat{\boldsymbol{e}}_s$. We visualize non-laminar PCF in the indicated midplane at $y = 0$.

Re = 350 via fold bifurcations (Section 9.4). The dynamical relevance of the three identified UPOs is discussed in Section 9.5.

9.2 Numerical simulations in symmetry subspaces

The velocity vector field $\boldsymbol{U}(x,y,z,t)$ and the pressure $p(x,y,z,t)$ in PCF are governed by the incompressible Navier-Stokes equations

$$\frac{\partial \boldsymbol{U}}{\partial t} + (\boldsymbol{U}\cdot\nabla)\,\boldsymbol{U} = -\nabla p + \tilde{\nu}\nabla^2\boldsymbol{U}\,, \tag{9.1}$$

$$\nabla\cdot\boldsymbol{U} = 0\,, \tag{9.2}$$

in a three-dimensional channel. The channel domain is considered as periodic in the two lateral dimensions x and z, such that the velocity field repeats in space as $\boldsymbol{U}(x,y,z,t) = \boldsymbol{U}(x+L_x,y,z,t)$ and $\boldsymbol{U}(x,y,z,t) = \boldsymbol{U}(x,y,z+L_z,t)$ over the lateral domain size L_x and L_z. The Navier-Stokes equations are nondimensionalized by the half-gap height h and the wall velocity U_w leading to the dimensionless Reynolds number $\mathrm{Re} = U_w h/\nu$. No-slip boundary conditions at the walls are imposed such that $\boldsymbol{U}(y=\pm1) = \pm\hat{\boldsymbol{e}}_s$. The unit vector $\hat{\boldsymbol{e}}_s = \cos(\theta_s)\hat{\boldsymbol{e}}_x + \sin(\theta_s)\hat{\boldsymbol{e}}_z$ describes the streamwise direction in which the walls move. The streamwise direction may be rotated by θ_s relative to the x- and z-direction. The nondimensional Navier-Stokes equations with these boundary conditions admit the linear velocity profile $\boldsymbol{U}_0(y) = y\hat{\boldsymbol{e}}_s$ as laminar flow solution (Figure 9.1).

We perform direct numerical simulations (DNS) of PCF in domains sufficiently large to contain turbulent-laminar stripes. Such large-scale DNS can be computationally demanding. We employ the MPI-parallel code CHANNELFLOW 2.0 (Gibson et al., 2019). The code implements a pseudo-spectral method based on Fouier-Chebychev decompositions of the velocity fluctuation field $\boldsymbol{u}(x,y,z,t) = \boldsymbol{U}(x,y,z,t) - \boldsymbol{U}_0(y)$. An implicit-explicit multistep algorithm of 3rd order is used for time marching. The mean pressure gradient is fixed at zero along the streamwise and the spanwise direction. DNS of weakly turbulent PCF at Re = 350 in a large numerical domain of size $[L_x, L_z] = [197, 87.5]$ with $[N_x, N_y, N_z] = [852, 33, 340]$ dealiased spectral modes and walls moving with $\theta_s = 0$ along the x-dimension result in self-organized oblique turbulent-laminar stripes predominantly oriented along the domain diagonal at $\theta = \pm 24°$. However, the large-scale pattern is subject to statistical fluctuations in the pattern wavelength and orientation, as already observed previously (Duguet et al., 2010). Oblique stripe patterns may drift in space, break up, and form again. To reduce the complexity of the spatio-temporal dynamics, we will impose additional discrete symmetries of PCF. Imposing a discrete symmetry disallows instabilities that would break this symmetry and reduces the number of degrees of freedom in the numerical simulation. Thereby, imposed symmetries also reduce the number of dimensions of the accessible state space. In the following, $N = N_x \times N_y \times N_z \approx 1.1 \times 10^6$ degrees of freedom in the above described DNS-setup are reduced by more than one order of magnitude.

The governing equations (9.1-9.2), complemented with periodic boundary conditions and imposed wall velocity at $\theta_s = 0°$, are equivariant under reflections and translations in the x- and z-direction

$$\pi_{xy}[u,v,w](x,y,z,t) = [-u,-v,w](-x,-y,z,t)\,, \tag{9.3}$$

$$\pi_{z}[u,v,w](x,y,z,t) = [u,v,-w](x,y,-z,t)\,, \tag{9.4}$$

$$\tau(a_x,a_z)[u,v,w](x,y,z,t) = [u,v,w](x+a_xL_x,y,z+a_zL_z,t)\,, \tag{9.5}$$

with continuous real-valued shift factors $a_x, a_z \in [0,1)$. Symmetry transformations (9.3-9.5) generate a symmetry group $S_{\mathrm{pcf}} = \langle \pi_{xy}, \pi_z, \tau(a_x,a_z) \rangle$, where $\langle\rangle$ denotes all products between the listed transformations. For tilted domains with wall velocities at $\theta_s \neq 0$ and $-90° < \theta_s < 90$, the reflections π_{xy} and π_z are broken. Only their product $\pi_i = \pi_{xy}\pi_z$, the inversion symmetry

$$\pi_i[u,v,w](x,y,z,t) = [-u,-v,-w](-x,-y,-z,t) \tag{9.6}$$

remains a symmetry of PCF in the considered domain. We denote the symmetry group in tilted domains as S'_{pcf}. To impose a particular symmetry $\sigma \in S_{\mathrm{pcf}}$ on a velocity field $\boldsymbol{u}$, we apply the projection $(\sigma\boldsymbol{u} + \boldsymbol{u})/2$. Such a projection requires the additional property $\sigma^2 = 1$. Once $\boldsymbol{u}$ is σ-symmetric, the time evolution of $\boldsymbol{u}$ will remain σ-symmetric because the governing equations are equivariant under σ (Cvitanović et al., 2017). Thus, imposing symmetries on a

flow confines the flow and its time evolution to a symmetry subspace containing only flows that are invariant under the imposed symmetries.

Changing the spatial extent of a double-periodic domain imposes different discrete translation symmetries on the flow and is therefore another way to change the symmetry-subspace of the flow. Previous numerical studies have systematically varied the domain size to investigate turbulent-laminar patterns in different symmetry subspaces (Philip and Manneville, 2011; Chantry et al., 2017). Here, we aim for reducing the complexity of the spatio-temporal dynamics of a sustained oblique stripe pattern while trying to preserve the pattern characteristics of a large-scale wavelength and an oblique orientation. Starting from a regular stripe pattern in a large domain we systematically impose additional discrete symmetries in S_{pcf} or reduce the domain size. We consider simulations of oblique stripe patterns in four different symmetry subspaces, $\mathbb{A}$-$\mathbb{D}$, of PCF at Re = 350:

$\mathbb{A}$: Inversion symmetry π_i is imposed on PCF in the large periodic domain $[L_x, L_z] = [197, 87.5]$ with x-aligned wall velocities, $\theta_s = 0°$. The number of degrees of freedom is $N_{\mathbb{A}} = N_x \times N_y \times N_z/2 = 562\,320$. A snapshot of a regular stripe pattern with pattern wavelength $\lambda = 40$ and orientation at $\theta = 24°$ along the domain diagonal is shown in Figure 9.2a. Imposing π_i prohibits drift of the large-scale pattern by fixing the pattern's spatial phase in x and z. In this case, the center of a laminar region coincides with the center of the domain (Figure 9.2a).

$\mathbb{B}$: We impose the periodicity of a tilted periodic domain of extent $[L_x, L_z] = [10, 40]$ and orientation $\theta_s = 24°$. The grid resolution is $[N_x, N_y, N_z] = [42, 33, 170]$. No reflection symmetry is imposed. The number of degrees of freedom is $N_{\mathbb{B}} = N_x \times N_y \times N_z = 235\,620$. The tilted domain allows to simulate a single spatial period of turbulent-laminar stripes whose geometry matches the boundary conditions of the domai with $\lambda = L_z = 40$ and $\theta = \theta_s = 24°$. The domain is identical to the one used in Barkley and Tuckerman (2007). A snapshot from the simulation is periodically repeated in Figure 9.2b.

$\mathbb{C}$: Again, a single stripe period is simulated in a tilted domain like for subspace $\mathbb{B}$ but with additionally imposed π_i-symmetry. The corresponding symmetry subspace, resolved with $N_{\mathbb{C}} = N_x \times N_y \times N_z/2 = 117\,810$ degrees of freedom, contains the mean flow of the stripe pattern in a tilted domain of size $[L_x, L_z] = [10, 40]$ (Barkley and Tuckerman, 2007) and also the stripe equilibrium reported in Reetz et al. (2019a). The emerging oblique stripe pattern is shown in Figure 9.2c.

$\mathbb{D}$: In the final step of reducing the complexity of the dynamics, we impose a shift-inversion symmetry $\pi_{si} = \pi_i \tau(0.5, 0.5)$ in addition to the symmetries of subspace $\mathbb{C}$. The number of degrees of freedom is $N_D = N_x \times N_y \times N_z/4 = 58\,905$. The π_{si}-symmetry changes the wavelength of the emerging oblique stripe pattern from $\lambda = 40$ to $\lambda = 20$ (Figure 9.2d).

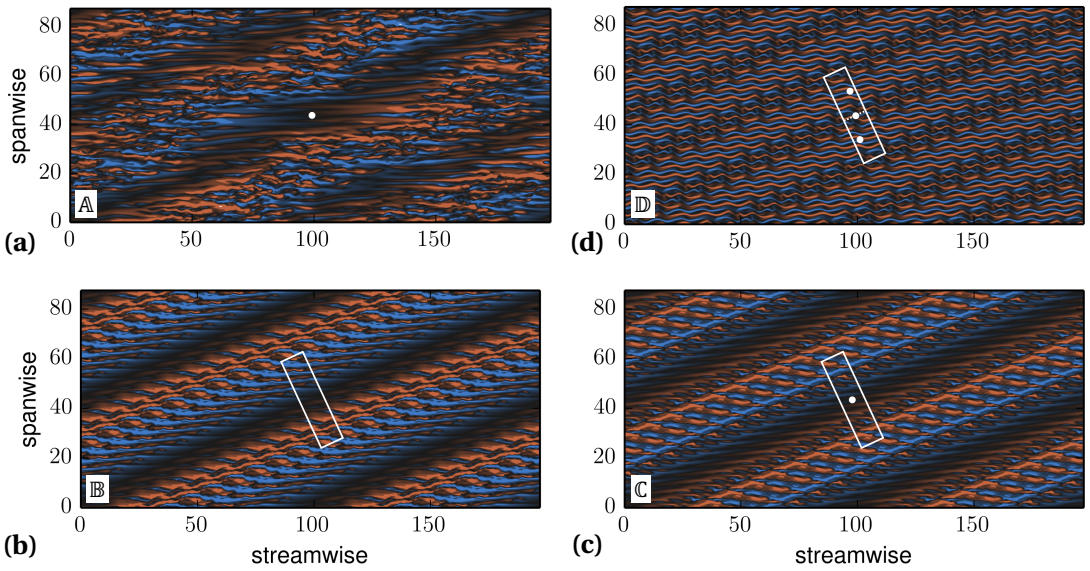

Figure 9.2 – Imposing symmetries reduces the complexity of the oblique stripe pattern at Re = 350 from **(a)** to **(d)**. The contours indicate streamwise velocity at midplane ($y = 0$). **(a)** Snapshot from a DNS in a periodic domain of extent $[L_x, L_z] = [197, 87.5]$ with additionally enforced σ_i-symmetry. **(b)** Periodically repeated snapshot from a DNS in a periodic domain of extent $[L_x, L_z] = [10, 40]$ and tilted at $\theta = 24°$ against the streamwise direction. **(c)** Like in **(b)** but with inversion symmetry σ_i imposed additionally. **(d)** Like in **(c)** but with shift-inversion symmetry σ_{si} imposed additionally. This symmetry enforces a pattern wavelength of $\lambda = 20$, while cases **(a-c)** have a pattern wavelength of $\lambda = 40$.

Oblique stripe patterns with π_{si}-symmetry and wavelength $\lambda = 20$ have been observed in the bifurcation sequence towards the stripe equilibrium solution (Reetz et al., 2019a) but are typically not naturally selected in less confined domains.

Robust oblique stripe patterns are observed in all four DNS runs over a time interval of $\Delta t = 1\,500$. Beyond this time interval, stripes typically either break up, leading to defects in the large-scale pattern (observed for DNS in $\mathbb{A}$), or decay to laminar flow (observed for DNS in $\mathbb{B}$-$\mathbb{D}$). In the time interval over which the pattern characteristics are robust, the domain averaged velocity norm

$$||u||_2(t) = \frac{1}{(2L_xL_z)^{1/2}} \left(\int_0^{L_x} \int_{-1}^{1} \int_0^{L_z} \boldsymbol{u}^2(x,y,z,t)\, dx\, dy\, dz \right)^{1/2} \tag{9.7}$$

fluctuates at different amplitudes in the four different subspaces (Figure 9.3). In the higher-dimensional subspace $\mathbb{A}$, temporal velocity fluctuations at different uncorrelated locations in

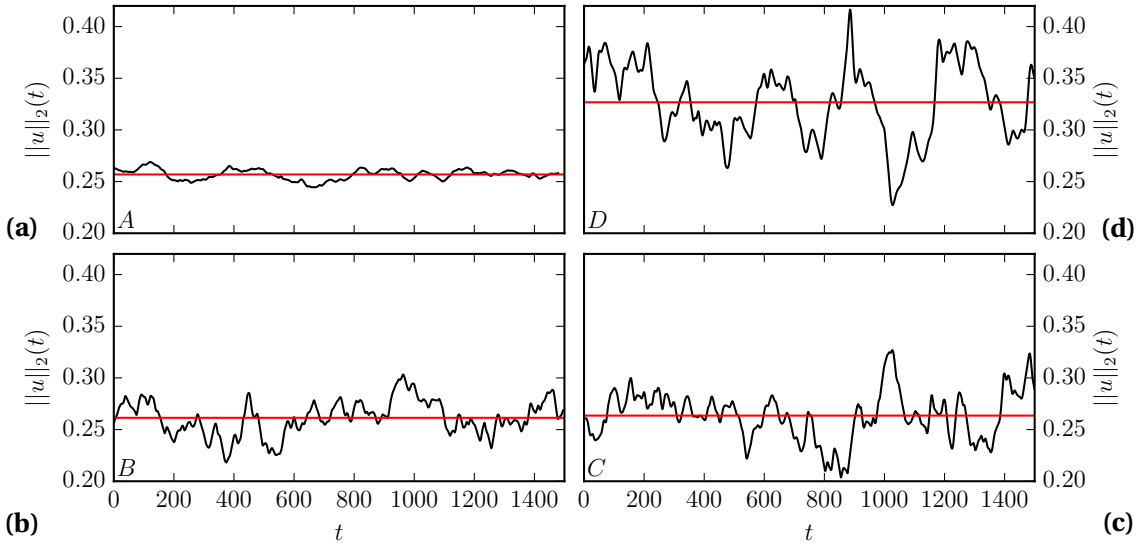

Figure 9.3 – Time series from DNS in four different symmetry subspaces corresponding to the four snapshots in Figure 9.2 **(a-d)** showing instance $t = 0$ in **(a-d)** of the present figure. While the amplitudes of the temporal fluctuations differs significantly between the cases **(a-d)**, the mean values of $||u||_2$ (horizontal red lines) is approximately equal in the symmetry subspaces of cases **(a-c)**. Case **(d)** has a different mean because the imposed shift-inversion symmetry disallows the oblique stripe patterns at wavelength $\lambda = 40°$, present in **(a-c)**, and enforces a pattern wavelength of $\lambda = 20$.

the domain statistically compensate each other more than in the lower-dimensional subspace $\mathbb{D}$. There, the imposed symmetries correspond to spatial correlations that reduce the number of independently fluctuating modes. This induces higher amplitude fluctuations. Thus, the fluctuation amplitude of norm $||u||_2(t)$ can be used as a proxy for the spatio-temporal complexity of the pattern dynamics simulated at equal Re.

The temporal average of $||u||_2(t)$ over $\Delta t = 1500$ is the same for oblique stripes in subspaces $\mathbb{A}$-$\mathbb{C}$ (red lines in Figure 9.3), suggesting that the imposed symmetries do not change the pattern's mean flow. In subspace $\mathbb{D}$ however, the shift-inversion symmetry π_{si} enforces a pattern wavelength of $\lambda = 20$. This increases the temporal mean from $||u||_2 = 0.26$, observed for stripes with $\lambda = 40$, to $||u||_2 = 0.33$. Thus, the mean pattern in symmetry subspace $\mathbb{D}$ is qualitatively and quantitatively different from the patterns in $\mathbb{A}$-$\mathbb{C}$. All patterns are obliquely oriented at $\theta = 24°$ and periodic over wavelength $\lambda = 40$. Note that subspace $\mathbb{A}$ is well suited to accommodate a pattern of this geometry but does not contain the subspaces $\mathbb{B}$-$\mathbb{D}$. Subspace $\mathbb{B}$ however contains $\mathbb{C}$ and $\mathbb{D}$. Including the subspaces $\mathbb{B}$-$\mathbb{D}$ of the tilted domain into the subspace of a non-tilted domain requires choosing a non-tilted domain with at least $[L_x, L_z] = [98.5, 394]$.

The geometric condition to make the flow in tilted and non-tilted domains commensurable is discussed in Reetz et al. (2019a).

There is no obvious additional symmetry to further reduce the complexity of the spatio-temporal dynamics of oblique stripe patterns beyond subspace $\mathbb{D}$. Other additional shift-symmetries enforce periodicity on even smaller pattern wavelengths than $\lambda = 20$, that are not observed for self-organized stripe patterns in large domains.

9.3 Edge of chaos in symmetry subspaces

Despite reducing the number of degrees of freedom to the presumable minimum for supporting oblique stripe patterns, the dynamics in the symmetry subspaces remains chaotic. To identify periodic orbits, we follow the established approach to confine the dynamics to the edge of chaos. Using the edge-tracking algorithm implemented in CHANNELFLOW 2.0 (Gibson et al., 2019), we follow two trajectories inside the edge of chaos in symmetry subspace $\mathbb{C}$ and $\mathbb{D}$, respectively. The Reynolds number is again fixed at Re = 350. The initial condition was chosen arbitrarily from the DNS in $\mathbb{C}$ and $\mathbb{D}$. We confirmed that the state approached by edge-tracking does not depend on the initial condition in these two cases. Edge-tracking in $\mathbb{C}$ follows a chaotic trajectory indicating a chaotic edge state (Figure 9.4a). Chaotic edge states have been described previously for pipe flow (Schneider et al., 2007) and PCF (Duguet et al., 2009). In $\mathbb{D}$, the trajectory approaches a near-periodic edge state (Figure 9.4b).

The chaotic edge state in $\mathbb{C}$ differs clearly from the chaotic state found by DNS in $\mathbb{C}$ (Figure 9.3c). The mean L_2-norm of the trajectory in the edge of chaos in $\mathbb{C}$ is with $||u||_2 = 0.18$ significantly smaller than for the trajectory in the DNS with $||u||_2 = 0.26$. Likewise, the L_2-norm of the near-periodic edge state in $\mathbb{D}$ is with $||u||_2 = 0.24$ lower than the simulated state in $\mathbb{D}$ with $||u||_2 = 0.33$ (Figure 9.3d).

In summary, a chaotic edge state is found in $\mathbb{C}$. By additionally imposing the shift-inversion symmetry π_{si}, a much simpler, almost periodic edge state is found in $\mathbb{D}$.

9.4 Unstable periodic orbits

The near-periodic oscillations in the edge of chaos in symmetry subspace $\mathbb{D}$ indicates the presence of an unstable periodic orbit (UPO). Periodic orbits satisfy the recurrency condition

$$\mathscr{F}^T(\boldsymbol{u}(x,y,z,t);\mathrm{Re}) - \boldsymbol{u}(x,y,z,t) = 0\,. \tag{9.8}$$

The operator $\mathscr{F}^T(\boldsymbol{u};\mathrm{Re})$ integrates the Navier-Stokes equations for PCF at a specific Re from the initial velocity field $\boldsymbol{u}$ over time period T. A velocity field solving (9.8) can be found via

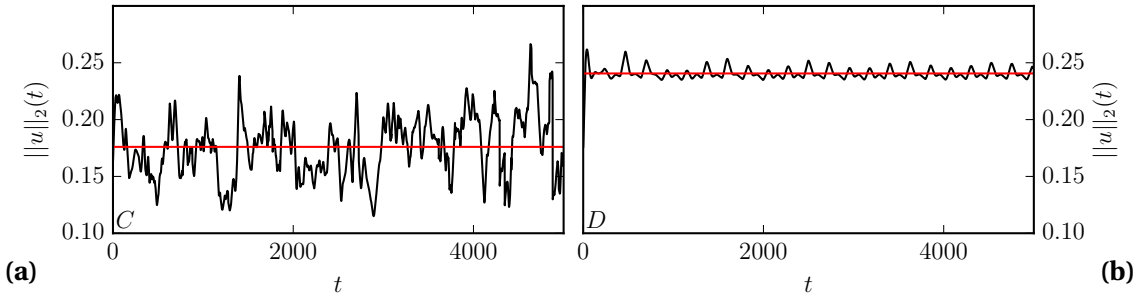

Figure 9.4 – Time series of edge tracking at Re = 350 in different symmetry subspaces. Both results are computed in a periodic domain of extent $[L_x, L_z] = [10, 40]$ and tilted at $\theta = 24°$ against the streamwise direction. In addition, centro-inversion σ_i is imposed in **(a)**, and shift-inversion σ_{si} is imposed in **(b)**. The mean values of $||u||_2$ (horizontal red lines) differ like in DNS in the same two symmetry subspaces (Figure 9.3c,d). Only when imposing σ_{si} the edge-tracking approach yields a simple edge state.

Newton-Raphson iteration. Since subspace $\mathbb{D}$ is still high-dimensional ($N = 58\,905$), equation (9.8) is solved with a matrix-free Newton-Krylov method. We use the Newton-Krylov method implemented in the nonlinear solver library of CHANNELFLOW 2.0 to converge and numerically continue invariant solutions under the changing control parameter Re (Gibson et al., 2019). In order to converge the periodic orbits discussed here, a multi-shooting method with two shots is required (Gibson et al., 2019).

Using the last velocity field obtained from edge-tracking in subspace $\mathbb{D}$ as initial state for the Newton-Krylov iteration yields an UPO with period $T = 225.4$. The spatial structure of the UPO is composed of wavy velocity streaks whose amplitude is modulated in time and space along the orbit. The amplitude modulations represent a standing wave oscillation with wavelength $\lambda = 20$ along the z-direction of the tilted domain (Fig. 9.5). The standing wave has anti-nodes at $z \in \{0, 10, 20, 30, 40\}$ where the imposed inversion symmetries have their points of reflection. The locations of these symmetry points are marked by black dots in midplane sections showing velocity and vorticity contours in Fig. 9.5c,d. Instances $t = 7$ and $t = 109$ along the orbit show intense localized velocity and vorticity fluctuations. These localized intense fluctuations are centered around the symmetry points (see blue and red contours in Fig. 9.5c,d). The intense fluctuation regions have also a large x-y-averaged velocity norm (Fig. 9.5b) and coincide with velocity streaks that are more wavy than outside these regions where streaks are more straight (Fig. 9.5b). Thus, the UPO is a standing wave that periodically exchanges regions of high amplitude wavy velocity streaks and low amplitude near-straight velocity streaks. We name this UPO “oblique standing wave" and denote it by OSW_1.

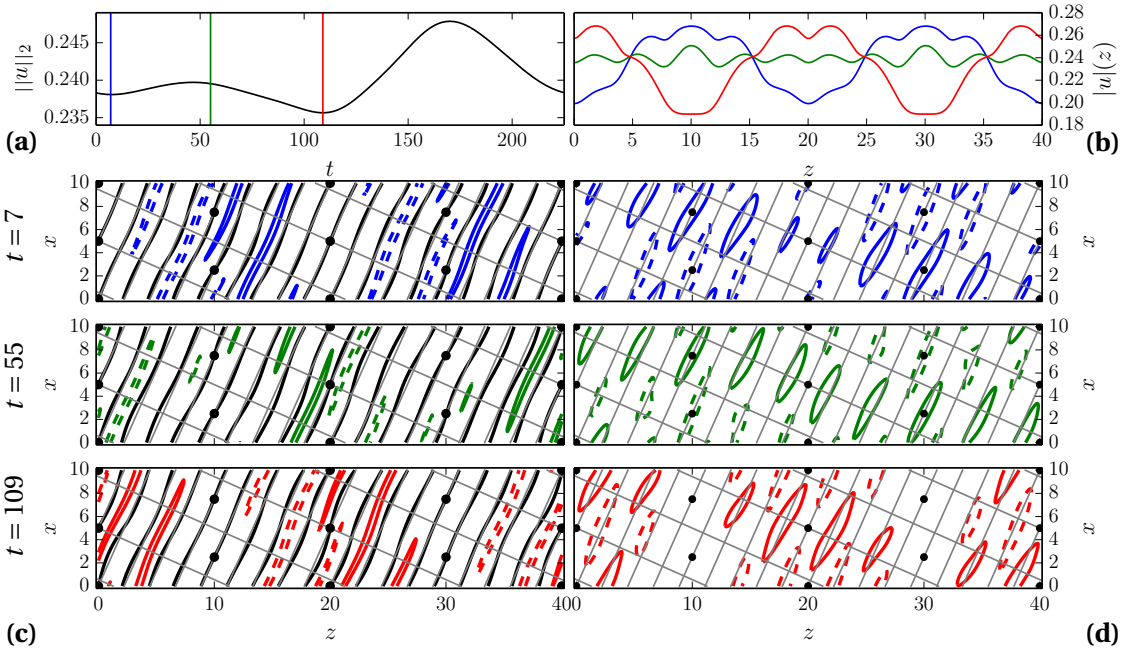

Figure 9.5 – Unstable periodic orbit OSW_1 in the edge of chaos describes a slow standing wave modulation. **(a)** Velocity norm $||u||_2$ oscillations over period $T = 225.4$ with two local maxima and minima. The local minima correspond to the instances of large amplitude modulations as indicated by the x-y-averaged squared velocity profiles $|u|(z) = (2L_x)^{-1/2}(\int \boldsymbol{u}^2 dxdy)^{1/2}$ in **(b)**. These instances are further illustrated by midplane contours of streamwise velocity **(c)** and streamwise vorticity **(d)**. The black contours in **(c)** mark the critical layer with $u = 0$. The grey grid indicates the streamwise and the spanwise directions. The midplane structure oscillates locally between high-amplitude wavy velocity streaks generating much vorticity and low-amplitude near-straight velocity streaks generating little vorticity.

The phase velocity of the standing wave oscillation in the streamwise direction is $c = \lambda_s/T = 0.22$. The streamwise pattern wavelength of OSW_1 with $\lambda = 20$ and $\theta = 24°$ is $\lambda_s = \lambda/\sin(\theta) = 49.2$. Due to the chosen nondimensionalization, time is measure in advective time units $T_a = h/U_w$. Note that the period $T = 223.4$ of OSW_1 approximately equals one viscous diffusion time unit, $T \approx T_d = h^2/\nu = 350$. Thus, the periodic orbit OSW_1 satisfies an approximate resonance condition between diffusion time and cross-pattern propagation time,

$$\frac{\lambda}{\sin(\theta)} \approx \frac{c\,h^2}{\nu}\,. \tag{9.9}$$

This condition represents a dispersion relation for the standing wave. The relation between λ and θ in (9.9) is similar to the approximate relation $\lambda/\sin(\theta) \approx \mathrm{Re}/\pi$ that has been suggested

from measured forces in the mean flow of simulated oblique stripe patterns at pattern wavelength $\lambda = 40$ in the symmetry subspace $\mathbb{B}$ (Barkley and Tuckerman, 2007). Consequently, the intrinsic spatio-temporal dynamics of OSW_1 has similar characteristic scales as the mean flow of oblique stripe patterns at pattern wavelength $\lambda = 40$.

Numerical continuation of OSW_1 up in Re indicates a reducing oscillations amplitude for Re up to 450 (Fig. 9.6a). The reduced amplitude remains approximately constant for $450 < \mathrm{Re} < 700$ (not shown). For decreasing Re, the oscillation amplitude increases and the branch leads to a sequence of two smooth folds at Re = 327 and Re = 367, respectively. Further along the branch a succession of sharp folds emerges in the interval $300 < \mathrm{Re} < 330$ (Fig. 9.6a). We have encountered such sharp and irregular folds previously by continuing equilibrium solutions underlying stripes (Reetz et al., 2019a) and interpret them as an indicator for a particular frustration process: The frustration arises when continuous changes of invariant solutions along a branch are hindered by geometric constraints imposed by the periodic boundary conditions. The folded solution branches connect three periodic orbits at Re = 350 (Figure 9.6a). We index these orbits as they are encountered along the branch, OSW_i with $i = 1,2,3$.

The dynamical stability of each orbit is characterized by calculating the spectrum of eigenvalues at Re = 350 using Arnoldi iteration in subspace $\mathbb{D}$. All three periodic orbits are dynamically unstable and have one dominating purely real unstable eigenvalue of $\omega_r \approx 0.035$. Moreover, all three periodic orbits have at least one additional unstable eigenvalue in the interval $0 < \omega_r < 0.01$ (Figure 9.6b). Consequently, none of the three periodic orbits OSW_i is an edge state which requires a single unstable eigenvalue (Skufca et al., 2006; Schneider et al., 2007). The initially found periodic orbit OSW_1 has in total five unstable eigenvalues, three real and one complex pair of eigenvalues. Of the three UPOs, OSW_3 is the least unstable one in terms of number of unstable eigenvalues as well as absolute value of the leading eigenvalue with maximum ω_r.

The stability properties of the three UPOs raise the question if all of them are part of the attractor in the edge of chaos, and if not, if all of them are yet embedded within the edge of chaos. To study the attractor in the edge of chaos, edge-tracking is performed for 10 000 advective time units. The state space trajectory over the last 1 000 time units is projected together with the state space trajectories of all orbits $OSW_{1,2,3}$ onto a plane indicating kinetic energy input $I(t)$ and dissipation $D(t)$, where

$$I(t) = 1 + \frac{1}{2A}\int_A \left(\left.\frac{\partial u_s}{\partial y}\right|_{y=-1} + \left.\frac{\partial u_s}{\partial y}\right|_{y=1} \right) \mathrm{d}x\,\mathrm{d}z \tag{9.10}$$

$$D(t) = \frac{1}{V}\int_\Omega |\nabla \times (\boldsymbol{u} + y\hat{\boldsymbol{e}}_s)|^2 \mathrm{d}x\,\mathrm{d}y\,\mathrm{d}z \tag{9.11}$$

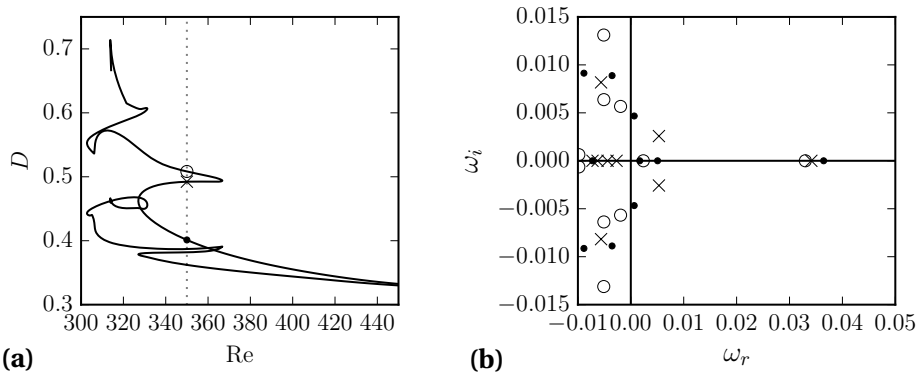

Figure 9.6 – **(a)** Bifurcation diagram of the unstable periodic orbit along Re, computed via numerical continuation. The two curves indicate maximum and minimum dissipation D over one period. Towards high Re, the oscillation amplitude reduces. Towards low Re, the branch undergoes folds leading to three periodic orbits coexisting at Re = 350 (dashed line). **(b)** Spectrum of eigenvalues of the three unstable periodic orbits at Re = 350: OSW_1 (•), OSW_2 (×), OSW_3 (◯). The spectrum is calculated in the symmetry subspace $\mathbb{D}$.

with the streamwise unit vector $\hat{\boldsymbol{e}}_s = \cos(\theta_s)\hat{\boldsymbol{e}}_x + \sin(\theta_s)\hat{\boldsymbol{e}}_z$ and the streamwise velocity component $u_s = \boldsymbol{u}\cdot\hat{\boldsymbol{e}}_s$. The quantities are normalized by cross-section area $A = L_x L_z$ and volume $V = 2L_x L_z$ of the numerical domain, respectively. The projection yields the phase portrait in Figure 9.7b that clearly reveals how the edge-tracking trajectory (grey dots) clusters around OSW_1 but not around OSW_2 or OSW_3. Thus, of the three UPOs only OSW_1 is part of the attractor in the edge of chaos. The edge-tracking trajectory, even after 9000 time units, does still not coincide with OSW_1 (Inset in Fig. 9.7b). This supports the above discussion that OSW_1 is not an edge state and may only be part of an attractor in the edge of chaos.

For each of the UPOs, the time series $I(t)$ and $D(t)$ almost coincide along the orbits (Figure 9.7a). This leads to the property that the phase portrait in Figure 9.7b shows orbits that are elongated along and entangled around the diagonal line $D = I$. The quantities $I(t)$ and $D(t)$ are highly correlated and do not provide a good projection to illustrate the oscillatory behaviour along the three orbits. A second projection is defined in terms of the two quantities

$$\alpha(t) = \mathbb{R}\left\{\widetilde{\boldsymbol{u}^2}\right\}(i=0, j=0, k=2)\,, \tag{9.12}$$

$$\beta(t) = \mathbb{R}\{\widetilde{\boldsymbol{\omega}_s}\}(i=0, k=2,)\,. \tag{9.13}$$

Here, $\mathbb{R}\{\}$ returns the real part of spectral quantities indicated by $\widetilde{\cdot}$, namely the Fourier- and Chebyshev-transformed kinetic energy $\boldsymbol{u}^2 = \boldsymbol{u}^2(x,y,z,t)$ and streamwise vorticity $\boldsymbol{\omega}_s = (\nabla\times\boldsymbol{u}(x,y=0,z,t))\cdot\hat{\boldsymbol{u}}_s$ at midplane. Fourier modes in x and z are indexed by i and k. Chebyshev modes in y are indexed by j. Thus, $\alpha(t)$ and $\beta(t)$ are the time-dependent absolute values of

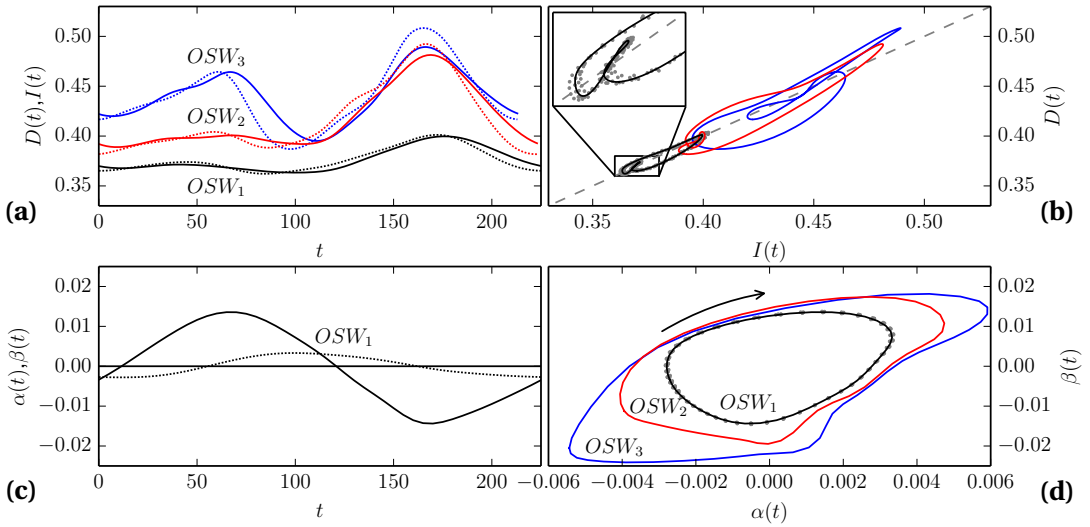

Figure 9.7 – Two different projections for a phase portrait of the three unstable periodic orbits $OSW_{1,2,3}$ underlying slow oblique standing waves. Time series of kinetic energy input $I(t)$ and dissipation $D(t)$, defined in (9.10) and (9.11), and of $\alpha(t)$ and $\beta(t)$, defined in (9.12) and (9.13), for periodic orbit OSW_1 are plotted in in panels **(a)** and **(c)**, respectively. The corresponding phase portraits of all three periodic orbits $OSW_{1,2,3}$ are plotted in **(b)** and **(d)**. The edge-tracking trajectory for $9000 < t < 10000$ in subspace $\mathbb{D}$ (grey dots) clearly indicates orbit OSW_1 as part of the attractor in the edge of chaos. However, the distribution of points along this trajectory does not exactly coincide with the trajectory of OSW_1 (inset in panel b). This suggests that OSW_1 is part of a more complex attractor in the edge of chaos.

the second Fourier mode in z of the mean kinetic energy density and midplane streamwise vorticity, respectively. This Fourier mode corresponds to the dominant mode of the standing wave oscillations, shown by the z-profile in Figure 9.5b. Along the orbit of OWR_1 with period $T = 225.4$, $\alpha(t)$ and $\beta(t)$ oscillate with a phase lag of approximately $T/4$ (Figure 9.7c). In this projection, the phase portrait of the three periodic orbits $OSW_{1,2,3}$ shows disentangled near-circular loops along which the dynamics revolves in a clockwise sense (Figure 9.7d). Consequently, the quantities $\alpha(t)$ and $\beta(t)$ illustrate the oscillatory behaviour of the periodic orbits better than $I(t)$ and $D(t)$.

Having identified a good state space projection to display the intrinsic temporal dynamics of the three standing waves with oblique amplitude modulation, we investigate the relevance of these UPOs for the turbulent dynamics in subspace $\mathbb{D}$. Figure 9.8a shows the turbulent time series also plotted in Figure 9.3d in terms of $\alpha(t)$ and $\beta(t)$. Here, the phase lag between $\alpha(t)$ and $\beta(t)$ is not constant, varying between approximately in phase and out-of phase. We have computed four transiently turbulent trajectories in subspace $\mathbb{D}$ that all exceed $t = 1000$

before decaying to laminar flow. Projecting them onto $\alpha(t)$, $\beta(t)$ and $||u||_2(t)$, we find an unstructured cloud of points (Figure 9.8c-d). Yet, the phase portrait clearly indicates the role of the three UPOs for the turbulent dynamics: In the α-β plane, the orbits are located in the center of the cloud implying that the orbits well represent the turbulent mean of $\alpha(t)$ and $\beta(t)$. When including $||u||_2(t)$ into the projection, the orbits mark the lower bound of the turbulent saddle. Prior to decay, the state trajectories are close to the orbits in these projections (Figure 9.8). That decaying trajectories transiently visit the periodic orbits is plausible because the periodic orbits are embedded in the edge of chaos. When perturbing OSW_i with their most unstable eigenmode, trajectories either intrude the turbulent saddle or decay to laminar flow depending on the sign of the perturbation (Figure 9.8e,f). This provides evidence that all orbits are indeed embedded in the edge of chaos.

9.5 Discussion

We study the spatio-temporal dynamics of oblique stripe patterns in PCF at Re = 350 within a numerical dynamical systems analysis. Patterns in four different symmetry subspaces are simulated using DNS in doubly periodic domains of different size and with additionally imposed discrete symmetries. Imposing symmetries reduces the spatio-temporal complexity of the turbulent patterns. It is shown that inversion symmetric oblique stripe patterns at orientation $\theta = 24^\circ$ with pattern wavelengths of $\lambda = 40$ and $\lambda = 20$ are transiently sustained in a minimal periodic domain. In the most confined symmetry subspace, edge-tracking approaches a slow periodic orbit with a pattern wavelength $\lambda = 20$ and a period $T = 225.4$ comparable to the viscous diffusion time scale. This unstable periodic orbit represents a standing wave oscillation modulating wavy velocity streaks. The oscillation exchanges regions of high-amplitude wavy streaks with regions of low-amplitude near-straight streaks on the time-scales of viscous diffusion. Numerical continuation of the periodic orbit towards lower Re indicates a solution branch that undergoes two folds such that three periodic orbits coexist at Re = 350. All three periodic orbits represent standing waves, are weakly unstable and embedded in the edge of chaos but have more than one unstable eigenvalue unlike edgestates. Interestingly, the most unstable periodic orbit was approached during edge-tracking.

Oblique stripe patterns are typically not observed at a pattern wavelength of $\lambda = 20$ in experiments or numerical simulations. However, the intrinsic dynamics of the three periodic orbits discussed in this chapter provide relevant insights into possible selection mechanism for a pattern wavelength and an orientation angle of stripes under less confined conditions. First, the standing wave modulation involves skewing and bending effects of wavy velocity streaks (Figure 9.7d). Such skewing and bending effects are characteristic features that were also found in the analysis of the recently described stripe equilibrium solution (Reetz et al., 2019a) and in the detailed analysis of snakes-and-ladders bifurcation structures of spanwise

localized wavy velocity streaks (Gibson and Schneider, 2016). The maximum degree of skewing or bending of wavy velocity streaks against the streamwise direction is related to the maximum degree to which periodic domains resolving wavy velocity streaks can be tilted. The angle of tilt of the periodic domain reflects the angle of obliqueness of the stripe pattern. Thus, the range of skewing and bending of wavy streaks that is observed along the UPOs discussed here may suggest the range of orientation angles at which stripes can form. Second, the period of the UPOs is on the order of the viscous diffusion time scale, a characteristic time scale of the mean flow of oblique turbulent-laminar stripes. The approximate resonance condition for the standing wave oscillations, Equation (9.9), couples the pattern orientation angle θ with the pattern wavelength λ via the phase velocity c. This relation is similar to the condition derived in Barkley and Tuckerman (2007) based on the dominating force balance of the mean flow of oblique turbulent-laminar stripes at wavelength $\lambda = 40$. The existence of a standing wave with $\lambda = 20$ that oscillates on the time scales of the pattern's mean flow suggest that similar wave solutions also exist with a pattern wavelength of $\lambda = 40$, the typically observed wavelength in experiments.

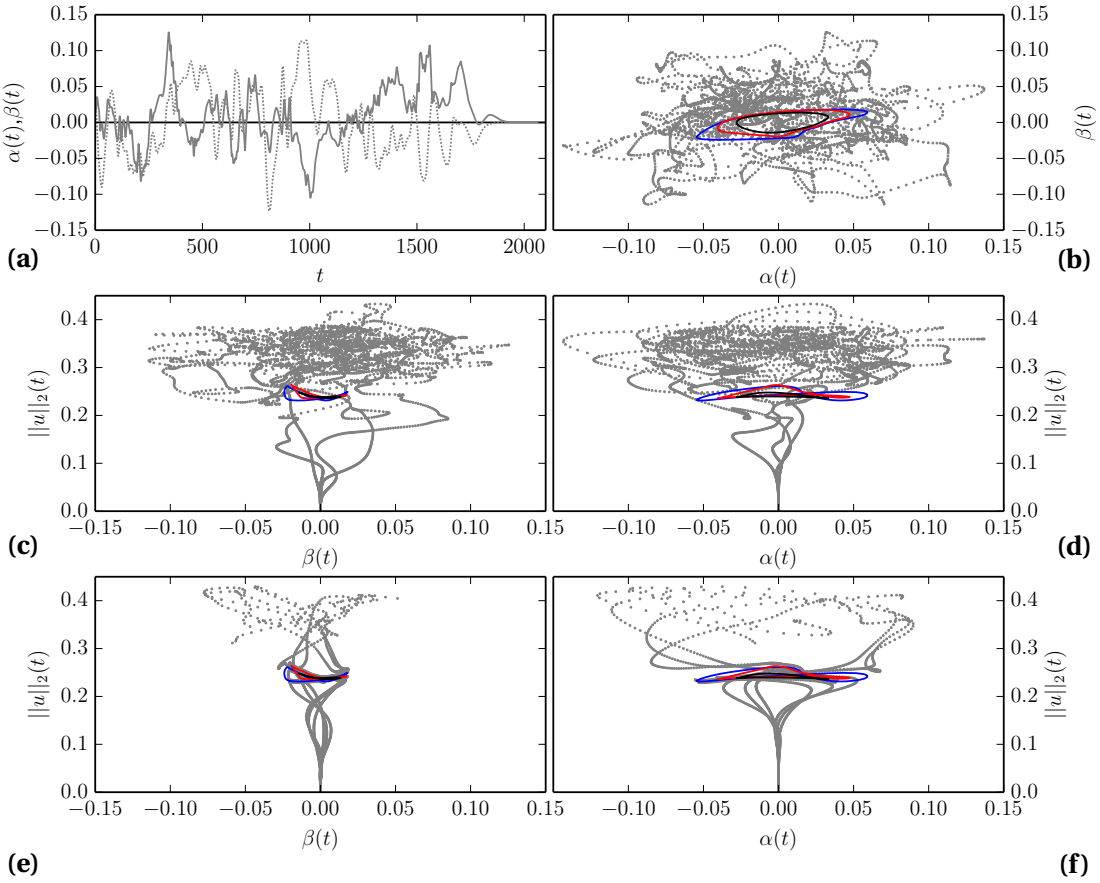

Figure 9.8 – Turbulent trajectory in subspace $\mathbb{D}$ (compare with Figure 9.3) is plotted in terms of $\alpha(t)$, $\beta(t)$ and $||u||_2(t)$. Panel **(a)** indicates the longest of four simulated time series of $\alpha(t)$ (dotted) and $\beta(t)$ (solid) that exceed $t = 1000$ before decaying to laminar flow. All four time series are shown in the phase portraits **(b-d)** that illustrate that the three periodic orbits mark the lower bound of the turbulent saddle in $||u||_2(t)$.

10 Conclusions and perspectives

The previous sections discussed and concluded on individual topics. Here, general conclusions are drawn. These conclusions are based on the summary of all results presented in this thesis as well as on the development of numerical tools for a dynamical systems approach to wall-bounded shear flows. The conclusions lead to specific Perspectives for future research.

Previous observations of turbulent patterns in experiments and simulations of two different wall-bounded shear flows, ILC and PCF, raised the question of how these patterns emerge. The results in the present thesis provide a dynamical systems description of various turbulent patterns in ILC and of oblique turbulent-laminar stripes in PCF. For all studied turbulent patterns, the following hypothesis has been confirmed:
If a turbulent pattern with spatio-temporally regular and complex features is observed in a wall-bounded shear flow, there exists an invariant solution which supports the observed dynamics and thereby explains certain regular and complex features in the observed turbulent pattern.

Regular pattern features. The existence of an exact invariant solution of the governing fluid flow equations can explain how wall-bounded shear flows can give rise to a regular pattern. The flow structure of the invariant solution and the associated regular spatial and temporal properties, like wavelength, orientation and oscillation period, emerge in the flow when the dynamics approaches the state space neighborhood of the specific invariant solution.

Complex dynamics. Spatio-temporally complex dynamics is supported by coexisting unstable invariant solutions and their dynamical connections in state space. The particular dynamics depends on the geometry of the state space structure in which the unstable invariant solutions are embedded. The present thesis discusses the dynamical relevance of invariant solutions in terms of their stability and connectivity by studying phase portraits and bifurcation structures. However, more details need to be revealed to fully understand how invariant solutions are embedded in complicated state space structures. The following

subsections discuss specific conclusions and future perspectives for turbulent patterns in ILC and PCF.

10.1 Complex dynamics in time

Unstable invariant solutions may influence complex temporal dynamics of turbulent patterns in different ways.

Transiently visited invariant solutions. A state space trajectory describing the temporal dynamics of the flow may transiently visit the state space neighborhood of invariant solutions. This type of transient dynamics is observed in ILC by studying state space trajectories starting from unstable laminar flow in minimal periodic domains (Chapter 4). There, sequences of transient visits are clearly indicated when plotting the temporal dynamics in phase portraits. For oblique stripe patterns in PCF, transient visits of invariant solutions are less obvious. The state space of stripes in PCF is larger and invariant solutions are generally more unstable than in ILC (e.g. Figure 8.2). Observing clear transient visits is thus less likely. Unstable invariant solutions in a large state space are also found for transverse oscillations in ILC (Figure 5.12). The conditions for clearly observing transient visits of invariant solutions are not well understood.
Perspective: To understand how unstable invariant solutions could be transiently visited, constructing heteroclinic connections would yield insights. One approach to construct heteroclinic connections has previously been implemented in *Channelflow* and applied to previously published invariant solutions in PCF (Farano et al., 2019). Constructing heteroclinic connections between the invariant solutions discussed in the present thesis, might allow to better understand transient visits of these invariant solutions.

Reminiscence of invariant solutions along orbits. Besides transiently visited invariant soltuions, a second mechanism for transiently emerging patterns has been identified in the present thesis. In cases with subcritical bifurcations, the pattern of invariant solutions along the subcritical solution branch may be observed transiently at supercritical control parameters where the corresponding invariant solutions do not exist. This case is described in Sections 4.4.3 and 5.3.1 for the transient skewed varicose pattern in Rayleigh-Bénard convection. This observation suggests a correspondence between flow structure of subcritical invariant solutions and temporal instances along supercritical state space orbits.
Perspective: A detailed analysis of such a correspondence might help to understand the reminiscence of subcritical state space structures, involving invariant solutions, along supercritical state space orbits.

Intrinsic temporal dynamics of invariant solutions. Equilibrium solutions, traveling waves and periodic orbits have either steady or oscillatory dynamics. When unstable invariant

solutions are transiently visited, their intrinsic temporal dynamics affects the state space trajectories which becomes observable in the flow. An illustrative example is the single unstable periodic orbit underlying chaotic crawling rolls in ILC (Section 6). In chaotic flow, a large number of unstable periodic orbits can be expected to be dense in the chaotic attractor. Knowing many of them may allow to determine statistical properties of the chaotic dynamics using periodic orbit theory (Cvitanović, 1995).
Perspective: Applying periodic orbit theory to turbulent ILC could capture statistical properties like turbulent heat transfer. Identifying a large number of periodic orbits appears easier in ILC than in other pure shear flows.

10.2 Complex dynamics in space

Equilibrium solutions that capture the spatial coexistence of different patterns may be interpreted in terms of space dynamics. The lateral pattern of the stripe equilibrium in PCF, discussed in Section 8, represents a torus in space. This torus captures the coexistence of high and low amplitude wavy velocity streaks in space. High and low amplitude wavy streaks also exist separately from each other as small-scale periodic invariant solutions (Figure 7.3a,b). Since coexistence of invariant solutions in dissipative systems at equal control parameters may support spatial coexistence of these solution (Knobloch, 2015), the coexistence of invariant solutions in ILC, as indicated by the bifurcation structures discussed in Section 5, suggests the existence of invariant solutions describing how the associated patterns can coexist in space.
Perspective: The construction of invariant solutions that capture the spatial coexistence of two different patterns in ILC would better explain the spatial complexity observed in experiments and simulations, like defects or localized patterns.

10.3 Wavelength selection

Confining the state space of turbulent patterns to particular symmetry subspaces has been a key step in all successful identifications of invariant solutions discussed in the present thesis. This includes discrete reflection symmetries as well as descrete translation symmetries. The latter correspond to confining the analysis to a subspace of a minimal periodic domain. In minimal domains, patterns wavelengths are imposed by the size of the domain. In extended experiments or simulations however, pattern wavelengths are not constrained by boundary conditions and can be selected 'freely' by the flow. This unconstrained selection is not captured by dynamical systems analysis in the present thesis. Turbulent patterns in ILC and PCF have been studied in very specific minimal periodic domains. Three different approaches to study wavelength selection are proposed.
Perspective A: Numerical continuation in the domain size allows to explore the existence and

stability properties of invariant solutions at smoothly varying pattern wavelengths.
Perspective B: Appropriate domain sizes for convection patterns in ILC were suggested by previous Floquet analysis. A future analysis of turbulent patterns in wall-bounded shear flows using *Channelflow* would benefit from having a tool for Floquet analysis implemented in *Channelflow*.
Perspective C: The problem of wavelength selection can be solved by constructing localized invariant solutions. Patterns that are localized within a homogeneous background state are not constrained in their wavelength. Such invariant solutions can directly be compared with experimentally observed patterns.

10.4 Standing and traveling waves across patterns

Different periodic orbits have been identified that represent standing wave solutions. The periodic orbit SSW, underlying subharmonic oscillations in ILC (Section 4.4.2), bifurcates together with a traveling wave solution in equivariant Hopf bfirucations from straight convection rolls with $O(2)$-symmetry in the streamwise dimension (Section 5.3.2). Like SSW, the periodic orbit TO, underlying transverse oscillations in ILC (Section 4.4.2), represents a subharmonic standing wave solution. However, TO bifurcate from transverse rolls (TR) which are patterned in the streamwise dimension (Section 5.3.5). Similarly, the periodic orbits $OSW_{1,2,3}$, underlying oblique stripe patterns in PCF (Section 9), represent standing waves across a non-homogeneous pattern, namely wavy velocity streaks. For TO and $OSW_{1,2,3}$, no related traveling wave solution has been found. All discussed standing wave solutions have in common that they satisfy an approximate resonance condition involving either diffusion time scales (see Equation 9.9) or mean advection time scales (see Equation 5.24).
Perspective A: The approximate resonance relations (9.9) and (5.24) suggest that exact resonance might be favorable for invariant solutions underlying standing waves. Exact resonance is obtained by changing the size of the numerical domain.
Perspective B: Equivariant bifurcations are not expected for TO and $OSW_{1,2,3}$ due to the absence of $O(2)$-symmetry in the streamwise direction. However, corresponding 'traveling wave' solutions might exist. This conjecture is based on the observations that in both turbulent patterns, switching diamond panes in ILC and oblique turbulent-laminar stripes in PCF, convection rolls and velocity streaks drift across the pattern. The drift relies on locations in space where rolls/streaks emerge and decay. Since rolls/streaks not only drift but emerge and decay, the underlying invariant solutions are expected to be technically periodic orbits rather than traveling waves.
Perspective C: Switching diamond panes in ILC and oblique turbulent-laminar stripes in PCF are both turbulent patterns with preferred oblique modulations against the streamwise direction. Since both patterns have underlying standing wave solutions, investigating the

analogy between the two patterns might reveal more insights. Homotopy transformations between ILC and PCF as suggested in the next conclusion might be a useful approach.

10.5 Correspondence of patterns in ILC with patterns in PCF

Due to the existence of many different single state attractors in ILC, the dynamical systems analysis of ILC is simpler than the analysis of PCF. Since ILC and PCF are both wall-bounded shear flows that have the Navier-Stokes equations and the same discrete reflection symmetries in common, homotopy transformations from ILC to PCF might be an appropriate approach to transfer state space structures that have been understood in ILC to PCF.
Perspective: Since the boundary conditions of ILC have been implemented in a general form (Section 2.2.5), the tools for homotopy transformations exist. However, preliminary results of homotopy transformations suggest arising difficulties along numerical continuations. These difficulties might stem from the fact that the cubic laminar flow profile in ILC creates shear forces of opposite sign. At the walls shear is positive, in the bulk shear is negative. During homotopy transformation, one shear region expands and the other shear region shrinks and finally vanishes. If invariant solutions of ILC rely on bulk and/or wall shear, homotopy transformations using numerical continuation might not work.

Bibliography

G Ahlers and R P Behringer. Evolution of Turbulence from the Rayleigh-Bénard Instability. *Physical Review Letters*, 40(11):712–716, mar 1978. ISSN 0031-9007. doi: 10.1103/PhysRevLett.40.712.

Hiroshi Aida, Takahiro Tsukahara, and Y. Kawaguchi. Development of a Turbulent Spot Into a Stripe Pattern in Plane Poiseuille Flow. In *Proceedings of the Seventh International Symposium on Turbulence and Shear Flow Phenomena*, pages 1–6, Ottawa, Canada, 28-31 July, 2011. Begell House Inc. URL http://www.dl.begellhouse.com/references/3ce1b491115b5c16,60d8a9681cb3cfc7,3a76090a414f4250.html.

C D Andereck, S S Liu, and H L Swinney. Flow regimes in a circular Couette system with independently rotating cylinders. *Journal of Fluid Mechanics*, 164:155–183, 1986. doi: 10.1017/S0022112086002513.

Athanasios C. Antoulas. *Approximation of Large-Scale Dynamical Systems*. Society for Industrial and Applied Mathematics, jan 2005. ISBN 978-0-89871-529-3. doi: 10.1137/1.9780898718713. URL http://epubs.siam.org/doi/book/10.1137/1.9780898718713.

John Argyris, Gunter Faust, and Maria Haase. Routes to chaos and turbulence. A computational introduction. *Philosophical Transactions - Royal Society of London, A*, 344(1671):207–234, 1993. doi: 10.1098/rsta.1993.0088.

D Armbruster, J Guckenheimer, and P Holmes. Heteroclinic cycles and modulated travelling waves in systems with O(2) symmetry. *Physica D*, 29(3):257–282, 1988. doi: 10.1016/0167-2789(88)90032-2.

Uri M Ascher, Steven J Ruuth, and Brian T R Wetton. Implicit-Explicit Methods for Time-Dependent Partial Differential Equations. *SIAM Journal on Numerical Analysis*, 32(3):797–823, jun 1995. ISSN 0036-1429. doi: 10.1137/0732037. URL http://epubs.siam.org/doi/abs/10.1137/0732037http://epubs.siam.org/doi/10.1137/0732037.

M. Avila, F. Mellibovsky, N. Roland, and B. Hof. Streamwise-Localized Solutions at the Onset of Turbulence in Pipe Flow. *Physical Review Letters*, 110(22):224502, may 2013. ISSN 0031-9007. doi: 10.1103/PhysRevLett.110.224502.

D Barkley. Simplifying the complexity of pipe flow. *Physical Review E*, 84(1):016309, jul 2011. ISSN 1539-3755. doi: 10.1103/PhysRevE.84.016309.

Dwight Barkley. Theoretical perspective on the route to turbulence in a pipe. *Journal of Fluid Mechanics*, 803(2016):P1, 2016. ISSN 0022-1120. doi: 10.1017/jfm.2016.465. URL http://www.journals.cambridge.org/abstract{_}S0022112016004651.

Dwight Barkley and Laurette S. Tuckerman. Computational Study of Turbulent Laminar Patterns in Couette Flow. *Physical Review Letters*, 94(1):014502, jan 2005. ISSN 0031-9007. doi: 10.1103/PhysRevLett.94.014502. URL http://link.aps.org/doi/10.1103/PhysRevLett.94.014502.

Dwight Barkley and Laurette S. Tuckerman. Mean flow of turbulent–laminar patterns in plane Couette flow. *Journal of Fluid Mechanics*, 576:109–137, 2007. ISSN 0022-1120. doi: 10.1017/S002211200600454X. URL http://www.journals.cambridge.org/abstract{_}S002211200600454X.

B J Bayly, S A Orszag, and T Herbert. Instability mechanisms in shear-flow transition. *Annual Review of Fluid Mechanics*, 20:359–391, jan 1988. ISSN 0066-4189. doi: 10.1146/annurev.fl.20.010188.002043.

C Beaume, E Knobloch, G P Chini, and K Julien. Modulated patterns in a reduced model of a transitional shear flow. *Physica Scripta*, 91(2):1–24, 2016. ISSN 14024896. doi: 10.1088/0031-8949/91/2/024003. URL http://dx.doi.org/10.1088/0031-8949/91/2/024003.

A. Bergeon and E. Knobloch. Natural doubly diffusive convection in three-dimensional enclosures. *Physics of Fluids*, 14(9):3233–3250, sep 2002. ISSN 1070-6631. doi: 10.1063/1.1493790. URL http://aip.scitation.org/doi/10.1063/1.1493790.

Eberhard Bodenschatz, Werner Pesch, and Guenter Ahlers. Recent Developments in Rayleigh-Bénard Convection. *Annual Review of Fluid Mechanics*, 32(1):709–778, 2000. ISSN 0066-4189. doi: 10.1146/annurev.fluid.32.1.709. URL http://www.annualreviews.org/doi/abs/10.1146/annurev.fluid.32.1.709.

E Brand and J F Gibson. A doubly-localized equilibrium solution of plane Couette flow. *Journal of Fluid Mechanics*, 750:R3, 2014. ISSN 0022-1120. doi: http://dx.doi.org/10.1017/jfm.2014.285.

Nazmi Burak Budanur and Predrag Cvitanović. Unstable Manifolds of Relative Periodic Orbits in the Symmetry-Reduced State Space of the Kuramoto–Sivashinsky System. *Journal of Statistical Physics*, 167(3-4):636–655, may 2017. ISSN 0022-4715. doi: 10.1007/s10955-016-1672-z. URL http://link.springer.com/10.1007/s10955-016-1672-z.

J Burke and E Knobloch. Localized states in the generalized Swift-Hohenberg equation. *Physical Review E - Statistical, Nonlinear, and Soft Matter Physics*, 73(December 2005):1–15, 2006. ISSN 15393755. doi: 10.1103/PhysRevE.73.056211.

F H Busse. Non-linear properties of thermal convection. *Reports on Progress in Physics*, 41(12): 1929, 1978a. doi: 10.1088/0034-4885/41/12/003.

F H Busse and R M Clever. Instabilities of convection rolls in a fluid of moderate Prandtl number. *Journal of Fluid Mechanics*, 91(02):319, 1979. ISSN 0022-1120. doi: 10.1017/S002211207900015X.

F H Busse and R M Clever. Three-dimensional convection in an inclined layer heated from below. *J. Eng. Math.*, 26(1):1–19, 1992. ISSN 0022-0833. doi: 10.1007/BF00043222.

F H Busse and R M Clever. The sequence-of-bifurcations approach towards an understanding of complex flows. In Daniel N Riahi, editor, *Mathematical Modeling and Simulation in Hydrodynamic Stability*, pages 15–34. World Scientific, 1996.

F H Busse and R M Clever. Bursts in Inclined Layer Convection. *Phys. Fluids*, 12(8):2137–2140, 2000. doi: 10.1063/1.870459.

F. H. Busse and J. A. Whitehead. Oscillatory and collective instabilities in large Prandtl number convection. *Journal of Fluid Mechanics*, 66(1):67–79, oct 1974. ISSN 14697645. doi: 10.1017/S0022112074000061. URL http://www.journals.cambridge.org/abstract{_}S0022112074000061.

F.H. Busse. Non-linear properties of thermal convection. *Rep. Prog. Phys.*, 41(41), 1978b. URL http://iopscience.iop.org/0034-4885/41/12/003.

C Canuto, M Y Hussaini, A Quarteroni, and T A Zang. *Spectral Methods in Fluid Dynamics*. Springer Berlin Heidelberg, Berlin, Heidelberg, 1988. ISBN 978-3-540-52205-8. doi: 10.1007/978-3-642-84108-8.

C. Canuto, M. Y. Hussaini, A. Quarteroni, and T. A. Zang. *Spectral Methods: Fundamentals in Single Domains*. Springer, 2006. ISBN 9783540307259. doi: 10.1007/978-3-540-30726-6. URL http://www.amazon.com/Spectral-Methods-Fundamentals-Scientific-Computation/dp/3540307257/sr=1-1/qid=1172681680/ref=sr{_}1{_}1/002-9880249-7216022?ie=UTF8{&}s=books.

Claudio Canuto and Giovanni Sacchi Landriani. Analysis of the Kleiser-Schumann method. *Numerische Mathematik*, 50(2):217–243, 1986. ISSN 0029599X. doi: 10.1007/BF01390431.

G J Chandler and R R Kerswell. Invariant recurrent solutions embedded in a turbulent two-dimensional Kolmogorov flow. *Journal of Fluid Mechanics*, 722:554–595, mar 2013. ISSN 0022-1120. doi: 10.1017/jfm.2013.122.

Matthew Chantry, Laurette S. Tuckerman, and Dwight Barkley. Universal continuous transition to turbulence in a planar shear flow. *Journal of Fluid Mechanics*, 824, 2017. ISSN 14697645. doi: 10.1017/jfm.2017.405.

Yen-Ming Chen and Arne J. Pearlstein. Stability of free-convection flows of variable-viscosity fluids in vertical and inclined slots. *Journal of Fluid Mechanics*, 198:513, 1989. ISSN 0022-1120. doi: 10.1017/S0022112089000236.

F Chillà and J Schumacher. New perspectives in turbulent Rayleigh-Bénard convection. *The European physical journal. E, Soft matter*, 35(7):58, 2012. ISSN 1292-895X. doi: 10.1140/epje/i2012-12058-1. URL http://www.ncbi.nlm.nih.gov/pubmed/22791306.

Pascal Chossat and Gerard Iooss. *The Couette-Taylor Problem*, volume 102. Springer, 1994. ISBN 9781461287308.

R M Clever. Finite Amplitude Longitudal Convection Rolls in an Inclined Layer. *Journal of Heat Transfer*, 95(3):407, 1973. ISSN 00221481. doi: 10.1115/1.3450072. URL http://heattransfer.asmedigitalcollection.asme.org/article.aspx?articleid=1435657.

R. M. Clever and F. H. Busse. Instabilities of longitudinal convection rolls in an inclined layer. *J . Fluid Mech*, 81:107–127, 1977. ISSN 00442275. doi: 10.1007/BF01603815.

R. M. Clever and F. H. Busse. Three-dimensional Convection in a Horizontal Fluid Layer Subjected to a Constant Shear. *Journal of Fluid Mechanics*, 234:511–527, 1992. ISSN 0022-1120. doi: 10.1017/S0022112092000892.

R M Clever and F H Busse. Tertiary and Quarternary Solutions for Convection in a Vertical Fluid Layer Heated From the Side. *Chaos Solitons Fractals*, 5(10):1795–1803, 1995.

R M Clever and F H Busse. Tertiary and quaternary solutions for plane Couette flow. *Journal of Fluid Mechanics*, 344:137–153, 1997. doi: 10.1017/S0022112097005818.

R M Clever, F H Busse, and R E Kelly. Instabilities of longitudinal convection rolls in couette flow. *Zeitschrift fuer angewandte Mathematik und Physik ZAMP*, 28(01):771–783, 1977. ISSN 00442275. doi: 10.1007/BF01603815.

D Coles and C W Van Atta. Progress report on a digital experiment in spiral turbulence. *Aiaa J.*, {4}(11):1969, 1966. URL papers2://publication/uuid/1A23026D-BF93-4F33-B172-83083354CED0.

Donald Coles. Transition in circular Couette flow. *Journal of Fluid Mechanics*, 21(03):385–425, mar 1965. ISSN 0022-1120. doi: 10.1017/S0022112065000241. URL http://www.journals.cambridge.org/abstract{_}S0022112065000241.

Marie Couliou and Romain Monchaux. Growth dynamics of turbulent spots in plane Couette flow. *Journal of Fluid Mechanics*, 819:1–20, 2017. ISSN 14697645. doi: 10.1017/jfm.2017.140.

J D Crawford and E Knobloch. Symmetry and symmetry-breaking bifurcations in fluid dynamics. *Annual Review of Fluid Mechanics*, 23:341–87, 1991. doi: 10.1146/annurev.fluid.23.1.341.

M. C. Cross and P. C. Hohenberg. Pattern formation outside of equilibrium. *Reviews of Modern Physics*, 65(3):851–1112, jul 1993. ISSN 00346861. doi: 10.1103/RevModPhys.65.851.

Michael Cross and Henry Greenside. *Pattern Formation and Dynamics in Nonequilibrium Systems*. Cambridge University Press, 2009. ISBN 9780511627200. doi: 10.1017/CBO9780511627200. URL http://ebooks.cambridge.org/ref/id/CBO9780511627200.

P Cvitanović. Recurrent flows : the clockwork behind turbulence. *Journal of Fluid Mechanics*, 726:1–4, 2013. doi: 10.1017/jfm.2013.198.

P Cvitanović and Bruno Eckhardt. Periodic orbit expansions for classical smooth flows. *Journal of Physics A: Mathematical and General*, 24(5):L237–L241, mar 1991. ISSN 0305-4470. doi: 10.1088/0305-4470/24/5/005.

P Cvitanović, R Artuso, G Mainieri, G Tanner, and G Vattay. *Chaos: Classical and quantum*. chaosbook.org, Niels Bohr Institute, Copenhagen, 2016. URL chaosbook.org.

P Cvitanović, R Artuso, R Mainieri, G Tanner, and G Vattay. Section 10 "Flips, slides and turns". In *Chaos: Classical and Quantum*. Niels Bohr Institute, Copenhagen, version 15 edition, 2017.

Predrag Cvitanović. Dynamical averaging in terms of periodic orbits. *Physica D: Nonlinear Phenomena*, 83(1-3):109–123, may 1995. ISSN 01672789. doi: 10.1016/0167-2789(94)00256-P. URL http://linkinghub.elsevier.com/retrieve/pii/016727899400256P.

Karen Daniels, Brendan Plapp, and Eberhard Bodenschatz. Pattern Formation in Inclined Layer Convection. *Physical Review Letters*, 84(23):5320–5323, 2000. ISSN 0031-9007. doi: 10.1103/PhysRevLett.84.5320.

Karen E Daniels and Eberhard Bodenschatz. Defect turbulence in inclined layer convection. *Physical review letters*, 88(3):034501, 2002. ISSN 0031-9007. doi: 10.1103/PhysRevLett.88.034501.

Karen E Daniels, Richard J Wiener, and Eberhard Bodenschatz. Localized transverse bursts in inclined layer convection. *Physical review letters*, 91(11):114501, 2003. ISSN 0031-9007. doi: 10.1103/PhysRevLett.91.114501.

Karen E. Daniels, Oliver Brausch, Werner Pesch, and Eberhard Bodenschatz. Competition and bistability of ordered undulations and undulation chaos in inclined layer convection. *Journal of Fluid Mechanics*, 597:261–282, 2008. ISSN 0022-1120. doi: 10.1017/S0022112007009615. URL http://www.journals.cambridge.org/abstract{_}S0022112007009615.

F. Daviaud, J Hegseth, and P Berge. Subcritical Transition to Turbulence in Plane Couette Flow. *Physical Review Letters*, 69(17):2511–2514, 1992.

J. G. A. de Graaf and E. F. M. van der Held. The relation between the heat transfer and the convection phenomena in enclosed plane air layers. *Applied Scientific Research, Section A*, 3:393–409, 1953.

A de Lozar, F Mellibovsky, M Avila, and B Hof. Edge State in Pipe Flow Experiments. *Physical Review Letters*, 108(21):214502, may 2012. ISSN 0031-9007. doi: 10.1103/PhysRevLett.108.214502.

John E Dennis and Robert B Schnabel. *Numerical methods for unconstrained optimization and nonlinear equations*. SIAM, 1996.

H A Dijkstra, F W Wubs, A K Cliffe, E Doedel, A L Hazel, V Lucarini, A G Salinger, E T Phipps, J Sanchez-Umbria, H Schuttelaars, L S Tuckerman, and U Thiele. Numerical Bifurcation Methods and their Application to Fluid Dynamics: Analysis beyond Simulation. *Communications in Computational Physics*, 15(1):1–45, 2014. ISSN 18152406. doi: 10.4208/cicp.240912.180613a.

S. Dong. Evidence for internal structures of spiral turbulence. *Physical Review E - Statistical, Nonlinear, and Soft Matter Physics*, 80(6):1–4, 2009. ISSN 15393755. doi: 10.1103/PhysRevE.80.067301.

Yohann Duguet and P Schlatter. Oblique Laminar-Turbulent Interfaces in Plane Shear Flows. *Physical Review Letters*, 110(3):034502, jan 2013. ISSN 0031-9007. doi: 10.1103/PhysRevLett.110.034502.

Yohann Duguet, P Schlatter, and D S Henningson. Localized edge states in plane Couette flow. *Physics of Fluids*, 21:111701, 2009. doi: 10.1063/1.3265962.

Yohann Duguet, P Schlatter, and D S Henningson. Formation of turbulent patterns near the onset of transition in plane Couette flow. *Journal of Fluid Mechanics*, 650:119–129, 2010. doi: 10.1017/S0022112010000297.

Bruno Eckhardt, Tobias M. Schneider, Bjorn Hof, and Jerry Westerweel. Turbulence transition in pipe flow. *Annual Review of Fluid Mechanics*, 39(1): 447–468, 2007. ISSN 0066-4189. doi: 10.1146/annurev.fluid.39.050905.110308. URL http://www.annualreviews.org/doi/abs/10.1146/annurev.fluid.39.050905.110308http://www.annualreviews.org/doi/10.1146/annurev.fluid.39.050905.110308.

J Eckmann. Roads to turbulence in dissipative dynamical systems. *Reviews of Modern Physics*, 53:643–654, oct 1981. ISSN 0034-6861. doi: 10.1103/RevModPhys.53.643.

W. S. Edwards, L. S. Tuckerman, R. A. Friesner, and D. C. Sorensen. Krylov Methods for the Incompressible Navier-Stokes Equations. *Journal of Computational Physics*, 110(1):82–102, 1994. ISSN 00219991. doi: 10.1006/jcph.1994.1007.

M. Farano, S. Cherubini, J.-C. Robinet, P. De Palma, and T. M. Schneider. Computing heteroclinic orbits using adjoint-based methods. *Journal of Fluid Mechanics*, 858:R3, jan 2019. ISSN 0022-1120. doi: 10.1017/jfm.2018.860. URL https://www.cambridge.org/core/product/identifier/S0022112018008601/type/journal{_}article.

P. R. Fenstermacher, Harry L. Swinney, and J. P. Gollub. Dynamical instabilities and the transition to chaotic Taylor vortex flow. *Journal of Fluid Mechanics*, 94(1):103–128, sep 1979. ISSN 0022-1120. doi: 10.1017/S0022112079000963. URL https://www.cambridge.org/core/product/identifier/S0022112079000963/type/journal{_}article.

R.P Feynman, R.B Leighton, and M Sands. *The Feynman lectures on physics, Vol. 2*. Addison-Wesley, Reading, MA, 1964. ISBN 0-201-02117-X ; 978-0-201-02117-2. URL http://www.dfi.uchile.cl/marcel/Pdf/Course/FI33a200701/(ebook)FeynmanLecturesonPhysicsCompleteVolumes2-.pdf.

M Frigo and SG Johnson. The Design and Implementation of FFTW3. *Proceedings of the IEEE*, 93(2):216–231, feb 2005. ISSN 0018-9219. doi: 10.1109/JPROC.2004.840301.

Uriel Frisch. *Turbulence: The Legacy of A. N. Kolmogorov*. Cambridge university press, 1995.

K Fujimura and R E Kelly. Mixed mode convection in an inclined slot. *Journal of Fluid Mechanics*, 246:545–568, 1993. ISSN 0022-1120. doi: 10.1017/S0022112093000266.

G Z Gershuni and E M Zhukhovitskii. Stability of plane-parallel convective motion with respect to spatial perturbations. *Prikl. Mat. i Mekh.*, 33(5):855–860, 1969.

J. F. Gibson and E. Brand. Spanwise-localized solutions of planar shear flows. *Journal of Fluid Mechanics*, 745:25–61, apr 2014. ISSN 0022-1120. doi: 10.1017/jfm.2014.89. URL http://www.journals.cambridge.org/abstract{_}S0022112014000895.

J. F. Gibson, J. Halcrow, and P. Cvitanović. Visualizing the geometry of state space in plane Couette flow. *Journal of Fluid Mechanics*, 611, sep 2008a. ISSN 0022-1120. doi: 10.1017/S002211200800267X. URL http://arxiv.org/abs/0705.3957http://dx.doi.org/10.1017/S002211200800267Xhttp://www.journals.cambridge.org/abstract{_}S002211200800267X.

J F Gibson, J Halcrow, and P Cvitanović. Visualizing the geometry of state space in plane Couette flow. *Journal of Fluid Mechanics*, 611:107–130, aug 2008b. ISSN 0022-1120. doi: 10.1017/S002211200800267X.

J F Gibson, J Halcrow, and P Cvitanović. Equilibrium and traveling-wave solutions of plane Couette flow. *Journal of Fluid Mechanics*, 638:243–266, 2009. doi: 10.1017/S0022112009990863.

John F. Gibson and Tobias M. Schneider. Homoclinic snaking in plane Couette flow: bending, skewing and finite-size effects. *Journal of Fluid Mechanics*, 794(2013):530–551, may 2016. ISSN 0022-1120. doi: 10.1017/jfm.2016.177. URL http://arxiv.org/abs/1509.08424http://www.journals.cambridge.org/abstract{_}S0022112016001774.

John F Gibson, Florian Reetz, Sajjad Azimi, Alessia Ferraro, Tobias Kreilos, Hecke Schrobsdorff, Mirko Farano, Ayse Ferhan Yesil, Simon S Schütz, Massimiliano Culpo, and Tobias M Schneider. Channelflow 2.0. *in preparation*, 2019.

J P Gollub and H L Swinney. Onset of Turbulence in a Rotating Fluid. *Physical Review Letters*, 35(14):927–930, 1975. doi: 10.1103/PhysRevLett.35.927.

Martin Golubitsky and Ian Stewart. *The Symmetry Perspective*. Springer, 2002.

Donald D. Gray and Aldo Giorgini. The validity of the boussinesq approximation for liquids and gases. *International Journal of Heat and Mass Transfer*, 19(5):545–551, 1976. ISSN 00179310. doi: 10.1016/0017-9310(76)90168-X.

J Guckenheimer and P Holmes. *Nonlinear oscillations, dynamical systems and bifurcations of vector fields*, volume 42 of *Applied Mathematical Sciences*. Springer-Verlag, 1983.

J Halcrow, J F Gibson, P Cvitanović, and D Viswanath. Heteroclinic connections in plane {Couette} flow. *Journal of Fluid Mechanics*, 621:365–376, feb 2009. ISSN 0022-1120. doi: 10.1017/S0022112008005065.

John E Hart. Stability of the flow in a differentially heated inclined box. *Journal of Fluid Mechanics*, 47(03):547, 1971a. ISSN 0022-1120. doi: 10.1017/S002211207100123X. URL http://www.journals.cambridge.org/abstract{_}S002211207100123X.

John E Hart. Transition to a wavy vortex régime in convective flow between inclined plates. *Journal of Fluid Mechanics*, 48(2):265–271, 1971b. ISSN 14697645. doi: 10.1017/S0022112071001587.

S. Hashimoto, A. Hasobe, T. Tsukahara, Y. Kawaguchi, and H. Kawamura. An experimental study on turbulent-stripe structure in transitional channel flow. In *Proceedings of the Sixth International Symposium on Turbulence, Heat and Mass Transfer*, pages 193–196, Rome, Italy, 14-18 September, 2009. Begell House Inc. ISBN 978-1-56700-262-1. doi: 10.1615/ICHMT.2009.TurbulHeatMassTransf.2370. URL http://www.dl.begellhouse.com/references/1bb331655c289a0a,79a1a64252fdbc4b,39a032e27147214a.html.

John J Hegseth, C D Andereck, F Hayot, and Y Pomeau. Spiral Turbulence and Phase Dynamics. *Phys. Rev. Lett.*, 62(3):257–260, 1989.

Björn Hof, Casimir W H van Doorne, Jerry Westerweel, Frans T M Nieuwstadt, Holger Faisst, Bruno Eckhardt, Hakan Wedin, Richard R Kerswell, and Fabian Waleffe. Experimental observation of nonlinear traveling waves in turbulent pipe flow. *Science*, 305(September): 1594–1598, 2004. ISSN 1095-9203. doi: 10.1126/science.1100393.

Björn Hof, Jerry Westerweel, Tobias M Schneider, and Bruno Eckhardt. Finite lifetime of turbulence in shear flows. *Nature*, 443(7107):59–62, sep 2006. ISSN 0028-0836. doi: 10.1038/nature05089. URL http://www.nature.com/doifinder/10.1038/nature05089.

K G T Hollands and L Konicek. Experimental study of the stability of differentially heated inclined air layers. *International Journal of Heat and Mass Transfer*, 16(7):1467–1476, 1973. ISSN 00179310. doi: 10.1016/0017-9310(73)90153-1.

E Hopf. A mathematical example displaying features of turbulence. *Communications on Pure and Applied Mathematics*, 1(4):303–322, dec 1948. ISSN 00103640. doi: 10.1002/cpa.3160010401.

Takahiro Ishida, Geert Brethouwer, Yohann Duguet, and Takahiro Tsukahara. Laminar-turbulent patterns with rough walls. *Physical Review Fluids*, 2(7):073901, 2017. ISSN 2469-990X. doi: 10.1103/PhysRevFluids.2.073901.

J Jiménez and P Moin. The minimal flow unit in near-wall turbulence. *Journal of Fluid Mechanics*, 225:213–240, 1991. doi: 10.1017/S0022112091002033.

Javier Jiménez. Coherent structures in wall-bounded turbulence. *Journal of Fluid Mechanics*, 842:P1, may 2018. ISSN 0022-1120. doi: 10.1017/jfm.2018.144. URL https://www.cambridge.org/core/product/identifier/S0022112018001441/type/journal{_}article.

Matthew P. Juniper and R.I. Sujith. Sensitivity and Nonlinearity of Thermoacoustic Oscillations. *Annual Review of Fluid Mechanics*, 50(1):661–689, 2018. ISSN 0066-4189. doi: 10.1146/annurev-fluid-122316-045125.

G Kawahara, M Uhlmann, and L van Veen. The significance of simple invariant solutions in turbulent flows. *Annual Review of Fluid Mechanics*, 44(1):203–225, jan 2012. ISSN 0066-4189. doi: 10.1146/annurev-fluid-120710-101228.

C. T. Kelley. *Solving Nonlinear Equations with Newton's Method*. Society for Industrial and Applied Mathematics, jan 2003. ISBN 978-0-89871-546-0. doi: 10.1137/1.9780898718898. URL http://epubs.siam.org/doi/book/10.1137/1.9780898718898.

R E Kelly. The onset and development of thermal convection in fully developed shear flows. *Advances in applied mechanics*, 31:35–112, 1994.

Robert M Kerr. Rayleigh number scaling in numerical convection. *J . Fluid Mech*, 310, 1996.

R R Kerswell. Recent progress in understanding the transition to turbulence in a pipe. *Nonlinearity*, 18(6):R17–R44, nov 2005. ISSN 0951-7715. doi: 10.1088/0951-7715/18/6/R01.

Taras Khapko, Tobias Kreilos, Philipp Schlatter, Yohann Duguet, Bruno Eckhardt, and Dan S Henningson. Localized edge states in the asymptotic suction boundary layer. *Journal of Fluid Mechanics*, 717:R6, 2013. doi: 10.1017/jfm.2013.20.

L. Kleiser and U. Schumann. Treatment of incompressibility and boundary conditions in 3-D numerical spectral simulations of plane channel flows. In E. Hirschel, editor, *Proceedings of the Third GAMM — Conference on Numerical Methods in Fluid Mechanics*, pages 165—-173, Viewweg, Braunschweig, 1980.

E. Knobloch. Oscillatory convection in binary mixtures, 1986. ISSN 10502947.

E. Knobloch. Spatial Localization in Dissipative Systems. *Annual Review of Condensed Matter Physics*, 6(1):325–359, mar 2015. ISSN 1947-5454. doi: 10.1146/annurev-conmatphys-031214-014514. URL http://www.annualreviews.org/doi/abs/10.1146/annurev-conmatphys-031214-014514http://www.annualreviews.org/doi/10.1146/annurev-conmatphys-031214-014514.

D.a. Knoll and D.E. Keyes. Jacobian-free Newton–Krylov methods: a survey of approaches and applications. *Journal of Computational Physics*, 193(2):357–397, jan 2004. ISSN 00219991. doi: 10.1016/j.jcp.2003.08.010.

Tobias Kreilos. *Turbulence Transition in Shear Flows and Dynamical Systems Theory*. PhD thesis, Philipps-Universität Marburg, 2014.

Tobias Kreilos and Bruno Eckhardt. Periodic orbits near onset of chaos in plane Couette flow. *Chaos: An Interdisciplinary Journal of Nonlinear Science*, 22(4):047505, 2012. ISSN 10541500. doi: 10.1063/1.4757227.

Tobias Kreilos, Gregor Veble, Tobias M. Schneider, and Bruno Eckhardt. Edge states for the turbulence transition in the asymptotic suction boundary layer. *Journal of Fluid Mechanics*, 726:100–122, 2013. ISSN 00221120. doi: 10.1017/jfm.2013.212.

Tobias Kreilos, Bruno Eckhardt, and Tobias M Schneider. Increasing Lifetimes and the Growing Saddles of Shear Flow Turbulence. *Physical Review Letters*, 112(4):044503, jan 2014. ISSN 0031-9007. doi: 10.1103/PhysRevLett.112.044503.

M. Krupa. Robust Heteroclinic Cycles. *Journal of Nonlinear Science*, 7(2):129–176, 1997. ISSN 09388974. doi: 10.1007/BF02677976.

Martin Krupa and Ian Melbourne. Asymptotic stability of heteroclinic cycles in systems with symmetry. *Ergodic Theory and Dynamical Systems*, 15(1):121–147, 1995. ISSN 14694417. doi: 10.1017/S0143385700008270.

L D Landau and E M Lifschitz. *Fluid Mechanics*. Elsevier Science, 2nd edition, 1987.

Oscar E Lanford. The Strange Attractor Theory of Turbulence. *Annual Review of Fluid Mechanics*, 14:347–364, 1982.

Grégoire Lemoult, Konrad Gumowski, Jean-Luc Aider, and José Eduardo Wesfreid. Turbulent spots in channel flow: an experimental study: large-scale flow, inner structure and low-order model. *The European physical journal. E, Soft matter*, 37(4):25, 2014. ISSN 1292-895X. doi: 10.1140/epje/i2014-14025-2. URL http://www.ncbi.nlm.nih.gov/pubmed/24771238.

Grégoire Lemoult, Liang Shi, Kerstin Avila, Shreyas V Jalikop, Marc Avila, and Björn Hof. Directed percolation phase transition to sustained turbulence in Couette flow. *Nature Physics*, 12(March):254–258, 2016. ISSN 1745-2473. doi: 10.1038/nphys3675. URL http://arxiv.org/abs/1510.07868{%}5Cnhttp://www.nature.com/doifinder/10.1038/nphys3675.

Timothy M Lenton, Hermann Held, Elmar Kriegler, Jim W Hall, Wolfgang Lucht, Stefan Rahmstorf, and Hans Joachim. Tipping elements in the Earth's climate system. *Proceedings of the National Academy of Sciences*, 105(6):1786–1793, 2008. ISSN 0027-8424. doi: 10.1073/pnas.0705414105.

Edward N Lorenz. Deterministic Nonperiodic Flow. *Journal of the Atmospheric Sciences*, 20(2):130–141, mar 1963. ISSN 0022-4928. doi: 10.1175/1520-0469(1963)020<0130:DNF>2.0.CO;2. URL http://journals.ametsoc.org/doi/abs/10.1175/1520-0469{%}281963{%}29020{%}3C0130{%}3ADNF{%}3E2.0.CO{%}3B2.

A Lundbladh and A V Johansson. Direct simulation of turbulent spots in plane Couette flow. *Journal of Fluid Mechanics*, 229:499–516, apr 1991. ISSN 0022-1120. doi: 10.1017/S0022112091003130.

W. V. R. Malkus. Boussinesq equations. *Notes on the 1964 Summer Study Program in Geophysical Fluid Dynamics at the Woods Hole Oceanographic Institution Vol. 1*, pages 1–12, 1964.

Paul Manneville. Turbulent patterns in wall-bounded flows: A Turing instability? *EPL (Europhysics Letters)*, 98(6):64001, 2012. ISSN 0295-5075. doi: 10.1209/0295-5075/98/64001. URL http://stacks.iop.org/0295-5075/98/i=6/a=64001?key=crossref.c94893b87a78bd6b1f51345b544f8540.

Paul Manneville. Laminar-Turbulent Patterning in Transitional Flows. *Entropy*, 19(7):316, 2017. ISSN 1099-4300. doi: 10.3390/e19070316. URL http://www.mdpi.com/1099-4300/19/7/316.

Konstantin Melnikov, Tobias Kreilos, and Bruno Eckhardt. Long-wavelength instability of coherent structures in plane Couette flow. *Physical Review E*, 89(4):043008, apr 2014. ISSN 1539-3755. doi: 10.1103/PhysRevE.89.043008.

Isabel Mercader, Joana Prat, and Edgar Knobloch. Robust heteroclinic cycles in two-dimensional Rayleigh-Bénard convection without Boussinesq symmetry. *International Journal of Bifurcation and Chaos in Applied Sciences and Engineering*, 12(11):2501–2522, 2002. ISSN 02181274. doi: 10.1142/S0218127402006047.

Alvaro Meseguer, Fernando Mellibovsky, Marc Avila, and Francisco Marques. Instability mechanisms and transition scenarios of spiral turbulence in Taylor-Couette flow. *Physical Review E - Statistical, Nonlinear, and Soft Matter Physics*, 80(4):1–4, 2009. ISSN 15393755. doi: 10.1103/PhysRevE.80.046315.

Jiro Mizushima and Hiroki Tanaka. Transitions of natural convection in a vertical fluid layer. *Physics of Fluids*, 14, 2002a. ISSN 00319015. doi: 10.1143/JPSJ.71.2898.

Jiro Mizushima and Hiroki Tanaka. Transition Routes of Natural Convection in a Vertical Fluid Layer. *Journal of the Physical Society of Japan*, 71(12):2898–2906, 2002b. ISSN 00319015. doi: 10.1143/JPSJ.71.2898.

Stephen W Morris, Eberhard Bodenschatz, David S Cannell, and Guenter Ahlers. Spiral defect chaos in large aspect ratio Rayleigh-Bénard convection. *Physical Review Letters*, 71(13):2026–2029, 1993. ISSN 00319007. doi: 10.1103/PhysRevLett.71.2026.

M Nagata. Three-dimensional finite-amplitude solutions in plane Couette flow: bifurcation from infinity. *Journal of Fluid Mechanics*, 217(-1):519, aug 1990. ISSN 0022-1120. doi: 10.1017/S0022112090000829. URL http://www.journals.cambridge.org/abstract{_}S0022112090000829.

C. Nore, L. S. Tuckerman, O. Daube, and S. Xin. The 1:2 mode interaction in exactly counter-rotating von Kármán swirling flow. *Journal of Fluid Mechanics*, 477(477):51–88, 2003. ISSN 00221120. doi: 10.1017/S0022112002003075.

Wilhelm Nusselt. *Die Wärmeleitfähigkeit von Wärmeisolierstoffen*. PhD thesis, 1908.

R Peyret. *Spectral Methods for Incompressible Flows*. Springer-Verlag, 2002.

Jimmy Philip and Paul Manneville. From temporal to spatiotemporal dynamics in transitional plane Couette flow. *Physical Review E - Statistical, Nonlinear, and Soft Matter Physics*, 83(3): 036308, 2011. ISSN 15393755. doi: 10.1103/PhysRevE.83.036308.

A. Pinter, M. Lücke, and Ch Hoffmann. Competition between traveling fluid waves of left and right spiral vortices and their different amplitude combinations. *Physical Review Letters*, 96 (4):1–4, 2006. ISSN 10797114. doi: 10.1103/PhysRevLett.96.044506.

Y Pomeau and P Manneville. Intermittent Transition to Turbulence in Dissipative Dynamical Systems. *Communications in Mathematical Physics*, 74:189–197, 1980. ISSN 0010-3616. doi: 10.1007/BF01197757.

A Prigent, G Grégoire, H Chaté, O Dauchot, and W van Saarloos. Large-Scale Finite-Wavelength Modulation within Turbulent Shear Flows. *Physical Review Letters*, 89(1):014501, jun 2002. ISSN 0031-9007. doi: 10.1103/PhysRevLett.89.014501.

Arnaud Prigent, Guillaume Grégoire, Hugues Chaté, and Olivier Dauchot. Long-wavelength modulation of turbulent shear flows. *Physica D: Nonlinear Phenomena*, 174:100–113, 2003. ISSN 01672789. doi: 10.1016/S0167-2789(02)00685-1.

M. R.E. Proctor and C. A. Jones. The interaction of two spatially resonant patterns in thermal convection. Part 1. Exact 1:2 resonance. *Journal of Fluid Mechanics*, 188:301–335, 1988. ISSN 14697645. doi: 10.1017/S0022112088000746.

Florian Reetz and Tobias M Schneider. Invariant states in inclined layer convection. Part 1. Temporal transitions along dynamical connections between invariant states. *arXiv*, 2019a.

Florian Reetz and Tobias M Schneider. Invariant state space structure of weakly turbulent inclined layer convection. *in preparation*, 2019b.

Florian Reetz, Tobias Kreilos, and Tobias M Schneider. Exact invariant solution reveals the origin of self-organized oblique turbulent-laminar stripes. *Nature Communications*, 10(1): 2277, 2019a. ISSN 2041-1723. doi: 10.1038/s41467-019-10208-x. URL https://doi.org/10.1038/s41467-019-10208-x.

Florian Reetz, Priya Subramanian, and Tobias M Schneider. Invariant states in inclined layer convection. Part 2. Bifurcations and connections between branches of invariant states. *arXiv*, 2019b.

David Ruelle and Floris Takens. On the Nature of Turbulence. *Communications in Mathematical Physics*, 20(3):167–192, 1971. doi: 10.1007/BF01646553.

By Douglas W Ruth, K G T Hollands, and A N D G D Raithby. On free convection experiments in inclined air layers heated from below. *Journal of Fluid Mechanics*, 96(3):461–479, 1980a.

Douglas W. Ruth, G. D. Raithby, and K. G. T. Hollands. On the secondary instability in inclined air layers. *Journal of Fluid Mechanics*, 96(3):481–492, 1980b. ISSN 0022-1120. doi: 10.1017/s0022112080002236.

Yousef Saad. *Iterative Methods for Sparse Linear Systems*. Society for Industrial and Applied Mathematics, jan 2003. ISBN 978-0-89871-534-7. doi: 10.1137/1.9780898718003. URL http://epubs.siam.org/doi/book/10.1137/1.9780898718003.

M Salewski, John F Gibson, and Tobias M Schneider. The origin of localized snakes-and-ladders solutions of plane Couette flow. 2019.

J Sánchez and M Net. On the Multiple Shooting Continuation of Periodic Orbits By Newton–Krylov Methods. *International Journal of Bifurcation and Chaos*, 20(01):43–61, jan 2010. ISSN 0218-1274. doi: 10.1142/S0218127410025399.

J. Sanchez, M. Net, B. Garcıia-Archilla, and C. Simo. Newton–Krylov continuation of periodic orbits for Navier–Stokes flows. *Journal of Computational Physics*, 201(1):13–33, nov 2004. ISSN 00219991. doi: 10.1016/j.jcp.2004.04.018. URL https://linkinghub.elsevier.com/retrieve/pii/S0021999104001895.

David G. Schaeffer and John W. Cain. *Ordinary Differential Equations: Basics and Beyond*, volume 65. 2016. ISBN 978-1-4939-6387-4. doi: 10.1007/978-1-4939-6389-8. URL http://link.springer.com/10.1007/978-1-4939-6389-8.

Tobias M Schneider, Bruno Eckhardt, and James A Yorke. Turbulence transition and the edge of chaos in pipe flow. *Physical Review Letters*, 99:34502, jul 2007. doi: 10.1103/PhysRevLett.99.034502.

Tobias M Schneider, John F Gibson, Maher Lagha, Filippo De Lillo, and Bruno Eckhardt. Laminar-turbulent boundary in plane Couette flow. *Physical Review E*, 78(3):037301, sep 2008. ISSN 1539-3755. doi: 10.1103/PhysRevE.78.037301. URL http://arxiv.org/abs/0805.1015http://link.aps.org/doi/10.1103/PhysRevE.78.037301.

Tobias M Schneider, J F Gibson, and J Burke. Snakes and Ladders: Localized Solutions of Plane Couette Flow. *Physical Review Letters*, 104(10):104501, mar 2010a. ISSN 0031-9007. doi: 10.1103/PhysRevLett.104.104501.

Tobias M Schneider, Daniel Marinc, and Bruno Eckhardt. Localized edge states nucleate turbulence in extended plane Couette cells. *Journal of Fluid Mechanics*, 646:441, mar 2010b. ISSN 0022-1120. doi: 10.1017/S0022112009993144. URL http://www.journals.cambridge.org/abstract{_}S0022112009993144.

J N Shadid and R J Goldstein. Visualization of longitudinal convection roll instabilities in an inclined enclosure heated from below. *Journal of Fluid Mechanics*, 215:61–84, 1990. ISSN 14697645. doi: 10.1017/S0022112090002555.

J D Skufca, James A Yorke, and Bruno Eckhardt. Edge of chaos in a parallel shear flow. *Physical Review Letters*, 96:174101, may 2006. doi: 10.1103/PhysRevLett.96.174101.

Philippe R. Spalart, Robert D. Moser, and Michael M. Rogers. Spectral methods for the Navier-Stokes equations with one infinite and two periodic directions. *Journal of Computational Physics*, 96(2):297–324, 1991. ISSN 10902716. doi: 10.1016/0021-9991(91)90238-G.

Steven H Strogatz. *Nonlinear Dynamics and Chaos with Student Solutions Manual: With Applications to Physics, Biology, Chemistry, and Engineering*. CRC Press, 2018.

Priya Subramanian, Oliver Brausch, Karen E. Daniels, Eberhard Bodenschatz, Tobias M. Schneider, and Werner Pesch. Spatio-temporal patterns in inclined layer convection. *Journal of Fluid Mechanics*, 794:719–745, 2016. ISSN 0022-1120. doi: 10.1017/jfm.2016.186. URL http://www.journals.cambridge.org/abstract{_}S0022112016001865.

Balachandra Suri, Jeffrey Tithof, Roman O. Grigoriev, and Michael F. Schatz. Forecasting Fluid Flows Using the Geometry of Turbulence. *Physical Review Letters*, 118(11):1–5, 2017. ISSN 10797114. doi: 10.1103/PhysRevLett.118.114501.

H L Swinney and J P Gollub. The transition to turbulence. *Physics Today*, 31(8):41, 1978. ISSN 00319228. doi: 10.1063/1.2995142.

Randall Tagg, W Stuart Edwards, Harry L Swinney, and S Marcus. Nonlinear standing waves in Couette-Taylor flow. *Physical Review A*, 39(7):3734–3738, 1989.

Nils Tillmark and P. Henrik Alfredsson. Experiments on transition in plane Couette flow. *Journal of Fluid Mechanics*, 235:89–102, 1992. ISSN 0022-1120. doi: 10.1017/S0022112092001046. URL http://www.journals.cambridge.org/abstract{_}S0022112092001046.

L N Trefethen and D Bau. *Numerical Linear Algebra*. SIAM, 1997. ISBN 0898713617, 9780898713619.

T Tsukahara, Y Seki, H Kawamura, and D Tochio. DNS of Turbulent Channel Flow with very low Reynolds Numbers. In *Proceedings of the Fourth International Symposium on Turbulence and Shear Flow Phenomena*, pages 935–940, Williamsburg, VA, USA, 27-29 Jun., 2005. Begell House Inc. URL http://www.tsfp-conference.org/proceedings/2005/tsfp4-ga-5.pdfhttps://arxiv.org/abs/1406.0248http://www.dl.begellhouse.com/references/3ce1b491115b5c16,34d18f9c601fac9f,56d8f25b7ee6529a.html.

Laurette S. Tuckerman and Dwight Barkley. Bifurcation analysis of the Eckhaus instability. *Physica D: Nonlinear Phenomena*, 46(1):57–86, oct 1990. ISSN 01672789. doi: 10.1016/0167-2789(90)90113-4. URL http://linkinghub.elsevier.com/retrieve/pii/0167278990901134.

Laurette S. Tuckerman and Dwight Barkley. Patterns and dynamics in transitional plane Couette flow. *Physics of Fluids*, 23(4):041301, 2011. ISSN 10706631. doi: 10.1063/1.3580263.

Laurette S Tuckerman, Tobias Kreilos, Hecke Schrobsdorff, Tobias M Schneider, and John F Gibson. Turbulent-laminar patterns in plane Poiseuille flow. *Physics of Fluids*, 26:114103, 2014. doi: 10.1063/1.4900874.

Laurette S. Tuckerman, Matthew Chantry, and Dwight Barkley. Patterns in Wall-Bounded Shear Flows. *Annual Review of Fluid Mechanics*, 52(1):343–367, 2020. ISSN 0066-4189. doi: 10.1146/annurev-fluid-010719-060221.

L van Veen, G Kawahara, and M Atsushi. On Matrix-Free Computation of 2D Unstable Manifolds. *SIAM Journal on Scientific Computing*, 33(1):25–44, jan 2011. ISSN 1064-8275. doi: 10.1137/100789804. URL http://epubs.siam.org/doi/abs/10.1137/100789804.

Charles M. Vest and Vedat S. Arpaci. Stability of natural convection in a vertical slot. *Journal of Fluid Mechanics*, 36(01):1, 1969. ISSN 0022-1120. doi: 10.1017/S0022112069001467. URL http://www.journals.cambridge.org/abstract{_}S0022112069001467.

D Viswanath. Recurrent motions within plane Couette turbulence. *Journal of Fluid Mechanics*, 580:339–358, 2007. ISSN 0022-1120. doi: 10.1017/S0022112007005459.

F Waleffe. Three-dimensional coherent states in plane shear flows. *Physical Review Letters*, 81: 4140–4143, nov 1998. doi: 10.1103/PhysRevLett.81.4140.

Fabian Waleffe. On a self-sustaining process in shear flows. *Physics of Fluids*, 9(June 1996):883, 1997. ISSN 10706631. doi: 10.1063/1.869185. URL http://link.aip.org/link/PHFLE6/v9/i4/p883/s1{&}Agg=doi{%}5Cnhttp://link.aip.org/link/PHFLE6/v9/i4/p883/s1{%}5Cnpapers2://publication/uuid/96F1BE98-548D-491B-B6A0-41B444840F39.

Fabian Waleffe, Anakewit Boonkasame, Leslie M Smith, Fabian Waleffe, Anakewit Boonkasame, and Leslie M Smith. Heat transport by coherent Rayleigh-Bénard convection Heat transport by coherent Rayleigh-Bénard convection. *Physics of Fluids*, 051702(May), 2015. doi: 10.1063/1.4919930.

S Weiss, G Seiden, and E Bodenschatz. Pattern formation in spatially forced thermal convection. *New Journal of Physics*, 053010:14; 053010, 2012. ISSN 1367-2630. doi: 10.1088/1367-2630/14/5/053010.

Xiangming Xiong, Jianjun Tao, Shiyi Chen, and Luca Brandt. Turbulent bands in plane-Poiseuille flow at moderate Reynolds numbers. *Physics of Fluids*, 27(4):041702, 2015. ISSN 10897666. doi: 10.1063/1.4917173.

T Zang and M Y Hussaini. Numerical experiments on subcritical transition mechanisms. In *23rd Aerospace Sciences Meeting*, Reston, Virigina, jan 1985. American Institute of Aeronautics and Astronautics. doi: 10.2514/6.1985-296. URL http://arc.aiaa.org/doi/10.2514/6.1985-296.

Thomas A. Zang. On the rotation and skew-symmetric forms for incompressible flow simulations. *Applied Numerical Mathematics*, 7(1):27–40, 1991. ISSN 01689274. doi: 10.1016/0168-9274(91)90102-6.

Acknowledgements

Doing a PhD is most of all a relationship between a person and a problem. I went into such a relationship hoping to understand a problem in-depth and to make my contribution. Thank you, Tobias, for providing the perfect environment for exactly this experience. You offered me a problem that I have enjoyed every single day of my PhD. Moreover, I am very grateful for the time in a growing lab in which team-work is so important, for your trust when I got challenged on multiple levels, for explaining me writing, and for all the inspiring scientific and non-scientific discussions with you. It was a great pleasure to be your student.
I am very thankful for the scientific input that I received from Prof. Laurette Tuckerman and Prof. Edgar Knobloch during several conferences and workshops, in emails and at my thesis defense. I also thank Prof. François Gallaire for examining my thesis, and even more for many wonderful LFMI-ECPS activities over the years of my PhD. My gratitude also goes to Prof. William Curtin for presiding over the jury of the thesis defense. I thank Prof. John Gibson and Massimiliano Culpo for the discussions and the collaborative work on Channelflow 2.0.
I had the privilege to work together with many friends at the ECPS lab. I am very grateful to Tobias Kreilos who, during my first year, taught me everything I know about Channelflow and paved the way to make this a successful thesis. I thank Priya Subramanian who turned from a former office mate to a collaborator and who was supporting me throughout my PhD. I had the luck to have Sajjad Azimi as my PhD companion. Together, we started and shared all offices and problems with each other. Thank you, Sajjad, for your company, wisdom and support in all these years. I thank Simon, Alessia, Emilio, Omid, Geoffroy, Mirko, Ayşe and Hecke for sparkling lab activities, coffee breaks, code development, and other joint adventures. Thank you, Petra, for caring for us and your assistance during my PhD.
This thesis belongs as much to me as it belongs to Romy. Without her backing and unconditional support I would have not been able to do this PhD. Thank you so much, Romy and Björn, for your patience and love. I also thank the rest of my family, for their understanding and numerous travels to Switzerland. I am blessed with wonderful friends, old ones and new ones. I thank all of you for your friendship that outlasts a relationship with a problem.

Bern, 3 November 2019 Florian Reetz

Born 08.05.1988
as Florian Sprung
in Osterode/Harz

German

Married, One Child

Florian Reetz

Languages

German – mother tongue
English – excellent knowledge
French – basic knowledge
Norwegian – basic knowledge

ADDRESS
Freiburgstrasse 54
3008 Bern
Switzerland

PHONE
+49 157 56020397

EMAIL
fsprung@gmx.de

WEBSITE
channelflow.ch

EDUCATION

07/2015– 11/2019
PhD in Mechanical Engineering • EPFL • Switzerland

10/2012– 06/2015
M.Sc. in Physics • University of Hamburg • Germany
Master thesis at Max-Planck Institute for Dynamics and Self-Organization, Göttingen:
"Decay rates of helical and non-helical isotropic turbulence"

10/2008– 09/2012
B.Sc. in Geophysics/Oceanography • University of Hamburg • Germany
Exchange studies at National Oceanographic Center (2010-2011), Southampton, UK

06/2007
Abitur • Tilman-Riemenschneider-Gymnasium, Osterode • Germany

PROFESSIONAL EXPERIENCES

08/2013– 11/2013
Philips Medical Research • Hamburg • Germany
Project on computational fluid dynamics to study blood vessels

06/2012– 08/2012
Alfred-Wegener Institute • Ny Alesund, Spitzbergen • Norway
Scientific scuba diving assistance for studies on Fjord ecology

08/2007– 05/2008
DRK Ambulance • Osterode am Harz • Germany
Ambulance service

TEACHING EXPERIENCES

Teaching assistant:
Incompressible fluid mechanics (EPFL Master 2016-2018, by T. Schneider)
Fluid mechanics (Uni. Hamburg Bachelor 2012)
Physics 1 and 2 (Uni. Hamburg Bachelor 2009-2010)

Student supervision (semester projects):
Heat transport in Rayleigh-Bénard convection (EPFL Bachelor 2018)
Optimal sinker II (EPFL Bachelor 2017)
Optimal sinker I (EPFL Bachelor 2016)

CONFERENCES AND WORKSHOPS

Conference talks:

- "Nonlinear dynamics of bursting spots in subcritical inclined convection", ETC17, Torino, Italy, 03-06/09/2019
- "Spatially localized invariant solution of inclined layer convection: how transverse bursts emerge", EFMC12, Vienna, Austria, 09-13/09/2018
- "Spatially localized invariant solution of inclined layer convection: how transverse bursts emerge", Pattern formation in fluids and soft matter, University of Leeds, UK, 06-09/08/2018
- "Emergence of invariant solutions underlying oblique turbulent-laminar stripes in plane Couette flow", APS March Meeting, Los Angeles, California, 05-09/03/2018
- "Invariant solutions of turbulent-laminar stripes in plane Couette flow", Euromech Symp. 591: 3D instability mechanisms transitional and turbulent flows, Bari, IT, 18-20/09/2017
- "Spots, stripes and turbulence", Scitas, EPFL, 15/06/2017

Seminar talks:

- "Pattern formation in the transition to turbulence in shear flows", Department of Mathematics, University of Leeds, UK, 25/04/2017
- "Spots and stripes: how turbulent-laminar patterns form in shear flows", MEGA seminar, EPFL, 23/05/2019

Poster:

- "Exact coherent states and nonlinear dynamics of inclined layer convection", The 6th Bremen winter school and symposium: dynamical systems and turbulence, 12- 16/03/2018

SCHOLARSHIPS

Ambassadorial Scholarship, Rotary International, 2010/2011

**Ce document a été imprimé au Centre d'impression EPFL,
imprimerie climatiquement neutre, certifiée myClimate.**